DISS. ETH NO. 30187

Increasing fine sediment source, flux, and connectivity understanding using novel measurement techniques and self-made turbidity sensors

A thesis submitted to attain the degree of
DOCTOR OF SCIENCES
(Dr. Sc. ETH Zürich)

presented by

Jessica Droujko
MSc ETH in Maschineningenieurwissenschaften
born on 19.06.1993

accepted on the recommendation of
Prof. Dr. Peter Molnar, Examiner
Prof. Dr. Daniel Farinotti, Co-examiner
Prof. Dr. Stuart Lane, Co-examiner
Prof. Dr. Gabriel Singer, Co-examiner
Prof. Dr. John Selker, Co-examiner

2024

Acknowledgements

This dissertation represents not just the culmination of years of research and hard work, but also a journey filled with support, guidance, and collaboration from many incredible individuals. It is with a deep sense of gratitude that I acknowledge those who have made this journey not just possible, but also enjoyable and immensely rewarding.

Firstly, I extend my heartfelt thanks to Michael, Pascal, and Thomas from the machine tools lab. Their generosity in allowing me unfettered access to the machines, their patience in calibrating tools, and their guidance in using them have been invaluable. Their contribution to crafting some of the most precise parts for the sensor, especially Michael's collaboration in designing the first version, has been instrumental in the success of this project.

I am equally grateful to Lucien, Luzia, and Dani from the LUIW Lab for ensuring I always had lab access and everything I needed at my disposal. Their support was crucial in facilitating my research activities without hindrance.

A special thanks goes to Manuela, whose patience and diligence with the endless stream of receipts and reimbursements kept the administrative side of this project running smoothly. Your efficiency and understanding did not go unnoticed.

My fieldwork friends, Fanzi, Jens, and Srividya, deserve a huge shoutout for their assistance on the Vjosa. Your help was pivotal in collecting the data necessary for our findings. Similarly, Jan's meticulous work in weighing over 50 Seston filters and correlating them with their metadata was a significant contribution to our work.

For the invaluable fieldwork assistance on the Spöl and the Rhône, I am thankful to Ludovico, Constance, Maria, and Jovan. Your help was crucial in gathering essential data from these challenging environments.

Martin from the electronics lab, your guidance in sourcing LiPo batteries and strong cables, and educating me about part selection, have been fundamental in enhancing the reliability of our sensors.

Marius, you were always generous to lend me any tools I needed, always there to answer my questions, and would always find a solution to any problem I had (even if you didn't have the answer, you would connect me with someone that did), and for that, I am utmost grateful.

Felix, your contributions to the Spöl fieldwork, PCB design, and enduring my indecisiveness have been remarkable. Moritz, your expertise in embedded programming, bug fixing,

and sensor installations until we achieved a LoRa signal, was indispensable.

To Stefano, for your companionship during the not-so-safe Rhône fieldwork and for being an incredible work bestie.

To the IfU group – Marius, Mosisa, Ludovico, Sophia, Sasha, Dennis, Scott, Anna, Maria, Jovan, Stefano, Yue, Darcy, Peter, and Paolo – my heartfelt thanks for the countless adventures, training sessions, BBQs, and group lunches. These shared moments and the laughter we enjoyed together fostered a motivating, supportive, and joyous work environment that I've come to cherish deeply.

To Prof. Dr. Gabriel Singer, for providing me with endless opportunities in Berlin and Innsbruck, and for taking me to Albania and teaching me about ecology, teamwork, and using science (and your voice) for river conservation.

To Ruben, for your guidance and patience in electronics and embedded programming and for holding my hand when these things drove me to frustration and tears.

To my family – my grandma, grandpa, sister, and mother – your unwavering love and support have been my foundation. Your reminder to tackle challenges or "eat an elephant one bite at a time" has been a guiding principle in my journey.

Last but certainly not least, I owe a debt of gratitude to my PhD supervisor, Prof. Dr. Peter Molnar. Five years ago, I approached you with no experience in electronics, embedded programming, or product design (which you didn't know). All I brought was a mechanical engineering degree and a vision. You not only believed in me and gave me the opportunity to build something that I considered important for my freshwater-friends (e.g. kayakers, fish), but you also nurtured that dream. For that, for this opportunity, I am eternally grateful.

Contents

Abstract

Riverine suspended sediments are necessary for regulating the balance of nutrients in water, play a large role in marine primary productivity, and are integral to the management of freshwater systems. However, excess amounts of these fine sediments can lead to several negative ecological effects and a general decline in water quality. Therefore, a deeper understanding of fine sediment dynamics is crucial. This dissertation sets out to enhance our understanding and monitoring capabilities of fine suspended sediment transport in river systems, a critical component influencing aquatic ecosystems, nutrient dynamics, and water quality. Given the pivotal role of sediment dynamics in shaping riverine, coastal, and marine environments, there's a pressing need for innovative monitoring techniques that overcome the limitations of traditional methods, characterized by high costs and constrained spatial-temporal resolution. This work, therefore, explores cost-effective, scalable solutions such as utilizing remote sensing technologies, novel sensor development, and deploying a sensor network to advance the state-of-the-art in fine sediment transport monitoring.

The first segment of this research investigates the potential of satellite data to identify sediment sources and sinks within smaller river systems. The successful application of Sentinel-2 satellite imagery, combined with ground-based turbidity measurements on the Vjosa River, expanded the spatial coverage of our monitoring efforts. This contributed to our understanding of sediment transport spatial variability and the identification of potential sediment sources and sinks within the river network, particularly highlighting the seasonal signal in sediment transport and changes upstream and downstream of tributaries and within river reaches. However, it was not possible to extract data on suspended sediment concentrations in the narrower upstream river sections where satellite visibility was limited. Therefore, this first part was a necessary step in understanding the limitations of satellite imagery. From this knowledge, I determined that there is a critical need to develop a new fine sediment monitoring solution that is both highly accurate and able to extract high spatio-temporal data in both large and small river systems.

Building upon the foundational insights gained, this dissertation progresses to the development and validation of a turbidity sensor designed to address the identified shortcomings from the previous part. This sensor offers accurate, reproducible, and affordable sediment monitoring for widespread application across river networks. Through meticulous design and testing, including comparative analyses with commercial probes using several sediment types, the sensor demonstrated its capability to provide high-quality measurements over a broad suspended sediment concentration range. In an additional step, the sensor was developed further to include a pressure and temperature sensor, data storage capabilities, and a larger battery. This newer version's performance was field tested in a challenging environmental condition and successfully measured the passage of a flood in a glacial stream.

The final phase of this dissertation applies the newly developed sensor technology in practical field studies, concentrating on the impacts of environmental or experimental floods (e-floods). The deployment of a sensor network during two e-floods on the Spöl river allowed for a detailed examination of the mobilization and distribution of sediments and the propagation of fine sediment waves and their ecological and downstream implications. This work contributed to more informed decision-making regarding the timing and magnitude of water releases. It also underscored the importance of considering the interactions between e-floods and existing river discharge conditions to mitigate potential siltation and ecological impacts downstream.

In conclusion, this dissertation underscores the importance of the novel sensor I developed and its application in a network to obtain high spatio-temporal resolution data in small and large river systems. While the initial chapters lay the foundation by addressing the limitations of existing monitoring methods and exploring the integration of remote sensing, the subsequent chapters focus on developing and testing the sensor and its applications under challenging environmental conditions to answer several research questions. This newly developed system not only addresses the critical gaps identified in earlier chapters but also underscores the potential of a high spatio-temporal resolution sensor network to enhance our understanding of suspended sediment dynamics in river systems. The insights from such a network can be further enhanced by leveraging satellite imagery and physically-based modeling. Applications of such a network are plentiful, from supporting civil engineering companies, hydropower operators, and gravel extraction businesses operating in rivers needing to comply with local regulations and to better manage fine sediments, to supporting river restoration projects and administration authorities searching for point and diffuse sources of pollution.

Zusammenfassung

Schwebstoffe in Flüssen sind für die Regulierung des Nährstoffgleichgewichts im Wasser notwendig, spielen eine große Rolle bei der Primärproduktivität der Meere und sind für die Bewirtschaftung von Süßwassersystemen unerlässlich. Ein Übermaß an diesen Feinsedimenten kann jedoch zu verschiedenen negativen ökologischen Auswirkungen und einer allgemeinen Verschlechterung der Wasserqualität führen. Daher ist ein tieferes Verständnis der Dynamik von Feinsedimenten von entscheidender Bedeutung. Diese Dissertation zielt darauf ab, das Verständnis und die Überwachungsmöglichkeiten für den Transport feiner Schwebstoffe in Flusssystemen zu verbessern. Diese Schwebstoffe sind eine entscheidende Komponente für aquatische Ökosysteme sowie für die Nährstoffdynamik und Wasserqualität.

Angesichts der entscheidenden Bedeutung der Sedimentdynamik für die Gestaltung von Fluss-, Küsten- und Meeresumgebungen besteht ein dringender Bedarf an innovativen Überwachungsmethoden. Diese sollten die Grenzen herkömmlicher Methoden überwinden, die durch hohe Kosten und begrenzte räumliche sowie zeitliche Auflösung gekennzeichnet sind. Diese Arbeit untersucht daher kosteneffiziente, skalierbare Lösungen wie die Nutzung von Bürgerwissenschaft, die Verwendung von Fernerkundungstechnologien, die Entwicklung neuartiger Sensoren und den Einsatz eines Sensornetzwerks, um den Stand der Technik bei der Überwachung des Feinsedimenttransports zu verbessern.

Im ersten Teil dieser Forschungsarbeit wird das Potenzial von Satellitendaten zur Ermittlung von Sedimentquellen und -senken in kleineren Flusssystemen untersucht. Durch den erfolgreichen Einsatz von Sentinel-2-Satellitenbildern in Verbindung mit bodengestützten Trübungsmessungen am Fluss Vjosa konnte die geografische Abdeckung unserer Überwachungsmaßnahmen erweitert werden. Dies trug zu unserem Verständnis der räumlichen Variabilität des Sedimenttransports und zur Identifizierung potenzieller Sedimentquellen und -senken innerhalb des Flussnetzes bei, wobei insbesondere das saisonale Signal des Sedimenttransports und die Veränderungen flussaufwärts und flussabwärts von Nebenflüssen und innerhalb von Flussabschnitten hervorgehoben wurden. Es war jedoch nicht möglich, Daten über die Schwebstoffkonzentrationen in den engeren stromaufwärts gelegenen Flussabschnitten zu extrahieren, wo die Satellitensichtbarkeit begrenzt war. Daher war dieser erste Teil ein notwendiger Schritt, um die Grenzen von Satellitenbildern und simplen Trübungssensoren zu verstehen.

Aus diesem Teil ergab sich die dringende Notwendigkeit, eine neue Lösung für die Überwachung von Feinsedimenten zu entwickeln. Diese Lösung sollte sowohl hochpräzise sein als auch in der Lage sein, umfangreiche räumlich-zeitliche Daten sowohl in großen als auch in kleinen Flusssystemen zu erfassen. Aufbauend auf den gewonnenen grundlegenden Erkenntnissen geht diese Dissertation zur Entwicklung und Validierung eines Open-Source-Trübungssensors über, der die im vorherigen Teil festgestellten Mängel beheben soll. Dieser innovative Sen-

sor stellt einen bedeutenden Fortschritt dar, da er eine genaue, reproduzierbare und erschwingliche Sedimentüberwachung für eine breite Anwendung in Flussnetzen ermöglicht. Sein Open-Source-Design erleichtert den Einsatz für umfangreiche, hochauflösende Sedimentstudien. Durch sorgfältige Entwicklung und Erprobung, einschließlich vergleichender Analysen mit kommerziellen Sensoren unter Verwendung verschiedener Sedimenttypen, hat der Sensor seine Fähigkeit unter Beweis gestellt, qualitativ hochwertige Messungen über einen breiten Konzentrationsbereich von Schwebstoffen zu liefern. Dies ebnet den Weg für eine verbesserte Überwachung des Sedimentflusses in größerem Maßstab. In einem weiteren Schritt wurde der Sensor um einen Druck- und einen Temperatursensor, Datenspeichermöglichkeiten und eine größere Batterie erweitert. Die Leistung dieser neueren Version wurde in einem Feldversuch unter schwierigen Umweltbedingungen getestet, wobei der Durchfluss eines Hochwassers in einem Gletscherbach erfolgreich gemessen wurde.

In der letzten Phase dieser Dissertation wird die neu entwickelte Sensortechnologie in praktischen Feldstudien angewandt, wobei der Schwerpunkt auf den Auswirkungen von Hochwasserereignissen zu Flusssystemen liegt. Der Einsatz eines Sensornetzwerks während zweier experimenteller Hochwasser am Spöl ermöglichte eine detaillierte Untersuchung der Mobilisierung und Verteilung von Sedimenten sowie der Ausbreitung von Feinsedimentwellen und ihrer ökologischen und flussabwärts gerichteten Auswirkungen. Diese Arbeit trug zu einer fundierteren Entscheidungsfindung in Bezug auf den Zeitpunkt und die Höhe der Wasserabgabe bei, um die gewünschten ökologischen Ergebnisse zu erzielen. Außerdem wurde deutlich, wie wichtig es ist, die Wechselwirkungen zwischen E-Fluten und bestehenden Abflussverhältnissen zu berücksichtigen, um mögliche Verschlammungen und ökologische Auswirkungen flussabwärts abzumildern.

Abschließend unterstreicht diese Dissertation die Bedeutung des von mir entwickelten neuartigen Open-Source-Sensors und seiner Anwendung in einem Netzwerk zur Gewinnung von Daten mit hoher räumlicher und zeitlicher Auflösung in engen Flusssystemen. Während die ersten Kapitel den Grundstein legen, indem sie sich mit den Grenzen bestehender Überwachungsmethoden befassen und die Integration von Bürgerwissenschaft und Fernerkundung untersuchen, konzentrieren sich die nachfolgenden Kapitel auf die Entwicklung und Erprobung des Sensors und seiner Anwendungen unter schwierigen Umweltbedingungen, um mehrere Forschungsfragen zu beantworten. Dieses neu entwickelte System schließt nicht nur die kritischen Lücken, die in früheren Kapiteln identifiziert wurden, sondern unterstreicht auch das Potenzial eines Sensornetzwerks mit hoher räumlicher und zeitlicher Auflösung, um unser Verständnis der Sedimentdynamik in Flusssystemen zu verbessern. Die Erkenntnisse aus einem solchen Netzwerk können durch die Nutzung von Satellitenbildern und physikalischer Überwachung weiter verbessert werden. Die Anwendungsmöglichkeiten eines solchen Netzes sind vielfältig und reichen von der Unterstützung von Tiefbauunternehmen, Wasserkraftwerksbetreibern und Kiesabbauunternehmen, die in Flüssen tätig sind und lokale Vorschriften einhalten und Feinsedimente besser verwalten müssen, bis hin zur Unterstützung von Flussrenaturierungsprojekten und Verwaltungsbehörden bei der Suche nach punktuellen und diffusen Verschmutzungsquellen.

Chapter 1 Introduction

1.1 Motivation and problem statement

The transfer of sediment from land to oceans is a crucial component of the global denudational cycle (Gregor, 1970; Wold and Hay, 1990), as well as the global terrestrial and marine biogeochemical cycles (Meybeck, 1994; Ludwig et al., 1996; Sanders et al., 2014). It significantly influences the functioning of riverine and coastal ecosystems (Roy et al., 2001; Arrigo et al., 2008; Terhaar et al., 2021; Descloux et al., 2013), and shapes the evolution of rivers, deltas, and other coastal landforms (Morton, 2003; McLaughlin et al., 2003; Seybold et al., 2009). Annually, approximately 36 Gt of sediment is eroded from the Earth's surface, with the highest rates of erosion often linked to intensive agriculture and rainfall (Borrelli et al., 2017). More than 2,000 of the world's largest rivers contribute to this sediment load, delivering an estimated 15.5–18.5 Gt of sediment annually to the global oceans. A dominant portion of this flux consists of fine-grained material, transported primarily as washload and suspended load (Peucker-Ehrenbrink, 2009; Syvitski and Kettner, 2011; Cohen et al., 2022). This accounts for about half of the estimated global annual soil erosion from land surfaces (Borrelli et al., 2017), emphasizing the significant role of riverine sediment before it reaches the ocean.

Riverine suspended sediments are pivotal in regulating the balance of nutrients (such as phosphorous, nitrogen, and silica) along coastlines and oceans (Nixon et al., 1996; Bernard et al., 2011). They play a significant role in marine primary productivity and are integral to the use and management of river water (Hauer et al., 2018). Excessive amounts of fine sediments in rivers can lead to heightened water turbidity. This increase in turbidity can have several adverse ecological effects. For example, the degradation of coral reefs (Brown et al., 2017), impairment of freshwater and marine fish populations (Kemp et al., 2011; Newport et al., 2021; Jensen et al., 2009), clogging of river beds in gravel-bed streams (Schälchli, 1992; Hauer et al., 2019b), and a general decline in water quality are all associated with an increase in turbidity. A notable recent issue is silica deficiency, resulting from reduced suspended sediment inputs due to river damming. This deficiency has been observed to exacerbate eutrophication by diminishing the role of diatoms in coastal food webs, which indirectly affects mesozooplankton such as copepods (Cotrim da Cunha et al., 2007; Justić et al., 1995). Therefore, a deeper understanding of fine sediment fluxes, their sources, and pathways is crucial. This understanding informs us about the many consequences of sediment dynamics, including nutrient outputs (e.g., nitrogen, phosphorus), pollution with sediment often a primary carrier of pollutants like mercury (Acquavita et al., 2021), impacts on the Earth's carbon budget (particularly the mobilization of soil carbon in long-term sinks) (Coppola et al., 2018), and the ecology of rivers and oceans, among other aspects.

The complex interactions between human activities and climate change significantly impact sediment production and transport. For instance, in High Mountain Asia, global warming is anticipated to boost sediment production by 10-30% (Li et al., 2021). Furthermore, alterations in rainfall patterns and land use could potentially escalate agricultural soil erosion by 30-66% globally (Borrelli et al., 2020). Generally, human activities are expected to amplify fluvial sediment delivery by up to 215% due to agriculture, while paradoxically

reducing the sediment reaching the oceans by 49% due to dam constructions (Syvitski et al., 2022). These large possible changes underscore the need for a comprehensive understanding of sediment dynamics.

While glacial erosion's efficiency may not significantly exceed that of fluvial erosion (Koppes and Montgomery, 2009), the fine sediment yields from glaciated mountain ranges, and particularly large ice sheets, constitute a notable portion of the sediment budget (Hallet et al., 1996). A recent estimate indicates that the Greenland ice sheet alone contributes about 8% of the fine sediment input to the global oceans, despite only accounting for 1% of the Earth's freshwater flux (Overeem et al., 2017). This highlights the increasing impact of global warming on sediment flux in cold environments (Beylich et al., 2016).

An important question is the relative role small and large rivers play in the global sediment flux. While recent studies emphasize the significance of large rivers in the overall global sediment flux (Cohen et al., 2022), smaller mountainous rivers, often overlooked, also play a significant role in sediment dynamics. These rivers, typically with basin areas under 10,000 km^2 and draining elevations above 1,000 m, contribute disproportionately more sediment per unit drainage area compared to larger rivers (Milliman and Farnsworth, 2013). Their contribution is critical yet often underestimated. Despite covering only about 10% of the land area that drains into global oceans, these sediment-rich, smaller mountainous basins are responsible for approximately 15% of the annual water discharge and a remarkable 45% of the annual suspended solids that reach the oceans (Milliman and Farnsworth, 2013). Furthermore, these smaller rivers are more frequently impacted by human activities. They are often subject to channelization for flood control, sediment trapping behind dams, or increased sediment inputs due to agriculture, mining, and intensive land use (Syvitski et al., 2022). In Europe, for instance, there are very few moderately-sized, unregulated rivers left where natural fine sediment dynamics can be observed and studied. It is estimated that over one million instream barriers fragment European rivers (Belletti et al., 2020), significantly altering their natural sediment dynamics.

The impact of human activities on sediment sources is starkly evident in the case of the three largest rivers draining into the Adriatic Sea: the Po, Adige, and Drini. Prior to the construction of dams, these rivers contributed about 25% of the sediment discharged into the Adriatic. The remaining 75% of the sediment input to the Adriatic came from 32 smaller rivers, each with drainage basins less than 7,000 km^2 (Milliman et al., 2016). Before damming, Albanian rivers alone accounted for approximately 60% of the total sediment entering the Adriatic, with the pre-dam Vjosa River discharging over 8.3 $Mtyr^{-1}$, where 80–85% of this flux was suspended load (Ciavola, 1999). To put this in perspective, when compared with the erosion rate of larger rivers – such as the Amazon at 204 $ty^{-1}km^{-2}$, the pre-dam Mississippi at 124 $ty^{-1}km^{-2}$, the St. Lawrence at 4 $ty^{-1}km^{-2}$, and the Yangtze River at 267 $ty^{-1}km^{-2}$ (Milliman and Farnsworth, 2013; Syvitski and Milliman, 2007) – the Vjosa's contribution stands at a remarkable 373 $ty^{-1}km^{-2}$ (Pessenlehner et al., 2022). This underscores the critical role of smaller rivers in the continental denudation cycle and, by extension, the global cycle.

A primary problem in erosion and fine sediment transport estimation is that these are extremely difficult to measure. Only accurate monitoring allows us to quantify the impacts of dam construction and erosion control (Wang et al., 2007; Hu et al., 2011), the natural erosion gradients across entire mountain ranges (Hinderer et al., 2013), and the influence of integration time on global erosion rates (Covault et al., 2013). Additionally, the monitoring

of suspended sediment is crucial for both freshwater and marine ecosystems, as nutrients and inorganic compounds, such as heavy metals, tend to bind readily to fine particles. The two main challenges of suspended sediment monitoring are related to scales, i.e. how do we effectively measure both large and small rivers and many sediment sources, and to methods, i.e. how do we extrapolate information from single-point measurements of suspended sediment concentrations (SSC) for example at outlets of basins (as done for the rivers draining into the Adriatic as previously mentioned), and which temporal sampling resolutions do we need.

Measurements of SSC at a basin outlet provide a comprehensive, basin-integrated perspective of potential hydroclimatically-driven sediment sources. These sources may include rainfall erosion, snowmelt hillslope erosion, glacial ice melt erosion, and even sedimentation from hydropower storage in dams (Costa et al., 2018a). In Alpine landscapes, a statistical partitioning of such sediment sources has revealed that sediment derived from glaciers significantly contributes to SSC variability and the overall sediment budget, even in heavily regulated catchments (Costa et al., 2018b). However, this statistical approach based on basin-averaged forcing falls short of offering a complete spatial understanding of sediment production and storage pathways within the catchment. It also fails to capture the effects of specific events. For instance, high-resolution (sub-daily) measurements of SSC can be instrumental in discerning the impact of hydroclimatic forces on activating sediment sources and their transport dynamics (Bakker et al., 2018; Battista et al., 2020b; Costa et al., 2018b). Such measurements can also offer deeper insights into these hydroclimatic forcings when paired with physically-based models (Battista et al., 2020b,c; Konz et al., 2011; Uber et al., 2021). Without such detailed SSC data, the accuracy and effectiveness of these models in capturing the complexities of sediment transport would be significantly limited.

Higher temporal resolution measurements of SSC, especially in glacier streams which deliver a notable portion of the earth's sediment budget (Hallet et al., 1996), are essential for identifying the dynamic sediment export rates linked to the development and evolution of subglacial channels and to diurnal cycles of ice melt. They are also crucial for assessing the contributions from proglacial sediment sources (Delaney et al., 2018a,b). When combined with grain size measurements, this highly resolved SSC data becomes invaluable for detailed hydraulic modeling. Such modeling is particularly useful for understanding the transport of glacially-derived sediment by meltwater drainage in subglacial streams (Ugelvig et al., 2018). This allows for a clearer understanding of how sediment moves in glacier-fed streams, showing the intricate processes at work in these specific environments.

The connection of hillslope sources to the fluvial network in proglacial areas significantly influences the variability of sediment production over time (Bakker et al., 2018; Lane et al., 2017). To fully understand these dynamics, a spatial perspective on the pathways of sediment production and storage within the catchment is necessary. This understanding extends beyond what can be obtained from single-site measurements typically conducted at the basin outlet. To capture the full extent of sediment dynamics, a new approach to sediment monitoring is necessary. Effective monitoring of sediment flux needs to account for the spatial and temporal variability in concentrations that result from the hydrological processes activating sediment. This variability is evident on both short timescales, such as storm-driven activation of sediment sources, and long timescales, like interannual variability (Morehead et al., 2003; Hu et al., 2011; Costa et al., 2018a,b). The latter is influenced by both climate variability and human activities, capturing the complexity of the sediment

cycle. Examples included in this thesis are climate variabilities in glacier-fed streams and human activities such as flood releases downstream of dams.

In this dissertation, I propose a new approach to sediment monitoring, designed to demonstrate the many physical connections between hydrology, river processes, and sediment fluxes. To adequately capture the relationships between sediment source activation and transport – whether on hillslopes, cultivated fields, vegetated areas, (glacial) streams, large rivers, or deltas – monitoring must occur at both high spatial (from source to sink) and temporal (matching activation timescales) resolutions. This approach must be comprehensive, capturing sediment dynamics from source to sink, in both large and small river systems. Current suspended sediment monitoring standards do not fully address these needs (high spatio-temporal resolution, various river sizes) in a scalable manner. I am convinced that this new type of data is crucial for three important purposes on the interface of hydrology and geomorphology: for developing a comprehensive understanding of sediment storages and budgets in Alpine basins (Bennett et al., 2014, 2013; Hirschberg et al., 2020), for unraveling the complex sediment connectivity pathways in such fluvial systems (Lane et al., 2017; Bakker et al., 2018), and ultimately for the calibration and validation of physically-based hydrological-sediment transport models (Molnar et al., 2006; Seybold et al., 2009; Konz et al., 2011; Battista et al., 2020b).

1.2 Background and State-of-the-Art

Despite the critical role of sediment fluxes in rivers, monitoring sediment concentrations remains a challenging task, particularly when compared to the hydrological monitoring of river stage and discharge. There are three primary methods for sediment concentration monitoring: (a) direct measurement of SSC in streams through intermittent water sampling; (b) continuous measurement of a surrogate parameter (e.g., turbidity) using permanently installed sensors, followed by estimation of SSC; and (c) measurement of water surface reflectance via calibrated remote optical sensors, such as satellites, UAVs, and cameras, followed by estimation of SSC based on these observations. However, each of these methods has its own set of challenges, which will be presented in this section, often limiting our ability to answer significant scientific questions with the typical SSC data collected.

1.2.1 Direct measurement of SSC using gravimetric sampling

The primary method for determining SSC in rivers or lakes is gravimetric analysis of water samples. This technique involves collecting water samples at regular or irregular intervals, from various locations and depths depending on the study's purpose. Common methods for sample collection include using a bottle or a pump to retrieve the sample from a specified depth. Once collected, the known volume of the water sample is passed through a filter, either on-site or later in the laboratory. This filter, whose material and pore size vary depending on the sediment type, is designed to trap the suspended sediment while allowing water to pass through. After filtration, the filter with the trapped sediment is dried in an oven at a controlled temperature to remove all moisture. The dried sediment and filter are then weighed using a precision balance, with the weight of the filter alone recorded before sample collection. The concentration of suspended sediment is then found using:

$$SSC = \frac{m_s}{V_T} = \frac{m_d - m_f}{V_w + V_s} \tag{1.1}$$

where m_s is the mass of the solid matter obtained by subtracting the mass of the dried filter (m_d) from the mass of the filter alone (m_f), and V_T is the total volume of the original sample, which is a sum of the volume of water (V_w) and the volume of solid matter (V_s).

There are two main techniques for gravimetric sampling: **bottle** or **pump** sampling. Bottle sampling involves submerging a jar into the water, whereas pump sampling uses a vacuum applied to a submerged pipe to collect a water sample for later laboratory analysis. In both bottle and pump methods, samples need to be taken to a laboratory for processing.

Gravimetric sampling is renowned for its precision and reliability, particularly with low sediment concentrations. It is a well-documented, widely-used method and serves as the standard for calibrating other types of samplers. Despite these advantages, the method is time-consuming, labour-intensive, and requires meticulous handling and lengthy processing of samples. While pump sampling is automated and requires less manual effort compared to bottle sampling, it still involves some degree of human handling. Both methods can encounter Particle Size Distribution (PSD) errors if the velocity at the jar or pipe's mouth does not match the stream's velocity, potentially leading to inaccurate capture of sand-sized particles (Wren et al., 2000). To address this in bottle sampling, several isokinetic sampling apparatuses have been developed. For pump sampling, the intake velocity of the pump should ideally match the local stream velocity, a challenging task given the stream's variable velocity.

The main deficit of both bottle and pump gravimetric sampling is their poor temporal resolution. Physical sampling becomes particularly challenging during high discharge events in mountain streams, where water velocities can exceed 2 ms^{-1} (Aleixo et al., 2020). These disadvantages render the methodology both costly and inefficient, especially considering that streams transport over 50% of their total sediment during flood events (Nelson and Benedict, 1951). Nevertheless, gravimetric sampling remains the primary method for measuring SSC and deriving sediment budgets for river basins (Milliman and Farnsworth, 2013; Poulier et al., 2019).

1.2.2 Continuous Measurement and Estimation of SSC with Sensors

To address the discontinuous nature of gravimetric sampling, several advanced techniques have been developed to provide a continuous, indirect estimate of SSC. These methods typically involve continuous measurements of a different parameter (often light intensity, sound wave intensity, or changes in harmonic frequency). Through a pre-established calibration equation, SSC = f(P), where P is the measured parameter, an SSC value is inferred. Although gravimetric sampling is still necessary to calibrate these instruments, these new techniques complement traditional methods by significantly enhancing **temporal resolution**.

The main techniques in this category include turbidimeters, acoustic devices, laser diffraction devices, vibrating tube densimeters, and nuclear gauges. Each of these devices operates on different principles and comes with its own set of advantages and drawbacks, which are summarized below.

Optical transmission and scatter

The simplest instrument based on optical scatter is the Secchi disk. This is a simple tool used to measure water transparency; it consists of a circular plate divided into quadrants

painted alternately black and white, which is lowered into the water until it is no longer visible, with the depth at this point indicating the clarity of the water. In this case, the light source is the Sun and the human eye is the detector. This device again require, and is limited by, physical labour. Therefore, it is not a good alternative to gravimetric sampling.

Proper optical scatter or transmission-based instruments function by projecting infrared or visible light into a sample. If the sample contains no particles, the light passes through unimpeded. However, if particles are present, they scatter the light, and this change in light intensity is measured using photodiodes placed at different angles relative to the light source as in Figure 1.1.

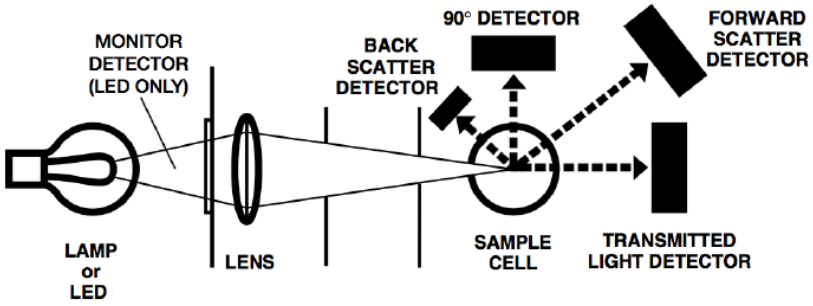

Figure 1.1: Principle of optical scatter and transmission to measure SSC. A light source (lamp or LED) is used to illuminate the water sample (sample cell) and detectors (backscatter, 90°, forward scatter, transmitted light) are placed at various angles to measure the amount of scattered light (from Sadar (1998)).

Optical scatter instruments, known as "turbidimeters" or "turbidity sensors," use various light sources, including LEDs or lasers. As Figure 1.1 shows, their designs vary featuring different detection methods like backscatter, transmission, 90^o scatter, or a combination of these. The reason for different detection sensor orientations is related to the response of light scatter by the sediment in the sample (Figure 1.2). For instance, the amount of light reaching the transmission detector decreases exponentially with increasing turbidity (or with increasing units of turbidity called "Nephelometric Turbidity Units" [NTU]). In contrast, the amount of light reaching the Nephelometric (90^o) detector is first zero and then rises to a peak with increasing turbidity before gradually falling again with increasing turbidity due to multi-scattering. This variety in sensor designs allows manufacturers to tailor products to specific needs, such as high-resolution at low turbidity or a wider measurement range. Usually, the use of several detectors at different angles allows the partial cancellation of errors due to wavelength absorption in samples (Bhardwaj et al., 2015).

There are both desktop and in-situ versions of these sensors. Desktop sensors analyze a water sample placed in a vial, while in-situ sensors are deployed directly in water bodies like lakes, rivers, or reservoirs, measuring within the environment itself.

Turbidity sensors are widely used in hydrology for long-term, high-resolution monitoring of river systems. By calibrating a relationship between SSC and turbidity, they can provide continuous SSC data at high temporal resolutions (typically hourly or sub-hourly). When paired with water discharge (Q) measurements, they help calculate sediment yield

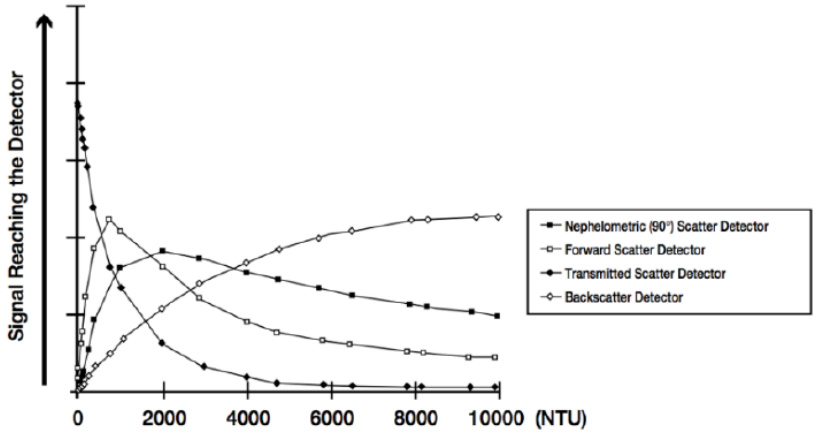

Figure 1.2: Proportion of light (signal) reaching each detector (backscatter, forward scatter, transmission scatter, and 90^o scatter) for a wide range of turbidities (NTUs) (from Sadar (1998)).

(SSC*Q). Their recent integration with the Internet of Things (IoT) has expanded their applications, including real-time monitoring and early warning systems.

However, these sensors have limitations. They require stable river cross-sections and significant infrastructure, making them expensive, and challenging to deploy widely. The sensors alone cost between 2'000–6'000€ as shown in Table 1.1. These deficiencies make widespread deployment (e.g. many sites along a river system to quantify spatial variability) next to impossible. Turbidity sensors also have particle-size dependencies and can reach saturation limits due to multiple scattering. Their readings, dependent on various factors like PSD, shape, and color, require calibration against gravimetric samples (Downing, 2006).

Table 1.1: Costs of popular commercial turbidity sensors.

***Sensor* and Manufacturer**	**Cost [EUR]**	**Year of offer**
AquaTROLL 600 by In-Situ	∼6'000	2019
DL-NTU-001 by Decentlab	2'243	2023
ClariVUE10 by Campbell Scientific	3'300	2022

Despite these drawbacks, turbidity sensors remain popular for high-resolution SSC monitoring. Efforts within the scientific community to develop affordable, open-source sensors have made strides in addressing cost concerns and are central to this thesis.

Low-cost turbidity sensors

Several innovative, low-cost turbidity sensors have been discussed in recent peer-reviewed literature. Gillett and Marchiori (2019) explored the use of inexpensive, commercially-available turbidity sensors typically found in household appliances like washing machines and dishwashers. These sensors operate on the principle of light attenuation, with the light detector positioned directly opposite the light source. However, Gillett and Marchiori

(2019) discovered that these analog attenuation sensors were unable to monitor small changes in turbidity with high resolution.

In addition to this past work, I attempted to create a turbidity sensor using attenuation-style dishwasher sensors and integrated this sensor into the Semester Project for Bachelor's students at ETH Zürich. This work can be found in Appendix A. However, based on this work we found that the sensors were prone to various errors, including saturation from incoming sunlight.

In a separate study, Trevathan et al. (2020) reconfigured and recalibrated a household appliance sensor (DF Robot SEN0189 Gravity, also based on attenuation) and designed a waterproof housing for field use. Their modified sensor demonstrated both durability and reliability during a year-long field deployment in dynamic environmental conditions. Despite these successes, they did not provide detailed information on the sensor's accuracy and faced challenges calibrating it for readings below 100 NTU, although their tests ranged from 0-20 NTU. Having a sensor with a broad measurement range (from 0–4000 NTU) enables us to measure the clear waters of Alpine rivers, but also the high river turbidity typical of precipitation events. Trevathan et al. (2020)'s sensor data was also affected by ambient stray light, a problem they initially couldn't resolve. Later, Trevathan et al. (2022) improved the sensor's calibration and accuracy by establishing a calibration procedure using formazin standards. They evaluated the sensor's electrical reading range, which led to a better understanding of its turbidity range and accuracy across a spectrum from 20–4000 NTU.

To increase the accuracy of low-cost, attenuation-style turbidity sensors, particularly in the 0-100 NTU range, Lambrou et al. (2014) and Wang et al. (2018b) modified these sensors by adding a detector at a 90^o angle to the incident light beam. This adaptation has shown promising results in terms of stability, linearity, sensitivity, reduced stray light interference, and an extended NTU measurement range, particularly when integrating a backscatter detector (Sadar, 1998). However, there are limitations in these studies. Lambrou et al. (2014)'s sensor was tested only in the 0-100 NTU range, which is very low turbidity in natural streams, without detailing how they achieved a 0.1 NTU resolution. Similarly, Wang et al. (2018b) focused their testing only within the 0-1000 NTU range.

Kelley et al. (2014) developed a low-cost, hand-held turbidity meter targeting drinking water quality in low-income communities worldwide. While this sensor was calibrated with and tested against a commercial turbidity sensor, its evaluation was limited to the 0-1000 NTU range. Additionally, reliance on commercial sensors for calibration is not advisable since their measurements have strong differences in reported values among the various sensors (Felix, 2017). Kitchener et al. (2019) approached the issue differently by conducting a sediment settling experiment using a modular PVC ring to hold light detectors at multiple angles (0^o, 10^o, 20^o, 90^o, 160^o) relative to an LED. They presented their findings in SI units of radiant intensity (mW/sr), diverging from the standard formazin-based NTU measurements. Although their device costs around ∼400€, it is not suitable for environmental deployment due to its design.

Gillett and Marchiori (2019) not only tested appliance sensors but also developed a flow-through sensor designed to attach to a PVC pipe, aimed at continuously monitoring turbidity at a cost of 64€. Their design, which utilized a large PVC diameter, required a powerful ambient LED and calibration under dark-room conditions. While effective in a

pump-test setup, this sensor is not suitable for environmental applications due to potential interference from ambient stray light. Jiang et al. (2020) focused on deep-sea applications, creating a turbidity sensor capable of functioning at depths over 3400 meters. Their design is based on a backscatter principle, with the detector positioned at an angle of $< 45^o$ relative to the incident LED beam. However, this sensor is effective only within the 0-20 FNU range (FNU and NTU are comparable units of turbidity).

Rocher et al. (2021) developed two distinct turbidity sensor prototypes to detect illegal discharges in sewage systems. Both prototypes utilized five visible spectrum LEDs and one IR LED, differing mainly in the arrangement and position of these six LEDs. They measured scattered light using a combination of a photoresistor and a photodiode, positioned at 0^o and 180^o, resulting in four detectors in total. While these initial prototypes could not quantify the exact amount of suspended solids, they successfully detected the presence and variations in solid concentrations. Rocher et al. (2022, 2023) refined their design, using just an IR LED and an RGB LED, with a photodiode and photodetector placed at both 90^o and 180^o relative to the LEDs. This improved design and calibration allowed them to measure not just turbidity but also differences in suspended solids, aiming to distinguish the proportion of solids versus algae in a sample. However, this sensor is currently a desktop device and isn't suitable for long-term in-situ monitoring. In a related development, Parra et al. (2018) devised a system capable of identifying different sources of turbidity, such as sediment, green phytoplankton, or brown phytoplankton. This is particularly useful in fish farming applications. Their sensor, similar to Rocher et al. (2023)'s, utilizes multiple LEDs of different wavelengths and an IR photodiode and photoresistor (for the visible spectrum) placed at 180^o.

Building on their previous work (Eidam et al., 2022), Langhorst et al. (2023) developed two new versions of the OpenOBS-328 logger. The first version features an Iridium satellite connection, enabling remote data transmission in remote catchments. The second version, named OpenOBS, is designed for educational purposes in classrooms. Their device is self-contained, with the option to order electronics with an assembled PCB. The sensor components include PVC tubing and parts created with 3D printing. However, details about the device's accuracy have not been shared (Droujko and Molnar (2023) & Appendix B).

In summary, the development of low-cost turbidity sensors, as evidenced by the various studies and prototypes discussed, represents a significant stride in environmental monitoring (e.g. Droujko and Molnar (2023) & Appendix B). These innovations have made turbidity measurement more accessible and versatile, catering to diverse applications from sewage monitoring to educational purposes. Despite the promising developments in low-cost turbidity sensor technology, a critical aspect remains open, and that is the calibration of these sensors in a systematic way to SSCs with a view for their use in natural river applications. In fact, none of these previously developed low-cost alternatives have explicitly quantified the measurement range of their devices in terms of sediment concentration, specifically in grams per liter (gL^{-1}). While formazin calibration has been commonly employed, there is a notable absence of mixing tank experiments that compare the accuracy of these low-cost sensors against commercial sensors or provide a sediment-specific calibration. This gap underscores a pressing need for future research to conduct comprehensive mixing tank experiments and sediment-specific calibrations. Such efforts are crucial to validate and enhance the practical applicability and accuracy of these low-cost turbidity sensors, ensuring their effectiveness in real-world sediment monitoring scenarios.

Turbidity sensor networks

Calibrated turbidity sensors enable the collection of high temporal resolution SSC data, surpassing the capabilities of traditional gravimetric sampling. While the use of multiple turbidity sensors to enhance spatial resolution is not new, it typically involves costly equipment. For instance, Abe et al. (2012) installed five commercial turbidity sensors across two subcatchments to monitor sediment transport on a catchment scale. Thollet et al. (2021) created six long-term hydro-sedimentary stations in a system of nested catchments. Chen and Han (2018) further advanced this approach by integrating a WiFi-based wireless sensor network for urban water quality monitoring. They deployed the AquaTROLL 600 from In-Situ at three locations in Bristol harbour for a month. This sensor, also used in Chapter 2, measured parameters like dissolved oxygen, conductivity, turbidity, temperature, and pH. Although effective in detecting diurnal cycles and daily variations in water quality parameters, the high cost of the AquaTROLL 600, especially for remote data transfer, poses a major challenge to the widespread implementation of a dense network necessary for high spatial resolution monitoring.

It is important to note that many suspended sediment monitoring networks operated by governmental agencies are in fact not networks suitable for sediment source identification in the first place, due to the low density of stations in independent catchments. For example, in Switzerland the Federal Office for the Environment (BAFU) monitors turbidity continuously at only 15 of their roughly 260 streamflow monitoring stations (6%) (BAFU, 2024). I am proposing a turbidity network, not to replace such stations, but to complement them in selected river basins where a sediment source challenge exists.

Acoustic methods

Acoustic methods measure SSC in water by emitting sound waves, which interact with sediment particles, either attenuating or scattering the sound. Several instruments use this measurement principle to determine SSC. One such instrument is the Acoustic Discharge Measurement (ADM) device. Operating on a single-frequency acoustic method based on attenuation, it utilizes acoustic transducers set up across a flow section, such as in narrow channels or hydropower plant tunnels. Ultrasonic pulses are transmitted into the water, with the flow rate determined by the Doppler shift of the signal, and the SSC is calculated from the attenuation of the received signal due to sediment particles (Felix et al., 2016).

Another instrument, the Acoustic Doppler Current Profiler (ADCP), emits high-frequency (1–5 MHz) sound waves in short bursts ($\sim$10μs). These waves interact with sediment particles and partially scatter back to the transducer. The ADCP measures both the frequency shift, which indicates particle velocity, and the intensity of the backscattered signal, providing an estimate of SSC. Advanced ADCPs can also estimate mean grain size using different frequencies when combined with gravimetric samples (calibration to SSC). ADCPs are typically used for spatially-distributed SSC measurements across river cross-sections and in lakes, offering a detailed view of sediment distribution within the water column.

The multi-frequency and depth profiling capability makes acoustic methods versatile for diverse sediment monitoring applications. They provide non-intrusive, high spatial and temporal resolution data. However, their accuracy can be affected by various factors like high particle concentration, organic material presence, shallow or deep waters, and a wide range of particle sizes and shapes (Aleixo et al., 2020). Despite efforts to account

for these changes, challenges persist. These methods are also expensive and not ideally suited for long-term deployment in dynamic river systems due to battery and data logging limitations. Additionally, collecting high spatial resolution data across a river's cross-section requires moving the acoustic device laterally over the water's surface. For instance, Aleixo et al. (2020) were one of the first to build long-term ADCP measurement stations on the Secchia and Devoll rivers but only measured 1D horizontal profiles, due to the increased labour demands associated with comprehensive 2D cross-sectional measurements. For larger scale measurements, such as along a river stretch or network, multiple acoustic stations or manual relocation of the device is necessary, both of which are costly and labour-intensive. This limits the temporal and spatial resolution capabilities of acoustic methods.

Laser Diffraction

Laser diffraction instruments, like the Laser In-situ Scattering and Transmissometer (LISST), use a laser to analyze particles in a water suspension. The LISST has a ring-shaped array of detectors, each capturing light scattered by particles at specific angles, correlating to different particle sizes. The intensity of light scattered at each angle indicates the quantity of particles of that size, allowing the instrument to measure both SSC and PSD.

LISST instruments are highly regarded for their dual capability of measuring SSC and PSD, a feature not common in other methodologies. However, they have their limitations. They are typically restricted to measuring small particle sizes ($< 500\ \mu$) and lower sediment concentrations (< 5 g/L) (Felix et al., 2013; Wren et al., 2000). To measure higher concentrations, samples often need to be diluted before analysis with the LISST, then the SSC is calculated backward from these diluted measurements. This process adds labour and complexity to an already expensive tool, which costs ∼40'000€. Due to these costs and the high risk of damage, LISST instruments are not generally used for widespread deployment or long-term in-situ monitoring.

Other instrumental techniques

Besides the previously mentioned methods, there are other in-situ instrumental techniques for determining SSC. However, they are not widely implemented due to challenges in long-term monitoring in streams or because they introduce significant sources of error.

One such instrument is the **Vibrating Tube Densimeter**. The operating principle of this instrument is that the density of the fluid flowing through the vibrating tube can be determined from the natural frequency of the tube, which decreases as the mass in the tube increases. Despite its precision, Vibrating Tube Densimeters are costly, priced at around ∼14,000€, and have been used in limited scenarios, such as by Felix et al. (2016) for measurements up to 13 g/L in a hydropower plant sampling pipe. However, these instruments are susceptible to various sources of error, including changes in dissolved solid concentrations, water temperature, pressure, flow rate, and the presence of debris or algae on the tube's walls, and are really only suitable for laboratory or very controlled situations (Wren et al., 2000).

Another method that has not gained popularity is the **Nuclear Sediment Gauge**. This technique uses the backscatter of isotopes or radiation to estimate SSC (Wren et al., 2000). It is not only expensive but also raises human health and environmental concerns. Due

to these issues and the availability of alternative methods, Nuclear Sediment Gauges have not seen further development or many applications.

1.2.3 Measurement of water surface reflectance by remote sensing

Addressing the challenges highlighted in Section 1.1, particularly the need for identifying sediment sources and pathways beyond just catchment outlet yields, calls for monitoring SSC at multiple points both upstream and downstream of tributaries and other local sources. However, taking direct SSC samples at numerous locations within a river system is impractical due to the significant labour required for such high-resolution data collection. While constructing a large, dense network of turbidity sensors is a theoretical possibility, it hasn't been realized on a large scale due to the high costs associated with commercial sensors (Gillett and Marchiori, 2019).

An alternative approach to these methods is the utilization of water surface reflectance data obtained from remote optical sensors. These sensors can include satellites, Unmanned Aerial Vehicles (UAVs), or terrestrial photography. This technique offers a less labor-intensive and potentially more cost-effective way to monitor SSC over extensive areas and many points within a river system.

Satellites

Remote sensing of turbidity through satellite imagery offers promising potential due to its spatial distribution, repeatability, and affordability, albeit with a trade-off in accuracy. Turbidity monitoring via satellite is based on the reflectance of the water surface, influenced by various parameters like chlorophyll, suspended sediment, and dissolved organic matter. The inherent color of natural waters, determined by concentrations of dissolved and suspended matter combined with biological activity (e.g. Novoa et al., 2015; Wang et al., 2018a; Ritchie et al., 2003), affects surface reflectance in predictable ways. This predictability makes optical satellite remote sensing feasible for oceans, coastal areas, and large lakes or rivers. Figure 1.3 shows the principle of measuring irradiance from satellite images. The irradiance measured by satellites typically includes water-leaving radiance, water-surface reflectance, and atmospheric scattering and absorption. Atmospheric correction is needed to isolate the water-leaving reflectance (R_{rs}), which contains the turbidity or SSC signal. When calibrated with ground measurements, satellite data can provide valuable SSC estimates at large scales, but with limitations in temporal resolution due to satellite overpasses and limitations in spatial resolution due to larger spatial footprint.

Past studies have used satellite imagery to estimate SSC in water bodies (DeLuca et al., 2018; Martinez et al., 2009), additional water quality parameters (Kuhn et al., 2019; Wang and Sohn, 2018), and even detecting the presence of perennial streams in dryland environments (Wang and Vivoni, 2022) and monitoring benthic habitats in shallow ocean ecosystems (Wang et al., 2022). Many studies have correlated remotely sensed reflectance from large water bodies with in-situ turbidity or SSC measurements, primarily focusing on inland lakes, coastal areas, and large rivers (Doxaran et al., 2002; Yunus et al., 2020; Wei et al., 2018; Schiebe et al., 1992; Wass et al., 1997; Vanhellemont and Ruddick, 2015; DeLuca et al., 2018; Martinez et al., 2009). These studies have successfully derived empirical relationships between reflectance indices and turbidity or SSC (Yunus et al., 2020; Kaba et al., 2014). The advantage of this empirical method is its flexibility in fitting the

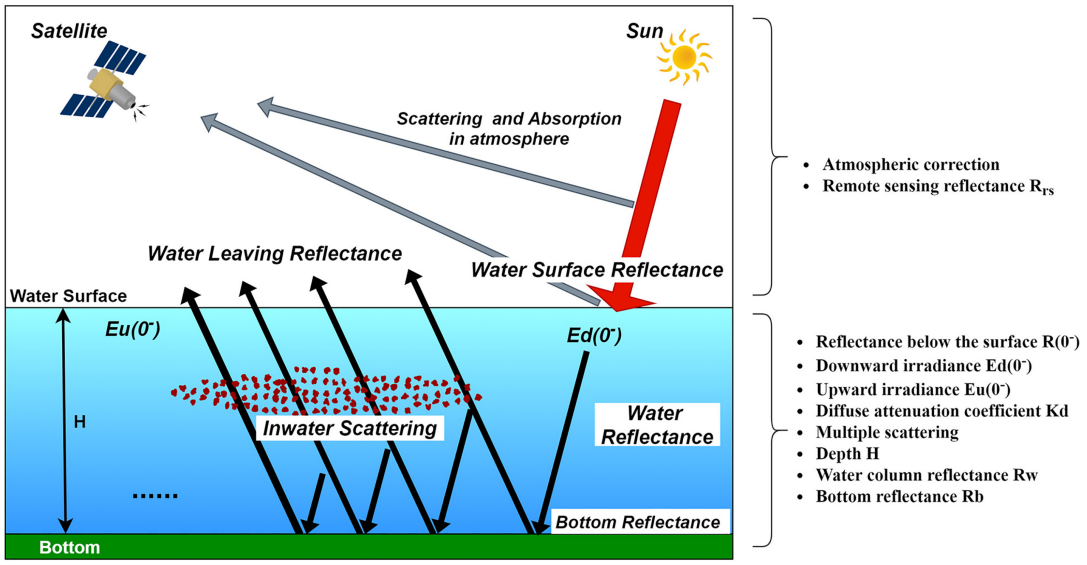

Figure 1.3: The signal reaching the satellite is a mixture of the water-leaving irradiance, the water-surface reflectance, and scattering and absorption in the atmosphere (from Wang et al. (2022)).

best relationship without predefined assumptions. However, since these relationships vary depending on the study site, sediment source material, and satellite imagery (Yunus et al., 2020), a new relationship must be established for each waterbody, sometimes even for different reaches within a river.

In contrast, less attention has been paid to inland rivers, often due to the insufficient spatial resolution of open-access satellite images. Satellite analyses are only feasible if the image resolution is adequate to represent the river width. For example, studies in the Amazon showed that SSC variations could be linked to overbank flow and sediment resuspension in lakes (Fassoni-Andrade and de Paiva, 2019). Similarly, Gardner et al. (2021) compiled a database of river color for over 108,000 km of rivers in the USA with river widths exceeding 60 m, but studies on narrower rivers are limited.

High-resolution, open-access satellite missions like Sentinel-2 (10 m resolution) have not yet been extensively used to estimate turbidity or SSC in narrow rivers (e.g. less than 60 m in width). Establishing a relationship between remote sensing reflectance and in-situ measurements, i.e. groundtruthing, is a necessary step in the use of remote sensing for SSC estimation. This could involve using a small network of turbidity sensors to extract turbidity data along a complex river system, enabling the spatial distribution of SSC to be mapped. Such data could identify sediment sources and pathways in a catchment by linking longitudinal changes in reflectance (SSC or turbidity) to tributaries and river reaches. These sources and pathways could then be related to changes in rainfall variability in the catchment, as a proxy for runoff. Investigating the natural variability in reflectance across different seasons would also be informative.

In conclusion, a proof-of-concept study for estimating water turbidity in narrow, morphologically diverse rivers from satellite images is warranted. This approach has the potential to identify fine sediment sources and pathways along river networks and obtain spatially-distributed datasets, despite the trade-off in temporal resolution and problems related to

signal extraction in river valleys with changing widths, riparian vegetation, human intrusions in floodplains, etc.

Other remote sensing tools based on water spectral reflectance

River turbidity and other water quality indicators can also be monitored using terrestrial photography (Goddijn and White, 2006; Fricke and Baschek, 2014). Recent developments include the use of UAVs for various monitoring tasks, such as assessing submerged aquatic vegetation (Flynn and Chapra, 2014; Rotta et al., 2018), seagrass (Nahirnick et al., 2019), and the tree shading of rivers (Bachiller-Jareno et al., 2019).

Mobile phone cameras offer another practical approach for optical sensing of turbidity. For instance, Leeuw and Boss (2018) developed the *HydroColor* app, designed for citizen science applications. This app instructs users to take a series of photographs from which turbidity is then estimated. However, this method doesn't account for variations in smartphone camera exposure settings, leading to significant uncertainties. Additionally, it requires users to have a photographer's 18% grey card for reference. Gao et al. (2022) addressed this challenge by calculating water reflectance from smartphone photos with automatic exposure settings. They employed a five-color reference card to establish a non-linear relationship between reflectance and the digital numbers in the photographs, enabling turbidity estimation. Malthus et al. (2020) conducted an extensive study using both the *HydroColor* and *EyeOnWater* smartphone apps over four months at 32 inland water sites with varying sediment and algal concentrations. They concluded that while the *EyeOnWater* app could accurately capture water color on the Forel-Ule scale, it was not suitable for deriving a turbidity relationship. They also found the *HydroColor* app to be prone to image processing errors.

Despite these innovations, all ground-based optical sensing methods face limitations. They are hindered by labour costs, the need for accurate ground-based turbidity or SSC data for calibration, and susceptibility to environmental factors such as light conditions, optical transmission, and visibility. These constraints make them less attractive for reliable, long-term monitoring of SSC in river systems and limit their application to opportunistic one-at-a-time measurement.

1.3 Research questions and objectives

In Section 1.1, I highlighted the importance of fine sediment production and transport on a global scale and its significant impact on riverine, coastal, and marine ecosystems. I made the point that to effectively identify, model, and understand the physical connections between hydrology, river processes, and sediment fluxes, there is a pressing need for suspended sediment monitoring data with high spatial and temporal resolutions.

However, as Section 1.2 outlined, the current direct monitoring, indirect in-situ (also discussed in Appendix A), and indirect reflectance-based tools each have their limitations. I conclude that none of these methods have thus far provided both high-resolution spatial and temporal data, due to various challenges such as the intensive labour required for gravimetric analysis, the high costs associated with in-situ sensor-derived SSC, or the inherent limitations in remote sensing capabilities.

This doctoral dissertation aims to investigate the limitations of these methodologies and aims to contribute to the development of a monitoring system capable of high temporal and spatial resolution SSC measurements for sediment source identification and tracking in both small and large river systems, and to provide some first examples of the use of such a system.

1.3.1 Research questions

I divide the research questions into three groups: A) analyzing the current available methods and utilizing satellite data for SSC estimation (RQ1); B) development of my own open-source, and low-cost sensor (RQ2) and its testing (RQ3); and C) providing a first application to an environmental flood monitoring case and answering a range of questions related to sediment sources and transport pathways (RQ4). The research questions are as follows:

RQ1 Can the new, high-resolution (10m) Sentinel-2 mission be combined with a small network of commercial turbidity sensors to extract SSC data from a relatively narrow river network? Can sediment sources and sinks be identified using the aforementioned sensing methods within a river catchment? Can the fraction of contribution from these sources be quantified? When and how are sediment sources activated by hydroclimatic forcing (e.g. heavy rainfall) or by processes that lead to seasonality, like snowmelt?

RQ2 Can a new highly accurate device for turbidity or SSC monitoring in rivers be developed at a low cost? Can this device overcome problems with traditional sensors (expensive, point-based, low accuracy) and offer benefits such as easy deployability, mobility, and end-to-end integration for the user?

RQ3 Can this new sensor be designed in a way that it can be built by hobbyists and people with limited programming knowledge? Can this system be deployed in difficult environmental settings (e.g. flood, glacier stream), and do its technological requirements (e.g. power, connectivity) enable such measurements?

An important application being studied in the Swiss National Park is the use of experimental or environmental floods (called "e-floods") to mobilize fine sediment in the river bed. Such floods have important ecological consequences but high resolution SSC measurements have not yet been conducted in this context. This raises the question:

RQ4 How can new, high-resolution sensing inform when and where possible sources of sediment are being activated during an e-flood? How can such sensing better optimize river management practices and better inform stakeholders about the geomorphological and ecological consequences of releasing e-floods under sub-optimal hydroclimatic conditions?

1.3.2 Research objectives

My approach to addressing the research questions in Section 1.3.1 consists of analyzing satellite imagery and its use and limitations when applied to an entire river catchment. The central part of my dissertation is the design, development, and testing of a novel, low-cost, highly accurate turbidity sensor, intended for use in a sensor network. Finally, I aim to apply this novel measurement device in a field-based pilot study in the Alps: in

the Spöl River for an e-flood purpose.

My approach is structured into three research objectives (RO). The first involves investigating current low-cost sensing options such as open-access satellite images. The second objective is focused on developing a new, smart sensor for turbidity measurement in rivers, leading to the third objective: the application of my novel device in a field-based study. More specifically, the objectives of this dissertation are to:

RO-A To analyze Sentinel-2 satellite imagery, supported by a small commercial turbidity sensor network on the Vjosa River in Albania, to extend our investigation beyond the immediate vicinity of the sensor locations, offering a broader perspective on sediment dynamics and distribution in natural river systems. **(RQ1)**

RO-B Create, test, deploy, and analyze a low-cost, accurate, open-source turbidity sensor with end-to-end integration, suitable for challenging river environments. This phase will include analyzing measurement principles of turbidity sensors, exploring temporal sampling options and calibration methods, and developing end-to-end integration from data to user. These sensors will be developed using advanced Arduino programming and practical 3D printing techniques. The goal is to create an affordable sensor that is accurate across a wide range of turbidity (0–4000 NTU) and SSC (0–10 g/L) levels. This sensor will aim to overcome several limitations associated with traditional sensors, such as complex calibration requirements, and operate on minimal power. The sensor will be tested with various sediment types and compared to commercial sensors in a mixing tank experiment. It will also be tested under harsh environmental conditions such as during a flood in a glacial stream. We will provide a robust methodology for use and further refine the sensor based on feedback from various sediment types and riverine environments. This phase is crucial for gathering critical feedback to enhance the sensor's design and functionality, with subsequent improvements informed by experiences in the third part (RO-C) of our research. **(RQ2–RQ3)**

RO-C Investigate spatial and temporal variability of suspended sediment in alpine fluvial systems through a field-based pilot study. The study will apply our sensing technology to the Spöl River during environmental floods ("e-floods"), focusing on the redistribution of fine sediments for ecological purposes (Robinson et al., 2018). This phase will emphasize working under challenging environmental conditions and leveraging targeted sensing of turbidity and SSC. **(RQ4)**

1.4 Organization of thesis

This thesis is a cumulative dissertation comprising four scientific articles and two supplementary chapters. Each chapter delves into a distinct aspect of fine sediment measurement technology and analysis, emphasizing both theoretical exploration and practical application advancements. These include the use of satellite imagery, novel sensors, and sensor networks to analyze fine sediment behavior across different environmental settings. The chapters, and their context and applications in relation to advancing fine sediment source and pathway identification, are shown in Figure 1.4

Chapter 2 investigates the integration of data from a network of commercial multiparameter sensors with Sentinel-2 satellite imagery to identify sediment sources and sinks in river

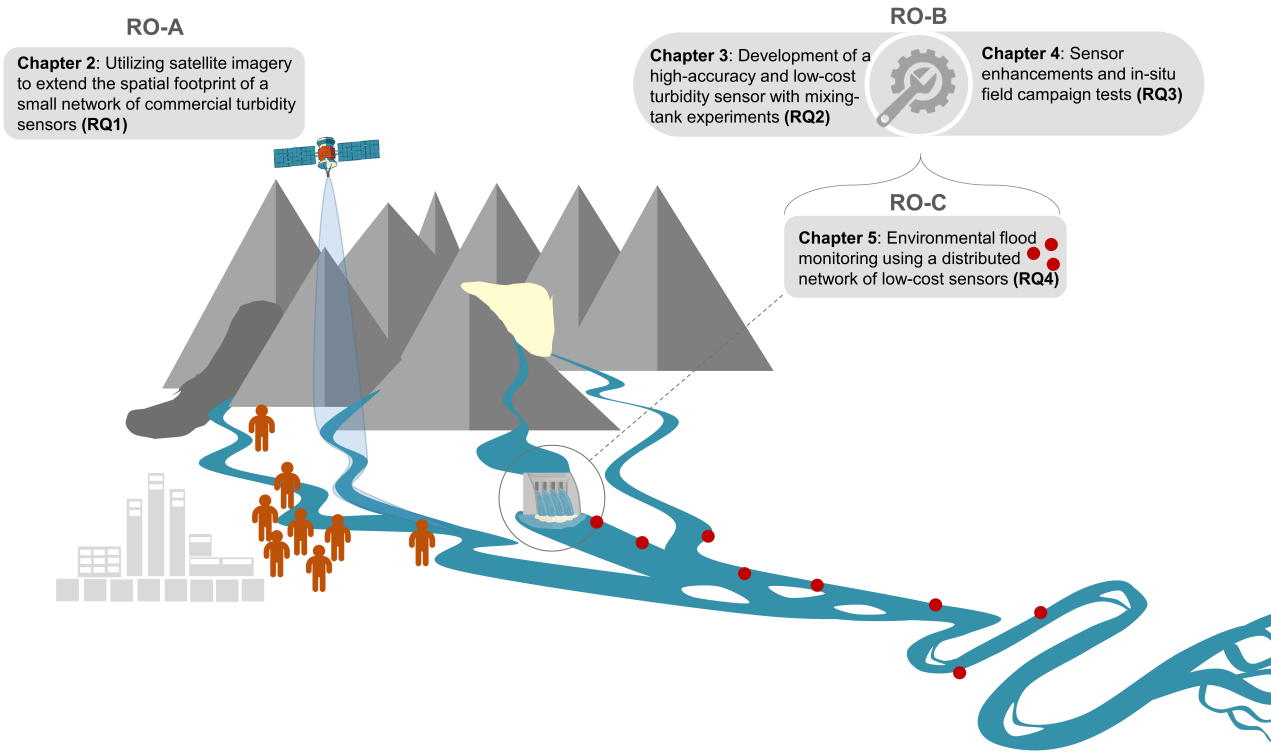

Figure 1.4: Visualization of the cumulative dissertation organized by the three research objectives (RO-A-B-C) and comprising of the four chapters and answering the four research questions (RQ1–RQ4). The first three chapters (2–4) explore the use of different technologies to obtain high spatial and temporal resolution SSC data. The final chapter (5) focuses on field applications using these technologies.

systems. This chapter details a two-year study along the Vjosa River in Albania, using four commercial sensors and analyzing approximately 100 satellite images to enhance ground-based sensor data and quantify various aspects of sediment dynamics. **This paper was published in Earth Surface Dynamics (Droujko et al., 2023b)**.

Chapter 3 describes the design and development of a new, low-cost, open-source turbidity sensor. This chapter describes the development, testing, and comparison of these sensors against commercial models in different sediment types, demonstrating their cost-effectiveness and precision. It is the core technology chapter of this dissertation. **It was published in Scientific Reports (Droujko and Molnar, 2022).**

In Chapter 4, the thesis transitions to how the sensor from Chapter 3 can be transformed into a durable, standalone multi-parameter device. Enhancements to the sensor are described, including increased battery capacity and a custom PCB shield designed for the Arduino MRKWAN 1310, along with the addition of a pressure and temperature sensor. The sensor's practicality and effectiveness are evaluated during a flood in the Ötztal Ache in Austria. **This chapter was published in HardwareX (Droujko et al., 2023a), including all open-access directions for building the sensor.**

Chapter 5 focuses on the application of a high-resolution sensor network developed from my novel sensor in the previous chapters to monitor fine sediment movement during experimental floods. The chapter covers studies conducted during the 2021 and 2023 floods on the Spöl River, deploying 4 to 7 sensors across the Spöl and Inn rivers to track the sediment wave and hypothesize about its potential ecological and downstream impact. **This chapter is in preparation for journal submission.**

Chapter 6 concludes the thesis with final remarks and future outlooks, summarizing the contributions of this work to the field of sediment monitoring and suggesting directions for further research.

Chapter 2 Sediment source and sink identification using Sentinel-2 and a small network of turbidimeters on the Vjosa River

Authors: Jessica Droujko, Srividya Hariharan Sudha, Gabriel Singer, and Peter Molnar
Journal: Earth Surface Dynamics, Copernicus Publications
Publication date: September 19th, 2023

Key findings:

1. We developed a workflow to estimate river turbidity profiles using high-resolution Sentinel-2 satellite images, in-situ turbidity measurements for ground truthing, and a multivariate linear regression model between turbidity and satellite reflectance.

2. The extracted longitudinal river turbidity profiles were validated with two descents of the river with a turbidity sensor attached to a kayak.

3. The satellite-derived river profiles revealed variability in turbidity along the main stem with a strong seasonal signal, with the highest mean turbidity in winter along the entire length of the river.

4. Sediment sources and sinks could be identified and quantified from the river turbidity profiles. Sediment sources were mostly tributaries following basin-wide rainfall, but within-reach sources in river beds and banks were also found.

5. We used the data to estimate the mean annual fine sediment yield at Dorez at $\sim 2.5 \pm 0.6$ Mt yr $^{-1}$, in line with previous studies.

Author's contributions: The author collected the field measurements, designed the remote sensing methodology, extracted the data from the processed images, derived the results, discussed the findings, prepared the article, and incorporated the final review comments from the journal reviewer.

Coauthors' contributions: GS helped collect all field measurements with a contribution from SHS. All authors contributed to the design of the remote sensing methodology. SHS processed all satellite images and cleaned the data. PM contributed to the discussion of the findings. All authors contributed to the preparation of the article. GS acquired funding for the project.

Code Data Availability The code and data used to produce this work can be found in the Zenodo repository: 10.5281/zenodo.7590129.

Supplementary Material: The supplementary material supporting this article can be found in Appendix C.

2.1 Introduction

The transfer of sediment from land to oceans plays an important role in the global denudational cycle (Gregor, 1970; Wold and Hay, 1990), the global biogeochemical cycles (Meybeck, 1994; Ludwig et al., 1996; Sanders et al., 2014), the functioning of riverine and coastal ecosystems (Roy et al., 2001; Arrigo et al., 2008; Terhaar et al., 2021; Descloux et al., 2013), and the evolution of rivers, deltas and other coastal landforms (Morton, 2003; McLaughlin et al., 2003; Seybold et al., 2009). Present-day sediment export from the land surface to global oceans by large rivers is estimated at about 15.5-18.5 Gt per year, and the dominant part of this flux is fine grain transport by washload and suspended load (Peucker-Ehrenbrink, 2009; Syvitski and Kettner, 2011; Cohen et al., 2022). This is about half of the estimated global annual soil erosion from the land surface (Borrelli et al., 2017). Excessive amounts of fine sediment load in rivers leads to high water turbidity, which can be linked to the degradation of coral reefs (Brown et al., 2017), impairment of freshwater and marine fish populations (Kemp et al., 2011; Newport et al., 2021; Jensen et al., 2009), the clogging of river beds in gravel bed streams (Schälchli, 1992; Hauer et al., 2019b), and low water quality in general. However, riverine suspended sediments provide an important balance of nutrients (phosphorous, nitrogen, and silica) to the coast and ocean (Nixon et al., 1996; Bernard et al., 2011). And recent silica deficiency due to the reduction of suspended sediment inputs from river damming has been observed to exacerbate eutrophication by reducing the role of diatoms in coastal food-webs, which indirectly feeds mesozooplankton (copepods) (Cotrim da Cunha et al., 2007; Justić et al., 1995).

Although recent studies point to the importance of large rivers in the overall global sediment flux (Cohen et al., 2022), there is an increasing understanding that smaller mountainous rivers, with basin areas less than 10,000 km^2 and draining elevations higher than 1000 m, deliver disproportionately more sediment per unit drainage area than large rivers. These smaller mountainous basins rich in sediment sources cover only about 10% of the land area draining into global oceans but account for about 15% of the annual water discharge and 45% of the annual suspended solids reaching the oceans (Milliman and Farnsworth, 2013). The smaller rivers are also more likely to be subject to human disturbance, either by trapping sediment behind dams, or by increased sediment inputs due to agriculture, mining, and intensive landuse (Syvitski et al., 2022). In fact, in Europe, there are very few unregulated moderately-sized rivers, where natural fine sediment dynamics can be monitored and studied. And it is estimated that over 1 million instream barriers fragment European rivers (Belletti et al., 2020).

This is also the case with the three largest rivers draining into the Adriatic Sea (Po, Adige, and Drini) which would have accounted for 25% of the sediment discharged to the Adriatic prior to dam construction. The remaining 75% of the Adriatic's sediment input comes from 32 rivers, their drainage basins all being less than 7000 km^2 (Milliman et al., 2016). Prior to dam construction, Albanian rivers contributed about 60% of the total sediment entering the Adriatic (Milliman et al., 2016) with the Vjosa river discharging more than 8.3 Mt yr^{-1}, with suspended load accounting for 80–85% of this flux or 6.6–7.1 Mt yr^{-1} (Ciavola, 1999). In addition to its importance as a sediment source, the Vjosa river represents one of the last intact large river systems in Europe. Although the headwaters are dammed (potentially reducing the residual flow of the river) and there is one hydropower dam along one of the Vjosa tributaries (sediment source), the Vjosa features a largely unobstructed fluvial morphology over the entire river corridor. Its geological diversity and longitudinal continuity in water flow and sediment transport processes from its headwa-

ters to the Adriatic Sea represent an important reference system for dynamic floodplains that have already been lost all across Central Europe (Schiemer et al., 2018b). Due to the largely undisturbed catchment and high surface runoff production, where about 70% of the total river flow is estimated to come from surface runoff following rainfall (Hauer et al., 2021), fine sediment is regularly mobilized on hillslopes and in the channels, giving rise to a natural sediment regime with many sources and sinks within the river network.

Despite the importance of fine sediment fluxes in rivers such as the Vjosa, the monitoring of sediment concentrations for estimating sediment yields from river basins is extremely difficult when compared to hydrological monitoring of river stage and discharge. There are basically three different options available: (a) direct measurement of suspended sediment concentrations (SSC) in streams by periodic water sampling; (b) continuous measurement of turbidity by permanently installed sensors and estimation of SSC; and (c) estimation of SSC based on measurements of water surface reflectance by calibrated remote optical sensors (satellites, UAVs). In order to identify sediment sources and sinks along a river network, and not just sediment yields at the outlet, we would need to monitor SSC at many points upstream and downstream of tributaries and other local sources. The first two options, i.e. direct SSC measurements and in-situ measurements of turbidity would be impractical for this purpose because a large network of turbidity sensors or intensive SSC sampling would be needed. This is very labor intensive and costly, also because of a lack of cheap alternatives for turbidity sensing (Gillett and Marchiori, 2019). The third option with remote sensing of turbidity using satellite imagery has higher potential, as it is distributed in space, repeatable and affordable, despite being less accurate.

Turbidity monitoring by remote sensing is based on the reflectance of the water surface. The intrinsic color of natural waters is determined by a range of parameters, such as the concentrations of dissolved and suspended matter together with gross biological activity, e.g. chlorophyll, suspended sediment, coloured dissolved organic matter (e.g., Novoa et al., 2015; Wang et al., 2018a; Ritchie et al., 2003). These components affect water surface reflectance in a predictable way, which makes optical satellite remote sensing of oceans, coastal areas, and large lakes/rivers possible. Satellite imagery with multispectral ranges is even more useful for a range of water quality parameters (e.g., Wang and Sohn, 2018). Several studies have investigated the plausibility of relating the remotely sensed reflectance signals from large water bodies with in-situ turbidity or SSC measurements (Doxaran et al., 2002; Yunus et al., 2020; Wei et al., 2018; Schiebe et al., 1992; Wass et al., 1997; Vanhellemont and Ruddick, 2015; DeLuca et al., 2018; Martinez et al., 2009). A majority of these studies have examined inland lakes, coastal areas, or large rivers, and successfully obtained empirical relationships between reflectance indices and turbidity/SSC measurements (Yunus et al., 2020; Kaba et al., 2014). An advantage of this empirical method is that it does not a-priori prescribe a form for the relationship between turbidity and reflectance and instead allows data to dictate what is the best fit. However, this method is not physically-based and a new relationship must be established for each waterbody (potentially a new empirical relationship for every reach within a river) since these relationships depend on the study site, sediment source material, and the satellite imagery used (Yunus et al., 2020). In contrast to large water bodies, much less attention has been given to inland rivers, because open-access satellite images often do not provide sufficient spatial resolution. In rivers, satellite-based analyses are only possible if the spatial footprint (image resolution) is sufficient to represent the river width. For example, SSC variations could be captured with satellite imagery in the wide Amazon River (Fassoni-Andrade and de Paiva, 2019), and Gardner et al. (2021) built a database of river colour for 108,000 km

of rivers in the USA where the river widths were >60 m, but applications to less wide rivers are missing.

In this study, we explore the use of new remote sensing data from the high resolution satellite mission Sentinel-2 (10-m resolution) to estimate turbidity in the narrow and morphologically rich Vjosa River. To this end, we extracted turbidity data along the entire main stem of the Vjosa River using Sentinel-2 imagery calibrated to in-situ turbidity measurements from 2019–2021. We have two main aims in this research: First is to provide a workflow that allows the estimation of longitudinal profiles in turbidity from Sentinel-2 imagery in morphologically complex rivers, i.e. rivers with large changes in width, depth and channel planform. This allows us to quantify the natural variability in turbidity along the river system in different seasons from the two years of analysis. We support these long profile estimates with a lagrangian kayak-derived measurement of turbidity on two different trips. Second is to identify possible fine sediment sources and sinks in the catchment from the longitudinal changes in turbidity due to tributaries and within individual river reaches, and to relate these changes to rainfall variability in the catchment as a proxy for runoff. Finally, we check that the estimates of SSC and sediment yield at a gauged location on the Vjosa River from our remote sensing derived turbidity estimates agree with past studies. The overall goal of this work is to provide a proof of concept for the estimation of water turbidity in rivers similar to Vjosa with Sentinel-2 imagery, and to show the potential of identifying fine sediment sources and sinks along river networks with such data.

2.2 Methods

2.2.1 Study area and data

The Vjosa river is one of the last intact large river systems in Europe, with the exception of a dam in the headwaters (Aoos Fig. 2.1) and another on the Langarica tributary (upstream of Permet Fig. 2.1). Its headwaters are located in the Pindos mountains in Greece and it flows for 272 km in the North-West direction through Albania before reaching the Adriatic sea (Fig. 2.1). The river has a catchment area of 6706 km^2 (Simeoni et al., 1997). Along its course, the Vjosa channel pattern changes significantly, from deep gorges, areas with large alluvial fans and islands, large gravel and sand bars, to meanders and a river delta at the mouth (Hauer et al., 2021). The catchment is dominated by flysch deposits (47%), limestones (25%), clastic sediments (17%), sandstones (8%), metamorphic rocks (2%), and igneous rocks (less than 1%) (Hauer et al., 2019a). It was also found that the high loads of suspended sediments in the main stem are mostly derived from flysch deposits, and the high loads of coarse sediment are mostly derived from the limestone, clastic sediment and sandstone formations in the southern part of the catchment (Hauer et al., 2019a). The coastal lowlands are characterized by a typical Mediterranean continental climate, while in higher altitudes the climate resembles alpine conditions, but without glaciation (Schiemer et al., 2018b).

The Vjosa (known as Aoos in Greece) consists of five major tributaries: Voidomatis, Sarantoporos, Drinos, Bence, and Shushica. In this study, we focus on the main stem of the river from Konitsa to the outlet (Fig. 2.1).

The Vjosa River is poorly gauged. Daily streamflow is available only at Dorez (Fig. 2.1) for the period 1958–1989 (Schiemer et al., 2018b; Pessenlehner et al., 2022). Past bedload and suspended load measurements were only available from irregular and short field cam-

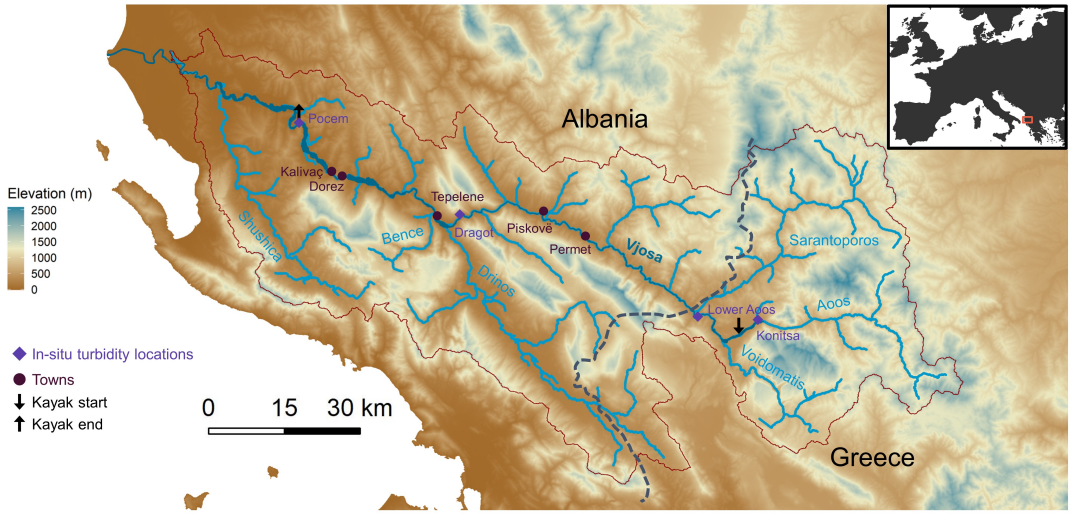

Figure 2.1: The Vjosa river catchment. The river originates in the Greek mountains and travels in the North-West direction through Albania before reaching the Adriatic sea. The Vjosa main stem (dark blue) and its five main tributaries (light blue) are marked. Some main towns are marked in dark red circles, the in-situ turbidity gauging stations are in purple diamonds, and the start and end of the kayak trips are marked with arrows. The catchment area is delineated by the red outline.

paigns in 2018 by Pessenlehner et al. (2022) at Pocem (Fig. 2.1). For this research, we installed four turbidity sensors on the main stem (orange diamonds in Fig. 2.1). The sensors were Aqua TROLL 600 by In-Situ and they measured water temperature, turbidity, pressure, dissolved oxygen concentration, and dissolved oxygen saturation. The sensors took measurements every 15 minutes for two years from May 2019–July 2021. Some of the sensors were lost throughout the study and did not record for this entire time period (Pocem and Konitsa sensors stopped recording in October 2019 and January 2021, respectively). Suspended sediment sampling was complemented by two kayak surveys in Spring 2019 and Fall 2020. These were 4 day trips during which a continuous turbidity profile was measured at 1-min resolution with the same sensor Aqua TROLL 600 attached to the bottom of a kayak. We call these lagrangian river profiles as the paddler was travelling downriver at speeds similar to or higher than the flow velocity. To fit the SSC-turbidity relationships we also periodically collected bottle samples, which were filtered to obtain SSC.

Spatial data for the catchment were obtained from E-OBS (daily precipitation) and CORINE (landcover). The digital elevation model (DEM) was obtained from Copernicus Digital Elevation Model (COP) and has a spatial resolution of 24×24-m. The DEM was used to derive flow accumulation along the river network and to compute river reach gradients. Daily precipitation data were averaged at subcatchment scales and summed over extended periods prior to the dates of satellite images as a proxy for runoff generation and streamflow.

2.2.2 Estimating turbidity from Sentinel-2 images

In order to estimate turbidity from the satellite images, the images needed to first be processed (atmospheric correction, cloud removal, etc.) and clipped to the studied river

section. A regression model was fitted using the data from the in-situ turbidity sensors and from the satellite pixels surrounding these sensors. This regression equation was then used to estimate turbidity for the entire main stem of the river for all available satellite images. The workflow of the procedure is shown in Figure 2.2, and the following sections explain the procedure in more detail.

Satellite images

Sentinel-2 (S2) satellite images over the catchment were collected for this study for the sensing period May 2019–July 2021 from the Copernicus Open Access Hub. Sentinel-2 products were chosen because they provide 10-m resolution images in the red (665 nm), green (560 nm), blue (490 nm), and near-infrared (NIR - 842 nm) bands. As the average active channel width of the Vjosa river ranges between 30 and more than 600 metres depending on river reach (Hauer et al., 2021), the S2 images are sufficient to resolve the flow width in most of the river reaches. Sentinel-2 also provides six additional 20 m resolution bands, one of which is the short-wave infrared band (1610 nm) which we used to identify deep water sections. Sentinel-2 records the radiance reflected from the top of the Earth's atmosphere across different parts of the electromagnetic spectrum, these products are called Level-1C (L1C). The ESA also provides Level-2A products, which are the Bottom of Atmosphere (BOA) reflectance images derived from atmospherically correcting the associated L1C products (ESA). However, in this study we use the L1C products and atmospherically correct the images ourselves using an algorithm that was specifically designed to process small, turbid, inland waterbodies (Vanhellemont and Ruddick, 2016). To cover the entire catchment during the study period, every five days two S2 L1C images (tiles T34TCK and T34TDK) were downloaded, and stitched together. This gives us a total dataset of 106 images in the study period (55 images from May 2019–July 2020, 51 images from Aug. 2020–July 2021).

Image processing methodology

The methodology used to process the S2 images is summarized in the flowchart in Fig. 2.2. Downloaded L1C products (Fig. 2.2-1) were corrected (Fig. 2.2-2) to eliminate atmospheric noise, negative reflectance values, and sunglint using the Python-based processor ACOLITE (Vanhellemont and Ruddick, 2016) and the remote sensing reflectance (Rrs) in the different spectral bands (e.g. 665 nm, 560 nm, 490 nm, 842 nm, 1610 nm, and 2190 nm) was extracted. The resulting atmospherically corrected images were then clipped (Fig. 2.2-3) to the active floodplain boundary to minimize the amount of data that needed to be processed. A manually created shapefile was used to outline the active floodplain boundary, similar to what would be mapped in a hydrogeomorphological context (e.g., Hauer et al., 2021). The remote sensing signal from a water surface contains two components, sub-surface reflectance from particles suspended in the water and bottom reflectance from the river bed. The sub-surface reflectance contains information on water clarity and is of interest to us, while the bottom reflectance is a noise component. Deep water sections are less likely to have bottom reflections and can be distinguished by their low reflectance in the short-wave infrared band of wavelength 1610 nm (Ji et al., 2009). For this reason, we first resampled the 1610 nm image (20×20-m resolution) into a 10×10-m grid and then extracted the deep-water pixels by using an upper cutoff value of 0.045 sr^{-1} (Fig. 2.2-4). This cutoff value was chosen for Rrs_{1610nm} (pixel values are from 0–1) through a visual inspection of the river. We began by applying different cutoff values to try to detect known deep water locations along the river. The cutoff value that was able to objectively detect the known deep-water locations along the river was selected. The contingency table created

for this cutoff method had a sufficiently low false negative rate of 7%. In using the cutoff on Rrs_{1610nm} we not only extract the deep water pixels within the active floodplain, but we also remove all other pixels (vegetation, dry bank surfaces, other water that is not deep, etc.). Our procedure also included the removal of pixels that are affected by clouds and cloud shadows (Fig. 2.2-5), with a MATLAB-based masking algorithm called Function of Mask (FMask) (Qiu et al., 2019). We used the default parameters in FMask for Sentinel-2 images, therefore a cloud probability threshold of 20% was used in the processing. Fmask then detects the clouds (and cloud shadows) present in the image and removes only these affected pixels in the image. We would also like to point out that our methodology to process the satellite images does not consider adjacency effects. The Dark Spectrum Fitting (Vanhellemont) algorithm used in this study is meant to avoid some of the issues associated with atmospheric correction over water in the presence of adjacency effects (Vanhellemont and Ruddick, 2018; Vanhellemont, 2019). Past studies have found that adjacency effects may not occur over all inland water bodies (Pahlevan et al., 2018) but they are important and should be investigated on narrow (and wide) rivers. However, investigating the effect of land adjacency would go beyond the scope of this work.

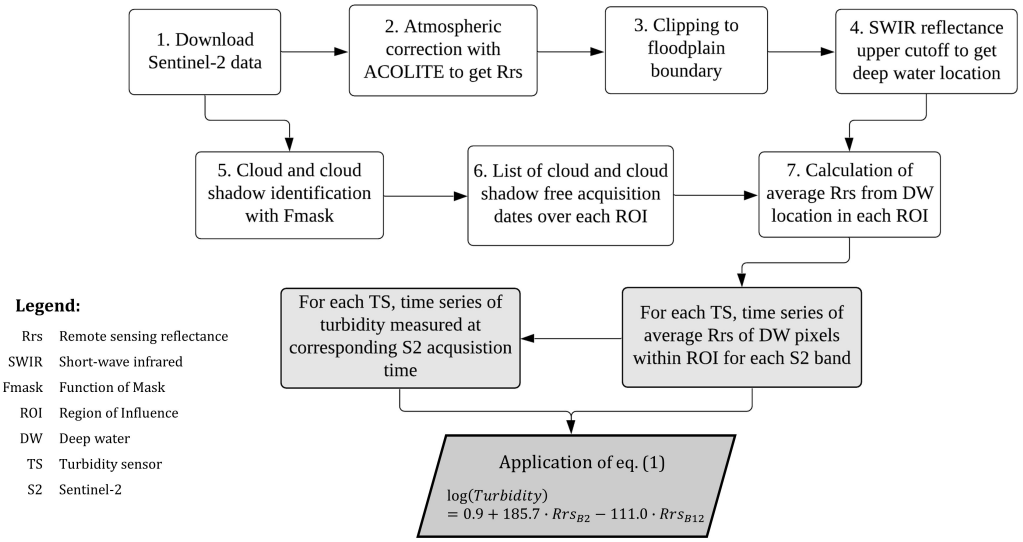

Figure 2.2: Flowchart summarizing the satellite image processing methodology and how to build the regression from the images. (1)–(6) describe the steps to process the images. Pixels in a 200-m diameter Region of Interest (ROI) around the sensors are averaged for each R_{rs} band (7). These average R_{rs} bands in deep water (DW) pixels at the time of corresponding in-situ measurements are used to build the regression using Equation (3.1).

Building a regression model

A regression model was built by relating the in-situ turbidity measurements at the four ground stations to the pixels in the immediate vicinity of the sensors. To obtain the representative reflectance coming from the water column surrounding the sensors, and not relying on a single pixel above the sensor, a circular buffer was selected around each sensor to mark its Region of Influence (ROI). The extent of the ROI was fixed at 200 m after comparing the mean reflectance of deep water, cloudless pixels within ROIs of different radii (500 m, 200 m, 100 m, and 10 m). After removing the clouds, cloud-shadows, and non-deepwater pixels within each ROI, the average R_{rs} for each spectral band was calcu-

lated (Fig. 2.2-7) for every satellite image. This resulted in on average 280 pixels (28,000 m^2) in each ROI for every acquisition day. In addition, at each sensor location, we extracted the closest in-situ turbidity measurements corresponding to the satellite acquisition times (where the maximum time offset between the satellite image and in-situ turbidity acquisition times is 15 minutes). This resulted in a data set containing the average R_{rs} of the 11 S2 bands and the in-situ turbidity data for each sensor location (ROI), over two years. This gave us 236 data points (13 at Pocem, 56 at Dragot, 75 at lower Aoos, and 92 at Konitsa).

A multiple linear regression analysis using ordinary-least-squares (OLS) was performed on the dataset above using the in-situ turbidity data (response variable in the range of 0–2800 NTU) and the average R_{rs} of the 11 S2 bands as separate potential predictor variables, with the goal to determine the regression line whose sum of squared residuals errors is minimum. We did this because we do not want to prescribe a-priori bands for the regression model, but rather let the data dictate what is the best fit. Histograms of average R_{rs} and turbidity data were checked to identify variables that require transformations which would result in better fitted regression models. A logarithmic transformation was applied to in-situ turbidity, converting its probability distribution from a right-skewed to a normal distribution and making $log(Turbidity)$ the new response variable. To avoid multicollinearity between the predictor variables which would lead to poor model fit, checks based on pairwise correlation coefficients and Variance Inflation Factors (VIF) were performed to choose only one among each set of collinear predictors (the correlation values between $log(Turbidity)$ and the different bands are shown in Supplementary Table C.1). After this step, regression models were fitted to different combinations of the chosen predictor variables (the 11 S2 bands), including different band ratios and their combinations, and the corresponding Bayesian Information Criterion (BIC) was compared. This way, only the average R_{rs} S2 bands (predictors) that have the highest and independent predictive power for in-situ turbidity (in NTU units) were chosen, as the BIC favours smaller, less complex models.

2.3 Results and Discussion

2.3.1 Regression model and uncertainty

The best performing multiple linear regression model for Log(Turbidity) in NTU units following the workflow in Fig. 2.2 described above was:

$$log(Turbidity) = 0.9 + 185.7 \cdot Rrs_{B2} - 111.0 \cdot Rrs_{B12} \tag{2.1}$$

The model was built with 226 data points and the residual standard error of the model is 1.613 log(NTU) or 5 NTU. Using the NTU-SSC rating curve, which we developed from observations (discussed later in Sec. 2.3.4), this gives us an error of 23.8 mg/L. The adjusted R^2 of the model in Equation (3.1), which explains the portion of the variance in turbidity by the two predictors, is $R^2 = 0.42$ (p-value $< 2 \cdot 10^{-16}$). The model statistics are shown in Table 4.2 and the 3D regression plot is in Supplementary Figure C.1. The P-values indicate a statistically significant relationship between the predictor(s) and the response variable. The Variance Inflation Factors (VIF) are < 5 meaning there is no multicollinearity problem present between the chosen predictors.

It is very difficult to compare our established relationship with those given in literature. First, not so many satellite studies have been conducted on rivers at this scale (due to

Table 2.1: Statistics for chosen regression model.

	Central Wavelength [nm]	Coefficients	Estimated. Std. Error	t value	P-value	VIF
Intercept		0.85	0.27	3.2	0.0018	
Rrs_{B2}	492	185.65	14.60	12.72	$< 2 \cdot 10^{-16}$	1.49
Rrs_{B12}	2186–2202	-110.96	12.64	-8.78	$4.5 \cdot 10^{-16}$	1.49

spatial resolution), and second because the relationships are purely empirical and dependent on sensor quality, frequency bands used, image processing, number of data points contained in the regression, sediment properties, flow regime, etc., there is little reason to expect any generality in the form of the predictor-response relations. Nevertheless, here we compare our results with some selected studies.

Onderka and Pekárová (2008) obtained a linear equation between the suspended particulate matter (SPM) and the calibrated radiance of the Landsat NIR band using a single-day image of the Danube. The equation had a standard error of 2.92 mg/L ($R^2 = 0.95$). However, their regression was built using 3 samples (0–60 mg/L) and validated using 12 samples (0–20 mg/L) only. Most of these samples came from a small impoundment area (∼16 km long). Bernardo et al. (2017) generated a quadratic equation relating total sediment matter (TSM) to the OLI5 band (narrow NIR) of the Landsat-8 satellite (p-value < 0.01 and $R^2 = 0.67$, satellite revisit time of 8 days). Their model was built on the Barra Bonita Hydroelectric Reservoir (series of reservoirs along the Tiete and Piracicaba rivers) using 23 samples over two sampling days. They were also able to achieve a low RMSE of 3.59 mg/L. Iacobolli et al. (2019) built a SSC empirical exponential equation using the 665nm (red) S2 spectral band ($R^2 = 0.05$). This was done with 35 samples from the estuary of the Aterno-Pescara river in Abruzzo and gave a RSME of 4.74 mg/L. The low errors in predicted SSC in all three studies above can be attributed to the small sampling interval, which covers only a narrow range of possible sediment concentrations, and the small area considered in the regression fits.

Doxaran et al. (2002) built a 3rd order polynomial using the reflectance ratio between NIR (850 nm) and green visible (550 nm) wavelengths of the SPOT satellite. They could estimate TSM concentration between 15–250 mg/L ($R^2 = 0.64$). The polynomial was built with 34 samples (13–985 mg/L) taken in July 2000, September 2000, July 2001, August 2001, and September 2001 at four locations (15–22km apart). Wass et al. (1997) used NERC's compact airborn spectral imager (CASI) to extract turbidity and SSC from the Humber estuary. Samples were collected from the bed of the estuary and calibrated to a spectrometer in a mixing tank for ranges 0–2000 mg/L. A linear relationship ($R^2 = 0.95$) was established between SSC and the 755.5–780.8 nm band (vegetation red-edge band). Unfortunately, neither of these works report the error of the regressions.

Sahoo et al. (2022) could achieve RMSE of 42.8–49.85 mg/L and R^2 of 0.65–0.77 on three different river sections of the Hooghly river using AquaMODIS' red band images. Finally, Wang et al. (2021) collected 62 SSC samples on the Yangtze river and using partial least squares, built a power equation using the ratio of the narrow NIR to the green band (B8a/B3, for both S2 and Landsat 8, $R^2 = 0.78$). They were able to obtain a RMSE of 24.1 mg/L, which is close to what we were able to obtain in our regression.

One commonality in the studies above is the use of red or NIR in the empirical relationships. Therefore, our use of the IR band is not surprising. Several of the above-mentioned studies conducted the regression analysis on shorter river sections, which will lead to a smaller standard error because local variability due to flow depth, bed morphology, landuse, geology, etc., is reduced. In order to create longitudinal turbidity profiles of the entire Vjosa main stem (272 km), our regression in Equation (3.1) was built on all four turbidity gauging stations at the same time, so that it captures also inter-site differences at the larger river basin scale. When instead, regression models were built for individual gauging stations with a 200 m ROI buffer we obtained lower standard errors (Table 2.2). All of the relative standard errors for the individual regressions (rel. std. errors between 0.87–1.52) are slightly lower than the error from the regression for all stations together (rel. std. error of 1.61). Additionally, the individual stations have R^2 larger than or equal to the original $R^2 = 0.42$, but their models chose entirely different bands than the original bands in Equation (3.1), but all of the selected bands in the new equations are either red or IR, as expected. However, predicting turbidity of the main stem using any one of these single-station regressions could lead to large prediction errors in river reaches with completely different geology, river morphology, and sediment sources/sinks. Additionally, the original Equation (3.1) does not perform dramatically worse than the individual station models.

Table 2.2: Model statistics for individual buffer stations at four locations along the main stem.

Location	Equation	Rel. Std. Error	R^2	P-value	Num. Observations
Pocem	$log(NTU) = -3 + 196.8 \cdot Rrs_{B2} + 37.9 \cdot Rrs_{B5}$	0.87	0.66	$1.7 \cdot 10^{-3}$	13
Dragot	$log(NTU) = 4.4 - 151.7 \cdot Rrs_{B11} + 107.8 \cdot Rrs_{B4}$	1.52	0.42	$5.2 \cdot 10^{-7}$	56
Lower Aoos	$log(NTU) = 0.7 + 98.8 \cdot Rrs_{B2} + 531.7 \cdot Rrs_{B6} - 428.3 \cdot Rrs_{B7} - 112 \cdot Rrs_{B12}$	1.11	0.40	$2.0 \cdot 10^{-7}$	69
Konitsa	$log(NTU) = 0.4 + 249.4 \cdot Rrs_{B4} - 217.9 \cdot Rrs_{B12}$	1.09	0.61	$2.2 \cdot 10^{-16}$	88

2.3.2 River turbidity profiles: validation and seasonality

The first aim of this paper was to extract the river turbidity profiles from the satellite imagery and investigate the spatial and seasonal signals present in the turbidity profiles. To this end, the regression equation from Eq. (3.1) was applied to every processed (cloud and cloud-shadow free, deep-water, atmospherically corrected) Vjosa pixel in 106 images over two years (55 images from May 2019–July 2020, 51 images from Aug. 2020–July 2021). Applying the regression to all of the river pixels resulted in 106 turbidity maps, one of which is shown in Figure 2.3a (from 23.10.2020). When all 106 images are averaged in time and binned into 100-m river segments in space to reduce pixel-to-pixel variability, we see an interesting signal of spatial variability in mean NTU along the Vjosa main stem (Fig. 2.3b). Mean NTU over the two-year period varies from near 0 in the upstream sections to between 200–300 NTU in the lower sections. The maximum predicted turbidity was 9856 NTU. Some of the spatial variability is connected to inputs from tributaries (e.g. Drinos and Bence), but there is also systematic variability within river sections that do

not have large tributary inputs (e.g. between 20-100 km upstream from the outlet in Figure 2.3b).

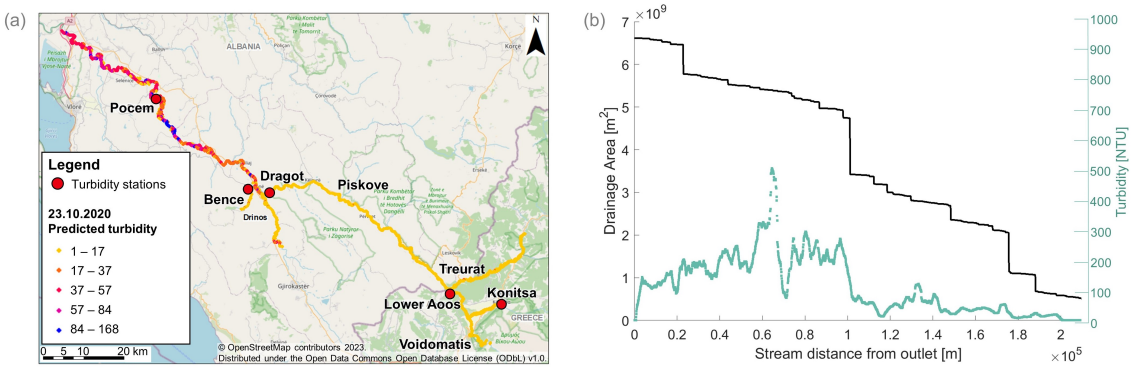

Figure 2.3: Turbidity data extracted from Sentinel-2 imagery for the entire Vjosa catchment using ©OpenStreetMap contributors 2023. Distributed under the Open Data Commons Open Database License (ODbL) v1.0. (a) Processed turbidity map for 23.10.2020. (b) Two year average longitudinal turbidity profile (green) and catchment area from the DEM (black), both plotted against the stream distance from the outlet.

A proper validation of the predicted river turbidity profiles from satellite imagery is not possible, as we do not have spatially distributed turbidity sensors along the river system. Instead, here we conducted a qualitative comparison with the kayak-derived river turbidity profiles. Using these types of Lagrangian measurements in rivers is not uncommon (Hensley et al., 2014; Baker et al., 2014; Kraus et al., 2017; Postacchini et al., 2015). Therefore, we have collected two turbidity profiles from a kayak and these are shown in Figure 2.4: one in Spring 2019 (a) and one in Fall 2020 (b). Since the river is 272 km long, the measurements were taken over 4-day kayak trips during a period with no rainfall in the catchment. The sensor used was the same AquaTROLL used at the ground stations, with a 1-min sampling resolution during the descent. Discharge in these plots was estimated using a log-log scaling relationship between catchment area and discharge. Discharge was measured empirically at selected sampling sites using an electromagnetic flowmeter (Ott MF Pro, Ott Hydromet, Kempten, Germany) at a minimum of 15 sites spread evenly across a river transect or by means of an acoustic Doppler profiler (SonTek River Surveyor) towed across the river and delivering a spatially continuous velocity field. These measurements were then used as calibration points in a Bayesian regression with priors taken from published scaling relationships (Burgers et al., 2014). Two discharge measurement campaigns were conducted: once in Spring 2019 and once in Fall 2019 (the latter was used to plot Q*T in Fig. 2.4b as a proxy for fine sediment load).

Although the kayak-derived measurements cannot be directly compared with individual satellite images as the former are lagrangian estimates over a 4-day sampling window, and the latter are snapshots in time which does not necessarily overlap with this window, we still can use these data to provide a qualitative proofing of the satellite data. Figure 2.4 reveals some consistent patterns in sediment inputs and fluxes. In both Spring and Fall, as the Sarantoporos joins the Aoos (at 175km from the outlet) both the turbidity and the Q*T increase. This increase is also evident in the satellite data in Fig. 2.3b with similar NTU values. There is also a peak at around 130km near Piskove (see Fig. 2.1 for location) in 2019 that quickly decays. This appears to be a sediment wave that was generated in

one of the tributaries, and is passing downriver. Both the turbidity and Q*T near Pocem (see Fig. 2.1 for location) is higher than in the headwaters and reaches about 15 NTU in 2019 and 120 NTU in 2020 in the kayak-derived data, while on the average the satellite images are predicting about 200 NTU for this location. As the kayak measurements were conducted during dry weather and low flows, while the satellite data cover an entire 2 year period with seasonality present, this difference is expected.

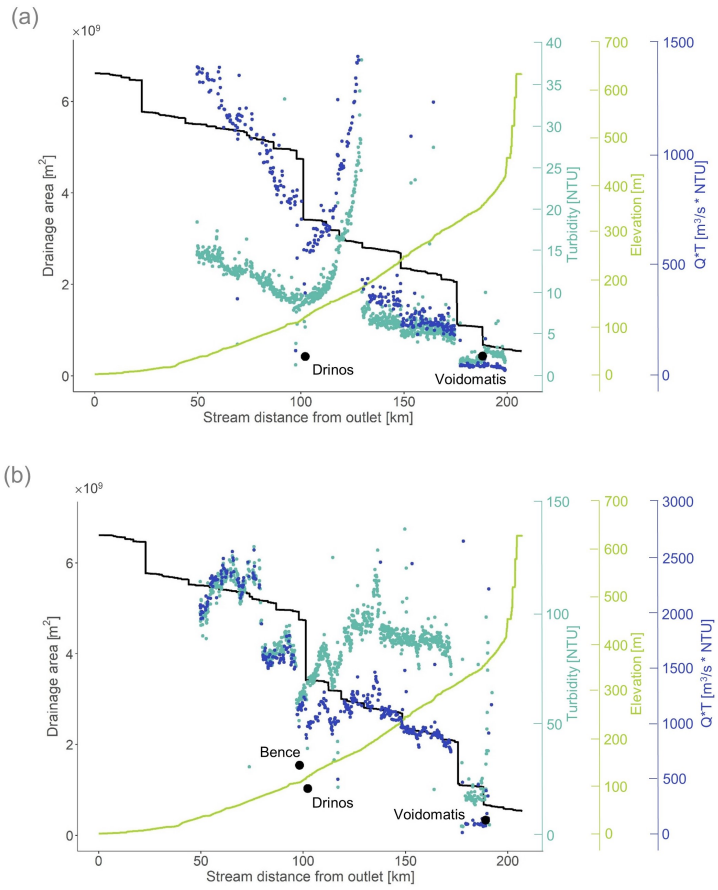

Figure 2.4: Longitudinal profiles from the kayak trips plotted along the distance from the outlet in (a) Spring 2019 and (b) Fall 2020. Teal points are turbidity measured by the AquaTROLL 600. Blue points represent a proxy for sediment load (discharge (Q) multiplied by turbidity (T)). The green line is the elevation of the river bed and the black line is the catchment area, both extracted from the DEM. Three larger black points mark the turbidity of the tributaries: Bence, Drinos and Voidomatis.

We now use the 106 satellite images to compute mean seasonal turbidity along the Vjosa main stem. Figure 2.5 shows a seasonal signal across two years of measurements, from May 2019–July 2021. It is evident that mean turbidity in the Vjosa is higher in Winter than the other seasons, especially Summer. Interestingly, in Piskove (130 km from outlet), there is a peak in turbidity that is seen in the Winter signal and not in the other seasons. This Winter peak is evident also in the two-year average in Fig. 2.3b and in the kayak-derived observations in Fig. 2.4. There are other recurring patterns in the seasonal signals and in the river profiles. For example, the jump in turbidity due to the Drinos tributary at 100 km and the dip in the braided section (75km). By inspecting individual images we conclude that these consistent changes in turbidity are independent of seasonality and likely have

to do with persistent sediment sources and sinks in these river reaches.

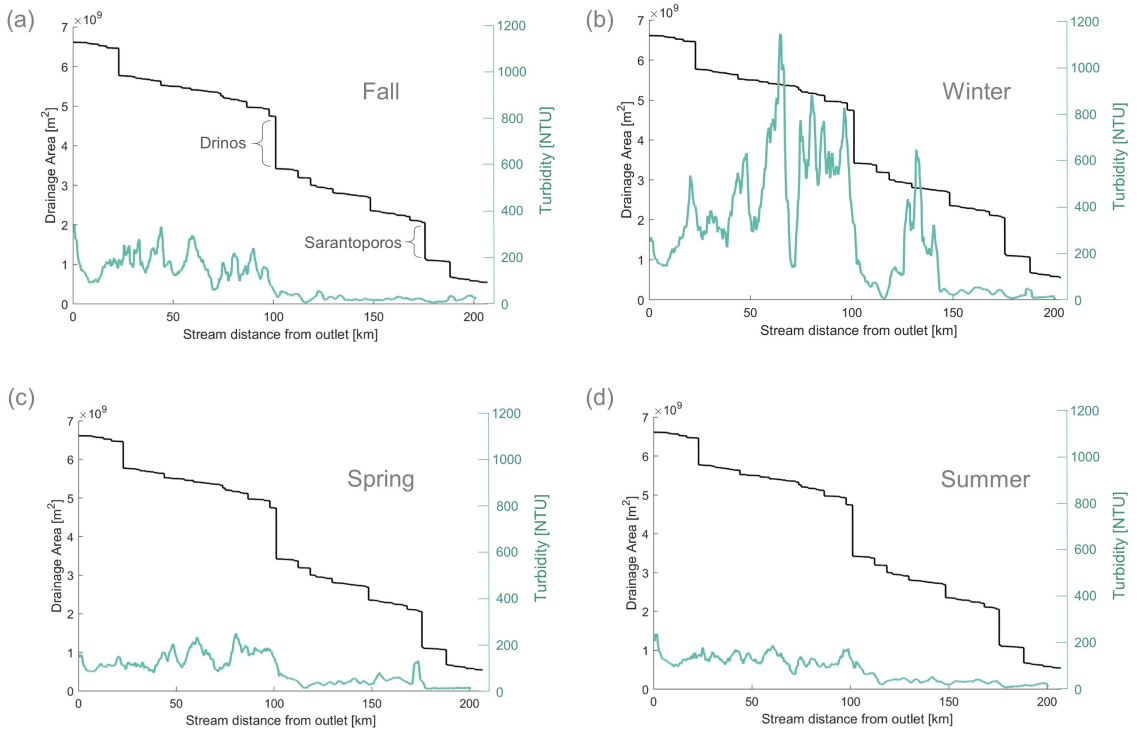

Figure 2.5: Seasonal longitudinal turbidity profiles (bluegreen) and catchment area from the DEM (black), both plotted against the stream distance from the outlet. (a) Fall is the average of all longitudinal profiles extracted from satellite images from September to November in both 2019 and 2020 (the two largest tributaries, Sarantoporos and Drinos, are marked), (b) Winter is from December 2019 to February 2020 and then again from December 2020 to February 2021, (c) Spring is from March to May in both 2020 and 2021 and with one additional image from May 2019, (d) Summer is from June–August in 2019 and 2020, and June–July in 2021.

2.3.3 Sources and sinks of sediment along river profiles

The second aim of this paper was to identify possible fine sediment sources and sinks in the Vjosa catchment from the longitudinal river turbidity profiles due to tributaries and within individual river reaches, and search for their possible activation by rainfall. To achieve this aim we computed changes in NTU upstream and downstream of every tributary $dNTU_{trib}$ and upstream and downstream of every river segment $dNTU_{rea}$ (Fig. 2.6):

Figure 2.6: Differences in turbidity (dNTU) calculated as the upstream turbidity subtracted from the downstream turbidity. The locations of upstream and downstream turbidity are shown in the two panels: LEFT for tributaries and RIGHT for river reaches between two tributaries.

Boxplots of $dNTU$ from all 106 satellite images are shown in Figure 2.7 where the X-axis gives the relative location of each tributary or center of reach (not to scale). If a tributary brings disproportionately more sediment or if sediment is mobilized within the reach (e.g. from the bed or banks), then $dNTU > 0$ and there is a sediment source. Conversely, if $dNTU < 0$ then water added by the tributary brings less sediment, or there is deposition of sediment within the reach and we have a sediment sink. The asterisks in Fig. 2.7 represent the sources and sinks with a statistically significant change in $dNTU$. The kayak-derived measurements in 2019 and 2020 are also shown as markers in the boxplots. Most of the kayak points fall within the whiskers of the $dNTU$ boxplots, confirming that the measurements taken during these low flow conditions lie within natural variability of turbidity at those locations. The kayak points fall within all boxplot whiskers except for the most upstream reaches/tributaries (at L/Lx = 0.81, 0.88, 0.91, and 0.94). There we theorize that the river is too narrow in the upstream section to extract proper reflectance data. Also, the river is much more clear upstream so the measurements from satellite images may fail.

The statistically significant fine sediment sources are found at Lx/L = 0.29, 0.53, 0.58 (reaches), and 0.5, 0.56 (tributaries). These river reaches and tributaries are surrounded by agricultural land and located in predominantly Flysch and clastic sediment geologies. All three of these factors could contribute as sediment sources to the increase in SSC. The two reaches at Lx/L = 0.53 and 0.58 are located within limestone canyons with springs, therefore we expect a decrease in SSC from the spring water dilution. However, we find that the SSC increases as we move downstream. One possible reason could be that river water is infiltrating into the bed in these limestone reaches, leaving a higher sediment concentration in the main stem. This would have to be confirmed with flow measurements. The reach at Lx/L = 0.29 has the largest median and variability of all of the statistically significant sources. This reach contains a large braided section which can act as a source of fine sediment from the river bed during high discharge conditions, but also as a sink during low discharge conditions. This reach however could also be a source due to meanwhile abandoned dam construction activities in Kalivaç, which could be producing larger quantities of fine material in recent years.

The statistically significant fine sediment sinks in the Vjosa are fewer than sources, and are located at Lx/L = 0.37 and 0.6 (tributaries). The estimated rates of change $dNTU$ here are likely caused by systematically lower sediment concentrations coming from these tributaries than already present in the main river. Although we could not identify relevant differences in catchment geology, vegetation cover or steepness in these catchments, it is conceivable that they have low sediment production rates. However, it is also notable that the changes in NTU downstream of these tributaries are very small, often close to the

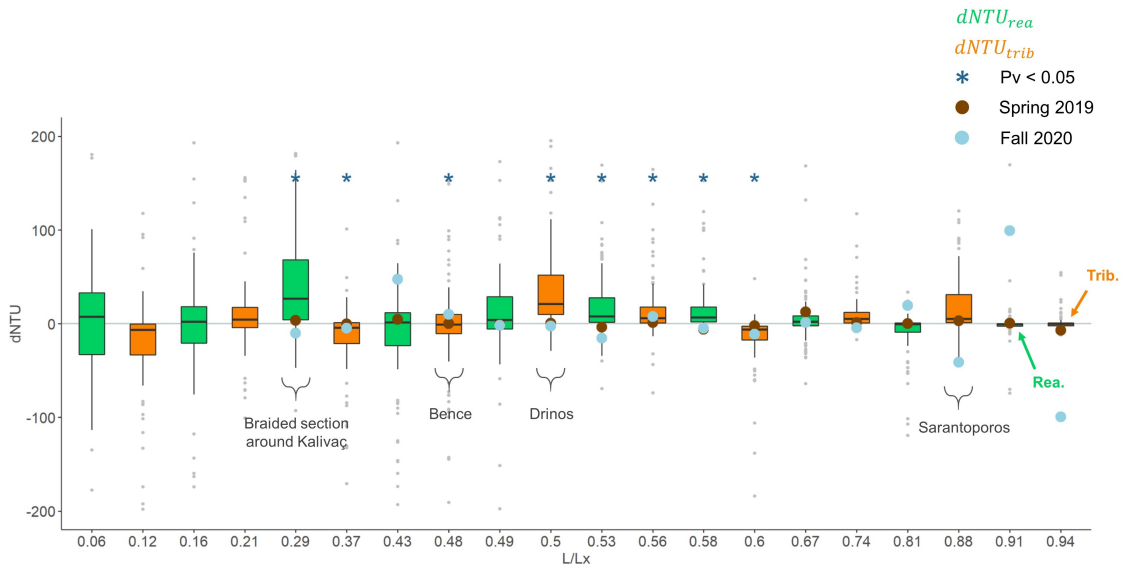

Figure 2.7: Boxplots of differences in satellite-derived turbidity ($dNTU$) for tributaries (orange) and reaches (green) plotted against the relative stream distance from the outlet (Lx/L). The boxplots were built using the 106 turbidity profiles over 2 years. The black line in the boxplot represents the median, the boxes extend to +/- one standard deviation, the whiskers extend to +/-1.5*IQR, and the light grey points are the outliers. Locations with a P-value < 0.05 are marked with a blue asterisk. The kayak points from Spring 2019 and Fall 2020 are marked as the brown and light blue circles, respectively. Some major tributaries and reaches are labeled.

standard error of the regression model in Eq. (3.1), and furthermore, at Lx/L = 0.37 the downstream section is constricted in a canyon with poorer satellite visibility. All of these factors result in the predictions here to be highly uncertain.

We hypothesize that the tributary and reach changes in NTU should be related to the strength of activation of sediment sources by rainfall and runoff. We test this hypothesis by dividing all tributary and reach $dNTUs$ into wet and dry days. Of our 106 available days/satellite images, we could obtain rainfall data for 101 days (up until the end of June 2021). We define dry days as days where there is less than 0.01 mm of cumulative rain over the last 6 days in the entire catchment and wet days are all other days (67 wet days and 34 dry days). On dry days mean $dNTU = 7.5$ for river reaches and $dNTU = 2.5$ for tributaries, suggesting there is very little sediment activation and sediment concentration is almost constant, while on wet days mean $dNTU = 4.4$ for river reaches and $dNTU = 30.2$ for tributaries, suggesting that tributaries indeed become sediment sources by rainfall-activated mobilization.

The empirical cumulative distributions of the $dNTU$ rates in Figure 2.8 show that rainfall affects both river reaches (a - green) and tributaries (b - orange) in the extremes. Interestingly, the $dNTU$ of river reaches tends to deviate stronger from $dNTU = 0$ in both the positive and negative directions (acting as both sources and sinks) with the presence of rainfall. However, tributaries tend to act more as sources ($dNTU > 0$) with the presence of rainfall. Performing a two-sample Kolmogorov-Smirnov test on the wet and dry day distributions for both the tributaries and reaches, we find that the two distributions (dry

and wet) are statistically significantly different (for tributaries: $D_{KS} = 0.15$ and P-value $= 1.58 \cdot 10^{-4}$; for reaches: $D_{KS} = 0.12$ and P-value $= 5.42 \cdot 10^{-3}$). The P-value is reported for significance level 5%.

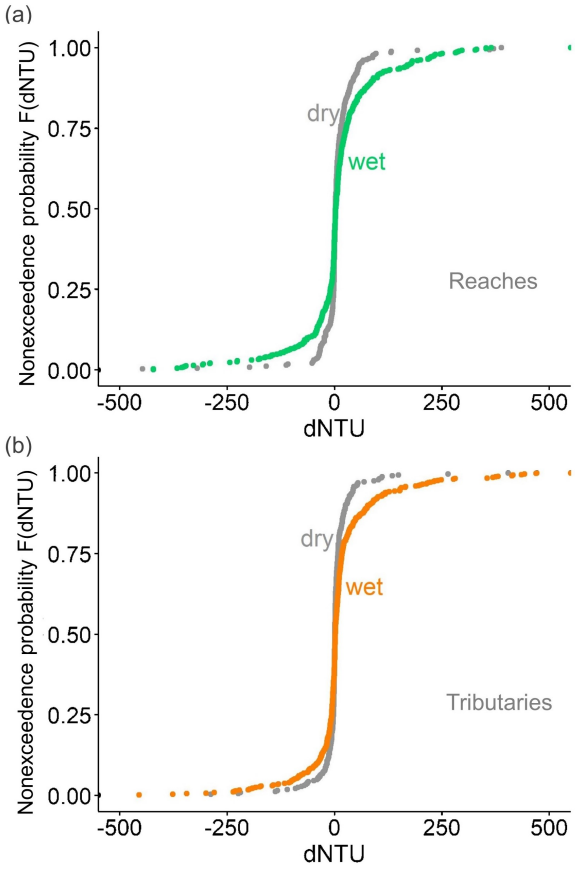

Figure 2.8: Empirical cumulative distributions for reaches (a) and tributaries (b) on dry and wet days.

2.3.4 Sediment load at Dorez

Finally, we conducted a plausibility check to see if the estimates of SSC and sediment load at Dorez (the single gauged location on the Vjosa River) from our remote sensing-derived turbidity estimates agree with SSC estimates of past studies. Using the satellite river turbidity profiles, we could estimate the annual sediment yield at Dorez, 70.5 km from the outlet (see location in Fig. 2.1). First, we computed the mean seasonal turbidity at the Dorez location in the longitudinal profile from the two years of satellite data in Figure 2.9a (e.g. SON boxplot is September, October, and November turbidity values in years 2019–2020). The boxplots were built using all the turbidity pixels around Dorez (70.46–70.58 km from the outlet). Second, the mean turbidity values were converted to SSC using the rating curve in Fig. 2.9b, where a power fit was found to best represent the NTU–SSC relationship (Holliday et al., 2003). The SSC data for this fit was obtained by taking water-sediment (gravimetric) samples on the main stem during our various campaigns from 2019–2021 and subsequently filtering the samples after each campaign the gravimetric samples were filtered using Whatman GF/F filters, the filters were weighed to obtain the sediment mass [mg] and the volume of filtered water was measured and combined with the volume of the

filtered sediment to obtain the total volume of the sample [L], this gave us the SSC in mg/L). These gravimetric samples were taken at Pocem, Dragot, Lower Aoos, and Konitsa (see Fig. 2.1). Similarly to the catchment-wide $Turbidity - R_{rs}$ Equation (3.1) (as opposed to different relationships applied to different reaches, as explained in Section 3.3.1), we wanted to create a catchment-wide $Turbidity - SSC$ relationship. This relationship was also necessary since we neither have SSC samples or turbidity measurements in the Dorez reach. And although this relationship introduces uncertainty when estimating SSC in the Dorez reach, it can be applied to any section of the river. Using the $Turbidity - SSC$ relationship in Fig. 2.9b, the two-year seasonal average SSCs were found to be: Winter - 10.4 g/L, Spring - 5.1 g/L, Summer - 8.5 g/L, and Fall - 14.9 g/L. Third, the daily discharge (m^3/s) at Dorez from 1958–1989 (Pessenlehner et al., 2022) was used to compute the mean seasonal discharge in two-year periods, which corresponds to our measurement duration period. This daily discharge data from 1958–1989 was used because there is no alternative long-term discharge data available in the catchment. Two-year periods were averaged so that we capture possible natural variability at biannual timescales in the discharge record. The two-year seasonal discharges were then multiplied by the mean seasonal SSC to get the seasonal sediment load for two years and cumulated to get total annual loads. This approach gives us biannual estimates of fine sediment loads which have the same seasonal mean concentrations as our estimates, but different annual discharges. The results in Fig. 2.9c show that the resulting mean annual sediment yield in Dorez has a decreasing tendency due to lower discharges in time. Our best estimate of the mean annual sediment load at Dorez assuming that sediment concentrations follow our estimates is $\sim 2.5 \pm 0.6$ Mt/y, which is in agreement with 1.4–2.5 Mt/y reported by Pessenlehner et al. (2022) at this location.

A suspended sediment yield of $\sim 2.5 \pm 0.6$ Mt/y is remarkable for such a small catchment. This amounts to an erosion rate of 373 t/y/km^2 (for a catchment area of 6704 km^2). In comparison to the Amazon, the pre-dam Mississippi, the St. Lawrence and the Yangtze rivers, which each produce 204 t/y/km^2, 124 t/y/km^2, 4 t/y/km^2 and 267 t/y/km^2 of suspended load, respectively (Milliman and Farnsworth, 2013; Syvitski and Milliman, 2007). The sediment production by the Vjosa is similar to other small mountainous rivers nearby (Ofanto, Achelos, and Simeto rivers all have a catchment area less than 7000 km^2 and deliver 333, 611, 238 t/y/km^2, respectively (Milliman and Farnsworth, 2013)). This puts the need for conservation of small mountainous rivers into perspective and enables us to understand Albania's push for the Vjosa National Park: a National park along the entire Vjosa river. Such a park would prevent any hydropower plants from being built, thus avoiding the obstruction of the necessary flow of sediment (Martini et al., 2022; Schiemer et al., 2018a, ch. 1).

2.4 Conclusion

In this study, we have shown the potential and limitations of using high-resolution open-access satellite S2 images for estimating water turbidity in relatively narrow and morphologically complex rivers, with the purpose of detecting possible sediment sources and sinks, their activation by rainfall, and estimating sediment yield in mountainous catchments.

The first result presented here was the extraction of 106 longitudinal river turbidity profiles for the entire 270 km main stem of the Vjosa River in Albania for every available and cloud-free satellite image from May 2019 to July 2021 using a multivariate regression

model fitted to four ground stations. The river profiles revealed variability in turbidity due to both tributary and within-reach inputs. The profiles also revealed a seasonal signal, with the highest mean turbidity in winter along the entire length of the river and visible local inputs by tributaries. Lagrangian river turbidity profiles were also measured along the entire main stem during two kayaking trips and used as a qualitative validation of sediment concentration variability.

The second result presented here was that sediment sources and sinks could be identified and quantified from the river turbidity profiles, both for tributaries and within river reaches. The river basin and network acted as a sediment source most of the time, significant sediment sinks were rare, but did exist. Sediment sources were mostly tributaries following basin-wide rainfall, but also within-reach sources in river beds and banks were possible. Finally, as a plausibility check we estimated the total fine sediment yield at Dorez at $\sim 2.5 \pm 0.6$ Mt/y, which is in line with previous studies and reveals the importance of the Vjosa River as a sediment source into the Adriatic worthy of protection.

In this study, we have largely ignored the effects of land adjacency. It would be interesting to see a future study that investigates at which point (e.g. at which river width) does land adjacency not affect the pixels in the middle of the river. With this information, we could incorporate the effects of land adjacency and determine how to correct these effects. The methodology developed in this study may be applied to other river systems, this was our guiding principle. However, there are several steps that are site-specific, e.g. downloading S2 images, developing shapefiles to delineate the floodplain boundary, determining the deep-water threshold cutoff value (taken from visual inspection of known deep locations in the river), and the availability of at least one in-situ sensor measuring turbidity to establish the $Turbidity - R_{rs}$ relationship. We see an opportunity of utilizing online tools (e.g. Google Earth Engine) to not only make the data processing faster (no need to store the S2 and processed ACOLITE images on a local drive) but to also create a transferable workflow for future studies.

Satellite images have been used for the quantification of turbidity in large water bodies, wide rivers, lakes and coastal zones. Here we show that such high resolution data have potential for suspended sediment quantification also in smaller, narrower and morphologically diverse mountain rivers, despite some loss in accuracy. The applications of such analyses are many, from identifying erosion hotspots, sediment source activation processes, various local point sources, glacial channel networks, in streams and large rivers, to river deltas. This work provides a proof of concept and workflow which lays the foundation for future studies into improving the accuracy and reducing the uncertainty in such analyses.

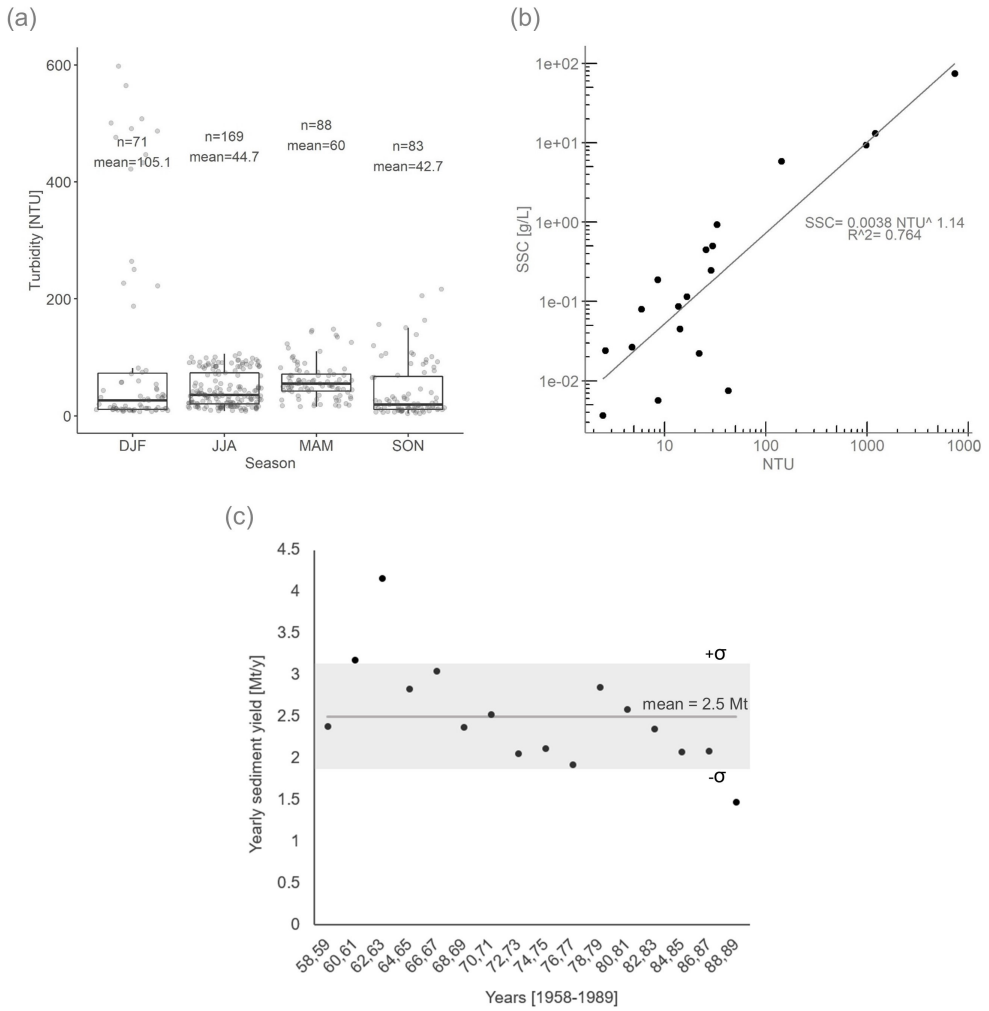

Figure 2.9: Sediment yield calculation. (a) Boxplots of turbidity at Dorez across two years grouped by season. The horizontal line in the boxplot is the median, the boxes extend to ±std. dev., the whiskers extend to ±1.5·IQR, and the points are the outliers. Above each boxplot is the number of observations and the mean for each season. More observations than the number of images (106 images, Sec. 2.3.2) because we took all of the pixels around Dorez (between 70.46–70.58 km from the outlet, mean of ∼5 pixels). (b) Power model fit between turbidity [NTU] and SSC [g/L] for seston samples we collected throughout our field campaigns. (c) Yearly sediment yield for the years 1958–1989, calculated using the seasonal turbidity averages over two years and discharge data from 1958–1989, the mean is marked with the grey line, the $\pm\sigma$ is marked with the grey shading where $\sigma = 0.63$ Mt.

Chapter 3 Open-Source, Low-Cost, In-Situ Turbidity Sensor for River Network Monitoring

Authors: Jessica Droujko and Peter Molnar
Journal: Scientific Reports
Publication date: June 20th, 2022

Key findings:

1. We have created a smart water turbidity sensor that is multi-site, accurate and affordable, which detects scattered light from an LED source using two detectors in a control volume, and can be placed in a river.

2. We compare several replicates of our sensor to different commercial turbidity probes in a mixing tank experiment using two sediment types over a wide range of typical concentrations observed in rivers.

3. Our results show that we can achieve precise and reproducible turbidity measurements in the 0–4000 NTU or 0–16 g/L range.

4. Our sensor can also be used directly as a suspended sediment sensor and bypass a lengthy and potentially dangerous calibration to Formazin.

5. The developed turbidity sensor is much cheaper than existing options of comparable quality and is especially intended for distributed sensing across river networks. The sensor was also published open-source so others can recreate and iterate on the design.

Author's contributions: The author designed and built the sensors, conceived and conducted the experiments, and contributed to the discussion of the results and review of the manuscript.

Coauthors' contributions: PM provided guidance and supervision of the project and contributed to the discussion of the results and review of the manuscript.

Data Availability The datasets generated during and/or analysed during the current study are available in the Zenodo repository: 10.5281/zenodo.5789513.

Supplementary Material: The supplementary material supporting this article can be found in Appendix D.

3.1 Introduction

Fine sediment production and transport is an important process at the global scale, affecting riverine, coastal and marine ecosystems (Arrigo et al., 2008; Sanders et al., 2014; Hauer et al., 2018). Present-day fine sediment export from the land surface to global oceans by large rivers is estimated at about 15.5-18.5 Gt per year (Peucker-Ehrenbrink, 2009; Syvitski and Kettner, 2011) and this is about half of the estimated global annual soil erosion from the land surface (Borrelli et al., 2017). However, it remains very difficult to estimate suspended sediment yields in rivers because of the high variability in along-stream suspended sediment concentrations (SSC) and inadequate monitoring thereof.

The primary method to determine SSC is gravimetric analysis of bottle samples taken at river cross-sections in regular or irregular intervals. This method is reliable but has many disadvantages such as being discontinuous (poor temporal resolution), inefficient and costly (high effort for collection/transport/analysis of the samples, long processing times). Sediment budgets for river basins are usually derived from these direct measurements of SSC (Milliman and Farnsworth, 2013; Poulier et al., 2019). Continuous SSC data at high temporal resolutions can be obtained by dedicated in-situ sensors which measure turbidity (T), and by calibrating a relation between SSC and T. In river cross-sections where measurements of water discharge (Q) are also made, sediment yield (QS) is then computed as QS=SSC*Q. High resolution estimates of SSC can be used to quantify human effects on sediment production, for example the effects of dam construction and erosion control (Wang et al., 2007; Hu et al., 2011), the natural erosion gradients over entire mountain ranges (Hinderer et al., 2013), the role of sampling in global erosion rates (Covault et al., 2013), and many others. Measurements of SSC at a basin outlet can give us a basin-integrated picture of possible hydroclimatically-driven sources of sediment, like rainfall erosion, snowmelt hillslope erosion, glacier ice melt erosion, even hydropower storage in dams (Costa et al., 2018a). These measurements of SSC are also important for understanding the impact of hydroclimatic forcing on activating sediment sources and transport dynamics, and physically-based modelling thereof (Bakker et al., 2018; Battista et al., 2020a; Costa et al., 2018b; Konz et al., 2011; Uber et al., 2021).

High temporal resolution monitoring using in-situ turbidity sensors at, for example, glacier streams is useful for identifying the time-dependent sediment export rates connected to the development and evolution of subglacial channels and the possible contributions of proglacial sediment sources (Delaney et al., 2018a,b). Together with grain size measurements, highly resolved SSC data can be used for the detailed hydraulic modelling of glacially-derived sediment transport by meltwater drainage in subglacial streams (Ugelvig et al., 2018). Hillslope source connectivity to the fluvial network in proglacial areas is also an important modulator of time-dependent sediment production (Bakker et al., 2018; Lane et al., 2017). Such process understanding requires a spatial perspective on sediment pathways of production and storage within the catchment which cannot be achieved by single-site measurements. Additionally, the main deficiency of point river measurements by devoted suspended sediment monitoring sensors is that they are expensive (e.g. state-of-the-art turbidity sensor by Campbell is about €6000, In-Situ is €7000), making widespread deployment at many sites along a river system to quantify spatial variability next to impossible. Nevertheless, this is currently the state-of-the-art measurement in both small and large river systems.

An alternative to ground point measurements is remote sensing. The spatial distribution

of SSC can be obtained using satellite imagery which is based on the reflectance of water surface as it is affected by a range of parameters (chlorophyll, suspended sediment, dissolved organic matter, etc.). Dissolved and suspended sediment concentrations together with gross biological activity affect the intrinsic colour of natural waters (Novoa et al., 2015; Wang et al., 2018a), which makes optical satellite remote sensing of oceans, coastal areas, large lakes/rivers possible. When calibrated with ground measurements, such satellite data can be very useful for SSC estimates (DeLuca et al., 2018; Martinez et al., 2009) and can give a range of additional water quality parameters (Wang and Sohn, 2018) at large scales but not with high temporal resolutions (repeatability given by satellite overpasses) and with poor point accuracy. In rivers, satellite-based analyses are only possible if the spatial footprint is sufficiently large. For example, in the Amazon SSC variations with satellite imagery were shown to follow overbank flow, and could be explained by resuspension of sediments in depression lakes (Fassoni-Andrade and de Paiva, 2019) only because the river is very wide.

Optical sensing of river turbidity, and other water quality indicators, is also possible with terrestrial photography (Goddijn and White, 2006; Fricke and Baschek, 2014). Optical sensing of turbidity by mobile phone cameras (Leeuw and Boss, 2018) is an application that has broad appeal for some ground applications. However, all ground-based and UAV optical sensing methods are limited by cost, poor temporal resolution, and are strongly affected by many environmental constraints (light, good optical transmission, visibility, etc.), which make them currently not very suitable for regular long-term monitoring of SSC in rivers.

We argue that a new type of sediment monitoring is necessary to demonstrate the many physical connections between hydrology, river processes, and sediment fluxes. The connections between sediment source activation and transport on hillslopes, cultivated fields, vegetated surfaces, subglacial channel networks, in streams, large rivers, and deltas, all require sediment monitoring at high spatial (from source to sink) and temporal (activation timescale) resolutions that are not fully guaranteed by any of the standard approaches in economically-effective ways. This new data is needed for developing an understanding of sediment storages and budgets in Alpine basins (Bennett et al., 2014, 2013; Hirschberg et al., 2020), revealing intricate details of sediment connectivity in such fluvial systems (Lane et al., 2017; Bakker et al., 2018), and for calibrating physically-based hydrological-sediment transport models (Molnar et al., 2006; Seybold et al., 2009; Konz et al., 2011; Battista et al., 2020a). For this reason, we propose here an affordable turbidity sensor that can be used to create a distributed suspended sediment monitoring network.

3.1.1 State-of-the-art in low-cost turbidity sensing

Several novel turbidity sensors have been documented in peer-reviewed literature. Gillett and Marchiori (2019) investigated the use of low-cost, commercially-available appliance turbidity sensors (such as those found in washing machines and dishwashers). These sensors work on the principle of light attenuation, where the light detector is placed 180^o from the incident light. Gillett and Marchiori (2019) found that these analog attenuation sensors could not achieve a sufficiently high resolution to monitor small changes in turbidity. Trevathan et al. (2020) recalibrated an appliance sensor (DF Robot SEN0189 Gravity - also attenuation style) and built a waterproof housing for field deployments. However, they did not report on the accuracy of the sensor and were not able to calibrate below 100 Nephelometric Turbidity Units (NTU) (although their test measurements were between

0-20 NTU). Additionally, the data obtained by their sensor was influenced by ambient stray light and they were not able to overcome this problem.

To improve the accuracy of an attenuation-style sensor in the 0-100 NTU range, Lambrou et al. (2014) and Wang et al. (2018b) equipped these attenuation sensors with a detector at 90^o to the incident beam. This method provides good stability, linearity, sensitivity, low stray light, and increases the NTU measurement range (when incorporating the backscatter detector) (Sadar, 1998). The use of several detectors at different angles allows the partial cancellation of errors due to wavelength absorption in samples (Bhardwaj et al., 2015). However, Lambrou et al. (2014)'s sensor was only tested from 0-100 NTU and did not report on how the 0.1 NTU resolution was obtained. Additionally, Wang et al. (2018b) only tested their sensor within the 0-1000 NTU range. Kelley et al. (2014) created a low-cost, hand-held turbidity meter meant for investigating drinking water quality in low-income communities around the world. This sensor was calibrated with and tested against a commercial turbidity sensor but only in the 0-1000 NTU range. Additionally, using commercial turbidity sensors to calibrate is not advisable since their measurements have strong differences in reported values among the various sensors (Felix, 2017). Kitchener et al. (2019) conducted a sediment settling experiment by constructing a modular PVC ring that could hold light detectors at several angles (0^o, 10^o, 20^o, 90^o, 160^o) to the illuminating LED. They reported their results in SI units of radiant intensity (mW/sr) instead of using formazin and obtaining units of NTU. Their device did however cost around 340GBP and cannot be deployed for environmental applications.

In addition to testing the appliance sensors, Gillett and Marchiori (2019) created a flow-through sensor meant to be attached to a PVC and continuously monitor turbidity for 64€. However, due to the nature of their design (large PVC diameter), they used a very powerful ambient LED and calibrated their sensor under dark-room conditions. This sensor can be used in a pump-test setup, as they've shown, but is unsuitable for environmental applications where ambient stray light will interfere with the measurement. Jiang et al. (2020) created a turbidity sensor for deep-sea applications, reaching depths of over 3400 meters. The sensor was based on a backscatter principle (the detector is positioned at $< 45^o$ relative to the incident LED beam) but is only suitable in the 0-20 FNU range (FNU and NTU are interchangeable units of turbidity). Additionally, the sensor is claimed to cost under $40 however, the bill of materials does not include sensor housing costs and all of the components used.

3.1.2 New sensor design

In this paper, we propose an open-source and low-cost turbidity sensor that can be used for in-situ river network deployment. Based on the review above and on the work carried out in the Supplementary Methods - First prototype section (Appendix D), we have designed a sensor with the following features. (1) The sensor has one light source and two detectors at different angles to each other for partial cancellation of errors (Bhardwaj et al., 2015). (2) It takes the difference between two measurements (LED off and on) to reduce ambient light effects. (3) It covers a large suspended sediment range 0-4000 NTU or 0-16 g/L concentration. (4) The sensor is low-cost and open-source so it can be built by users. (5) The sensor can be installed in a river system for in-situ measurements.

We built three different versions of our open-source sensor, which can be seen in Figure 3.1. The operating principle of all three versions are the same, the differences lie in the con-

struction of the devices and in the detector angles within the control volume. Versions A and B are made from machined PVC whereas version C is 3D printed from PLA. Versions A and C have detectors at 90^o and 135^o relative to the LED and version B has detectors at 45^o and 135^o. We built 2-3 replicates of each version giving a total of eight open-source sensors to test in this work. For more details on versions A, B, and C, see Section 4.4 and Supplementary Table D.4.

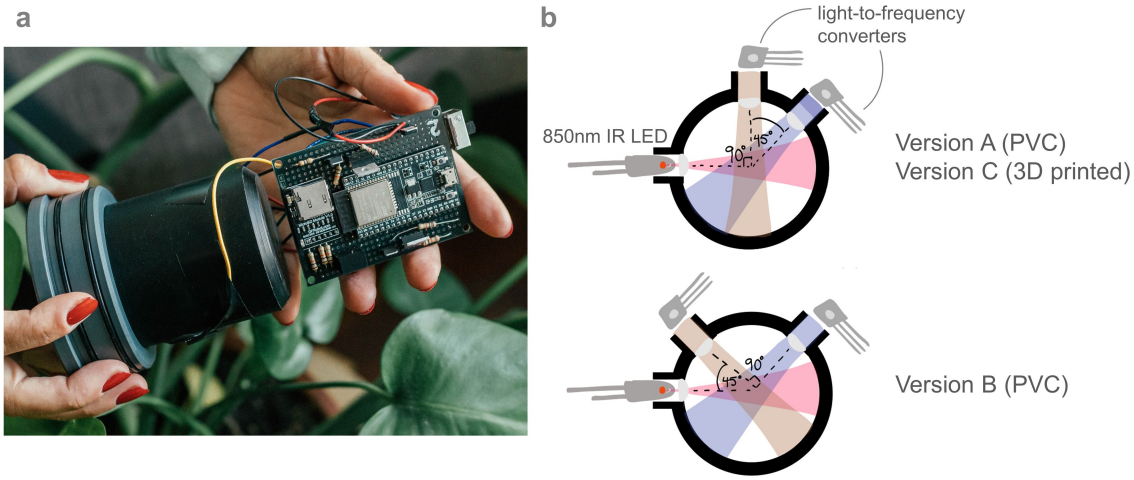

Figure 3.1: Our open-source sensor. a) the sensor without the waterproof housing (see Section 4.4 for the sensor with housing), the sensing head is in black machined PVC, the circuit board is also shown, b) operating principle behind our open-source sensors, an LED illuminated the sample in the cavity and the quantity of scattered light is measured by the detectors in Hz, three different versions are depicted: versions A and B are made from machined PVC whereas version C is 3D printed, versions A and C have detectors at 90^o and 135^o relative to the LED and version B has detectors at 45^o and 135^o.

3.2 Results and Discussion

3.2.1 Comparison NTU-SSC between open-source sensor and commercial sensors

We tested sensor versions A-B-C against three Endress+Hauser (E&H) sensors (two are model CUS51D and one is CUS52D) in a mixing tank setup with two different sediment types: Feldspar ($d_{50} = 30\mu m$) and sediment collected from the Fieschertal channel ($d_{50} = 90\mu m$) (Felix, 2017).

Figure 3.2 shows the eight open-source sensor results overlayed with the three E&H results for Feldspar (Fig. 3.2 a-c) and Fieschertal (Fig. 3.2 d-f) sediment in three different ranges. All eight open-source sensors are plotted with version A in yellow gradient, version B in red gradient, and version C in purple gradient. Every point is a mean which was computed using all of the values, at every SSC level, recorded over the length of the experiment (30min per every SSC level in Feldspar and 15min per every SSC level in Fieschertal - see Section 4.4 for more details).

Our open-source sensors provide very similar measurements between the replicates of in-

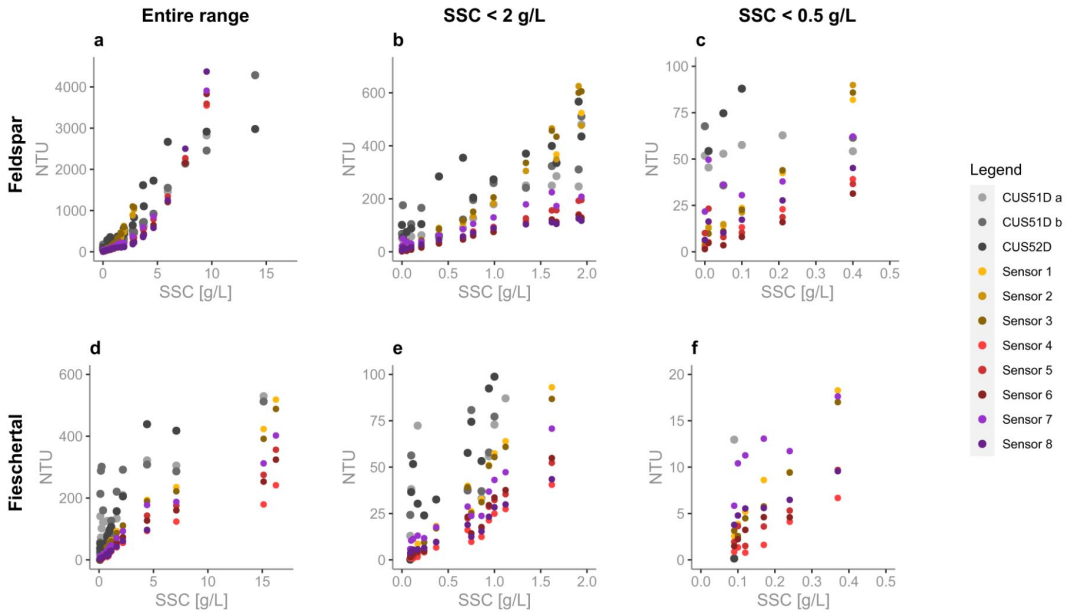

Figure 3.2: Mean NTU vs. SSC comparison in Feldspar sediment (a-c) and Fieschertal sediment (d-f) for the full measurement range (a and d), from 0-2 g/L (b and e), and from 0-0.5 g/L (c and f). The three E&H sensors are plotted in grey gradient (first CUS51D in light-grey, second CUS51D in mid-grey, CUS52D in dark grey). Version A sensors are in yellow gradient (Sensor 1 in bright yellow, Sensor 2 in mid-yellow, Sensor 3 in dark yellow). Version B sensors are in red gradient (Sensor 4 in bright red, Sensor 5 in mid-red, Sensor 6 in dark-red). Version C sensors are in purple gradient (Sensor 7 in bright purple, Sensor 8 in dark purple). At higher SSC one of the 3D printed (version C) sensors failed.

dividual sensor versions for the full 0-16 g/L range, down to 0.25 g/L (Fig. 3.2 b-c and e-f). As expected, at these very low concentrations the sensor replicates start to disagree. For example, the three version B sensors (red gradient) show that all measurements are repeatable down to 0.05 g/L (in Feldspar) and 0.25 g/L (in Fieschertal). Our version C sensors (purple gradient) follow a similar trend down to 0.1 g/L (in Feldspar) and 0.25 g/L (in Fieschertal) but with an offset in the NTU values between the two version C sensors therefore, creating less “repeatable" results (NTU comparison between sensors is more difficult). One possible explanation could be that these sensors were 3D printed with a hobby-printer, and are therefore less precise, than the machined sensors. Another possible explanation for the offset is the sensor placement around the cylindrical tank (see Fig. 3.10). We consider version A and B sensors to be suitable for future testing and possibly for distributed applications. Alternatively, the version C sensors can be used for the monitoring of trends, but we have lower confidence in the absolute values.

In contrast, the E&H sensors do not provide similar measurements for all three sensors or even when comparing two sensors of the same model (CUS51D) for the entire measurement range. Both CUS51D sensors do provide similar measurements in both Feldspar and Fieschertal but only above 2g/L (Fig. 3.2 a and d), meaning that these two sensors give “repeatable” results (turbidities could be compared at two sites along a river network with these sensors). In general, the CUS51Ds’ measurements cannot be compared to the CUS52D’s measurements, since their readings differ highly at SSCs above 2 g/L (Fig. 3.2 a and d) and the CUS52D inexplicably plateaus after 5g/L. No clear relationship between NTU and SSC can be observed below 2 g/L (Fig. 3.2 b-c and e-f) for all three sensors, even

if all sensors are from the same manufacturer and have been calibrated from 0-4000 NTU. This is important because many alpine river applications have such low SSCs. Finally, none of the E&H sensors are able to give sensible results for the entire 0-16 g/L range. Further details on the E&H performance are in Supplementary Figure C.11.

3.2.2 Sensor uncertainty

An important characteristics of a sensor is its measurement uncertainty, i.e. fluctuations in measurements in time for a given sediment concentration. Figure 3.3 reports this uncertainty for each SSC level in both Feldspar and Fieschertal sediments, where the measurement uncertainty is defined by:

$$\epsilon = \frac{NTU_i - \overline{NTU}}{\overline{NTU}} \tag{3.1}$$

where NTU_i is a single NTU measurement and $\overline{NTU}$ is the mean of all NTU_i measurements (at a specific SSC level). All of the values that were recorded over the length of the experiment were used to plot this figure. On average, for every SSC level the open-source sensors made 91 and 425 measurements in Feldspar and Fieschertal sediment, respectively (sampling rate of ~1 Hz but the sensors were put to sleep periodically during the Feldspar experiments). Whereas for every SSC level the E&H sensors made on average 1421 and 1013 measurements in Feldspar and Fieschertal sediment, respectively (sampling frequency of 1 Hz). Raw data in Fig.3.3 a and d represents the uncertainty at each SSC level for all eight of our open-source sensors combined. CUS51D (Fig.3.3 b and e) represents the uncertainty at each SSC level for both CUS51D sensors. CUS52D (Fig.3.3 c and f) represents the uncertainty at each SSC level for the one CUS52D sensor. The mean and median are identical if the distribution of the uncertainties are symmetric, which is the case for our sensors for most of the concentration range. However, the mean and median disagree for very low and high sediment concentrations, where the uncertainty distribution is non-symmetric.

The uncertainty reported by the open-source sensors increases as SSC increases in Feldspar powder and we see that there are clear sediment-type dependent differences for both our and the commercial sensors. However, our open-sensor results are much more consistent (both sediment types have fluctuations within ±10% (Fig. 3.3 a and d) of the mean) than the E&H sensors that have extremely large fluctuations.

In practical applications we envision that the sensors will collect raw data at a chosen frequency, and this data will be internally processed by taking the mean over a sampling interval, to be stored in the logger (SD card). Figure 3.4 shows the uncertainty from the processed data for Fieschertal sediment. The processed data in this case was obtained by taking the mean over bins of 20 measurements from the raw data, which would be a typical application in field settings with sampling interval 20s (measurement at 1Hz). This way, we can expect most of our data (IQR) to land between ±5% of the mean, showing the importance of averaging to reduce variability as opposed to trusting single measurements.

Note in Fig. 3.4 that the measurement uncertainty is very stable over a large range of SSCs. This consistency is a desired property of the sensors as we expect large fluctuations in SSCs in real river applications. For example, the mean SSC observed across 13 Swiss suspended sediment monitoring stations is 0.11 g/L. However, we will be using these sensors in Alpine rivers that are transporting fine sediment and not those that are always have clear water.

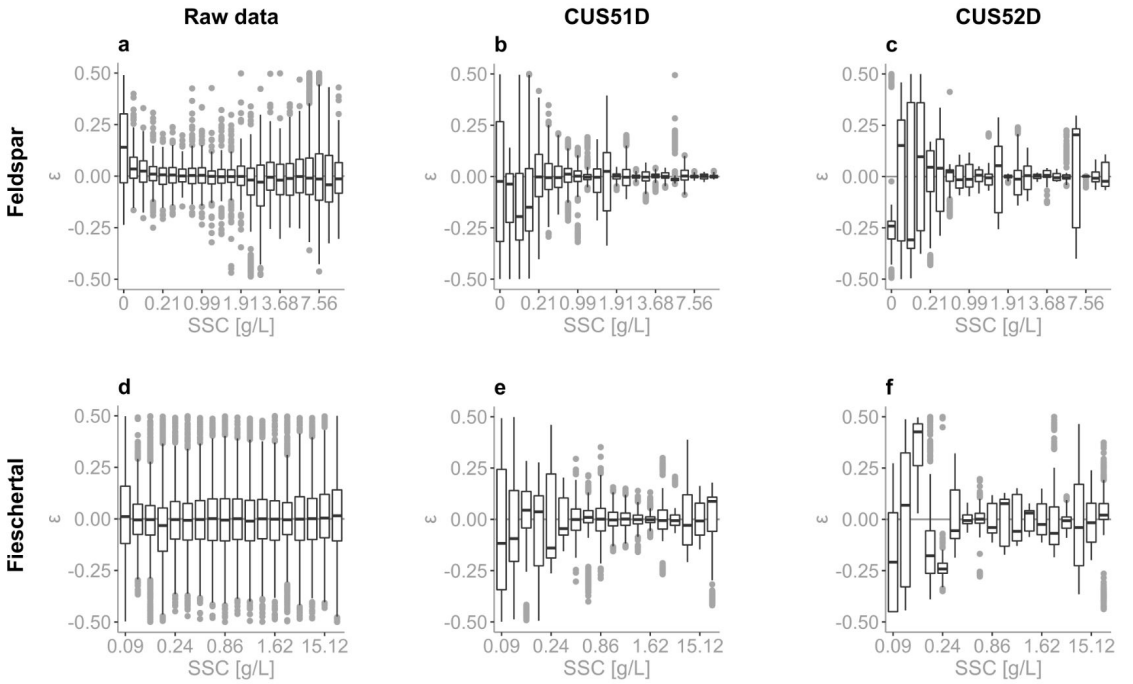

Figure 3.3: Measurement uncertainty vs SSC in Feldspar (TOP) and Fieschertal (BOTTOM). Uncertainty is defined by $(NTU_i - \overline{NTU})/\overline{NTU}$. Raw data (a and d) represents the uncertainty at each SSC level for all eight of our open-source sensors. CUS51D (b and e) represents the uncertainty at each SSC level for both CUS51D sensors. CUS52D (c and f) represents the uncertainty at each SSC level for the one CUS52D sensor. The boxes represent the interquartile range (IQR), the black line within the boxplot is the median, the bars extend to ±1.5*IQR, and the grey points are outliers.

Therefore, the mean SSC of 11 rivers, excluding the two rivers with the lowest SSC, is 0.129 g/L. The measurement that is exceeded on average 5% of the time is about 0.4 g/L and all of the maximum events fall below 16 g/L except for three events (at 23 g/L, 55 g/L and 71.4 g/L). For more details please see Supplementary Fig. D.12. This is well within our tested range and gives us confidence that we can capture well both low and high sediment transport conditions.

3.2.3 Calibration of new sensor to SSC

NTU as a unit of measure of turbidity is not intuitive for monitoring SSC, as this unit is not universally comparable between watersheds and sensors; you cannot assume that 1000 NTU in two different rivers (or in the same river but using two different sensors) means that there is the same SSC [g/L] present. This is because turbidity does not only depend on SSC, but also on the Particle Size Distribution (PSD), shape, and particle material properties such as colour (reflectivity), density, refractive index, and surface roughness (Downing, 2006; Gippel, 1995; Sutherland et al., 2000). This holds in general and also affects our sensors, however our version A and B sensors overcome this issue of repeatability at least within the same sediment type (Fig. 3.2).

Observing our open-source sensor performance in Feldspar (Fig. 3.2 a-c), we see that the relationship between NTU and SSC is linear in the sub 2 g/L range and becomes non-linear with increasing SSC. This is in line with what was observed by Holliday et al. (2003) and

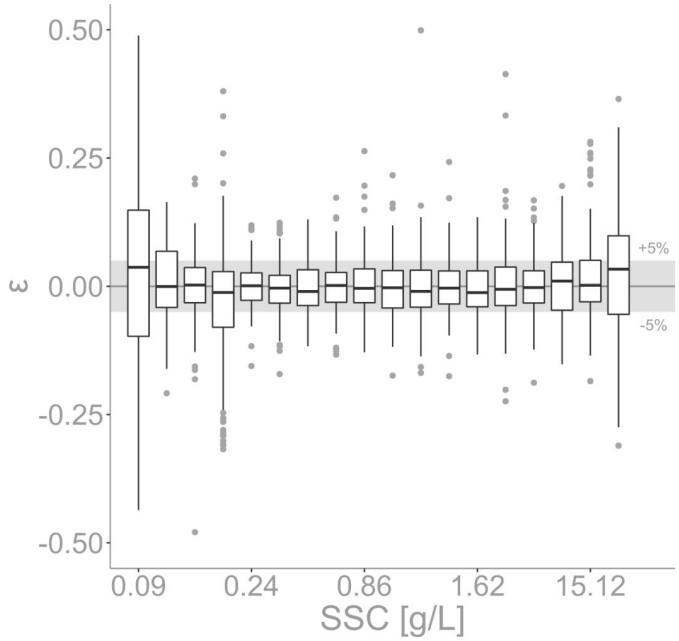

Figure 3.4: Processed measurement uncertainty vs SSC in Fieschertal sediment. Uncertainty is defined by $(NTU_i - \overline{NTU})/\overline{NTU}$. The plot represent the uncertainty at each SSC level for all eight sensors combined. To obtain this processed data, the mean was taken over bins of 20 measurements (of the raw data from Fig. 3.3 d). The boxes represent the interquartile range (IQR), the black line within the boxplot is the median, the bars extend to ±1.5*IQR, and the grey points are outliers.

several others (Baker et al., 2001; Matos et al., 2019). Kelley et al. (2014) tried to use a linear model to calibrate NTU and SSC but had to split their model into several ranges of NTU. Holliday et al. (2003) found through experiments that the relationship between turbidity and SSC follows:

$$SSC = a(NTU)^b \tag{3.2}$$

where a and b are regression-estimated coefficients and b is approximately equal to one for all particles. But in general, for every watershed and sediment type, it is likely that both a and b will be different. For example, Costa et al. (2018a) found $a = 0.56$ and $b = 1.25$ in their investigated alpine catchment whereas Felix et al. (2018) found $a = 0.59$ and $b = 1$ in their HPP storage tunnel. In our case, at larger SSCs the relationship diverges from linearity (Fig. 3.2). Therefore, when working with these sensors, its important to realize that a doubling in SSC can mean a doubling in NTU at lower NTUs and a quadrupling at higher NTUs (for example, 1 to 2 g/L can give 100 to 200 NTU but 10 to 20 g/L can give 1000 to 4000 NTU).

It is known that the NTU-SSC relationship will depend on sediment type. According to Sadar (1998) and Tran et al. (2006), particles with sizes much smaller than the wavelength of the incident light will scatter light with roughly equal intensity in all directions. Particles larger than the wavelength of the incident light will create a spectral pattern that results in greater light scattering in the forward direction than in the other directions. Therefore, the reported differences in NTUs in Feldpar and Fieschertal sediment (Fig. 3.2) are likely due to the shape and size of the two sediment types. This shows the importance

of calibrating the sensors with sediment samples collected at the river where the sensors would be installed.

Our eight open-source sensors were in a first step calibrated using several dilutions of 4000 NTU Formazin and deionized water: 0, 3, 6, 10, 40, 70, 100, 400, 700, 1000, 2000, and 4000 NTU, as is commonly done in turbidity sensors. However, the sensors calibrated in this way (see Supplementary Methods - First Prototype section in Appendix D), failed to produce data measured in Feldspar and Fieschertal sediment. This is because Formazin scatters light evenly in all directions, which is not true in natural sediment where the directionality of scattered light is highly sensitive to particle grain size. This is demonstrated in Fig. 3.5, where a peak in light detected by the 135^o detector in Feldspar powder (Fig. 3.5a) can be observed, whereas in Fieschertal powder (Fig. 3.5b) there is no peak and the amount of light detected plateaus around 5 g/L. The 45^o detector (Fig. 3.5c-d) shows a linear increase in the amount of light received in both sediments but the quantity of light received by the detector in Feldspar (Fig. 3.5c) is much higher than in Fieschertal sediment (Fig. 3.5d). Similar results were found previously (Matos et al., 2019) and similar figures for Formazin are presented in Supplementary Fig. C.6.

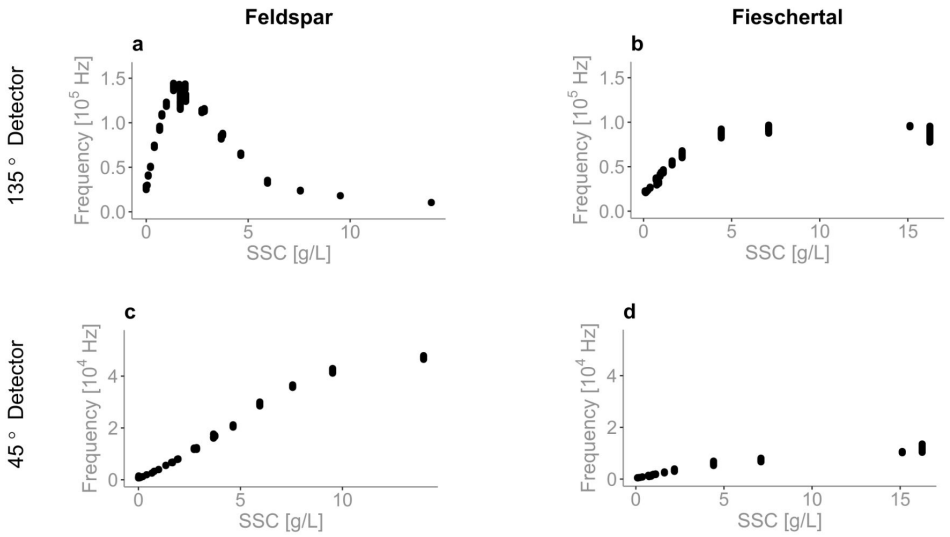

Figure 3.5: Measured light intensity vs. SSC comparison. Light intensity (measured by the detectors in Hz) shown for the two detectors (135^o and 45^o) in Sensor 5 for Feldspar sediment (a and c) and Fieschertal sediment (b and d).

For this reason, in a second step we developed the Formazin calibration model for the mixing tank experiments (for the results shown in Fig. 3.2-3.4) using only the 90^o (versions A and C) and 45^o detectors (version B) in four distinct NTU ranges (0-10, 10-100, 100-1000, 1000-4000 NTU). The model using only one detector in each sensor (used in Fig. 3.2-3.4) is of the form:

$$NTU = \alpha + (\beta \times d) + (\gamma \times d^2) \tag{3.3}$$

where α is the y-intercept, β is the first order coefficient associated with the measured light intensity d from the 45^o or 90^o detector (90^o in versions A and C, 45^o in version B) and γ is the second order coefficient from the same detector. The resulting models for Sensor 6 for the four different NTU ranges (0-10, 10-100, 100-1000, and 1000-4000 NTU)

are shown in the Supplementary Fig. C.13 and their coefficients are in Supplementary Table D.5.

Finally, we challenge the need to calibrate the sensors to NTU in order to predict SSC from a separate NTU-SSC relation, which compounds estimation errors. Our sensors are meant for use in a range of different rivers with various grain sizes and shapes (therefore, constantly changing the direction of scattered light). We envision that one can directly calibrate SSC observations to the reflected light intensity observed by the combined detectors. This can be done in laboratory calibration experiments or in on-site river applications by measuring suspended sediment concentration in a few samples that cover a range of SSCs.

In this approach we calibrated the light intensity measured by the detectors for each open-source sensor directly to SSC, separately for the Feldspar (Figure 3.6 a-c) and Fieschertal (Fig. 3.6 d-f) sediment. The model used is of the form:

$$SSC = \alpha+(\beta_1\times d_1)+(\beta_2\times d_2)+(\gamma_1\times d_1^2)+(\gamma_2\times d_2^2)+(\delta_1\times d_1^3)+(\delta_2\times d_2^3)+(\eta_1\times d_1^4)+(\eta_2\times d_2^4) \tag{3.4}$$

where α is the y-intercept, d_1 is the light intensity measured by the 45^o or 90^o detector (90^o in versions A and C, 45^o in version B), d_2 is the light intensity measured by the 135^o detector (in versions A-B-C), $\beta_{1,2}$-$\eta_{1,2}$ are the 1st-4th order coefficients associated with d_1 and d_2. Figure 3.6 shows SSC mean predictions against observations for all versions of the sensor. The fit is excellent across the entire range of SSC with $R^2 > 0.98$, with the main benefit due to the multiple linear regression using both detectors. Analysing the versions separately, all sensors are now able to predict well in the entire SSC range down to 0.4 g/L in Feldspar (Fig. 3.6c, with version A performing well down to 0 g/L) and down to 0.25 g/L in Fieschertal (Fig. 3.6f, with versions A and B performing well down 0.12 g/L and 0.17 g/L, respectively). Here the 3D printed sensors (version C) do not perform as well. An improvement in the 0-0.5g/L range can probably be done by splitting the model and having two separate linear calibrations. The advantage of the open-source sensors is that the user does not need to use the 4th order model as we have done, and is free to chose their own model.

It is important to note that avoiding the Formazin calibration step has additional benefits. By calibrating from the detector output directly to SSC, we are able to save up to a week's worth of lab work and we are able to avoid exposure to Formazin, a known carcinogen. Collecting gravimetric samples and calibrating directly to SSC might seem like a lot of work, but this needs to anyway be done when installing turbidity sensors in a river network to collect SSC data. Additional problems with Formazin calibration can be found in Supplementary Discussion - Problems with calibrating NTU with Formazin (Appendix D).

A conceptual example of how direct calibration of the open-source sensor to SSC would work in a real case and how this calibration gives a more representative SSC reading is shown in Figure 3.7. From Monday to Saturday there are isolated rainfall events which occur only in certain subcatchments, as depicted in Fig. 3.7. Each subcatchment has a different grain size distribution and different grain properties, which in turn scatter light differently (creating different scatter spectra). A sensor is located near the outlet of a catchment. The sensor works by measuring the quantity of scattered light (at a specific angle) and it is consistently measuring this value only. A rainfall event on Monday in a subcatchment with very fine particles gives rise to an SSC of 10g/L at the sensor location

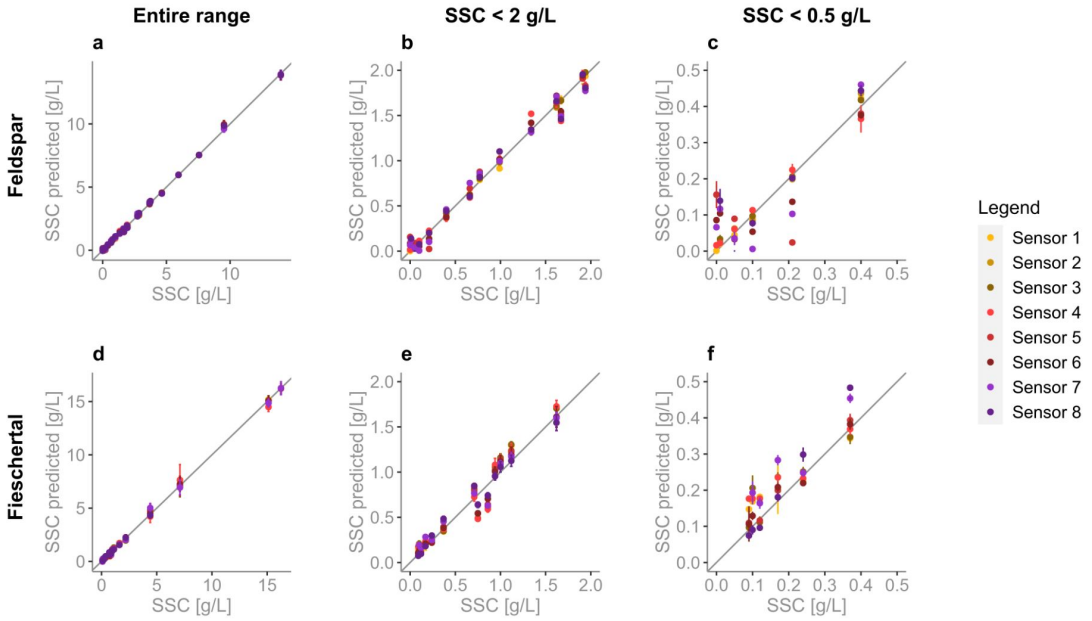

Figure 3.6: SSC measured vs. mean predicted in three different ranges of Feldspar (a-c) and Fieschertal (d-f) sediments as predicted from a fourth order multiple linear regression SSC model created for each of our open-source turbidity sensors (all of them $R^2 > 0.984$). Version A sensors are in yellow gradient (Sensor 1 in bright yellow, Sensor 2 in mid-yellow, Sensor 3 in dark yellow). Version B sensors are in red gradient (Sensor 4 in bright red, Sensor 5 in mid-red, Sensor 6 in dark-red). Version C sensors are in purple gradient (Sensor 7 in bright purple, Sensor 8 in dark purple). The error bars are ± one standard deviation.

(gravimetrically determined SSC from a bottle sample). However, these fine particles do not scatter light strongly in the direction of the sensor detector. This causes the calibration points to sit above our calibration curve (low light detected - similar to Feldspar). Whereas, a rainfall event on Saturday in a subcatchment with very coarse particles, giving rise to an SSC of 15g/L, scatters light strongly in the direction of the sensor detector (even more than is expected at this SSC). This causes the calibration points to sit below our calibration curve (higher amount of light detected - similar to Fieschertal).

The combination of response curves (Fig. 3.5) from multiple detectors can produce good reflectance curves for a range of sediment types (sources) and concentrations (Fig. 3.6). The mixing of these response curves over many events leads to a robust calibration curve for the entire catchment. However, the measurements of individual flood events will have errors when using a sensor at the outlet of the catchment. As our sensors can be used as cheaper alternatives, this limitation is overcome by placing several of these sensors within subcatchments in order to narrow the uncertainty in SSC. By calibrating the affordable sensors to the SSC of each individual subcatchment, our sensor response would be unique to the sediment type of the subcatchment. In this way, sediment sources with possibly different sediment properties may be identified.

3.3 Outlook

In the future, we would like to incorporate a temperature and pressure sensor into our sensors to also monitor the stage and temperature of the river. A wiper is absolutely es-

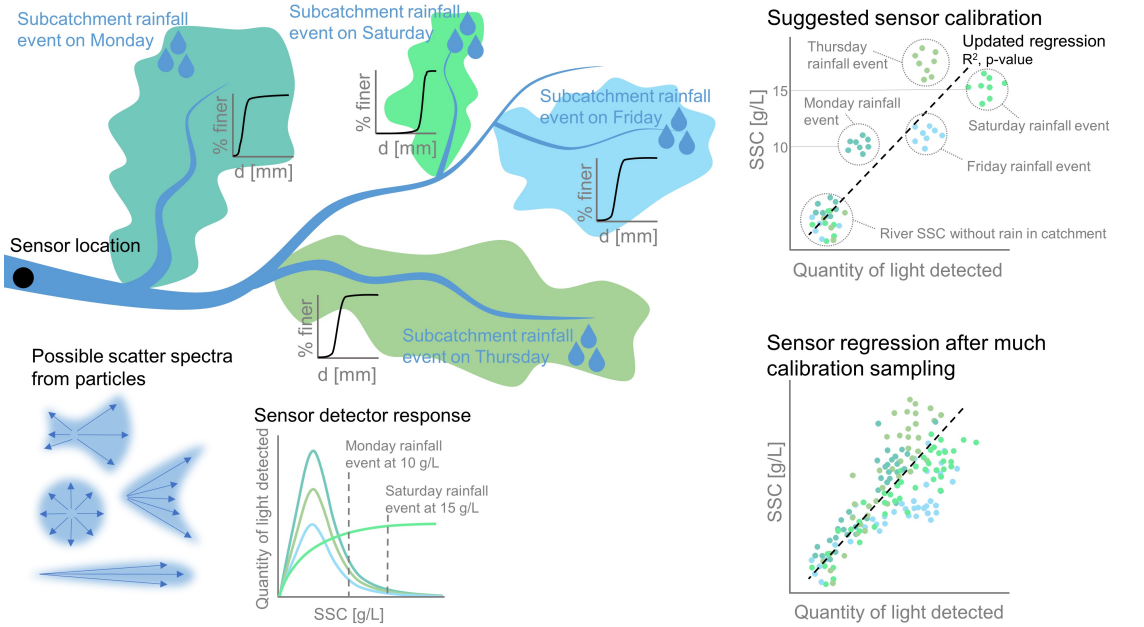

Figure 3.7: Conceptual scheme of a direct calibration of SSC to the light detected by a sensor in a river with several subcatchments that all have different sediment types and grain size distributions and therefore, emit different scatter spectra. In this example, every subcatchment experiences an isolated rainfall event on a different day. The sensor detectors at the downstream end of the river have a different light intensity response depending on the sediment type. After sampling many different events, a single calibration curve representative of the different subcatchment sediment sources and their activation frequencies can be obtained.

sential in the sensor design for long-term monitoring. We will be sure to include it in our next prototype. The Hz-SSC calibration curve, along with the number of sediment-water samples necessary to create this curve, should also be investigated further. It is clear that over a longer timescale that the catchment properties will change, causing a change in the Hz-SSC calibration curve (which is also the case for traditional NTU-SSC turbidity sensors). Therefore, our sensors are not intended to replace long-term river monitoring, but rather provide short-term identification related to changes in water quality, and finding sediment sources and their activation.

Our hope is that the affordable, open-source SSC sensor brings accessibility to global river research. Blog posts with fabrication instructions can be found on our website (Droujko, 2021a). With a fully transparent design, students, researchers, and organizations are able to build, install, use, and repair the instruments themselves, ultimately eliminating waste and making the data from our world's rivers, lakes, and oceans available to all.

3.4 Methods

The basic design of our turbidity sensor was created with an infrared (IR) LED and two light detectors at different angles relative to the LED. The design principle can be seen in Figure 3.8. An LED at 850nm was selected (TSHG6200 by Vishay Semiconductor Opto Division) because water as a medium does not reflect this wavelength. The detectors chosen are the TSL237S-LF by AMS and they were chosen for two reasons: 1) they convert light

to a digital output frequency and so variations in voltage or current driven by temperature fluctuations in the field environment, that affect an analog detector, are eliminated; 2) this sensor responds to light in the 320nm to 1050nm range and has a peak responsivity at 700nm. An ESP32 was chosen as the microcontroller for this sensor instead of an Arduino Uno (a common microcontroller chosen for hobbyists) because of its superior number of timers. Since the detectors output a digital pulse with varying frequency proportional to the light intensity, the chosen microcontroller should have at least two timers to compute frequency, one to count pulses and one to count the elapsed time, for each detector. Therefore, the Arduino can only be used to convert the digital output of one detector and the ESP32 is needed because it has the required four timers to resolve the digital signal of two detectors.

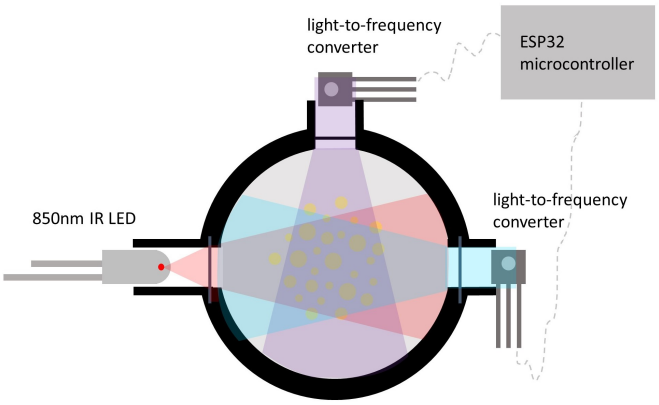

Figure 3.8: Sensing principle behind the open-source turbidity sensor.

With the above design in mind, we built several versions of our first turbidity sensor prototype and tested it with Formazin, a popular turbidity sensor calibration liquid. Details about focusing lenses, ambient stray light elimination, detector placement, and calibration model can be found in the Supplementary Methods - First prototype section (Appendix D).

In order to test the turbidity sensors in a real-world setting, we designed a mixing tank experiment where our sensors can be compared to commercially-available sensors. In order to submerge our sensors into a mixing tank and take many measurements over several hours, a second prototype of the turbidity sensor was created.

3.4.1 Second prototype construction

From the Supplementary Methods - First Prototype (Appendix D), it was found that focusing lenses were necessary for the design of the sensor, whereas long-pass filters (eliminating stray ambient light) were unnecessary since the same effect is achieved using the off-on differencing measurement method (Matos et al., 2020). Additionally, for our chosen LED and detector parts, it is important to avoid the 180^o detector placement since the detector becomes saturated by the incoming light (see Supplementary Methods - First Prototype in Appendix D for more details).

With this in mind, the second prototype was based off of Sensors 3 and 4 found in Supplementary Methods - First Prototype section (Appendix D) because we wanted to test the detector orientations further. It has three different versions (A, B, and C) and 2-3

replicates of each version (to see the variation from construction) and all of the sensors and replicates are summarized in Supplementary Table D.4. Version A has detectors at 90^o and 135^o relative to the LED and version B has detectors at 45^o and 135^o. Unlike the first prototypes created in the Supplementary Methods - First Prototype section (Appendix D) that had a 3D-printed sensing head, these first six sensors have sensor heads that were made by machining a solid piece of black PVC. However, with the hope to keep this project accessible to everyone, we also created two additional replicates (version C) but with a 3D-printed sensing head from PLA. All eight sensors details are listed in Supplementary Table D.4.

All eight sensors were housed in a simple waterproof housing made of standard PVC from the hardware store. The waterproof housing can be seen in Fig. 3.9a. Figure 3.9b shows the internal sensing head (black PVC) and the electronics of the sensor. We also see two O-rings on the left-hand side of both images. These, along with some vacuum grease, were used to keep the sensor waterproof. All of the electronics of the sensor were housed on a prototyping soldering board. The electronic schematic is found in Supplementary Fig. D.14 and the CAD for the PVC sensing head is available on this project's repository (Droujko, 2021b).

Figure 3.9: Open-source turbidity sensor - second prototype. a) Closed sensor with external PVC housing. b) Internal electronics of the sensor.

3.4.2 Commercial sensors

We tested three commercial turbidity sensors against our open-source sensors. These sensors were two CUS51Ds and one CUS52D, all from Endress+Hauser (E&H). The CUS51Ds are rated for a measurement range of 0 to 4000 FNU and are used for turbidity and suspended solids measurement at all stages of the wastewater treatment process and at primary water treatment applications with medium to high turbidity (Endress + Hauser, 2021a). The CUS52D is also rated for a measurement range of 0 to 4000 FNU, but unlike the CUS51D, the CUS52D can be used at every stage of the water treatment process, even at the lowest turbidity (Endress + Hauser, 2021b). The E&H sensors additionally needed to be hooked up to a data acquisition system (Liquiline CM442), which enabled the sensors to continuously measure while connected to a power source.

3.4.3 Cost

All of the parts purchased to make one of our open-source sensors are shown in Supplementary Table D.6. The total cost of one sensor is 61.37 CHF (Swiss Francs). It is worth noting that the cost of our sensor doesn't include calibration labor costs and we are not sure if the E&H sensors must undergo additional calibration and/or servicing prior to every use. Machined PVC is more expensive and harder to produce than simply 3D printing the sensing head. Therefore, before deciding to 3D print or purchase and machine PVC, the purpose of the sensor should be evaluated. If replicates of the sensor need to be made in order to create a distributed network of sensors within a watershed, then perhaps purchasing and machining PVC is worth the extra effort in order to have comparative results along the watershed. However, if only one sensor needs to be created and installed at the outlet of a water system in order to obtain a basin-integrated picture of the suspended sediments, then a 3D printed sensor is probably enough for this purpose and the extra time and cost would not contribute much to the final output. The 3D printed version can also be used to monitor trends in a distributed network instead of absolute values. Additionally, if the sensor is used for a school project then a 3D-printed sensor should suffice.

3.4.4 Mixing tank setup

Figure 3.10a shows the mixing tank setup with a 200L cylindrical tank and a line marking 140L of water when the tank is full with all 11 tested sensors. In the background, the green pump used to empty the tanks can be seen. Figure 3.10b shows the placement of the sensors around the tank along with the water level. In the center of the tank is the mixer, which is a drill with a paint mixing attachment. The mixer was used to suspend the sediment in the tank.

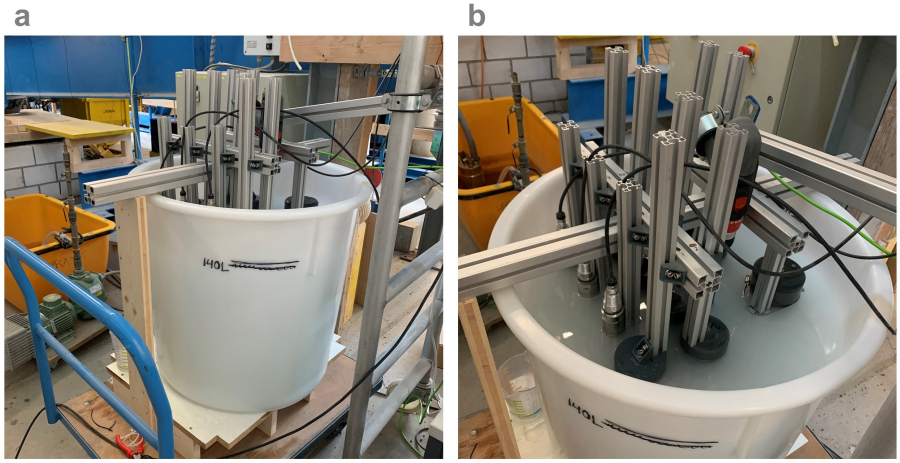

Figure 3.10: Mixing tank setup: a) cylindrical 200L tank, b) arrangement of 11 sensors (8 of ours and 3 commercial) within the tank and the mixing drill in the middle.

3.4.5 Sediment type

There were two different sediment types used in these experiments: Feldspar and sediment taken from the Fieschertal canal, both of which were used previously by Felix (2017).

Feldspar powder (Na-plagioclase) was chosen because of its abundance in the earth's crust. It was purchased from a manufacturer that sells Feldspar milled for pottery (Feldspat NA

LF 90). The Fieschertal sediments were collected from the deposits in the tailwater channels at the Fieschertal hydropower plant (HPP) in the Canton of Valais, Switzerland. This sediment was chosen because we are planning on using our open-source sensors to investigate sediment sources on the Rhone river such as the Fiescher glacier. The Fiescher HPP is located at the mouth of the Fiescher glacier, on the mountain stream Wysswasser which is a tributary of the upper Rhone. However, it should be noted that the finer sediments do not settle in the tailwater channel, therefore the Fiescher sediments are coarser than would be expected.

The particle size distribution (PSD) and the solid densities, ρ_s, of both powders were measured previously by Felix (2017). The PSD was measured from suspended samples with adequate dilution using a stationary laser diffractometer (LA-950 manufactured by Horiba). It was found that the Fieschertal sediments contained almost 80% by mass of fine sand ($d_{50} = 90\mu m$) whereas the Feldspar was mainly in the range of silt ($d_{50} = 30\mu m$)(Felix, 2017). The solid densities were measured using a helium expansion pycnometer and are $2.65 g/cm^3$ and 2.70 g/cm^3 for the Feldspar and Fieschertal sediment, respectively (Felix, 2017).

3.4.6 Experimental procedure

The experimental procedure was as follows. First, all of the sensors would be turned on and the clean tank would be filled with tap water. The E&H sensors take a measurement every second for the duration of the experiments. For the first experiment with the Feldspar, the open-source sensors were taking 3 measurements for 3 seconds every minute and sleeping between readings. For the next experiment with the Fieschertal sediment, the open-source sensors were taking a measurement every second (as the E&H sensors) without sleeping between readings.

With clear water in the tank, the mixing drill and measurements were started. Every 30 min afterwards, the water temperature of the tank was taken along with a water sample of around 300mL. Afterwards, a pre-defined amount of Feldspar sediment mixed with 300mL of tap water was added to the tank in order to increase its SSC in a step-wise manner. This experiment was repeated again for the Fieschertal sediment except since the open-sourced sensors were continuously measuring like the E&H devices, we were able to increase the SSC of the tank every 15 min instead of every 30 min. Every time we increased the SSC of the tank, we also wiped all of the bubbles off of the 11 sensors.

Afterwards, the water-sediment samples were taken to the lab and evaporated in a ventilated oven and the SSC was computed by weighing the dry sediment. Some tap water samples without sediment were also evaporated so we could determine the dissolved mineral concentration and subtract this from our calculated SSC.

Chapter 4 Ötz-T: 3D-printed open-source turbidity sensor with Arduino shield for suspended sediment monitoring

Authors: Jessica Droujko, Felix Kunz Jr., and Peter Molnar
Journal: HardwareX, Elsevier
Publication date: January 24th, 2023

Key findings:

1. Fine sediment transport is crucial for ecosystem health, nutrient cycles, and water quality, but high costs limit comprehensive monitoring across many locations.
2. An open-source, low-cost turbidity sensor was developed, enabling wider spatial coverage and accessibility for global river research compared to expensive commercial options.
3. The sensor utilizes optical scatter technology, is equipped with temperature and pressure sensors, and is designed for easy assembly and programming by non-experts.
4. Compared to commercial turbidity sensors (>3000€), our low-cost version (∼200€) allows for multiple deployment and therefore a high spatial coverage of sediment fluxes.
5. A field test during a flood in September 2022 on the Ötztal Ache, Austria, demonstrated the sensor's effectiveness and durability, highlighting its potential for broad application in environmental monitoring.

Author's contributions: The author conceptualized this work, curated the data, designed the project methodology and designed/built the sensor, administered the project, wrote the sensor software, and wrote the original and final drafts of the paper.

Coauthors' contributions: FKJ designed the PCB of the sensor and helped write some sections of the paper in the original and final draft. PM supervised the project and helped write the original and final drafts of the paper.

Data Availability The source files can be found at the following Zenodo repository: 10.5281/zenodo.7185235.

Specifications table

Hardware name	Ötz-T
Subject area	Environmental, planetary and agricultural sciences
Hardware type	Field measurements and sensors
Closest commercial analog	In-situ turbidity sensor. https://in-situ.com/en/aqua-troll-600-multiparameter-sonde
Open source license	GNU Affero General Public License v3.0
Cost of hardware	217 CHF
Source file repository	https://doi.org/10.5281/zenodo.7185235

4.1 Hardware in context

The transfer of sediment from land to oceans plays an important role in the global denudational cycle (Gregor, 1970; Wold and Hay, 1990), the global geochemical cycle (Meybeck, 1994; Ludwig et al., 1996), the function of coastal ecosystems (Roy et al., 2001; Arrigo et al., 2008), and the evolution of deltas and other coastal landforms (Morton, 2003; McLaughlin et al., 2003; Seybold et al., 2009). Proper monitoring of this sediment flux should capture the temporal and spatial variability in concentrations at suitable timescales. This variability in suspended sediment concentrations (SSC) can then be used to quantify human effects on sediment production (Wang et al., 2007; Hu et al., 2011), the natural erosion gradients over entire mountain ranges (Hinderer et al., 2013), and the uncertainty in erosion rates related to short-term sampling (Covault et al., 2013). It can also give us a better understanding of possible short-term hydrological processes in a catchment leading to sediment production, e.g. hillslope erosion by rainfall events, glacier ice melt erosion, even hydropower storage in dams, as well as longer-term variability caused by ongoing climate change (Morehead et al., 2003; Hu et al., 2011; Costa et al., 2018a,b). Measurements of SSC are also important for understanding how the impacts of hydroclimatic forcing on activating sediment sources may propagate through the river system in observations and also in physically-based hydrology-sediment models (Bakker et al., 2018; Battista et al., 2020a; Costa et al., 2018b; Konz et al., 2011; Uber et al., 2021). However, understanding such processes requires a temporal and spatial perspective on sediment pathways of production and storage within the catchment which cannot easily be achieved by current methods and sensing technology to measure SSCs.

The primary method to quantify SSC is by gravimetric analysis of bottle samples taken at river cross-sections in regular or irregular intervals. This method is reliable but has many disadvantages such as being discontinuous, inefficient and costly. Alternatively, the spatial distribution of SSC can be obtained using satellite imagery which is based on the reflectance of water surface as it is affected by suspended sediment. Dissolved and suspended sediment concentrations together with gross biological activity affect the intrinsic colour of natural waters (Novoa et al., 2015; Wang et al., 2018a), which makes optical satellite remote sensing of oceans, coastal areas, large lakes/rivers possible. When calibrated with ground measurements, such satellite data can be very useful for SSC estimates (DeLuca et al., 2018; Martinez et al., 2009; Fassoni-Andrade and de Paiva, 2019) and can give a

range of additional water quality parameters (Wang and Sohn, 2018) at large scales but not with high temporal resolutions (they are limited by the repeatability given by satellite overpasses) and with poor point accuracy. Terrestrial photography is another possibility to obtain SSCs from the optical sensing of river turbidity (Goddijn and White, 2006; Fricke and Baschek, 2014), for example by mobile phone cameras (Leeuw and Boss, 2018). However, all satellite, ground-based and UAV optical sensing methods are limited by cost, poor temporal resolution, insufficient spatial footprint, and are strongly affected by many other constraints, which make them currently not very suitable for regular long-term monitoring of SSC in rivers.

The current state-of-the-art method to obtain continuous SSC data at high temporal resolutions is by dedicated in-situ turbidity sensors, where via calibration a strong relation between turbidity and SSC can commonly be ensured. The main deficiency, however, of these commercial sensors is that they are expensive (e.g. state-of-the-art turbidity sensor by Campbell is about 6000€, In-Situ is 7000€), making widespread deployment at many sites along a river system to quantify spatial variability next to impossible.

The appealing alternative are low-cost turbidity sensors, and several such sensors have been documented in peer-reviewed literature, such as the appliance-based sensors of Gillett and Marchiori (2019) and Trevathan et al. (2020), the backscatter systems of Jiang et al. (2020) and Eidam et al. (2022), the dual-beam detectors of Lambrou et al. (2014) and Wang et al. (2018b), the handheld system of Kelley et al. (2014), and the flow-through systems of Kitchener et al. (2019) and again Gillett and Marchiori (2019). However, none of these systems are sufficiently accurate in the entire 0-4000 Nephelometric Turbidity Unit (NTU) range and also sufficiently robust for deployment in rivers in the field.

The open-source, low-cost, in-situ turbidity sensor for river network monitoring (Droujko and Molnar, 2022) which we developed in our group meets the criteria of sufficient range and accuracy, and suitability for river deployment. This sensor was calibrated for the full 0-4000 NTU range, in addition to 0-16g/L range, and errors were quantified in laboratory tests. Its performance was also compared to other commercially-available turbidity sensors. Although the first version was built for in-situ river network monitoring, there were several improvements that the sensor needed to undergo before long-term, underwater deployment could be possible. In this work, we present these improvements which lead to the Ötz-T (or Ötz-Turbidity, inspired by the natural mummy, Ötzi, found in the Ötztal alps in 1991), and we test this latest version during a flood event on the Ötztal Ache in September 2022.

4.2 Hardware description

The Ötz-T sensor is a 19cm long (9cm diameter) 3D printed standalone device used to measure the turbidity in rivers over extended periods of time and costs ∼25 times less than comparable commercial turbidity sensors. This sensor measures turbidity using and IR LED (850nm) and two IR detectors, and it also features a temperature and pressure sensor to obtain river temperature and stage.

The sensor features a custom printed circuit board (PCB) shown in Figure 4.1. The PCB is robust and was built to sit as a shield on top of the ultra low-power Arduino MKR WAN 1310. The Arduino MKR WAN 1310 was chosen as the microcontroller because it has several powerful features for our application. It houses a SAMD21 chip which is optimized

for low-power functionality and the MKR WAN 1310 also has LoRa built in, which we would like to utilize in future builds. Using an Arduino also enables us to program our device using the Arduino IDE, which we believe makes the project more accessible to those with less programming experience.

This shield has all the I2C connectors highlighted in green in Fig. 4.1. Since our IR detector has a fixed I2C address, we had to use the second I2C bus on the SAMD21. The second bus consists of the pins PA22 and PA23. It is important to note that these pins don't have 10k pull-up resistors built into the Arduino so we had to add them to our shield. To control the IR LED, we used a MOSFET together with an AL5809 (Fig. 4.1 purple highlight) which is a simple LED Driver. There is a small RTC circuit on the shield as well (Fig. 4.1 orange highlight). Even though the Arduino has an RTC built in, we decided to add an external one with a backup battery to keep track of time even if the Arduino is not powered. The commonly used DS3231 is very expensive and was not available to order at the time we designed the circuit. For this reason, we chose the PCF8523T which is much less expensive than the DS3231 but a bit less accurate; we observed a drift of 3min over a month of running the sensor. A simple micro SD Card (Fig. 4.1 blue highlight) was used to store the data. We have also included a stepper motor circuit and controller chip on the shield (Fig. 4.1 pink highlight), so we can control a stepper motor which we would use as a wiper to clean the optics on the sensor from biofouling and sediment deposits. However, due to the unavailability of the selected TMC2300 chip, we couldn't validate this circuit. The TMC2300 was chosen since it supports voltages as low as 2V, which is ideal for our battery-powered application.

There are two ways to power the shield: either with rechargeable LiPo batteries or with non-rechargeable alkaline batteries. We chose to use a rechargeable LiPo cell, where the jumper (J1) on the MKR WAN 1310 should always be shorted in this case.

The PCB is designed in a way that it directly mounts to the Arduino. Both our PCB and the Arduino are open-source and our PCB will remain open-source and can always be found in the Zenodo repository. We also have separate PCBs for the LED, the IR sensors, and the pressure/temperature sensor. The main purpose of these PCBs is to have a simple way to mount the sensors to the casing and connect the wires.

This shield is perfect for our application, but it can also be used for a wide variety of other applications. Our highlights include:

- Low-power Arduino MKR WAN 1310
- Programmed in Arduino IDE
- Entirely 3D printed
- Turbidity, pressure, and temperature sensor
- 2 separate i2C ports on three headers
- 2 IR detectors for direct light to SSC calibration
- SD card reader
- RTC with a backup battery
- Cost effective

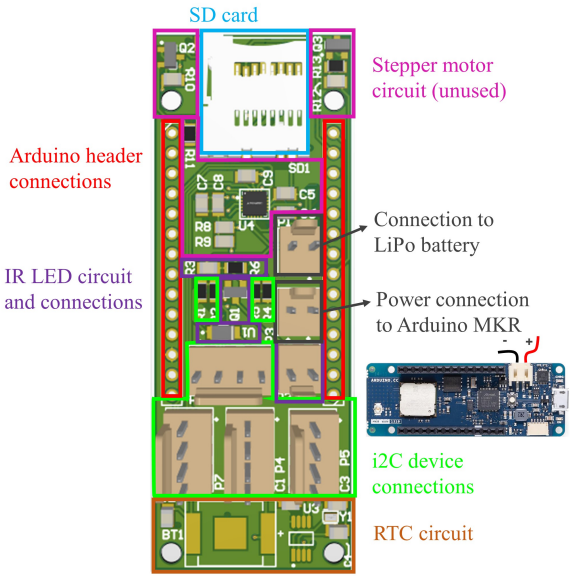

Figure 4.1: Map of the custom PCB shield. Coloured boxes have respective descriptions. This PCB should be stacked on top of the Arduino MKR WAN 1310 via the headers (red). The PCB also features a micro SD card slot (blue), battery connections to a LiPo battery and to the MKR (black), i2C connections for the pressure and IR sensors (green), an RTC circuit (orange), circuit and connection for the IR LED (purple), and an unused circuit for a potential stepper motor (pink).

4.3 Design files summary

CAD files

Design file-name	File type	Open source license	Location of the file
Thread	STEP	GNU General Public License v3.0	10.5281/zenodo.7185235
Cap	STEP	GNU General Public License v3.0	10.5281/zenodo.7185235
Teeth	STEP	GNU General Public License v3.0	10.5281/zenodo.7185235
LED_Zapfen	STEP	GNU General Public License v3.0	10.5281/zenodo.7185235
Detector_Zapfen	STEP	GNU General Public License v3.0	10.5281/zenodo.7185235

Thread.step: CAD file for the thread to be opened in any CAD software
Cap.step: CAD file for the housing lid to be opened in any CAD software
Teeth.step: CAD file for the teeth that hold the optical components, to be opened in any CAD software
LED_Zapfen.step: CAD file for the LED and lens holder, to be opened in any CAD software
Detector_Zapfen.step: CAD file for the detector and lens holder, to be opened in any CAD software

3D printing files

Design file-name	File type	Open source license	Location of the file
Thread	STL & 3MF	GNU General Public License v3.0	10.5281/zenodo.7185235
Cap	STL & 3MF	GNU General Public License v3.0	10.5281/zenodo.7185235
Teeth	STL & 3MF	GNU General Public License v3.0	10.5281/zenodo.7185235
LED_Zapfen	STL & 3MF	GNU General Public License v3.0	10.5281/zenodo.7185235
Detector_Zapfen	STL & 3MF	GNU General Public License v3.0	10.5281/zenodo.7185235

Thread.stl: STL file for 3D printing the thread
Cap.stl: STL file for 3D printing the housing lid
Teeth.stl: STL file for 3D printing the teeth that hold the optical components (LED zapfen and Detector zapfen)
LED_Zapfen.stl: STL file for 3D printing the LED and lens holder (“zapfen")
Detector_Zapfen.stl: STL file for 3D printing the detector and lens holder
Thread.3mf: PrusaSlicer file for the thread
Cap.3mf: PrusaSlicer file for the housing lid

Teeth.3mf: PrusaSlicer file for the teeth that hold the optical components (LED zapfen and Detector zapfen)
LED_Zapfen.3mf: PrusaSlicer file for the LED lens holder
Detector_Zapfen.3mf: PrusaSlicer file for the detector and lens holder

PCB files

Design filename	**File type**	**Open source license**	**Location of the file**
MainPCB	.SchDoc & .PcbDoc & Gerber & .kicad_pcb & .kicad_sch & .pdf	GNU General Public License v3.0	10.5281/zenodo.7185235
PressureSensor	.SchDoc & .PcbDoc & Gerber & .kicad_pcb & .kicad_sch & .pdf	GNU General Public License v3.0	10.5281/zenodo.7185235
LightSensor	.SchDoc & .PcbDoc & Gerber & .kicad_pcb & .kicad_sch & .pdf	GNU General Public License v3.0	10.5281/zenodo.7185235
IRDiode	.SchDoc & .PcbDoc & Gerber & .kicad_pcb & .kicad_sch & .pdf	GNU General Public License v3.0	10.5281/zenodo.7185235
SolderPasteStencil	svg	GNU General Public License v3.0	10.5281/zenodo.7185235

MainPCB.SchDoc: The Schematic File of the Main PCB
MainPCB.PcbDoc: The PCB File of the Main PCB
MainPCB.Gerber: The Gerber file used to order the Main PCB
MainPCB.kicad_pcb: .PcbDoc imported to KiCad so it can be edited without Altium
MainPCB.kicad_sch: .SchDoc imported to KiCad so it can be edited without Altium
MainPCB.pdf: Schematic as PDF
PressureSensor.SchDoc: The Schematic File of the Pressure Sensor PCB
PressureSensor.PcbDoc: The PCB File of the Pressure Sensor PCB
PressureSensor.Gerber: The Gerber file used to order the Pressure Sensor PCB
PressureSensor.kicad_pcb: .PcbDoc imported to KiCad so it can be edited without Altium
PressureSensor.kicad_sch: .SchDoc imported to KiCad so it can be edited without Altium
PressureSensor.pdf: Schematic as PDF
LightSensor.SchDoc: The Schematic File of the Light Sensor PCB
LightSensor.PcbDoc: The PCB File of the Light Sensor PCB
LightSensor.Gerber: The Gerber file used to order the LightSensor PCB
LightSensor.kicad_pcb: .PcbDoc imported to KiCad so it can be edited without Altium
LightSensor.kicad_sch: .SchDoc imported to KiCad so it can be edited without Altium
LightSensor.pdf: Schematic as PDF
IRDiode.SchDoc: The Schematic File of the IRDiode PCB

IRDiode.PcbDoc: The PCB File of the IRDiode PCB
IRDiode.Gerber: The Gerber file used to order the IRDiode PCB
IRDiode.kicad_pcb: .PcbDoc imported to KiCad so it can be edited without Altium
IRDiode.kicad_sch: .SchDoc imported to KiCad so it can be edited without Altium
IRDiode.pdf: Schematic as PDF
SolderPasteStencil.svg: File to lasercut the solderpaste stencil

Software files

Design file-name	**File type**	**Open source license**	**Location of the file**
main	INO	GNU General Public License v3.0	10.5281/zenodo.7185235
set_time	INO	GNU General Public License v3.0	10.5281/zenodo.7185235

main.ino: firmware file to upload onto the Arduino MKR WAN 1310 and run the data logging program
set_time.ino: firmware file to upload onto the Arduino MKR WAN 1310 and set the RTC

4.4 Bill of materials summary

Sensor housing components

Designator	**Component**	**Number**	**Cost per unit - CHF**	**Total cost - CHF**	**Source of materials**	**Material type**
Teeth	XPETG Matt 3D printing filament	56g	0.029 chf/g	1.62	Extrudr	Polymer
Thread	XPETG Matt 3D printing filament	90g	0.029 chf/g	2.61	Extrudr	Polymer
Cap	XPETG Matt 3D printing filament	146g	0.029 chf/g	4.23	Extrudr	Polymer
LED Zapfen	XPETG Matt 3D printing filament	2g	0.029 chf/g	0.06	Extrudr	Polymer
Detector Zapfen	XPETG Matt 3D printing filament	4g	0.029 chf/g	0.12	Extrudr	Polymer
O-ring	0101-001633, NBR 70 shore, ID: 80mm, thickness: 2.5mm	2	1.67	3.34	Kubo Tech AG	Polymer
Epoxy	3M Scotch-Weld DP100 Clear	1	28.62	28.62	Digi-Key	Polymer
Laqueur	UV-resistant gloss varnish	10%	9.95	0.995	Jumbo	Non-specific
Vacuum grease	Silikonfreies Laborfett glisseal HV, 60 g	10%	52.50	0.525	Borer	Non-specific

Optical components

Designator	**Component**	**Number**	**Cost per unit - CHF**	**Total cost - CHF**	**Source of materials**	**Material type**
LED1	TSHG6200	1	1.10	1.10	Mouser	Semiconductor
U1-LS / IR detector	TSL25911FN	2	1.74	3.48	Mouser	Semiconductor
Lenses	6mm plano convex lens	3	2.96	8.88	Nanyang City Jingliang Optical Technology Co., LTD	Inorganic

Power components

Designator	**Component**	**Number**	**Cost per unit - CHF**	**Total cost - CHF**	**Source of materials**	**Material type**
LiPo battery	Li-ion Rechargeable pack 3.7V 10.4Ah	1	41.45	41.45	RS Components	Non-Specific
Coin cell battery	1.55V coin 6.8MM	1	1.14	1.14	Digi-Key	Non-Specific

PCBs

Designator	**Component**	**Number**	**Cost per unit - CHF**	**Total cost - CHF**	**Source of materials**	**Material type**
Pressure PCB	PCB for the MS580305 BA01	1	0.3	0.3	JLC PCB	Non-Specific
IR detector PCB	PCB for the TSL25911FN	2	0.3	0.6	JLC PCB	Non-Specific
LED PCB	PCB for the LED	1	0.33	0.33	JLC PCB	Non-Specific
Main PCB	PCB for the main board	1	0.52	0.52	JLC PCB	Non-Specific

Electrical components

Designator	**Component**	**Number**	**Cost per unit - CHF**	**Total cost - CHF**	**Source of materials**	**Material type**
BT1	LR621	1	0.32	0.32	Mouser	Metal
C1, C2, C1-PS	100nF Capacitor	3	0.03	0.09	Mouser	Ceramic
C3, C4	10pF Capacitor	2	0.16	0.32	Mouser	Ceramic
C1-LS	1uF Capacitor	2	0.17	0.34	Mouser	Ceramic
DS1	HSMH-C190	1	0.49	0.49	Mouser	Semiconductor
P1, P2, P3, P1-LED	61900211121	4	0.44	1.76	Mouser	Non-specific
P4, P5, P6	61900411121	4	0.73	2.92	Mouser	Non-specific
Q1	2N7002LT1G	2	0.20	0.39	Mouser	Semiconductor
R1, R2, R4, R5	10k Resistor	4	0.03	0.12	Mouser	Non-specific
R7, R3	330R Resistor	1	0.29	0.29	Mouser	Non-specific
SD1	473521001	1	3.60	3.60	Mouser	Metal
SW1	Button	1	0.56	0.56	Mouser	Non-specific
U1	AL5809-100P1-7	1	0.40	0.40	Mouser	Semiconductor
U2	Arduino MKR 1310	1	38.68	38.68	Arduino	Semiconductor
U3	PCF8523T	1	1.63	1.63	Mouser	Semiconductor
Y1	32.768KHZ	1	1.33	1.33	Mouser	Other
J1_LS, J1_PS	5-146130-1	3	0.61	1.83	Mouser	Non-specific
U1-PS	MS580305BA01	1	27.91	27.91	Mouser	Semiconductor
2 Pin Connector Female	710-61900211621	2	0.139	0.278	Mouser	Non-Specific
4 Pin Connector Female	710-61900411621	3	0.188	0.564	Mouser	Non-Specific
4 Pin Connector Female	90143-0104 (Molex)	3	0.337	1.011	Mouser	Non-Specific
Crimp Contacts	90119-2109 Crimp	12	0.098	1.176	Mouser	Metal
Crimp Contacts	61900113722-DEC Crimp	16	0.141	2.256	Mouser	Metal
Wires	20AWG in Red, Green, Orange, Black	0.1m per color	2.03/m	0.81	Mouser	Non-Specific

4.5 Build instructions

Electronics

Order the PCBs. Order the PCBs using our Gerber Files or export your own Gerber files from Altium (the education license can be obtained for free). We used JLCPCB.com to order the boards; simply upload the Gerber files to the website. You should also select some specifications when ordering the PCB; we chose a two-layered board with FR-4 material and with a thickness of 1.6mm. We suggest ordering the solder paste stencil (Figure 4.2) but you can also create one yourself from a piece of aluminum foil and a laser cutter using our file SolderPasteStencil.svg.

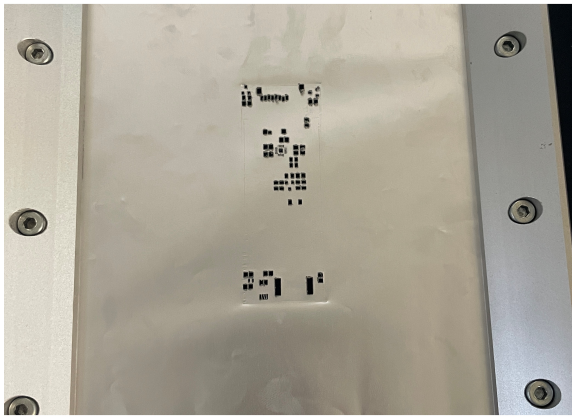

Figure 4.2: Makeshift stencil for solder-paste made with a laser cutter

Assemble PCBs. To assemble the PCB we used the re-flow process. After all the pads are covered with solder paste, you can place the parts on the pads according to the designators (Figure 4.3a). As soon as all the components are placed and you have confirmed that they are oriented correctly, you can place the PCBs in the oven to heat them up to solder the components (Figure 4.3b). It is also possible to solder the PCBs by hand. Finish the PCB assembly by adding a coat of acrylic laqueur (listed in the Bill of materials).

Connectors. The PCBs have many connectors to connect the different parts. All the 4 Pin Connectors, used for the I2C sensors, have the same pinout, see Table 4.1.

Table 4.1: Pinout and corresponding wire color of 4 Pin Connectors.

Pin	**Function**	**Color**
Pin 1	3.3V	Red
Pin 2	SCL Clock	Orange
Pin 3	SDA Data	Green
Pin 4	GND	Black

The 2 Pin Connectors are used for the IR LED and the battery connections (see the 4 Pin (green) and 2 Pin (purple and black) connections in Fig. 4.1). Use a clamp to crimp the

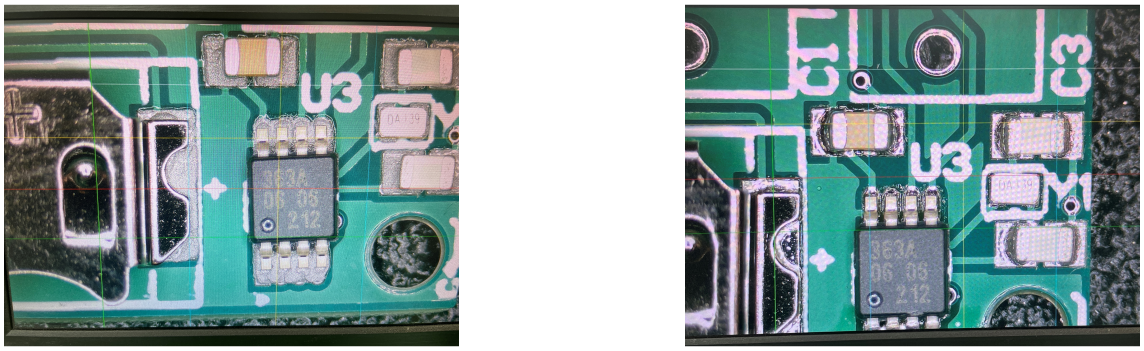

(a) (b)

Figure 4.3: Re-flow process. a) Components placed on the PCB with solder-paste on pads, b) PCB after soldering in the re-flow oven.

Molex connectors to the wires. The orientation of the connectors are marked in the Altium design files.

Sensor housing

3D printing components. Begin by 3D printing all of the .stl components listed in the Design files summary. Each component should be printed only once except the Detector_Zapfen.stl should be printed twice. For optimal printing performance, we suggest the following options when slicing the .stl files:

- "Avoid crossing perimeters" should be enabled so that there is less material to clean after printing.
- 5 perimeters, 5 bottom solid layers, and at least 0.15mm layer height for all components.
- The lens inserts (LED Zapfen and Detector Zapfen) should have a smaller layer height of 0.07mm.
- The Teeth have variable layer height ranging from 0.07-0.15mm. Layer height of 0.15mm for time optimization and a layer height of 0.07mm around where the Zapfen would fit into the teeth.

Figure 4.4 shows how to place the components on the printing bed for optimal printing. All of the components are placed on the bed to avoid overhangs and the ensure a smooth surface. The Zapfen are needed because without them it is very difficult to get a clean print in the Teeth around the lenses. Printing the Zapfen as separate components, as in Fig. 4.4 d and e, we get a high accuracy print that aligns the optical components to our satisfaction. We can then insert the Zapfen into the Teeth. If using Prusa I3 Mk3/Mk3S Filament Printer, we have provided the .gcode files, which can be used directly on the printer, and include all of the perimeter settings, predefined supports, and layer heights. We chose XPETG as the filament material since it does not dissolve when exposed to UV and water. Once the components have been printed, spray the Cap and Thread with acrylic laqueur (see Bill of materials). Although the components are waterproof, we have found that this helps keep water out of the walls of the 3D printed components.

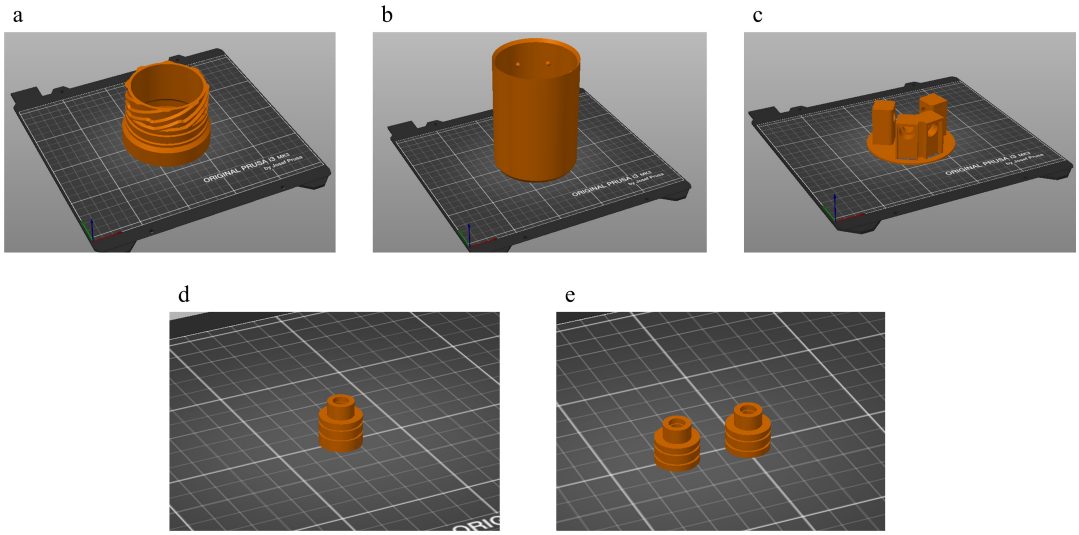

Figure 4.4: Optimal placement of components on 3D printing bed: a) thread, b) cap, c) teeth, d) LED zapfen, and e) detector zapfen.

Component assembly. Once all of the pieces are printed, assemble them as in Figure 4.5. Glue the lenses into the zapfen. Once the glue is dry we suggest testing if the lenses leak since this can destroy the IR detectors. Solder wires (according to Table 4.1) to the back of the LED, pressure, and IR detector PCBs. Then glue the IR detector and LED PCBs into the Zapfen. Glue the three Zapfen into the Teeth (the two IR detectors should be at 45^o and 135^o relative to the LED). Afterwards, glue the pressure sensor into the Teeth. We used the epoxy listed in the Bill of materials. Feed the wires from the LED, IR detector, and pressure/temperature sensor PCBs through the holes in the Teeth. Glue the Thread and Teeth together, then fill the Teeth with epoxy. Add/crimp the Molex 2-pin and 4-pin connectors to the wires (according to Table 4.1). Once the epoxy is dry, add the o-rings to the Thread and coat the o-rings in vacuum grease. Finally, connect the wires to the main PCB as in the layout in Fig. 4.1 and the provided schematic.

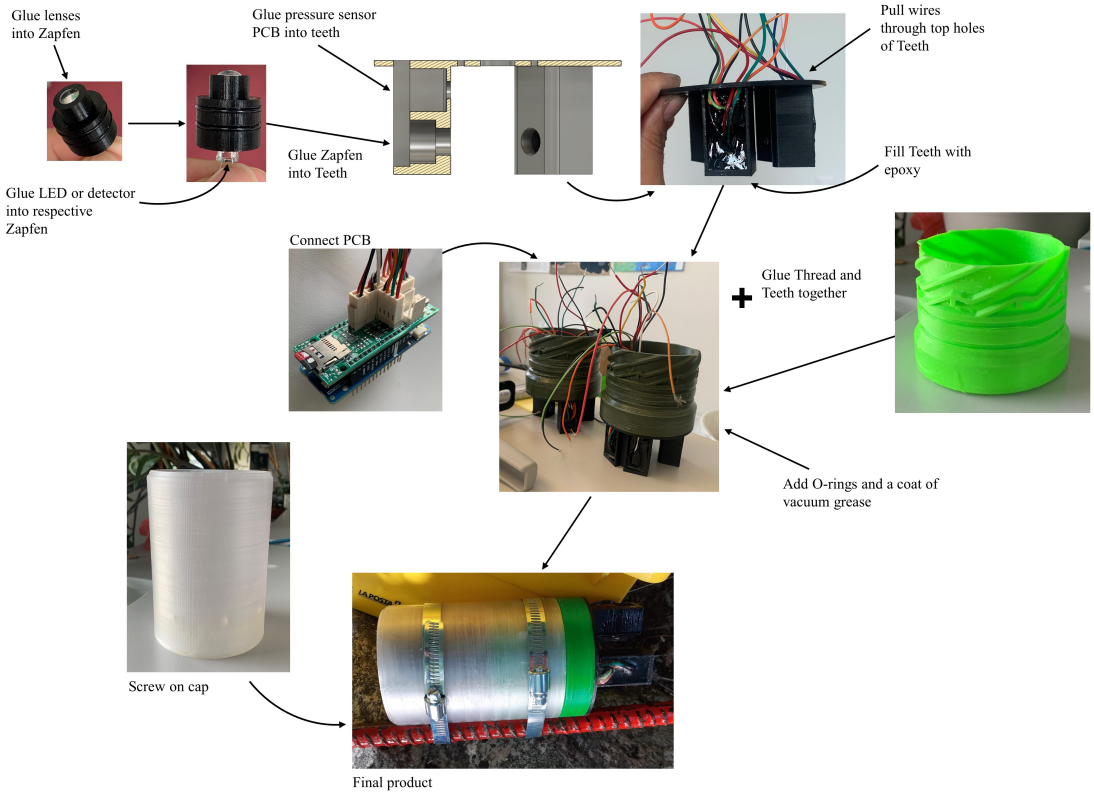

Figure 4.5: Assembly of sensor: beginning in the top left corner and following arrows until the Final Product.

4.6 Operation instructions

Begin by uploading the first program set_time.ino to the Arduino MKR WAN 1310. Please note that you will need a USB micro B cable to connect the Arduino to your computer and you will need Arduino IDE installed (Arduino, b). Please follow the instructions in set_time.ino about changing the date in the program. After the program has flashed, every time the Arduino restarts (disconnect and reconnect to power) it will restart the RTC time to the original compile time of the set_time.ino program. To mitigate this issue, the next program, main.ino, can be immediately flashed without disconnecting power or set_time.ino can be re-flashed after commenting-out line 79 (“setPCF85263();"). Follow by flashing main.ino onto the Arduino. Please note that additional libraries may need to be downloaded and added to your library (e.g. the MS5803-05 external library (Miller)). The main.ino program was written to take a measurement every hour (one measurement is an average of 15 measurements) to conserve battery, but this can be changed in the code if you require higher temporal resolution to capture larger variability e.g. from flushing of sediment from a dam.

After flashing the Arduino, disconnect the USB, insert a microSD card and connect the 3.7V LiPo battery. Once the battery is connected, the device should begin taking measurements. In order to avoid large sleep currents and accidentally using a corrupted card, we recommend using this SD card formatter (The SD Association) and testing the read-write capabilities of the cards with H2testw (Softpedia.com).

Once everything is running, we added some silica packets into the housing before closing the sensors for calibration, then installation.

Calibration

Before installation, we calibrated the sensor using three different dilutions of formazin: 0, 100, and 500 NTU. These three points were chosen because we wanted to limit our exposure to formazin, which is a known carcinogen, and we expected the Ötztal Ache's turbidity to be within this range since 90% of the time this river has an SSC of 5mg/L (Bundesministerium für Landwirtschaft, Regionen und Tourismus, 2021). In addition, our last open-source sensor (Droujko and Molnar, 2022) had 12 formazin calibration points and we wanted to see if we could obtain similarly accurate data with less calibration points. The form of the model that converts the digital IR light output to NTU is:

$$NTU = \alpha + (\beta \times D_{IR}) + (\gamma \times D_{IR}^2) \tag{4.1}$$

where D_{IR} is the digital reading output by the IR detector's ADC, and the calibration coefficients are listed in Table 4.2. The fit for the three NTU dilutions in shown in Figure 4.6. The residual standard error of this model is 2.26 NTU ($Adj.R^2 = 0.99$) and the P-value $< 2.2e-16$. This model was built using only the backscattering detector, other alternatives which combine detectors at different angles were compared in Droujko and Molnar (2022).

Table 4.2: Model statistics.

	Coefficients	P-value
α	-1.72	0.028
β	$3.49e-02$	$< 2e-16$
γ	$5.46e-06$	$< 2e-16$

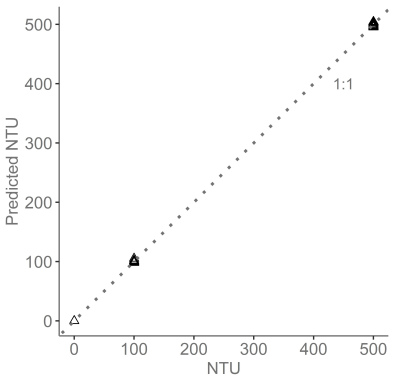

Figure 4.6: Predicted versus Observed NTU with the model. The model was calibrated using three formazin dilutions at 0, 100, and 500 NTU. The dotted line is the 1:1 line.

Safety concerns.

LiPo batteries can be extremely dangerous if mishandled; for example, if the positive and negative terminals touch, if they are left out in the sun, and/or if a NiCd/NiMH charger is accidentally used. Please follow manufacturers safety instructions.

4.7 Validation and characterization

Validation

We validated the sensor by installing it in the Ötztal Ache in Tirol over three days to measure the SSCs during the passage of a flood. The Ötz-T was installed ∼4.13 km downstream of the Tumpen dam (Figure 4.7). The Ötz-T sensor took one measurement every hour from 14.09.2022 15:35 to 17.09.2022 08:24. Each measurement consists of a temperature, a pressure, and a turbidity reading (which is an average of 15 turbidity measurements, see main.ino code). The Tumpen dam data was obtained from the Hydrographische Dienst Tirol; their measurements are made using a probe on the riverbank. In the following figures we are showing the measurements of the Ötz-T together with observations at the Tumpen dam upstream.

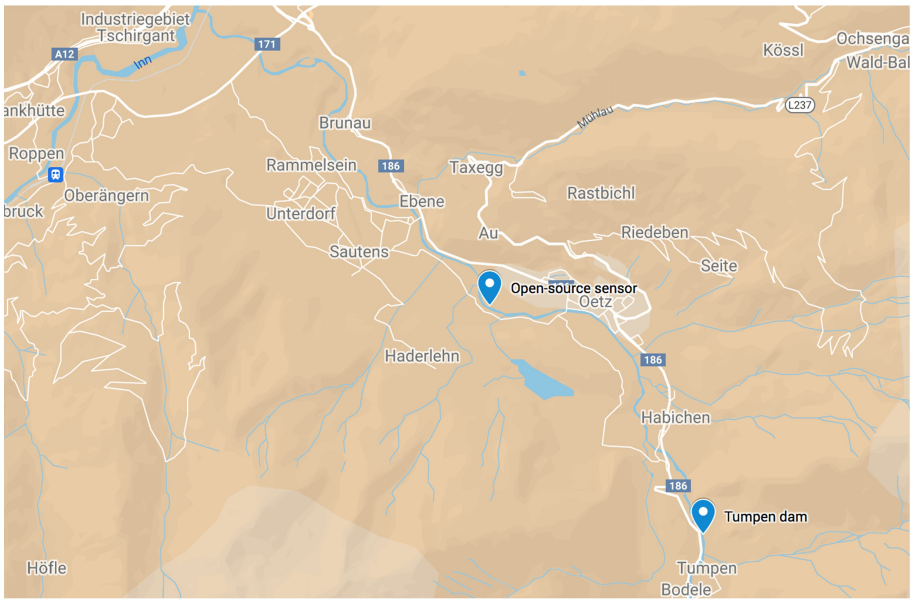

Figure 4.7: Ötztal valley, Austria. The Ötztal Ache flows North-West until it joins the Inn river. The Ötz-T sensor was located around 4.13 km downstream of the Tumpen dam.

The temperature measurements are shown in Figure 4.8a. The Ötz-T data (black) seem to follow the same trend as the data from the Tumpen dam (purple). However, the Ötz-T data seems to overestimate the temperature and an offset (delay) also seems be present. Although it is difficult to conclude about the origin of the offset due to the low recording resolution, it is likely that this is a real feature related to the attenuation of the flood waves in the 4.13 km reach between the measurements. At flow velocities of 0.5–1 m^3/s we may expect attenuation of 6–120 minutes.

The pressure measurements can be seen in Figure 4.8b. The Ötz-T pressure sensor is calibrated in a vacuum and the measurements plotted in Fig. 4.8b (black) are the Ötz-T absolute pressure minus the atmospheric pressure recorded in Imst, Austria for the same

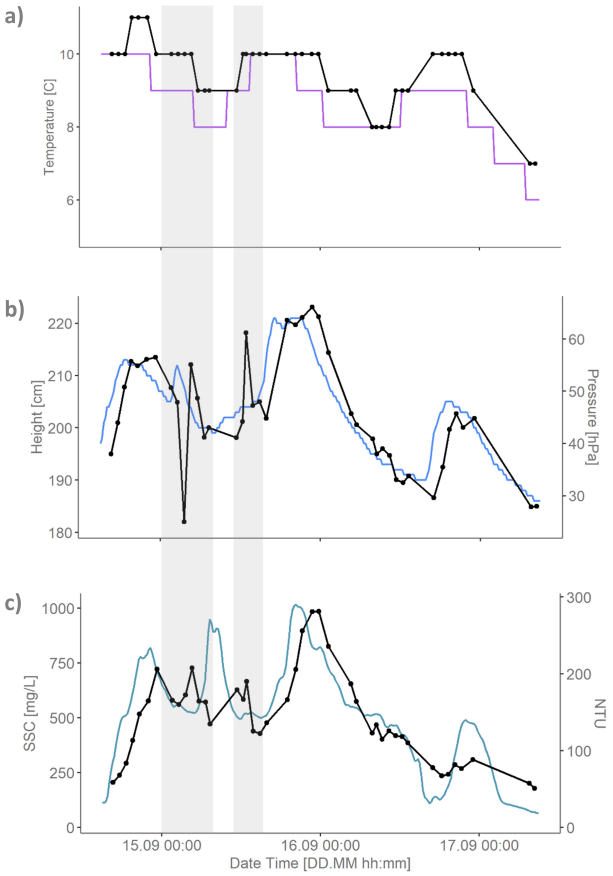

Figure 4.8: Comparison between the upstream Tumpen dam data and our downstream Ötz-T data. a) Temperature sensor comparison between Tumpen (purple) and Ötz-T (black dots and line), b) pressure sensor comparison between water level [cm] in Tumpen (blue) and Ötz-T pressure [hPa] (black dots and line) where Ötz-T pressure is the water pressure after removing the atmospheric pressure recorded at Imst, Austria, and c) comparison between SSC data [mg/L] from the Tumpen (teal) and the Ötz-T (black dots and line) turbidity data [NTU].

time period. The Tumpen data (blue) is the height of the water from their measurement probe. Both measurements follow the same trends but with a shift, which again can be attributed to flow attenuation over the 4.13 km of the river reach.

The turbidity measurements are shown in Figure 4.8c. The teal line is the SSC data from the Tumpen dam and the black dotted line is our Ötz-T turbidity data in units of NTU. The Tumpen SSC data is obtained via a turbidity probe on the river bank, which is then routinely calibrated to suspended sediment samples (Hydrographische Dienst Tirol). As can be seen in Fig. 4.8c, our turbidity data follows the trend of the SSC data (peaks and troughs) very well, again with the offset related to the delay of the sediment wave arriving to our downstream site. There are a few notable differences between the two datasets. First, around midnight on 15.09 (left grey highlight) there are two small sediment peaks in our turbidity data where there is only one large peak in the SSC data upstream. The pressure data (Fig. 4.8b, left grey highlight) observes a dip at the same time. Later (right grey highlight), there is again a peak in the pressure data and another NTU peak which is

not as large as the SSC peak. This suggests that there can be fluctuations in the stage-SSC relationship related to short term sediment flux variations (e.g. some disturbance to the flow regime around the gauge causing a drop in stage and rise in SSC). Another explanation is that SSC and NTU usually have a relationship of the form:

$$SSC = a(NTU)^b \tag{4.2}$$

where a and b are regression-estimated coefficients and are different for every watershed and sediment type (e.g. Costa et al. (2018a) found a=0.56 and b=1.25 and Felix et al. (2018) found a=0.59 and b=1). Therefore, we cannot expect a linear relationship between the SSC and the NTU data. This same explanation can be applied to the trough and peak occurring just before 17.09. An alternative explanation could be that there were not enough formazin calibration points between 0-100NTU to properly capture the trough. Whether these peaks and troughs could not be fully captured due to the minimal calibration points of the conversion between SSC and NTU should be validated in future studies.

Characterization

The sensor we have presented here is an improvement from the previous open-source turbidity sensor (Droujko and Molnar, 2022). This new version now incorporates a temperature and pressure sensor to monitor river stage and water temperature. It has an entirely 3D printed design so anyone with access to a hobby 3D printer can build the device. This sensor version now uses an Arduino MKR WAN 1310, enabling the microcontroller to reach extremely low power ($104\mu A$ (Arduino, a)) and with all of the i2C devices and the SD card, the sensor sleeps $\sim 200\mu A$. This low current draw extends the battery life of our device from one day (the previous sensor (Droujko and Molnar, 2022)) to one month. The sensor is also now programmed in the widely adapted Arduino IDE. Finally, the customized PCB shield is more robust than the previous prototyping board used.

There are many improvements that this sensor may still undergo. First, we would like to add a motor to the device to wipe the optics from any deposited debris or biofauling. This feature is necessary if the sensor is to be used in long-term deployments. We have found that the best micro SD cards add $110\mu A$ to the device sleep current, even when the cards were idle. For this reason, in the next version we plan on using an SPI flash to store the data while also including a micro SD card slot to retrieve the data quickly in the field. Additionally, the LED driver we chose pulled 200mA while taking measurements and significantly drained our battery. We aim to optimize this high LED current draw and improve the overall battery consumption of the device. Finally, the Ötz-T costs almost four times as much as our previous sensor version (61.37 CHF (Droujko and Molnar, 2022)). The parts of this sensor that increase the cost are the epoxy (28.62 CHF), the LiPo battery (41.45 CHF), the Arduino MKR WAN 1310 (38.68 CHF), and the MS5803-05 pressure/temperature sensor (27.91 CHF). All together these components account for 63% of the costs (or 136.66 CHF). We hope to eliminate some of these high costs by building our own microcontroller (eliminating the Arduino MKR), redesigning the teeth (to avoid the excessive use of epoxy), and switching to alkaline D-cell batteries.

Although we only used one of the two available IR detectors for our calibration and Ötztal measurements, the Ötz-T features two IR detectors. With enough gravimetric samples, the two IR detectors' ADC readings can be directly calibrated to SSC (e.g. calibrating D_{IR} from eqn.5.1 to SSC directly). Traditional calibration needs to anyways undergo a gravimetric calibration (NTU to SSC as in eqn.5.2) and in this way, one would avoid the

lengthy and dangerous formazin calibration step. In addition, using the D_{IR}-SSC calibration is a better representation of the entire catchment since the IR detector response curve changes with different grain type and particle size. Therefore, calibrating to catchment gavimetric samples leads to a calibration more representative of the catchment sediment types and particle size. And using two IR detectors instead of one leads to a better model fit (Droujko and Molnar, 2022).

Our hope is that the Ötz-T sensor brings accessibility to global river research for many applications. We think that with the transparent design presented here, researchers can build and repair the instruments themselves, ultimately making the data from our world's rivers, lakes, and oceans available to all.

Chapter 5 Sediment Dynamics in the Spöl and Inn Rivers During Environmental Floods as Seen Through High-Resolution Monitoring

Authors: Jessica Droujko, Jan Martini, and Peter Molnar
Publication date: In preparation

Key findings:

1. Environmental floods (e-floods) are conducted on regulated rivers in an attempt to incorporate pre-dam disturbances and redistribute the bed sediments, in the hopes to restore sandbanks, redistribute macroinvertebrate assemblages, and provide spawning habitats for fish.

2. We measured the 2021 and 2023 e-floods on the Spöl River in Graubunden, Switzerland using a high spatio-temporal network of suspended sediment concentration (SSC) sensors.

3. The SSC values recorded by our system during the e-floods resulted in erratic peaks of sediment that were much higher in amplitude and lasted longer than previously recorded values, exceeding the recommended maximum values for SSC set by the environmental authorities. We urge managers to consider high-resolution measurements to ensure these limits are not surpassed along the entire river section.

4. Sediment waves generated by e-floods in the Spöl River were observed to extend into the Inn River downstream, indicating the necessity of evaluating the broader ecological impacts of sediment redistribution. We found a total load of 1,297 and 1,936 t (in 2021 and 2023, respectively) delivered by the Spöl e-floods to the Inn, accounting for 0.76–1.14% of the total annual load delivered by the Inn.

5. 1D analysis revealed that the sediment waves' travel distance and settling patterns can be optimized using different combinations of e-flood and receiving river discharges. The potential for sediment waves to propagate beyond national borders highlights the importance of cross-border environmental cooperation and planning.

Author's contributions: The author conceptualized this work, built and deployed the sensors, curated the data, designed the project methodology, administered the project, did the data and 1D model analyses, and wrote the original and final draft of the paper.

Coauthors' contributions: JM and PM wrote the original and final draft of the paper. PM helped conceptualize this work and the 1D model and contributed to the discussion of the results.

Supplementary materials The PSD can be found at the following Zenodo repository: 10.5281/zenodo.10760041

5.1 Introduction

Rivers orchestrate a complex suite of ecological functions that extend far beyond their banks. They are crucial conduits for the transport of nutrients and sediments (Arrigo et al., 2008; Gregor, 1970; Nixon et al., 1996; Sanders et al., 2014; Ludwig et al., 1996; Terhaar et al., 2021; McLaughlin et al., 2003), shaping biodiversity (Descloux et al., 2013; Abell et al., 2008; Tierno de Figueroa et al., 2013; Dudgeon, 2000), influencing water quality, and providing a variety of ecosystem services supporting human livelihoods (Arthington et al., 2010; Postel et al., 1997). However, these ecosystems are threatened by humans, economic development, and climate change (Meybeck, 2003; Vörösmarty et al., 2010; WWAP, 2009; UNDP, 2006; Karl et al., 2009). Globally, two-thirds of rivers no longer flow unimpeded (Grill et al., 2019) and it is estimated over one million instream barriers fragment European rivers (Belletti et al., 2020).

Barriers, dams, and reservoirs heavily alter the river flow regime, having severe consequences on river ecosystems (Ward et al., 1999). Scientists have advocated for flow experiments to evaluate the effects of reservoir operations on freshwater ecology, rivers, floodplains, and deltas, and to create more scientifically-based operation guidelines (Walters et al., 1992; Souchon et al., 2008; Poff et al., 2003) which optimize economical and ecological benefits. To meet this need, environmental or experimental floods (e-floods), which aim to imitate the river's natural flow variability, have been implemented on selected streams globally (Konrad et al., 2011; Melis, 2011; King et al., 2010; Siebentritt et al., 2004; Cambray et al., 1997; Shafroth et al., 2010). These look to rework the bed sediments, increase spawning habitat availability and recruitment events, and improve the health of a desired fish population (King et al., 2010). In this sense, e-floods are thought to provide an opportunity for ecosystem recovery and ultimately aim to mitigate ecological issues by restoring the physical and biological components of the aquatic ecosystem.

Not all e-floods have only positive effects on downstream river systems. In the Grand Canyon, e-floods released by the Glen Canyon Dam are used to rebuild and maintain sandbars, provide camping beaches for tourists, create riparian habitats used by wildlife, and create a source of wind-borne sand to protect important archaeological sites from weathering and erosion (Melis, 2011). They were also intended to increase backwater and food availability to the native and endangered humpback chub. However, the implementation of these e-floods was found to instead displace the chub downstream and increase the mortality of the juveniles. The effect of geomorphology and flow regimes were also overestimated compared to water temperatures, where cold waters (released by Glen Canyon Dam) favoured the nonnative rainbow trout which caused a decrease in humpback chub populations (Melis, 2011). The sandbars were finally also eroded in subsequent months due to discharge fluctuations from hydropeaking (Melis, 2011). Others also did not succeed in promoting fish migration and spawning using e-floods, such as on the Olifants River in South Africa where the flow manipulations released cold, hypolimentic water (King et al., 1998).

Thirty-two e-floods have been released on the Spöl river in Graubunden, southeastern Switzerland between 2000–2016, stopping in 2016 because of toxic polychlorinated biphenyl contamination (PBC) of the sediments in Punt dal Gall dam (Klose, 2021). In this time, it was found that one or two e-floods per year enhance the long-term ecological integrity of the Spöl (Scheurer and Molinari, 2003) and when repeated annually, these benefits are maintained (Robinson and Uehlinger, 2008). Since the dam reduced spawning habitats

due to the clogged riverbed, and e-floods redistribute bed sediments, the e-floods should also continue in the long term if managers want to maintain pre-dam macroinvertebrate assemblages to sustain the food web and support the native brown trout. These studies also found that trout abundance was not reduced by the high flows and fish mortality was $< 2\%$. Therefore, the e-floods generally improved the fish habitat (spawning grounds) with an increase in redds (increased fish recruitment).

Although e-floods are designed to produce coarse bed material transport, they have the potential to also move large amounts of fine material in suspension, which can have negative ecological effects. This complicates the situation and calls for extensive data collection at high resolution to characterize the response of river systems to e-floods. Spatially extensive monitoring is needed to account for the influence of connectivity in river systems, especially concerning tributaries (Konrad et al., 2011; Consoli et al., 2022). In this context, the deployment of a high-resolution sensor network offers an unprecedented opportunity to closely monitor fine sediment dynamics during e-floods.

We apply such an innovative monitoring approach to the e-floods on the Spöl river in 2021 and 2023. By deploying a network of sensors across the Spöl and Inn rivers, this study aims to illuminate the advection and diffusion of the sediment wave, offering insights into the sedimentary behaviors that underpin river health and resilience. More specifically, we aim to a) show that high-resolution monitoring of SSC is necessary to capture fluctuations in SSC during e-floods, so that we can see when and where sediment is released from the river bed, banks, floodplain and supplied by released waters, we hypothesize that similar e-floods in the Spöl will release higher amounts of fine sediment when the storages are full; and b) demonstrate that relatively simple modeling of the e-flood fine sediment wave released downstream can be used to estimate and optimize how far the sediment wave can travel under different combinations of e-flood and receiving river discharges. This approach will prove valuable for river managers.

5.2 Study Site and e-floods on the Spöl

The Spöl river in Graubunden, Switzerland, with a catchment area of 286 km^2, flows from the Punt dal Gall dam that forms Livigno reservoir into the Inn River in Zernez. It is located in a dolomite geology and flows through steep canyon walls surrounded by mountainous terrain. Between Punt dal Gall and Zernez, the Spöl enters a secondary hydropower plant reservoir, which is 5.7 km downstream of Punt dal Gall, called Ova Spin (Figure 5.1). Our study reach begins 3.4 km downstream of Ova Spin, and encompasses the Spöl until it joins the Inn. Our study site continues for another 3.2 km along the Inn river (Figure 5.1).

Prior to the hydropower plant regulation taking effect in 1970, the Spöl carried a mean annual discharge of 8.6 m^3s^{-1}, with low flows in the Winter and floods ranging from 20–60 m^3s^{-1} from precipitation in the Summer (Robinson et al., 2023). Once these hydropower plants became operational, the mean annual discharge reduced to 1 m^3s^{-1}. The low transportability of fine sediment by this residual flow caused the riverbed to become clogged, reducing the spawning habitat of the native brown trout (Robinson et al., 2003). Sealing the hyporheic zone, an important habitat and refuge for many invertebrates, has consequences on its functional significance (Boulton et al., 1998; Stubbington, 2012). The lack of disturbances allowed the growth of dense algal mats and moss beds. This was followed by an increase of dominant species, such as the *Gammarus fossarum* or *Crenobia alpina*,

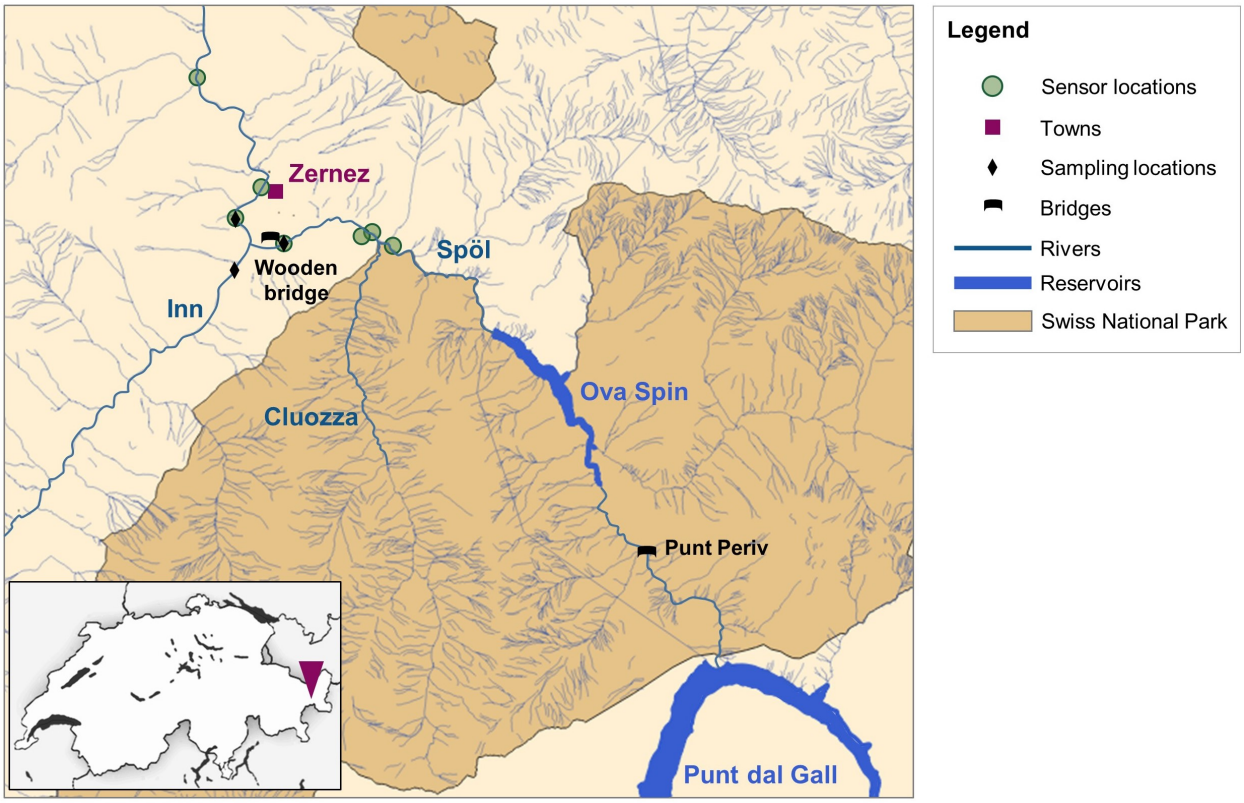

Figure 5.1: Map showing the study site. The Spöl begins in the Punt dal Gall reservoir and flows into the Ova Spin reservoir. The Spöl continues to flow downstream and is joined by the Cluozza River before entering the Inn River. Our sensor installation locations (green circles), gravimetric sampling locations (black diamonds), bridges (black bridge symbols), and the town of Zernez (square) are labeled. For example, at the Wooden bridge, we installed a sensor and we took samples.

and a general decline of diversity (Robinson et al., 2003). These issues led the Engadiner Kraftwerke Power Company, the Swiss National Park, and the state authorities to implement e-floods to improve the habitat conditions for brown trout, beginning in 2000. About 32 e-floods have been released between 2000 and 2016 from Punt dal Gall. Many of these e-floods were investigated over the past 20 years by several research groups across the Alps to answer a variety of research questions. The e-floods usually lasted half a day with step-wise discharge increase and decrease.

Due to the PBC contamination of the Punt dal Gall sediments in 2016 (Klose, 2021), the e-floods resumed in 2021 but only from the Ova Spin dam. We investigated two such e-floods on 23.06.2021 and 15.06.2023. In 2021, the e-flood started at 6:00 in the morning and lasted for 10.5 h until 16:30. The discharge was increased in a step-wise fashion during this time from the residual flow of 0.9 m^3s^{-1}, to 25.9 m^3s^{-1} in the middle of the day, and reduced to 0.9 m^3s^{-1} again in the evening. In 2023, the e-flood was longer and started at 4:30 in the morning lasting for 18.5 h until 23:00. The discharge was again increased from the residual flow of 0.9 m^3s^{-1} to 25.9 m^3s^{-1} in the middle of the day, and reduced to 0.9 m^3s^{-1} again in the evening. The discharges for both campaigns are shown in Figure 5.4.

5.3 Methods

5.3.1 Suspended Sediment Concentration (SSC) Monitoring

We built 7 multiparameter sondes that measure water temperature, pressure (proxy for stage), and SSC. These sensors were first tested in a mixing tank experiment with other commercial sensors and two different sediment types (Feldspar and sands taken from the tailwater channels of the Fieschertal river). They were shown to have low measurement uncertainty (±5%) for a large range of SSCs (0–15 gL^{-1}) (Droujko and Molnar, 2022). Afterwards, the sensors were tested during a flood on the Ötztaler Ache in Austria (Droujko et al., 2023a).

In this study, we deploy 4 (in 2021) and 7 (in 2023) of these sensors in a network to monitor SSC during the passage of e-floods. This represents a significant advancement over traditional sediment monitoring methods utilized over the last two decades. Historically, sediment data collection relied on infrequent, manual sampling, which limited the temporal resolution and often missed the transient sediment spikes associated with flood events. Alternatively, in-situ loggers were used to capture these events at high temporal resolutions, but owing to the high costs of these devices, they have not been deployed in a distributed manner. This led to a limited basin-integrated understanding of e-flood sediment dynamics. In contrast, our sensor network provides continuous, high spatio-temporal resolution data, capturing the dynamic changes in SSC along the downstream river segment affected by the e-flood. This enables the detection of fine-scale variations in suspended sediment load that were previously undetectable, offering a more accurate and comprehensive understanding of sediment transport patterns during e-floods. Such a network also provides insights into sediment source areas, transport mechanisms, and deposition patterns that were not possible with traditional sampling techniques.

Before the e-floods in 2021 and 2023, we installed the sensors along the Spöl and Inn rivers. The sensor locations are shown in Figure 5.1. In 2021, we installed 5 sensors at 4 locations. Two were located downstream of the Cluozza tributary (1.4 km upstream of the Wooden bridge) on each side of the river bank. This was done in anticipation that the bed sediments would be mobilized and that one of the sensors could be buried during the falling limb of the flood. This is exactly what happened, therefore, we only present the data from one of these sensors. Two sensors were installed at the Wooden bridge to check local variability and ensure that the sensors produced reproducible results. Finally, one sensor was placed 500 m downstream of the Spöl–Inn confluence. The sensors took one measurement every minute during the e-floods.

In 2023, we installed more sensors. One sensor was installed on the Spöl above the Cluozza and two were installed downstream on each side of the river bank (similar as in 2021). One sensor was installed at the Wooden bridge and three sensors were installed on the Inn at 339 m, 1.28 km, and 3.18 km from the Spöl-Inn confluence. These locations were selected to help identify 1) the fraction of SSC delivered by the tributary (resuspended near the Cluozza), 2) the fraction of SSC dilution on the Inn downstream of the Spöl, and 3) the fraction of sediment delivered by the dam. The measurement frequency of the sensors was 1 measurement every 2.5 minutes. All sensors in 2021 and 2023 were removed after the e-floods.

5.3.2 Collection and Analysis of Gravimetric Sediment Samples

To calibrate the sensors, which measure light scatter, to the actual concentration of sediments in suspension, as argued by Droujko and Molnar (2022), we took sediment-laden water samples at various locations during both campaigns. The sampling locations are marked in Figure 5.1. In 2021, we took samples at the Wooden bridge and on the Inn 1.3 km upstream of the Spöl–Inn confluence. In 2023, we additionally took samples at the closest (to the confluence) downstream Inn site (Figure 5.1). A summary of the number of samples and the time of sampling are shown in Table 5.1.

Table 5.1: Number of gravimetric samples and time of sampling for each campaign at the two (2021) and three (2023) locations shown in Figure 5.1.

	Number of Samples		Time of sampling	
Site name	2021	2023	2021	2023
Upstream Inn	19	3	Every 30–40min from 8:14–17:29	8:42, 14:49, 18:55
Downstream Inn	-	13	-	Every 30min from 7:05–10:30, every hour 10:30–14:34, 15:00
Wooden bridge	22	22	Every 30–40min from 6:40–18:00	Every 30min 5:00–10:30 and 14:30–17:30, every hour 10:30–14:30

The samples were collected using manual water bottle collection in volumes of 150–200 mL. After each e-flood, the samples were weighed, dried in an oven at 98 ^oC, and re-weighed. The SSC was then calculated using the following formula:

$$SSC = \frac{m_{dryweight}}{V_{total}} \tag{5.1}$$

where m_{dw} is the mass of the dried solids and where V_t is the total volume of the sample containing the water volume and the volume of solids.

In 2021, the samples from the upstream Inn site were used to establish the SSC of the Inn before its confluence with the Spöl. The average SSC of the (upstream) Inn from the 19 gravimetric samples during the e-flood was 0.7 gL^{-1}. The 22 samples from the Wooden bridge site were used to calibrate the 5 sensors in the experiment. The calibration was done as a regression between the raw data output from the sensors and the SSC (Droujko and Molnar, 2022).

In 2023, we took 13 gravimetric samples on the downstream Inn site and fewer (3) samples on the upstream Inn site. The average SSC of the Inn (upstream) during the e-flood was 0.14 gL^{-1}. The 13 gravimetric samples downstream were used to calibrate the sensors installed on the Inn. Similarly, the 22 samples at the Wooden bridge were used to calibrate the sensors installed on the Spöl. Site-specific calibration is advisable due to local sediment source properties that affect the amount of scattered light measured by our optical SSC sensors (Droujko and Molnar, 2022).

5.3.3 Discharge Data Acquisition

The discharge data for both e-floods was obtained at the Ova Spin plant by the Engadiner Kraftwerke Power Company which measured the discharge directly at the reservoir outlet. In 2021, discharge data was also computed at the Wooden bridge using a hand-held Surface Velocity Radar (SVR) from Decateur Electronics Europe and integrating these measurements using the velocity-area method (Herschy, 1993) by coupling with water-level readings that were taken every 15 minutes from a graduated rod that was installed on the bank of the river.
To calculate the discharge at the Wooden bridge in 2023, we computed a simple linear regression between the pressure data measured by our sensor (at this location) and the time-shifted discharge measured at Ova Spin. The time-shifted discharge is taken by shifting the discharge at Ova Spin by 1h 10 minutes. This was found because it took 22 minutes for the discharge wave to travel from the most upstream sensor site (upstream of the Cluozza in Figure 5.1) to the Wooden bridge (1.52 km), giving a speed of 1.15 ms^{-1} (as seen from the sensor pressure measurements). Therefore, from Ova Spin to the Wooden bridge (4.83 km), the water travel time was 1h10min.

5.3.4 Particle Size Distribution (PSD) Evaluation

The Particle Size Distribution (PSD) for fine sediment in suspension of 6 samples taken in 2023 was found using an LA-960 Laser Scattering Particle Size Distribution Analyzer, which measures particles between 10 nm – 5 mm. The d_{50} for each sample and their respective locations and sample times are shown in Table 5.2. The PSD for suspended sediment is mostly fine silt in both the Spöl and Inn. Additionally, we see a slight increase in d_{50} at 13:30 along the Spöl, pointing to a slight resuspension of coarser grains. The entire PSD is found in the Supplementary Materials.

Table 5.2: Calculated d_{50} from the PSD Analyzer for 6 samples taken along the Spöl and Inn during the 2023 e-flood.

Site	Sample time [hh:mm]	d_{50} [μm]
Wooden bridge	06:00	13.3
Wooden bridge	07:30	13.6
Wooden bridge	13:30	17.0
Downstream Inn	07:05	13.5
Downstream Inn	08:01	13.0
Upstream Inn	08:42	18.6

5.3.5 Steady State Advection

As a proof-of-concept, we present a first-order analysis of the e-flood's propagation along the Inn by solving the advection equation in 1D under steady-state discharge assuming particle size dependent settling velocity. This allows us to compute the distance at which the Inn SSC reaches a desired level for any input e-flood discharge and SSC. The advection equation for sediment concentration in a 1D channel is:

$$\frac{\partial vC}{\partial x} - \frac{\partial wC}{\partial z} = 0 \tag{5.2}$$

where w is the settling velocity, v is the flow velocity, C is the SSC, x is the distance along the flow direction, and z is the depth. Assuming gradually varied steady flow ($\partial v/\partial x = 0$), a constant velocity taken as the depth-average ($\overline{V} = Q/(Bh)$, where B is the Inn channel width and h is the depth), constant settling velocity ($\partial w/\partial z = 0$), and that the vertical concentration profile is a linear function of the depth and mean SSC (e.g $\partial C/\partial z = -\overline{C}/h$), the stream distance (L) that is necessary for the suspended solids to settle and for the Inn concentration to recede back to its pre-e-flood levels can be solved as:

$$L = -\frac{Q}{Bw} ln(\frac{c_L}{c_o}) \tag{5.3}$$

where L is the stream distance in km from the Spöl–Inn confluence, Q is the discharge of the Spöl and Inn ($Q = Q_{Inn} + Q_{Spl}$), c_L is the concentration of the Inn at the distance L, and c_o is the concentration of the Inn just after the confluence.
The distance L can be solved for various combinations of Ψ, the ratio of discharge between the Spöl and Inn ($\Psi = Q_{Spl}/Q_{Inn}$), and for various initial Spöl concentrations ($c_{Spl} = [2, 4, 8, 12, 20, 30] gL^{-1}$). The average width, B, was computed from satellite images, taking 14 transects along the study reach (Inn only), and was found to be 38.8 m ± 6.9. The concentration of the Inn just after the confluence is found from $c_o Q = c_{Inn} Q_{Inn} + c_{Spl} Q_{Spl}$, taking c_{Inn} as the upstream Inn SSC of 0.42 gL^{-1} (average concentration of the upstream Inn from the 2021 and 2023 floods) and taking Q_{Spl} to be 25.9 $m^3 s^{-1}$, which is the maximum discharge of the Spöl during the e-floods. Finally, the settling velocity (w) was taken as 0.134 mms^{-1} (fine flocculated silt) (Julien, 2010). Note that this steady state solution gives the distance L under the worst-case condition of the highest discharge during the e-flood, all other discharges during the e-flood would result in lower L.

5.4 Monitoring data

5.4.1 Sensor Performance and Data Reliability

The gravimetric samples, the data from the sensors for both campaigns (2021 and 2023), and the calibration curve are shown in Figure 5.2. The sensor data shown in this figure is from the same location where gravimetric samples were taken. We do not show the data from 2021 on the Inn because we did not take gravimetric samples on the Inn at the same location where the Inn sensors were logging. In 2021 on the Spöl (Figure 5.2a), a clear peak at 5.5 gL^{-1} is visible ∼7:30, subsequent peaks follow throughout the day, again reaching ∼ 5.5 gL^{-1}, until around 12:00, where the SSC begins to gradually drop. In 2023 on the Spöl (Figure 5.2c), the profiles of the SSC show one dominant peak of 10.8 gL^{-1} at the Wooden bridge and the subsequent peaks are of smaller amplitude. A very similar SSC variability is again seen lower downstream on the Inn river (Figure 5.2d), with lower amplitude due to dampening. The $SSC_{observed}$ and $SSC_{predicted}$ for Spöl 2021 and 2023 and Inn 2023 are shown in Figure 5.2b.

The SSC data from the two sensors at the Wooden bridge in 2021 are shown in Figure 5.3. Sensors 3 and 5 are producing very similar results. The scatterplot of contemporaneous measurements (Figure 5.3b) shows an almost perfect fit ($R^2 = 0.97$) with mean difference centered at $\overline{\Delta SSC} = 0$. Slight differences in the reported results are likely due to turbulent velocity fluctuations at small scales around both sensors.

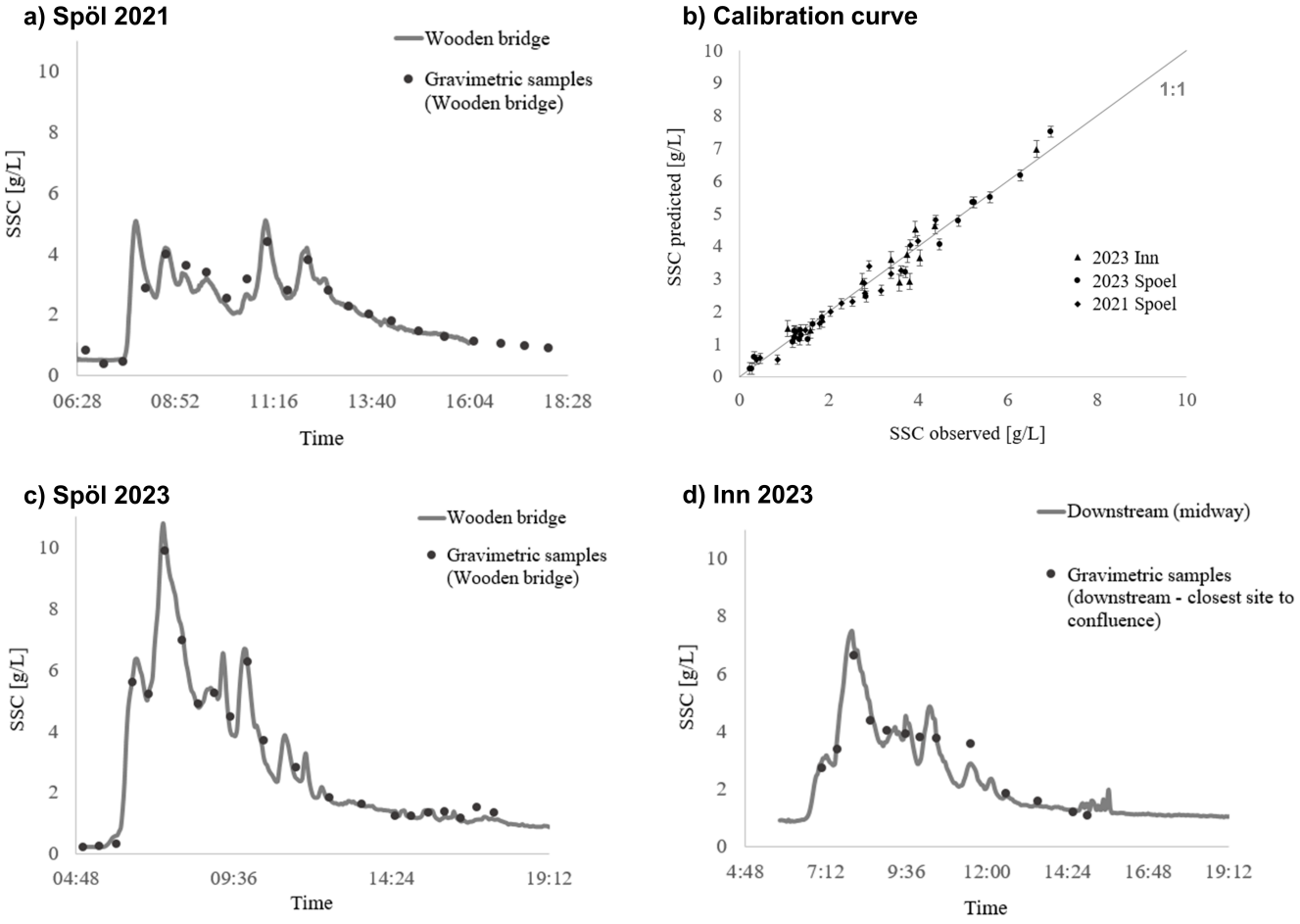

Figure 5.2: Comparison of the gravimetric samples and sensor outputs in 2021 on the a) Spöl and in 2023 on the c) Spöl and d) Inn downstream of Spöl. The scatterplot for the $SSC_{observed}$ (gravimetric samples) and the $SSC_{predicted}$ (from sensors) is shown in b)..

5.4.2 Dynamics of SSC During E-Floods

All of the sensor SSC data from the various sensing locations (in Figure 5.1) are shown in Figure 5.4 for 2021 (a–b) and 2023 (c–d) along with the e-flood discharge data. In both figures, the discharge is shown by the blue area plot and the SSC measured by the sensors are shown by the coloured lines.

In 2021 (Figure 5.4a–b), the discharge was increased in a step-wise fashion (see Sec. 5.2). At ∼7:45, we observe the largest sediment pulse of the day at 11.8 gL^{-1} in the upstream part of the Spöl (Figure 5.4a - green line) during ramping up of the discharge. At this location, we observed several sediment pulses throughout the day but none of them reached the magnitude of the first pulse. Further downstream at the bridge (grey line), we see these same pulses but at a lower amplitude than upstream (the highest concentration observed is 5 gL^{-1}). At the Wooden bridge, the sediment wave is also shifted by 13 minutes from the upstream location. The sensor in the Inn (Figure 5.4b - black line) also measured these same pulsations but again at a lower amplitude and the sediment peaks were shifted by another 8 minutes from the Wooden bridge location.

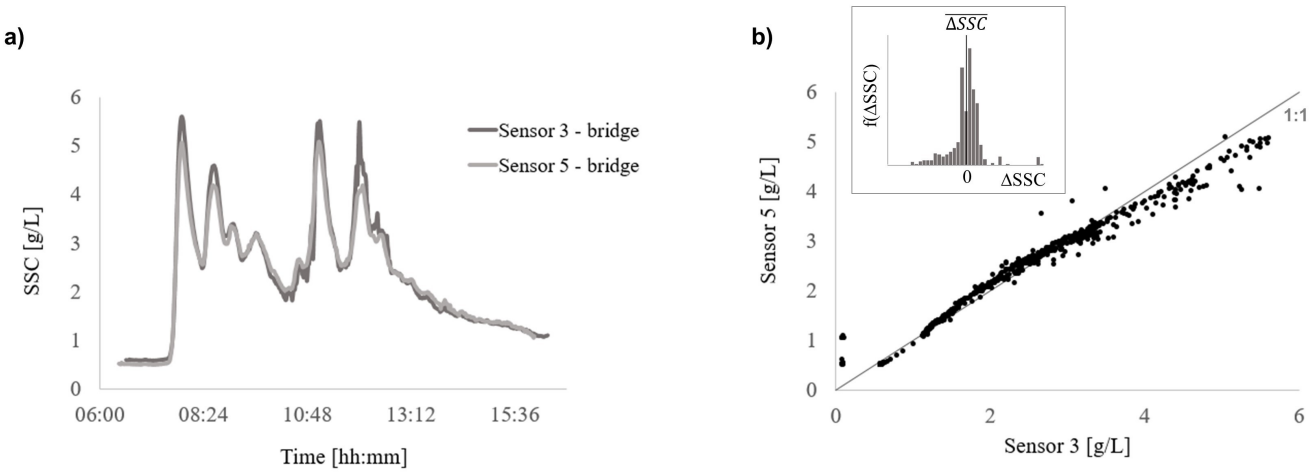

Figure 5.3: a) SSC time series of the two sensors installed at the Wooden bridge in 2021 and b) scatterplot of contemporaneous measurements (in g/L) with an $R^2 = 0.97$ and a distribution of the differences centered around $\overline{\Delta SSC} = 0$.

In 2023 (Figure 5.4c–d), the discharge was again increased in a step-wise fashion from 0.9 m^3s^{-1} to 25.9 m^3s^{-1}, and then again reduced to 0.9 m^3s^{-1} but this time with a much longer recession period (ramping up time was 6 hours). At ∼5:45, we observed a large sediment pulse in the Spöl (Figure 5.4c) between 5–7 gL^{-1} and later ∼7:30 we observed the largest pulse of the day between 8-11 gL^{-1} (at all locations along the Spöl - yellow, green, and grey lines). These pulses then propagate downstream and affect the concentration of the Inn (Figure 5.4d), represented by the black solid, black dotted, and yellow solid lines. Note that the sensor on the Inn located closest to the Spöl-Inn confluence (solid black line) only started recording ∼9:40.

In summary, the e-flood water volumes $5.2 \times 10^5 m^3$ (2021) and $9.1 \times 10^5 m^3$ (2023), had similar ramp-up limbs (5–6 h) and peaks at 25.9 m^3s^{-1}, but a longer recession occurred in 2023. In 2021, we observed several pulses of high SSC during the e-flood. Whereas during the 2023 e-flood, we observed a main early peak (during the ramp up) and gradual drop off in SSC.

5.5 Results & Discussion

5.5.1 Contributions of e-floods to Annual Sediment Budgets

The amount of fine sediment delivered by the Spöl to the Inn during the e-flood in 2021 was calculated by multiplying the SSC timeseries measured by the sensors at the bridge and the discharge timeseries measured at the bridge, then summing over the entire day. This resulted in a suspended sediment yield of 1,297 ± 75 t.

The National Long-Term Surveillance of Swiss Rivers (NADUF) program measured between 1998–2018 a mean annual suspended sediment flux of $30 \times 10^3 ty^{-1}$ on the Inn (twice weekly sampling) at S-Chanf (13.24 km upstream from the Spöl–Inn confluence) (Eawag: Swiss Federal Institute Of Aquatic Science And Technology and Federal Office For The Environment (FOEN), 2021). At Martinsbruck (Austrian boarder), Zobrist et al. (2004) reports a mean annual load (for 1974–1998) of $170 \times 10^3 ty^{-1}$. This means that yearly,

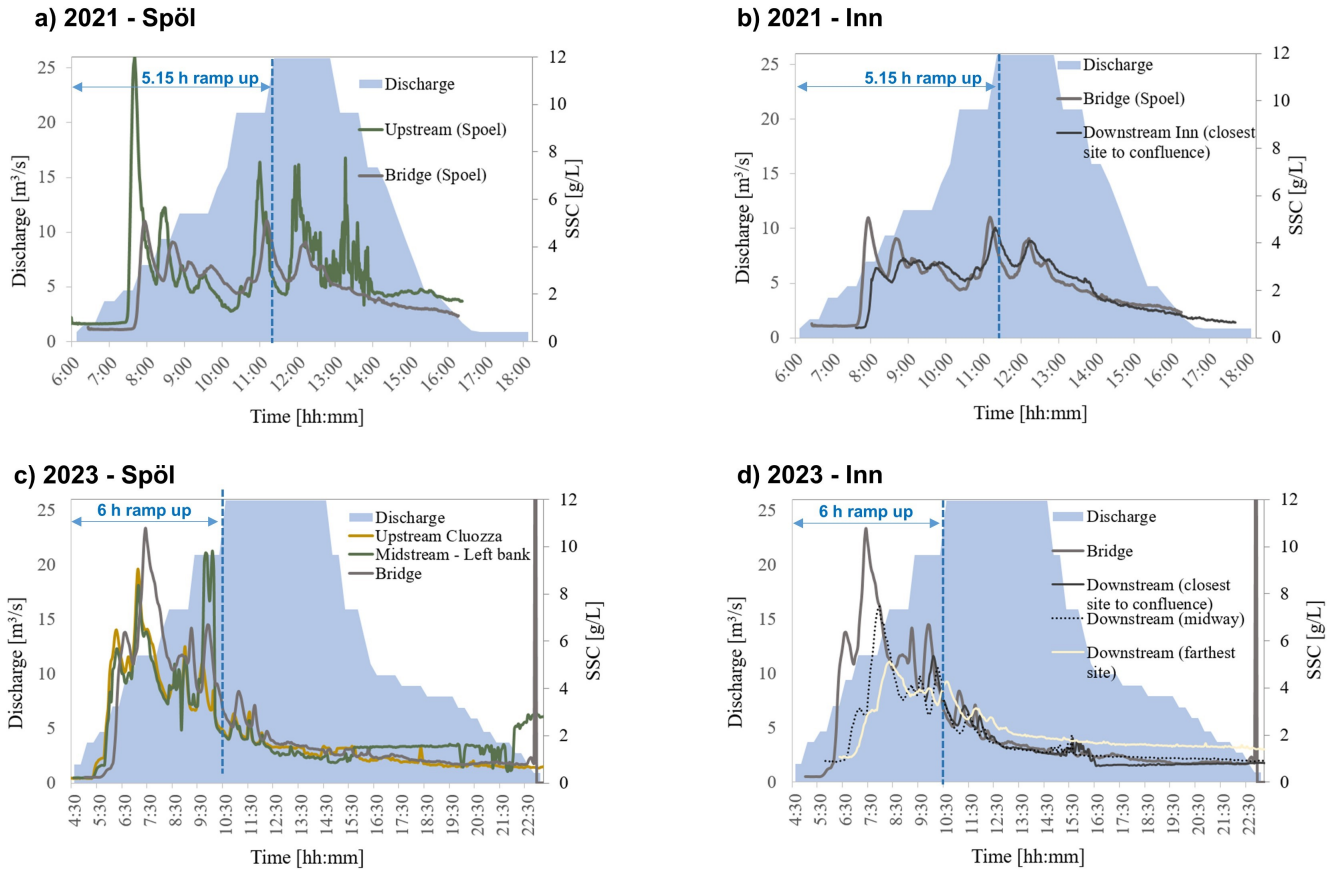

Figure 5.4: Discharge and SSC time series for the e-floods in 2021 on the a) Spöl and b) Inn. And in 2023 on the c) Spöl and d) Inn. For comparison purposes, the data at the Wooden bridge (in 2021 and 2023) is shown in all four panels. The discharge is shown by the blue area and the SSC is shown by the lines.

the upstream (of S-Chanf) Inn's contribution to the total load exported from Switzerland by the Inn is $\sim$ 18%. Therefore, during the 2021 e-flood, the Spöl delivered 0.76% of the total annual load exported by the Inn to Austria. It should be noted that due to the twice-weekly sampling at the NADUF stations, the annual yields are probably higher since coarse sampling usually only captures low concentrations.

Since we did not measure discharge at the same location as our sensors in 2023, we calculated the yield using the time-shifted discharge at the Wooden bridge (see Section 5.3.3). Using this obtained discharge timeseries, we multiplied it by the SSC timeseries from the entire day of the e-flood. We found that the suspended sediment yield delivered by the Spöl to the Inn on that day was 1,936 $\pm$ 133 t, which is 1.14% of the annual load of the Inn.

Table 5.3: Main information for the 2021 and 2023 e-floods. The c_{max} and c_{mean} are the values from the Wooden bridge.

Year	e-flood duration [h]	Q_{peak} $[m^3 s^{-1}]$	V_{water} $[m^3]$	c_{max} $[gL^{-1}]$	c_{mean} $[gL^{-1}]$	$V_{sediment}$ [t]
2021	5.15	25.9	5.2×10^5	5.5 $\pm$ 0.15	2.24 $\pm$ 0.15	1,297 $\pm$ 75
2023	6	25.9	9.1×10^5	10.8 $\pm$ 0.17	2.37 $\pm$ 0.17	1,936 $\pm$ 133

5.5.2 Interpretations of SSC Variability

The highest SSCs measured in any Spöl field campaign from 2000–2020 have been 8.2 gL^{-1} for 15 min by Ortlepp and Mürle (2003) (Imhoff cone measurements in mLL^{-1} converted to gL^{-1} using the equations by Pavanelli and Bigi (2005)). From our two campaigns, it is clear that infrequent sampling (low temporal resolution) is very unlikely to capture the high SSC peaks. For example, Figure 5.2a shows how our gravimetric sampling missed the first SSC peak at $\sim$7:54, but Figure 5.2b in 2023 shows how the timing of our gravimetric sampling captured the peak at $\sim$7:30. Therefore, it is highly possible that previous e-flood campaigns did not fully capture either the amplitude of the SSC peaks and/or the duration of the peaks.

The e-flood in 2000 measured by Ortlepp and Mürle (2003) was at Punt Periv (Figure 5.1) however, from Figure 5.4 it is not immediately clear that sites closest to the dam should always experience the highest SSCs. For example, in 2021 (Figure 5.4a), the highest SSCs observed by our sensors were at the upstream Spöl site (downstream of the Cluozza in Figure 5.1). However, in 2023 (Figure 5.4b) the highest SSCs observed by our sensors were at the Wooden bridge. This shows that fine sediment pulses produced by e-floods depend on where sediment is available (e.g. downstream of tributaries as found by Consoli et al. (2022)) and when it is resuspended from the bed, banks, floodplain, or in the water released from the reservoir. This was also observed by the Swiss National Park during the July cleaning of the accidental sediment spill: the SSC at Punt Periv was almost twice as high at the SSC at Punt dal Gall (Michael et al., 2013). Generally, environmental authorities set limits on the amount of SSC that is allowable in a river during flushing but we urge managers to consider high spatio-temporal resolution measurements to ensure these limits are not surpassed along the entire river section.

High-resolution measurements not only give a spatial understanding of SSC but also facilitate the discovery of new phenomena, leading to deeper insights. For example, when

comparing the two flood campaigns from 2021 and 2023, we observe different patterns of SSC pulsations. There are five SSC peaks in 2021 and three in 2023 throughout the flood, but the peaks in 2023 occur during the stepwise increase in discharge and before the maximum discharge (25.9 m^3s^{-1}) starting at 10:30.

In both years, the largest SSC peaks are observed with an increase in discharge up to 5 m^3s^{-1}. This could be due to the first initial release of water by the dam which carries with it all of the fine sediment that is resuspended mostly from the river bed downstream of the dam with the onset of the e-flood. Later when the discharge is increased from 10.5 to 20.9 m^3s^{-1} (in 2021) another pulse is triggered. This triggering effect is seen again at 12:00 and 13:00 in 2021 and at 10:00 in 2023. Additionally, just before the second 2023 peak (Fig. 5.4c), the SSC upstream of the Cluozza is lower than the SSC downstream of the Cluozza. Therefore, this second peak must be coming from the bed or banks around the Cluozza. These subsequent pulses can be caused by a) the e-flood inundation accessing new floodplain sediment sources (Consoli et al., 2022), b) by fine sediment being released from the bed due to bedload mobilization, or c) by an increase in SSC in the release waters. If the pulses are caused by the latter, avoiding this type of intermittent sediment triggering can be done by implementing Controlled Sediment Flushing Operation (CSFO), as Cattanéo et al. (2021). There, the reservoir was only partially emptied and the rate of emptying was controlled by constantly monitoring the SSC at the dam outlet; if the SSC exceeded a certain threshold, the rate of emptying was reduced. In this way, by harnessing real-time monitoring, the authors could avoid the large SSC peaks that are typical of reservoir flushing.

Additionally, our high spatio-temporal measurements capture the suspended sediment wave travel times. By calculating the offset in the peaks observed by the sensors, we found that the sediment wave traveled at 0.87 ms^{-1} along the Spöl before entering the Inn and increasing to 1.1 ms^{-1} (in 2021). Interestingly however, in 2023 we found that the sediment wave along the Spöl traveled much faster (at 1.76 ms^{-1}) compared to when it entered the Inn (1 ms^{-1}); the Inn sediment wave was traveling slower almost twofold although its discharge was twice as large (compared to the Spöl). This shows the non-linearity of the sediment concentration–discharge relationship.

5.5.3 Impacts of Fine Sediment on River Ecology

High SSC concentrations are a concern for fish and juvenile fish mortality. Newcombe and MacDonald (1991) found a mortality rate of 50% for juvenile salmon (Chinook) when exposed to SSCs of 1.4–9.4 gL^{-1} for 36 hours. Whereas Crosa et al. (2010) found that brown trout population downstream of a dam showed a severe density reduction of about 73% (from 11,000 to 3,000 individuals ha^{-1}) when the average SSC was 4–5 gL^{-1} within flushing periods, with occasional unpredictable peaks at 70-80 gL^{-1}. Espa et al. (2013) found a reduction in juvenile brown trout abundance after two weeks at 3–4 gL^{-1} and Grimardias et al. (2017) observed lower survival rate and many dead fish after a 13-day flushing with a mean SSC of 11 gL^{-s} with a peak at 48 gL^{-1}. It should also be noted that predicting the impacts of SSC on aquatic biota is site-specific (Bilotta et al., 2012) and most SSC thresholds are based on Salmonids tolerance (Collins et al., 2011; Berry et al., 2003).

The highest SSCs measured in any Spöl field campaign from 2000–2020 have been 8.2 gL^{-1}

for 15 min by Ortlepp and Mürle (2003). Ortlepp and Mürle (2003) found that these floods with this high concentration did not cause high fish mortality. In contrast, the reduction of periphyton and the enhanced flow dynamic increased spawning sites of the brown trout (*Salmo trutta fario* L.) which, lead to a population increase in the Spöl compared to the conditions between the dam construction and the start of the e-flood program (Robinson et al., 2023).

However, Gerster and Rey (1994) suggested that the maximum SSC for fish should not exceed 5 gL^{-1} and they observed damages to the fish gills and skin mucous layer at concentrations around 13.5 gL^{-1} (Imhoff cone measurements in mLL^{-1} converted to gL^{-1} using the equations by Pavanelli and Bigi (2005)). From our e-flood measurement campaigns, we find that gravimetric sampling does not always capture the maximum SSCs (see Sec. 5.5.2). Therefore, it is highly possible that past Spöl e-flood campaigns did, in fact, exceed the 5 gL^{-1} recommendation. Our system measured SSC pulsations above 5 gL^{-1} (lasting 3 hours) and above 8 gL^{-1} for at least 30 minutes, in both 2021 and 2023. The importance of high-frequency monitoring to ensure that managers are not exceeding environmental SSC limits cannot be understated.

The SSC profiles we report in Figure 5.4 are those typical for full drawdown flushing. One possibility to mitigate these high SSCs would be to combine partial reservoir emptying (CSFOs as shown by Cattanéo et al. (2021)) with high spatio-temporal instream SSC measurements. Cattanéo et al. (2021) were able to better control the SSCs below the dam and reduce their impact on fish communities, giving an average SSC of 3.47 gL^{-1} during the 10 days of flushing with peak concentrations between 10–15 gL^{-1} for 3 h 50 min. As the goal of e-floods is to improve the ecology of impacted waterways by rearranging bed sediments, CSFOs should be seriously considered as an alternative to full drawdown flushing which we have seen deliver high quantities of suspended sediments previously stored in the bed, floodplain, or reservoir.

Fine sediments also have multiple and often interacting impacts on macroinvertebrates, such as reducing habitat diversity by clogging, siltation, or enhancing toxic substances (e.g., the toxic PBC spill in the Spöl), with cascading consequences on food availability and food quality, or even food web changes (Jones et al., 2012; Consoli et al., 2023). They have also been shown to invert the expected summer-winter macroinvertebrate abundances downstream of dam water intakes that are flushed to remove accumulated sediments, often daily (Gabbud et al., 2019). Macroinvertebrates may also be directly affected by clogging or abrasion of the gills depending on species-specific behaviour (McKenzie et al., 2020). Thus, flow releases are intended to restore ecological dynamics and enhance physical streambed conditions (Robinson et al., 2018; Consoli et al., 2023; Crosa et al., 2010), taking into account a short-term reduction of macroinvertebrate density and diversity. In the Spöl the SSC peaks of the e-flood were closely followed by invertebrate drift peaks (Consoli et al., 2022). But re-establishing habitat diversity on a small scale is important for Alpine biodiversity that relies on habitat heterogeneity and its dynamics (Leitner et al., 2023; Robinson et al., 2023; Martini and Waringer, 2021). These restructured habitats, in fact, allow macroinvertebrates to recover relatively quickly after flushing operations (Crosa et al., 2010; Espa et al., 2019; Folegot et al., 2021; Consoli et al., 2022). In the Spöl, e-floods have been shown to affect the community composition and temporal productivity by reducing the abundance of very dominant species like the Amphipod (*Gammarus fossarum*) and allow a more alpine-like community (higher fraction of Ephemeroptera, Plecoptera, and Trichoptera) to recolonize this impacted river stretch (Robinson et al., 2003, 2004,

2023; Consoli et al., 2023).

However, as we show by our high spatio-temporal resolution sensing the amount of sediment delivered is much larger than originally anticipated. These higher peaks and longer exposures of fine sediments are also expected to a have higher impact on taxa abundances and also cause long-term alterations of the functional community composition (Jones et al., 2012; Folegot et al., 2021). On the one hand, the e-floods restructure habitat patches physically but also reshuffle the community as a large fraction of invertebrates is directly affected by the high SSC enhancing their drift. Thus, new habitat patches with reduced competition are quickly recolonized after the e-flood by each taxa according to their drift resistance, dispersal potential, and life-cycle strategy (Robinson et al., 2023; Buendia et al., 2013; Stubbington, 2012). In this sense, a flightless Amphipod species (e.g. *Gammarus fossarum* in the Spöl) will have a slower recolonization and recovery than taxa that emerge and can fly upstream. But these dominant taxa are known to have a significant negative effect on biodiversity and ecosystem functions especially in river sections downstream of dams, where the lack of patch dynamics favors their growing densities (Little and Altermatt, 2018; Consoli et al., 2022). On the other hand, taxa that emerge, often at around the same time, and have a flying adult stage have a quick and long dispersal potential or even avoid the high SSC of the e-flood while mating outside the water. Another way to avoid drift during e-floods is to find refuge from high SSCs in the hyporheic zone, a possibility for small specimens or juveniles of taxa with multiple flying phases which complete the first life cycle before the e-flood (e.g. *Baetis* sp., some Chironomidae or Simulidae species) (Folegot et al., 2021; Stubbington, 2012; Weigelhofer and Waringer, 2003). Such taxa even showed high-density peaks in specific years from the start of the e-floods (Robinson et al., 2023). E-floods coupled with a better understanding of sediment input, would also allow for more species-orientated patch dynamics crucial for many alpine taxa (Consoli et al., 2022).

In addition, most final larval stages, nymphs ready to emerge, are more prone to drift as they face higher shear stress, higher drag coefficient and higher exposition to SSCs, due to their larger size (Waringer, 1993; Waringer et al., 2022). In this case, habitat patches created by the e-flood are attractive for alpine taxa from other nearby rivers and tributaries, given the network topology and dispersal distances (Consoli et al., 2022; Alther and Altermatt, 2018; Tonkin et al., 2018). However, lethal e-flood disturbances would not allow these taxa to sustain a whole life cycle in this river sections. The affected habitat patches could represent a sink, or even a so-called, ecological trap. As a lot of invertebrates are attracted by this river section while they readily get flushed down and therefore, lost to the network. A higher temporal and spatial resolution of sediment loads can help managers to better time e-floods, and time water intake flushing (Gabbud et al., 2019), according to the life-cycle and specific needs of keystone species.

5.5.4 Downstream Implications of Sediment Management Practices

The many possible benefits of e-floods to the Inn have been highlighted by Robinson et al. (2023) and in Section 5.5.3. However, as the amount of fine sediment delivered by the Spöl to the Inn during these single-day events is around 0.76–1.14% of the total annual load, before making recommendations to implement such floods in a watershed, it is necessary to investigate the watershed as a whole. On the Colorado river, the e-floods terminate in Lake Mead however, the Spöl feeds into the Inn and the Inn crosses into Austria only 36.6 *km* after the confluence. It is necessary to understand how these e-floods affect the Inn

and if these floods are simply shifting a problem downstream, potentially to our neighbors.

Figure 5.5 shows a proof-of-concept first-order analysis of the e-flood's propagation (solving the advection equation in 1D under steady-state – see Sec. 5.3.5). Here, we show the stream distance (L - in km from the confluence) that is necessary for the suspended solids to settle and for the Inn concentration to recede back to its pre-e-flood levels (Inn levels upstream of the confluence). The settling distances were solved for different Ψ ratios (Q_{Spl}/Q_{Inn}) and Spöl concentrations (2, 4, 8, 12, 20, and 30 gL^{-1}).

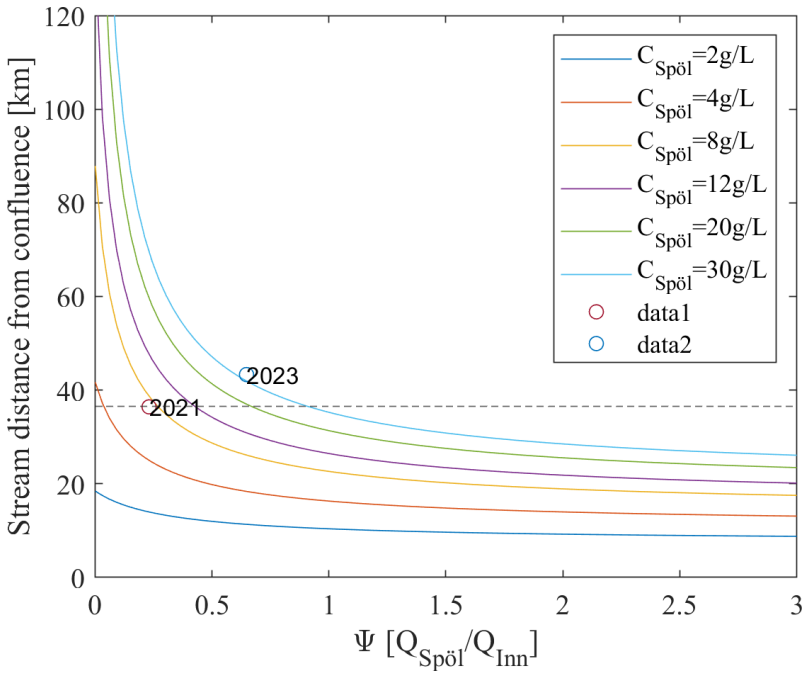

Figure 5.5: Sediment settling distance along the Inn for various combinations of Inn and Spöl discharges (called the Ψ ratio here). The lines represent different initial conditions of the Spöl concentration. The two floods in 2021 and 2023 are plotted as circles. The dotted line represents the Austrian border (36.6 km downstream of the confluence).

From Figure 5.5, it is clear that when the peak discharge of the Spöl is high relative to the discharge of the Inn ($\Psi > 1$) and when the concentration on the Spöl is less than 30 gL^{-1}, then the e-flood wave will settle before 36.6 km. If $\Psi = 1$, then the concentration of the Spöl must be equal to or less than $\sim$ 30 gL^{-1} for the e-flood wave to settle before 36.6 km. And if $\Psi<1$, then any Spöl concentration greater than 30 gL^{-1} will propagate further than 36.6 km.

Along with solving for L with the various Spöl peak e-flood concentrations, we have also included the two floods in 2021 and 2023 in Figure 5.5, which had maximum Spöl concentrations of 12.0 gL^{-1} (2021) and 10.8 gL^{-1} (2023) (from Section 5.4). The Inn concentrations, c_{Inn}, from the campaigns were also used (from Section 5.3.2 they are 0.7 gL^{-1} and 0.14 gL^{-1} for 2021 and 2023, respectively), and the Inn discharges taken downstream at the Tarasp-Scuol station (in the 24h before the flood) for 2021 and 2023 are 112 m^3s^{-1} and 40 m^3s^{-1}, respectively. It should be noted that the solution in Figure 5.5 is steady-state and the solution is for the maximum observed c_{Spl} and maximum e-flood Spöl discharge, so this represents a worst-case scenario.

In 2021 the discharge of the Spöl was 25.9 m^3s^{-1} and the discharge of the Inn was relatively high at 112 m^3s^{-1}, giving a low Ψ. Additionally, the maximum concentration of the Spöl was 12.0 gL^{-1} and the concentration of the Inn was 0.7 gL^{-1}. This meant that at 36.4 km downstream of the Spöl–Inn confluence, all of the fine sediment was predicted to settle. However, in 2023 because of the warm Winter and lack of snow cover, the discharge of the Inn was only 40 m^3s^{-1} with a much lower concentration of 0.14 gL^{-1}. The discharge of the Spöl remained at 25.9 m^3s^{-1} and the maximum concentration of the Spöl was 10.8 gL^{-1}. Under these conditions, the e-flood propagated to 43.3 km (the distance L where the Inn concentration returns to its pre-flood value) and potentially exceeded the Austrian border.

Understanding the various combinations of initial sediment concentrations and Ψ's can help basin managers determine how much water needs to be released in order for the activated suspended sediment (sediment being carried in the e-flood) to settle before international borders or any desired location in the downstream river.

For example, Equation 5.3 was solved for the Spöl dischage (Q_{Spl}) as a function of the Inn discharge (Q_{Inn}) and the Spöl SSC (c_{Spl}), which is plotted in Figure 5.6. Similarly, managers can use this figure to find the maximum allotted Spöl discharge which would ensure that all of the e-flood sediment settles before 36.6 km. For example, if on the morning of the planned e-flood the Q_{Inn} is 100 m^3s^{-1}, then the amount of water released into the Spöl from the reservoir should not exceed 14 m^3s^{-1} (for a c_{Spl} of 15 gL^{-1}) or 32 m^3s^{-1} (for a c_{Spl} of 6 gL^{-1}). This again highlights the importance of monitoring at several locations along the Spöl (and Inn); to know the SSC along the river and take immediate action.

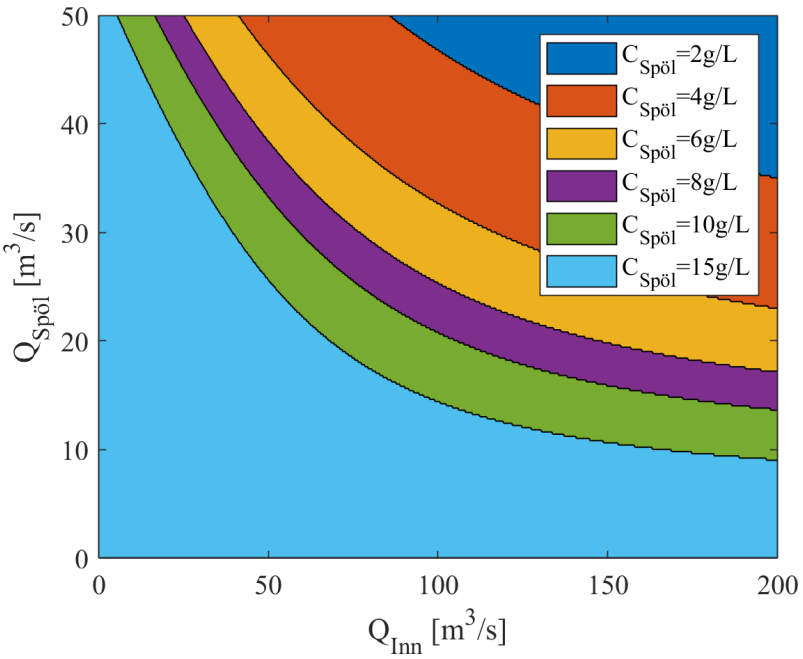

Figure 5.6: Required discharge of the Spöl river for different Inn river discharges for the fine sediment wave to settle before the Austrian border ($L = 36.6km$). The area under each curve represents the acceptable Q_{Spl}–Q_{Inn} combinations for various Spöl concentrations, c_{Spl}.

Although this 1D method is simple to use and to implement for reservoir and natural park managers, it largely ignores many of the complex connections between discharge and sediments and is therefore only used as a proof-of-concept. For example, when using this 1D methodology we assume steady state. Therefore, when we are searching for different Ψs (and by extension, different Q_{Inn}'s), we take the assumption that our selected Inn concentration is steady and doesn't change with increasing Inn discharge. In future work, unsteady flood waves should be a) simulated with their b) true channel geometry (e.g. non-constant width and slope) and considering c) multiple grain sizes. We should also d) account for hydraulic infrastructure which can stop fine sediment (e.g. at the Pradella hydropower plant).

5.6 Conclusions

This study has provided a comprehensive examination of the impacts of e-floods on sediment transport in the Spöl river and its downstream effects on the Inn river, emphasizing the ecological implications of SSC. Through high-resolution, high-spatial measurements, we have uncovered nuanced patterns of sediment pulsations induced by e-floods and their contributions to the annual sediment load to the Inn river. Our findings demonstrate the critical need for advanced monitoring techniques to accurately capture the dynamics of sediment transport and to inform river management practices that aim to mitigate adverse ecological impacts.

Our analysis revealed that high-resolution monitoring of SSC could capture patterns in SSC during e-floods, such as peaks and peak durations, and could also capture the sediment yields and sediment wave propagation along the Spöl and into the Inn. Our method informs when sediment storages are activated, but also lays the groundwork to determine how much sediment is released from the river bed, banks, floodplain, and supplied by released waters. We have also used a relatively simple proof-of-concept 1D model to estimate how far the sediment wave can travel under different combinations of e-flood and receiving river discharges, which we believe useful for river managers. The delivery of fine sediments to downstream sections, particularly in cross-border contexts, necessitates a careful evaluation of the timing, magnitude, and frequency of e-floods to prevent ecological degradation and to comply with environmental standards.

There is a pressing need for the implementation of integrated sediment management strategies that leverage high-resolution data and adaptive management approaches. To this end, we suggest the incorporation of CSFOs more frequently on an annual basis, offering a mechanism to control sediment release and minimize impacts on downstream river sections and aquatic ecosystems. Especially if the goal is to rearrange the downstream bed sediments for aquatic habitat, releasing stored sediments (bed, banks, floodplain, and reservoir) more often and in smaller quantities could be more beneficial than a single, large annual release. Moreover, the establishment of transboundary cooperative frameworks is essential for managing the cross-border implications of sediment transport and ensuring that river management practices are sustainable, equitable, and ecologically sound.

Future research should incorporate unsteady simulations for sediment transport and deposition, incorporating more complex hydrodynamic and sedimentological processes to improve the accuracy of predictions and management decisions. Additionally, long-term monitoring programs are needed to assess the cumulative impacts of e-floods on sediment dynamics,

river morphology, and ecosystem health. Such efforts will require collaboration among scientists, river managers, policymakers, and stakeholders across national boundaries to address the challenges of sediment management in a changing climate and to preserve the ecological integrity of river systems.

In conclusion, this study contributes valuable insights into the sediment transport dynamics induced by e-floods and highlights the critical role of informed, adaptive management in mitigating the ecological impacts of sediment management practices. As we move forward, the integration of scientific knowledge with stakeholder engagement and the exploration of innovative management strategies, such as more frequent CSFOs, will be key to achieving sustainable sediment management and river restoration goals.

Chapter 6 Conclusion

This chapter summarizes the main findings of the presented investigations by providing answers to the research questions (RQ) stated in Chapter 1. For quick reference, the relevant questions are reiterated at the beginning of each subsection. This is followed up by an outlook where possible future research directions for the sensor and network are outlined.

6.1 Summary

6.1.1 Research Objective A: Utilizing Remote Sensing to Obtain High Spatio-Temporal SSC Data

RQ1 Can the new, high-resolution (10m) Sentinel-2 mission be combined with a small network of commercial turbidity sensors to extract SSC data from a relatively narrow river network? Can sediment sources and sinks be identified using the aforementioned sensing methods within a river catchment? Can the fraction of contribution from these sources be quantified? When and how are sediment sources activated by hydroclimatic forcing (e.g. heavy rainfall) or by processes that lead to seasonality, like snowmelt?

Chapter 2 explores the calibration of high-resolution Sentinel-2 satellite imagery with ground-based commercial turbidity sensors to enhance suspended sediment concentration (SSC) data estimates across river networks (Doxaran et al., 2002; DeLuca et al., 2018; Vanhellemont and Ruddick, 2015; Yunus et al., 2020; Kaba et al., 2014), specifically focusing on the Vjosa River in Albania. In this chapter, a workflow was developed to provide such estimates. The application of atmospheric, cloud cover, and deep water corrections to the satellite images were necessary for accurate SSC estimation. The ground truthing and calibration were performed using four turbidity sensors placed along the Vjosa River close to tributaries. A multivariate linear regression model was developed to correlate satellite reflectance with measured turbidity, laying the foundation for estimating river turbidity profiles from satellite observations. The methodology included the validation of satellite-derived turbidity profiles with Lagrangian profiles obtained from two river kayak descents and was further validated by computing and comparing the mean annual suspended sediment yield to previous studies.

The main finding and demonstration of this chapter was that estimating the spatial variability of sediment transport and identifying potential sediment sources and sinks within the river network is possible. The study successfully demonstrated the capacity of combining satellite imagery with in-situ sensor data to offer a comprehensive view of sediment dynamics over time, particularly highlighting the seasonal signal in sediment transport and changes upstream and downstream of tributaries and within river reaches. This work was published in Earth Surface Dynamics (Droujko et al., 2023b).

The results from Chapter 2 significantly contribute to answering RQ2 by demonstrating that high-resolution satellite imagery, when integrated with a small network of ground-based turbidity sensors, can indeed extract valuable SSC data from geomorphologically complex braided river reaches, but not within the narrower upstream river sections where

satellite visibility was limiting (Gardner et al., 2021; Fassoni-Andrade and de Paiva, 2019). This combined method allows for the identification and quantification of sediment sources and sinks within a river catchment that is not attainable through traditional monitoring methods alone, which rely on basin-integrated analysis informed by a single sensor at a catchment outlet. The fraction of the contribution from these sources could not be quantified because we did not have the streamflow necessary; although we could obtain the difference in SSC from the individual sources and sinks when looking at the delta SSC above and below tributaries and within river reaches, translating these concentrations into yields would require the river discharges. Our method also allowed for the identification of seasonal patterns in the catchment fine sediment dynamics, showing the highest mean turbidity in the winter along the entire length of the river but the activation of catchment sediment sources by short-term hydroclimatic forcing would require many instances of good (cloud-free) imagery shortly before, during, and after a heavy rainfall event and flood. Time will allow us to collect such cases and explore these opportunities.

By validating the satellite-derived turbidity profiles with kayak-based measurements, the study also reaffirmed the reliability of remote sensing techniques in capturing the nuances of sediment transport in natural river systems. This research paves the way for a broader application of satellite imagery in environmental monitoring, offering a scalable, cost-effective solution for comprehensive sediment analysis across extensive river basins. The success of this approach in the Vjosa River case study highlights its potential for global application, particularly in regions where ground-based monitoring is challenging or resource-constrained, thus answering the critical need for enhanced SSC estimation methods in riverine research and management. Future work should combine this method with physical modeling of SSC and also integrating online data-provision and analysis tools, such as Google Earth Engine, to enhance the efficiency of the workflow.

6.1.2 Research Objective B: Development of My Own Open-Source, and Low-Cost Turbidity Sensor

RQ2 Can a new highly accurate device for turbidity or SSC monitoring in rivers be developed at a low cost? Can this device overcome problems with traditional sensors (expensive, point-based, low accuracy) and offer benefits such as easy deployability, mobility, and end-to-end integration for the user?

Chapter 3 is the main technology development part of this dissertation. It focuses on the development and evaluation of a new, highly accurate, low-cost device for turbidity and SSC monitoring in rivers. This initiative was driven by the necessity for a more accessible and financially viable option for extensive sediment monitoring across river networks (Bennett et al., 2014, 2013; Lane et al., 2017; Bakker et al., 2018; Battista et al., 2020b; Molnar et al., 2006). Our methodology was built upon previous research in open-source and low-cost turbidity sensing (Gillett and Marchiori, 2019; Trevathan et al., 2020; Lambrou et al., 2014; Wang et al., 2018b; Kelley et al., 2014) and involved designing a device capable of detecting scattered light from an LED source, using two detectors within a controlled volume of water. The sensor's performance was rigorously tested by creating 8 replicates of the sensor with different detection angles, lenses, filters, etc. These replicates were tested against various commercial turbidity probes in a controlled mixing tank experiment, which utilized two different sediment types across a broad range of concentrations typically observed in riverine environments. This work was published in Scientific Reports (Droujko and Molnar, 2022).

The results of these experiments demonstrated that the new sensor costing 62 CHF achieved precise and reproducible turbidity measurements within the 0–4000 NTU range, and also directly measured SSC up to 16 gL^{-1} without necessitating calibration to Formazin. This was achieved by careful selection of optical components (lenses, LED, detectors) and design of the optical system (angles and distances between components). This capability marked a significant advancement and was a necessary first step (before addressing data storage, battery power, etc., which were addressed later in RQ4), making the sensor not only a cost-effective alternative to existing monitoring equipment but also enhancing its utility by simplifying the data collection process. By bypassing the need for traditional calibration methods, the sensor could be readily deployed for distributed sensing tasks, providing detailed insights into sediment dynamics across various parts of a river system.

Addressing RQ3, the findings from Chapter 3 illustrate that it is indeed possible to develop a turbidity and SSC monitoring device at a low cost that is just as accurate as commercial alternatives. The sensor's design and functionality overcome several limitations associated with traditional sensors, such as low SSC measurement range, point-based monitoring constraints, and complex calibration requirements. Furthermore, the sensor's affordability and accuracy facilitate its integration into a networked monitoring system, offering a scalable solution for comprehensive sediment analysis. By providing an open-source sensor capable of delivering reliable data across a wide turbidity range, this research significantly contributes to the field of environmental monitoring. It paves the way for an enhanced understanding of sediment transport processes, demonstrating the feasibility of deploying advanced sensing technologies in varied riverine settings to capture the spatial and temporal variability of sediment fluxes effectively.

RQ3 Can this new sensor be designed in a way that it can be built by hobbyists and people with limited programming knowledge? Can this system be deployed in difficult environmental settings (e.g. flood, glacier stream), and do its technological requirements (e.g. power, connectivity) enable such measurements?

Chapter 4 further refines the open-source, low-cost sensor from Chapter 3, which focused mainly on the basic design of the optics, and creates the Ötz-T. This second development version of the sensor uses the same previous optical scatter design (an 850 nm LED light source and two infrared detectors) to accurately measure turbidity and SSC. However, it is slightly more expensive, at $\sim$ 200€ per unit, enabling it to be deployed for long-term environmental monitoring. This higher cost still compares very favourably against similar commercial turbidity sensors priced upwards of 3000€, offering a feasible solution for widespread deployment across river networks. This sensor represents a significant leap forward in making environmental monitoring technology accessible to a wider audience, including researchers, environmental managers, and citizen scientists (Droujko and Molnar, 2023; Eidam et al., 2022; Langhorst et al., 2023).

The methodological backbone of this project involved the sensor's open-source design, constructing 3D printed parts and utilizing an Arduino MKRWAN 1310 and coding framework. This allows for customization and easy replication by individuals without access to sophisticated manufacturing facilities or extensive programming knowledge. The Ötz-T also incorporates a temperature and pressure sensor to measure water temperature and stage (proxy for discharge). The sensor was built with a much larger battery and was field-tested during a flood event in September 2022 on the Ötztal Ache in Tirol, Austria. As this river is a glacial stream, this test was done to evaluate its performance in challenging

environmental conditions (low water temperature, possible snow and ice, high turbidity fluctuations and bedload transport, etc.) and the Ötz-T was indeed technologically capable of taking measurements under such conditions. This work was published in HardwareX (Droujko et al., 2023a).

Addressing RQ4, Chapter 4 provides the technical drawings, material lists, and all the details necessary to make your own Ötz-T sensor, and provides evidence of the viability of deploying this innovative system in mountain streams. The successful field test during a flood event demonstrates the sensor's robustness, accuracy, and utility in capturing the dynamics of sediment transport in real time. By providing high-resolution data on turbidity and SSC, the sensor enables a detailed analysis of sediment fluxes, contributing to a better understanding of sedimentary processes in fluvial systems. Furthermore, the sensor's open-source nature and low cost facilitate the expansion of monitoring networks, allowing for comprehensive coverage of river systems and the identification of critical sediment sources and sinks by deploying the sensors upstream and downstream of possible sediment sources, for example, tributaries, hillslope erosion areas, agricultural fields, etc.

6.1.3 Research Objective C: Providing Applications

RQ4 How can new, high-resolution sensing inform when and where possible sources of sediment are being activated during an e-flood? How can such sensing better optimize river management practices and better inform stakeholders about the geomorphological and ecological consequences of releasing e-floods under sub-optimal hydroclimatic conditions?

Chapter 5 provides an application of the use of turbidity sensing for floods. In Switzerland, the law requires that hydropower plant operators flushing their infrastructures monitor the turbidity downstream and cease the flushing when a critical value is exceeded. On top of this planned flushing, many dam water intakes in the Swiss Alps are flushed automatically, and the rate at which this happens has increased in recent time due to increased sediment availability from climate change and increased glacial melt (Gabbud et al., 2019; Bakker et al., 2019). This likely increases turbidity in downstream river sections. In Chapter 5, we monitored a planned flood release in the Spöl river over two years 2021 and 2023, and its impacts on the downstream Inn river. Such floods, called "e-floods," play an important role in enhancing river ecological integrity and redistributing bed sediments within river systems altered by hydropower operations (King et al., 2010; Scheurer and Molinari, 2003; Robinson and Uehlinger, 2008; Robinson et al., 2018, 2023). My focus on the e-floods in the Spöl was to understand their effects on sediment transport. The methodology centered on deploying a network of our SSC sensors during these e-flood events to monitor the mobilization and distribution of sediments and the passage of fine sediment waves. This network comprised 4 sensors in 2021 and was expanded to 7 sensors in 2023, strategically placed across the Spöl and Inn rivers to capture a comprehensive view of the sediment dynamics initiated by the e-floods.

The study revealed significant new findings, with the e-floods creating SSC patterns of high amplitude and duration, and pulsations exceeding expectations and established environmental thresholds in certain river reaches but not others. Our sensor network identified when and where sources of sediment were activated, from the river bed, banks, floodplain, and mobilized from the reservoir bed. However, the fraction of SSC contribution from the sources to the Spöl yield has not been established; this sets the stage for further long-term

distributed sensing to answer this question. Analysis of the sediment load delivered by the Spöl to the Inn during these events provided crucial insights into the effectiveness of e-floods in redistributing sediment and highlighted the need for careful management to avoid adverse downstream effects. A relatively simple 1D steady-state analysis revealed that the sediment waves' travel distance and settling patterns can be optimized using different combinations of e-flood and receiving river discharges. The potential for sediment waves to propagate beyond national borders highlights the importance of cross-border environmental cooperation and planning. This work is in preparation to be submitted.

Addressing RQ5, the deployment of the high-resolution sensor network in Chapter 5 enhanced the understanding of e-floods' impact on sediment dynamics and also showed the benefit of distributed sensing; enabling SSC monitoring in multiple reaches to make better and more informed decisions. This technological advancement and the data collected allowed for a detailed examination of the sediment wave's behavior, elevating the importance of considering the interactions between e-floods and existing river discharge conditions to mitigate potential siltation and ecological impacts downstream, for example on fish.

This chapter's findings illustrated how advanced sensing technology can inform the management of sediment in rivers affected by hydropower operations. The research demonstrates how a high-resolution sensing system can play a pivotal role in quantifying sediment transport processes. This approach not only aids in understanding the immediate effects of e-floods but also provides a foundation for developing strategies to enhance river health and resilience in the face of anthropogenic alterations.

6.2 Outlook

This dissertation's findings underscore the potential of integrating low-cost, high-resolution sensors into a sensor network to enhance our understanding of sediment dynamics in river systems. The insights from such a network can be further enhanced by leveraging satellite imagery and physically-based modeling. In addition to integrating the sensor into a network, the sensor I have developed in this dissertation has many more implications. It can be used in a classroom setting to educate students about building, calibrating, and deploying their own sensors. It can also be used to challenge students to develop their own research questions and decide where and when to deploy sensors to answer their scientific questions.

The sensor I developed can also be used to answer scientific questions in challenging environmental settings. I have begun to answer such questions during a pilot deployment downstream of the Rhône glacier. This work, outlined in Appendix E, is a qualitative assessment of river turbidity variations over one ablation season in 2023 in a glacial stream. The study explored the contribution of three fine sediment sources to the Rhône River turbidity below the Rhône glacier. Previous research indicates that the first source is the emptying of the bed and bank storages in winter when discharge is minimal (Floriancic et al., 2022), the second is the discharge of snow and ice melt accessing subglacial sediment stores during the ablation season (Delaney et al., 2018b), specifically looking at the Rhône glacier's influence, and the third is hillslope erosion from precipitation in the catchment, mainly on snow-free hillslope surfaces.

The methodology employed in this chapter involved the installation of a refined version of the sensor from Chapter 4 called the GlacierGuard. The sensor was placed downstream of

the Rhône glacier's proglacial lake, capturing data from March to October 2023 to observe changes in turbidity associated with the three fine sediment sources throughout this period. This data was complemented by meteorological and hydrological information from nearby climate stations and by sediment data from the basin outlet, providing a preliminary picture of the environmental conditions influencing fine sediment dynamics.

The results from this study showcased a clear pattern of low turbidity in winter provided by the background sediment evacuation rate from stores, then of turbidity increases during the ablation period, with a notable spike in late August that did not correspond with a significant increase in river discharge. This observation suggested alternative mechanisms of sediment mobilization, potentially involving transient storage and release from the proglacial lake or enhanced sediment availability due to snowmelt. The analysis highlighted the complexity of sediment transport in glacially influenced river systems and pointed to the need for further research into the connection between climatic forcing, glacier dynamics, and river sediment loads.

The findings of Appendix E shed light on the significant but complex role glaciers play as sources of fine sediment in alpine river systems. While the study provided valuable insights into how potential sediment source contributions (such as the role of the ablation season and the subglacial access to sediment stores as channels develop (Delaney et al., 2018b)) can be identified, it also underscored the limitations of deploying a single sensor to fully capture the intricate processes at play. In this sense, this work is a first look that our device can be deployed in difficult environments and collect accurate, high temporal resolution data, and we were able to capture the temporal variability in SSC driven by the development and evolution of a subglacier channel network. Future research, building on this foundation and deploying a sensor network along the glacier-fed river, is needed to quantitatively partition sediment contributions from different sources (Costa et al., 2018a), such as from automatically flushed sediment traps at dam water intakes (Gabbud et al., 2019; Bakker et al., 2019), and to better understand the mechanisms driving sediment mobilization and deposition in glacier-fed rivers.

A final version of the sensor that has been developed by the end of this dissertation is shown in Figure 6.1 and my other (non-academic) contributions to science are listed in Appendix D.

Our latest version, named the HydroHeidi, incorporates several improvements over the GlacierGuard sensor presented in Chapter E. The HydroHeidi is ultra low power, therefore we anticipate that it can be deployed longer than the 6 month deployment of the GlacierGuard in the Rhône (Appendix E). The HydroHeidi can also send data remotely leveraging LoRaWAN and the Swiss-wide Internet of Things (IoT) network from Swisscom. The data we collect is stored and displayed in a simple user interface provided by Akenza IO.

In the future, we plan to further incorporate a conductivity sensor to add to our temperature, pressure, and SSC sensors in the HydroHeidi, and we also plan to not only use LoRaWAN but also leverage remote data transfer through mobile networks (incorporating a GSM module) and through the Iridium satellite network. This type of data network is necessary, especially in areas where there is no established country-wide IoT network. For example, a team at the University of Lausanne installed our GlacierGuard sensor in Greenland (Figure 6.2) but summer floods destroyed all monitoring stations. Utilizing Iridium in this region would have enabled us to obtain the recorded data even if the sensors would

Figure 6.1: The latest version of our SSC sensor, the HydroHeidi. The box contains the battery and the LoRa module and the electronic components are inside the PVC tube.

be later lost.

I believe that many users can take advantage of the distributed sensing that I have developed and investigated throughout this dissertation. Firstly, I believe my sensing can support civil engineering companies operating in rivers. Flushing operations in hydropower systems (dams, water intakes) create downstream fine sediment pulses which need to be monitored at high resolution. A similar need may exist for gravel extraction business working within river beds, and other in-river-bed civil engineering operations. My sensing system can also support river restoration projects, as the Swiss government aims to restore 4000 km of rivers (FOEN, Bern, Switzerland, 2012) and the widened river sections will naturally serve as sediment traps. For fine sediment, clogging of interstitial habitat could be a problem. My sensors would allow upstream and downstream monitoring of every restoration project.

River administration authorities could also benefit from my system by enabling the identification of point and diffuse sources of pollution in rivers with fine sediment. For example, by intensive agriculture, mining tailings, and in urban rivers. Combined with a conductivity sensor, my HydroHeidi sensors can measure the change in water ion concentration by chemicals and additives. Therefore, they could be used for monitoring rivers downstream of industrial operations such as textile and paper production facilities, and to monitor excessive loads and emergency situations.

Distributed hydrological-sediment modeling would also benefit from the data support provided by my sensor networks. Fully distributed models have been developed to simulate pathway-based fine sediment transport (Battista et al., 2022; Battista, 2021). However, such models need measurements of SSC at many points along the river network for validation in order to eliminate non-uniqueness. My networks could open up new opportunities for testing models at many nested spatial scales.

Figure 6.2: LEFT: The GlacierGuard installed on a proglacial stream in Greenland. The red arrow shows the installation location. RIGHT: A closer look at the GlacierGuard sensor installed on a bridge along a Greenland proglacial stream (Image by Ian Delaney).

Future research should focus on expanding the deployment of these sensors across more diverse and challenging environments, further refining the technology based on field feedback, and exploring the integration of this data with advanced analytical methods to unlock deeper insights into sediment transport processes. Collaboration with the citizen science community should continue, leveraging improved sensor technology to engage a broader audience in environmental monitoring and conservation efforts.

The journey from identifying the limitations of existing turbidity sensors to developing a novel, accurate, and versatile sensing solution embodies the iterative nature of scientific discovery and technological innovation, setting the stage for future advancements in environmental monitoring.

Appendix A Developing an Accessible Turbidity Sensor for Student Education

A.1 Introduction

Engaging students in hands-on learning experiences is a powerful tool in student education. In recent years, it has gained prominence, particularly in environmental education where active participation of students can significantly enhance their understanding of ecological systems (Droujko and Molnar, 2023). Successful initiatives like environmental field trips and expeditions exemplify the potential of student education to foster experiential learning, especially to gather data on rivers in their local communities (Droujko et al., 2021).

In the realm of environmental science education, understanding water quality is of paramount importance. Rivers, lakes, and other freshwater systems are vital to ecosystems, industry, transportation, and agriculture (Arrigo et al., 2008; Terhaar et al., 2021; McLaughlin et al., 2003; Gregor, 1970; Nixon et al., 1996; Sanders et al., 2014; Ludwig et al., 1996; Descloux et al., 2013). They are also sensitive indicators of environmental changes and pollution (Nixon et al., 1996; Bernard et al., 2011; Acquavita et al., 2021). Traditional teaching approaches, while effective, can be limited in their ability to provide students with hands-on experiences and real-world applications. Here, experiential or lab-based education offers a promising alternative, potentially enabling broader engagement with environmental concepts and issues.

However, the effectiveness of student education in environmental monitoring hinges on the availability of appropriate tools that are both accessible to students and capable of producing reliable data. This brings us to the core investigation of this work: assessing the viability of using simple, low-cost turbidity sensors, similar to those in household appliances like dishwashers and washing machines, in an educational context. Specifically, we aim to determine whether these attenuation-style turbidity sensors can provide accurate data along with the high spatial and temporal resolution necessary for effective student learning. This exploration was one of the foundations for designing my own sensor in Chapters 3 and 4.

Addressing this question involves several key considerations: the ease of use and assembly of these sensors, the accuracy and reliability of the data they collect, and their suitability for use by students in diverse educational settings. The potential of such tools to democratize data collection, empowering students to actively participate in monitoring and understanding their local environment, is immense. This work, therefore, delves into the development, calibration, and field-testing of these turbidity sensors, evaluating their efficacy as tools for student-led environmental education.

A.2 Methodology

A.2.1 Building the Classroom Turbidity Sensor

A turbidity sensor designed for classroom assembly must be simple to construct, have an uncomplicated calibration process, and be capable of collecting good-quality data. The

importance of data quality extends beyond monitoring objectives; it allows students to engage with and understand the data, fostering an inherent motivation to continue data collection, and to engage with issues of the appropriate sampling rate related to process variability.

To meet these requirements, we chose to base our system on the senseBox, a microcontroller (MCU) developed for digital education and citizen science. The senseBox is already integrated into the Project Work of the BSc Environmental Engineering curriculum at ETH Zürich, making it a natural fit for our turbidity sensor.

Our turbidity sensor is composed of two DF Robot turbidity probes (DFRobot, 2024) housed in a tubular PVC casing with a cork top. It logs data onto the senseBox SD bee and is programmed using the Arduino framework. The sensor's design and a photograph of the completed assembly are illustrated in Figure A.1.

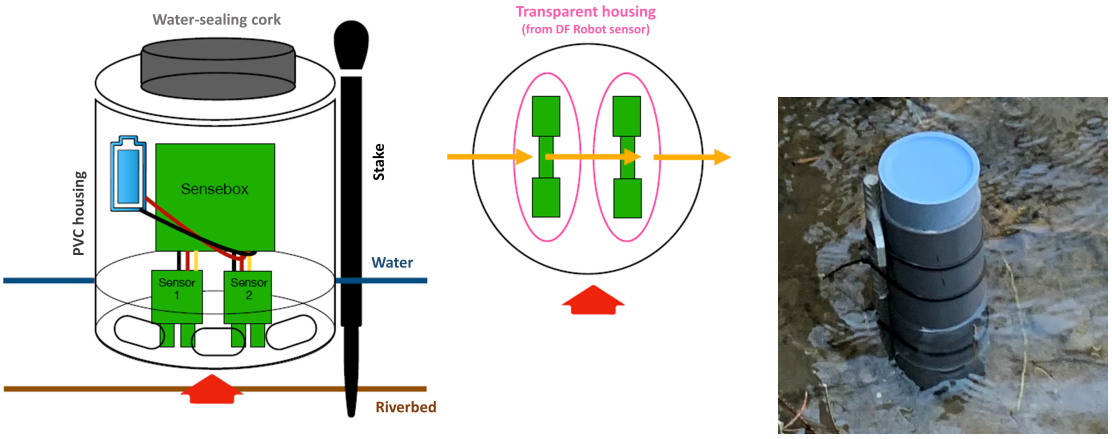

Figure A.1: The simple turbidity sensor. LEFT: The outline of the sensor, which contains the senseBox and batteries that are inside of a homemade PVC housing. The housing was closed with a big cork. The DFRobot analog probes are in a transparent housing that was glued to the PVC housing. This was done so that the turbidity probes can be directly connected to the senseBox while staying dry and still taking measurements through the small DF Robot transparent housings. RIGHT: the simple turbidity sensor installed in the Holderbach on ETH Hönggerberg campus.

The components selected for this sensor were chosen for their ease of understanding, availability, and user-friendly documentation and support. The complete list of components is detailed in Table A.1, all of which are readily available off-the-shelf. The senseBox SD bee is mounted onto the senseBox microcontroller, as depicted in Figure A.2, and the Analog-to-Digital Converter (ADC) from Adafruit, called the ADS1115, is connected through an i2C protocol to one of the digital connecting ports. The DF Robot probes are then linked to the ADS1115 (Fig. A.2). We opted to embed the transparent housing of the DF Robot probe directly into the PVC tube, allowing for a direct connection between the microcontroller and the probe, enabling underwater measurements. Additionally, redundancy is provided by connecting two DF Robot probes, which also allows the user to address measurement repeatability and error.

The sensor's operational codes are accessible in our Github repository (rivertechlabs, 2022).

Table A.1: List of components and their prices for one sensor (online prices from February 2024)

Item name	**Cost per item [CHF]**	**Quantity**
DF Robot Turbidity sensor	8.57	2
Adafruit ADS1115 16BIT ADC	12.41	2
senseBox MCU	42.24	1
SD bee	14.08	1
Illumination & UV Radiation sensor	18.77	1
3.7V Li-Ion Rechargeable battery pack 7.8Ah	34.90	1
Total cost [CHF]	151.95	

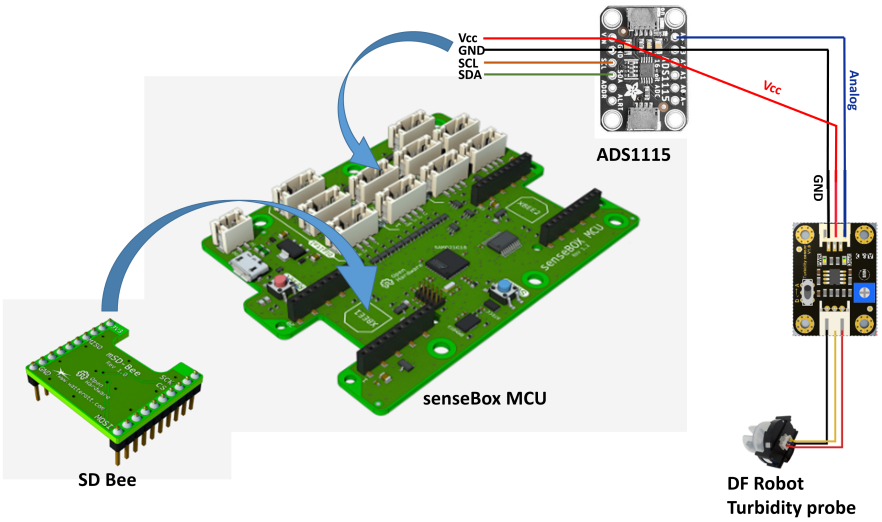

Figure A.2: Depiction of how the components are connected together inside the PVC housing. The SD bee is stacked onto the senseBox MCU. The DF Robot probe is connected to the ADC (ADS1115) which is then connected to the senseBox i2C connector. Our sensor setup uses two of these probes and ADCs.

We offer two distinct codes for student usage: one for basic sensor operation, including data logging onto the SD card, and another for taking turbidity measurements. Students are encouraged to merge these codes before uploading the final version onto the sensor, typically completed prior to deployment. To use the sensor, the final code is flashed onto the sensor. Before initiating a measurement or installing the sensor, the battery is connected, and the device is sealed with the cork.

A.2.2 Calibrating with Safe Materials

Before the sensor's final installation, it is crucial to educate users about calibration and its significance in environmental sensing. As described in Section 1.2.2, the DF Robot probes operate on the principle of light attenuation; more turbid water results in less light reaching the detector. These probes read the attenuated analog signal in voltage, starting at 3.7V in clear water and decreasing voltage as turbidity increases. When connected to the ADC, this voltage signal is converted into a digital number ranging from 0 to 65,536 (utilizing 16-bit ADCs). These digital numbers are then calibrated to units of turbidity (NTU).

The calibration of turbidity sensors to NTUs is ideally done with a liquid of known NTU. Formazine (formazin) is a heterocyclic polymer with uniform particle size used for this purpose, it is diluted with ultrapure water, to produce a liquid with known NTU, in which sensors are placed. Given the focus on student education and the hazardous nature of formazin, a known carcinogen, we opted for a safer calibration method using soy milk dilutions. This process was facilitated with an Observator Analite NEP-5000-LINK handheld sensor (Observator, 2024), with which we obtained an independent measurement of NTU. After preparing the dilutions, measurements were conducted using both the Observator instrument and the DF Robot probes, as demonstrated in Figure A.3a (each sensor took one measurement for every dilution). A second order polynomial was then fitted to the data (Fig. A.3b) and added to the sensor code (rivertechlabs, 2022). Once the calibration is done for both DF Robot probes, both calibration equations can be uploaded to the Arduino code so the sensor outputs two NTU measurements: one from each DF Robot probe.

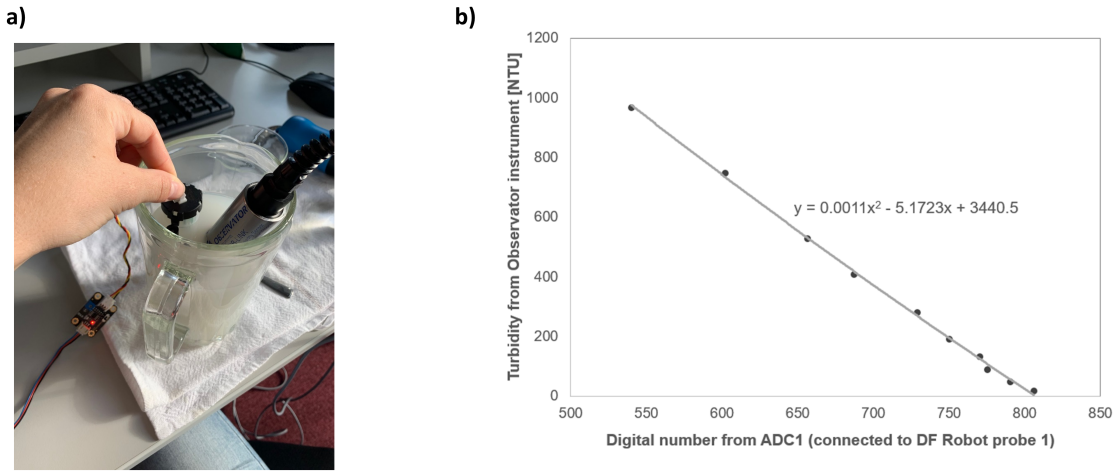

Figure A.3: Demonstration of how the probes were calibrated. a) Here we show a container of soy-water dilution. The Observator instrument and the DF robot probe are both measuring during calibration. b) Turbidity as measured by the Observator instrument as a function of the digital number output by the ADC connected to the DF Robot probe 1. The second order polynomial fitted to the data is shown on the figure.

A.2.3 Student-Led Field Testing of Turbidity Sensors

Two field campaigns were undertaken by the students to test their assembled turbidity sensors. The first campaign involved installing the sensor in Holderbach, a creek adjacent to the ETH Zürich Hönggerberg campus. From April 9 to May 1, 2021, students monitored turbidity using the sensor at a sampling resolution of ~ 1 measurement per minute. Additionally, a nearby rain gauge provided 10-minute precipitation totals and solar radiation. Figure A.4 captures images of the students during the sensor installation and the final setup in Holderbach.

The second field campaign focused on the Sihl and Limmat rivers, which both flow through Zürich. The Limmat River, originating from Zürich lake and extending for 35 km before joining the Aare River, contrasts with the Sihl, which is a 73km river starting in the moun-

Figure A.4: LEFT: Students installing the simple turbidity sensor in the Holderbach. RIGHT: The installed sensor in the Holderbach.

tains, traversing through a HPP reservoir, lightly populated forested area, and industrial urban areas, before eventually meeting the Limmat in Zürich. In this campaign, measurements were conducted on two separate occasions for each river. The motivation here is that Sihl is often turbid after rainfall events, while the Limmat, flowing out of the large Zürich lake, has very low turbidity. This gives the students a nice example of sediment mixing directly in Zürich. The Sihl River was first measured on May 9, then again on May 11, 2021. Similarly, the Limmat River was measured (upstream of the confluence with the Sihl) on April 18 and once more on May 11, 2021. During each river visit, the students collected data for a minimum duration of 30 minutes. The sampling resolution of the sensor was one measurement every second.

A.3 Results

A.3.1 Turbidity Trends in Holderbach Creek

The Holderbach campaign, conducted from 09.04.2021–01.05.2021, yielded insightful results, as depicted in Figures A.5 and A.6. These figures present data from turbidity probes 1 and 2, alongside solar radiation and nearby precipitation measurements. A key observation from the lower panels of Fig. A.5–A.6 is the impact of solar radiation on the turbidity readings. The middle panels indicate a few rainfall events, notably on 11.04.2021–12.04.2021 and 30.04.2021. The top panels reveal the turbidity data, where an apparent offset between probes 1 and 2 can be observed, a discrepancy that appears to increase over time.

A.3.2 Comparing the Sihl and Limmat Rivers

The timeseries of NTU measured by two probes in the Sihl and Limmat rivers are depicted in Figure A.7. A notable observation from this campaign is again the consistent offset between probes 1 and 2, amounting to approximately 150 NTU. During the Sihl River

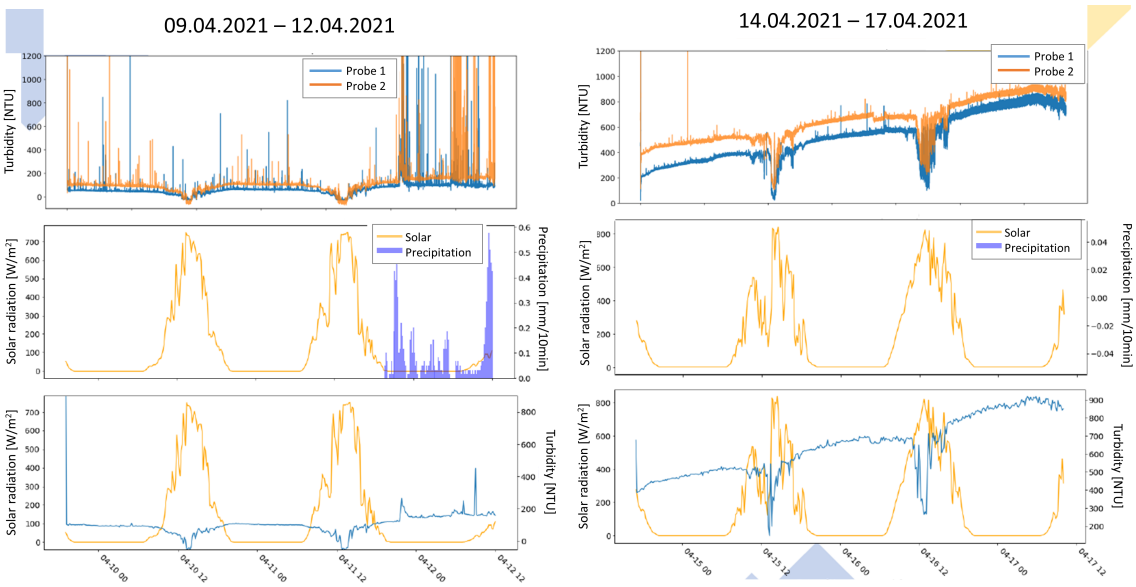

Figure A.5: Results from the Holderbach field campaign from 09.04.2021–12.04.2021 (LEFT) and 14.04.2021–17.04.2021 (RIGHT). The top panel shows the turbidity data from both DF Robot probes with a measurement frequency of ∼1 measurement per minute. The middle panel shows the solar radiation and precipitation in 10 minute totals. The bottom channel shows the solar radiation overlaid with the turbidity data from probe 1, which was resampled at ∼10 minute averages.

measurement on May 9, both probes generally exhibited similar turbidity trends, with a notable exception at 16:25 where probe 1 recorded an increase in turbidity while probe 2 showed a decrease. Interestingly, the turbidity in the Sihl was observed to remain constant on May 11.

In contrast, the Limmat River measurements on April 18 revealed large turbidity fluctuations, especially in probe 1, but relatively steady readings were noted. Similar to the Sihl, constant turbidity was observed in the Limmat on May 11.

A.4 Discussion

A.4.1 Insights from the Field Data Collection

The field data collection informed us about three important features of our simple turbidity probe setup: (a) there is a significant sensitivity to ambient light which needs to be removed; (b) there is a signal related to rainfall, but also large noise-related fluctuations; and (c) there is a bias between the two probes in each sensor, which means that measurements are hardly repeatable.

The Holderbach's turbidity data from 14.04.2021–17.04.2021, showed a consistent increase with notable decreases during daytime. These decreases corresponded with the rise in solar radiation, a pattern also observed from 09.04.2021–12.04.2021. An illuminating experiment conducted by the students, involving the gradual addition of soy milk to a water jar in daylight (Figure A.8), demonstrated that higher turbidity results in less solar radiation

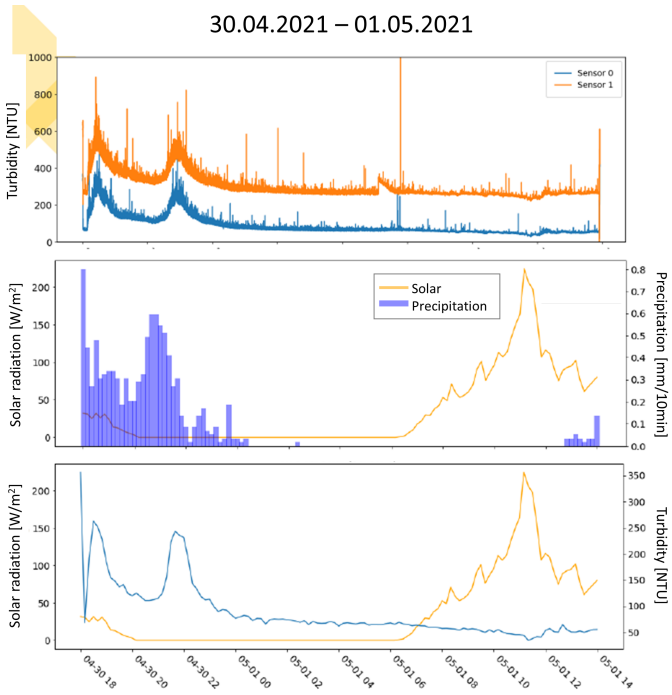

Figure A.6: Results from the Holderbach field campaign from 30.04.2021–01.05.2021. The top panel shows the turbidity data from both DF Robot probes with a measurement frequency of ∼1 measurement per minute. The middle panel shows the solar radiation and precipitation in 10 minute totals. The bottom channel shows the solar radiation overlaid with the turbidity data from probe 1, which was resampled at ∼10 minute averages.

reaching the probe. At approximately 65 NTU, the turbidity absorbs solar radiation (becomes saturated), negating its effect on the readings. Although the students calibrated the sensor as per Section A.2.2, but in dark room conditions, the sunlight effect was not evident in the data from 30.04.2021–01.05.2021, possibly due to higher turbidity levels on those days.

The rainfall events on 11.04.2021–12.04.2021 and 30.04.2021 are distinctly marked in the turbidity data, particularly on 30.04.2021. This observation indicates two key points: firstly, that simple sensors like ours can effectively monitor increased fine sediment concentration in rivers after rainfall events and sediment source lag times in rivers, and secondly, that the Holderbach is influenced by bringing sediment from hillslopes and channel banks into the stream.

In all three rivers, the consistent offset in turbidity readings between probes 1 and 2 was apparent. Given this persistent offset across all results, we infer that these simple sensors may not be suited for measuring absolute turbidity values. Instead, they are more effective in tracking temporal trends and correlations with rainfall and discharge. Therefore, a next step would be to investigate the sensor drift. During the field campaigns, constant turbidity was observed in the Sihl and Limmat rivers, with the exception of a noticeable fluctuation on 09.01.2021, in the Sihl river. Without concurrent solar radiation or precipitation data, it's challenging to ascertain the cause of this variability. Consequently, to obtain meaningful results, these simple sensors should ideally be complemented by other water quality observations, like temperature, conductivity, etc.

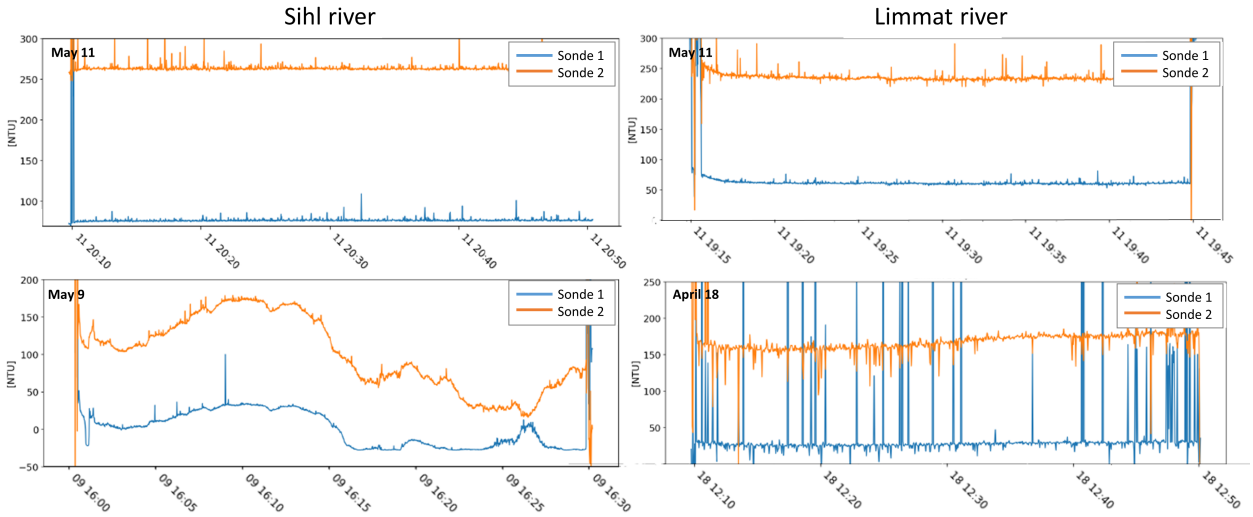

Figure A.7: Turbidity data from the Sihl (LEFT) and Limmat (RIGHT) comparison campaign on three different days for probe 1 (blue) and probe 2 (orange).

A.4.2 Evaluating the Turbidity Probe for Educational Applications

The simple turbidity probe serves as an effective educational tool, particularly in teaching students about environmental sensor calibration. Additionally, the presence of noise in our measurements presents an opportunity to educate students about data cleaning and filtering techniques. The sensor is also useful to educate students on sampling rates for investigation process variability.

Furthermore, our device incurred a cost of 151.95 CHF, though potential cost reductions could be explored, such as substituting the senseBox microcontroller with a more affordable Arduino Uno. The cork used for sealing the sensor, while not ideal for waterproofing, suffices for short-term data collection typical in educational contexts. However, requiring students to undertake calibration with commercial sensors or use hazardous substances like formazin is impractical, if not impossible. Therefore, delivering pre-calibrated sensors to students would be a more feasible approach for such campaigns, but more expensive.

A.5 Conclusion

This work has explored the use of simple, cost-effective, attenuation-style turbidity sensors in the realm of student education. By assembling, calibrating, and deploying these sensors in diverse river environments, we have gained a better understanding of their capabilities.

Our investigation reveals that while these sensors are invaluable as educational tools and are adept at identifying general trends in environmental data, they do not meet the high standards of accuracy required for precise scientific data collection. The field campaigns conducted at Holderbach and along the Sihl and Limmat rivers have highlighted their limi-

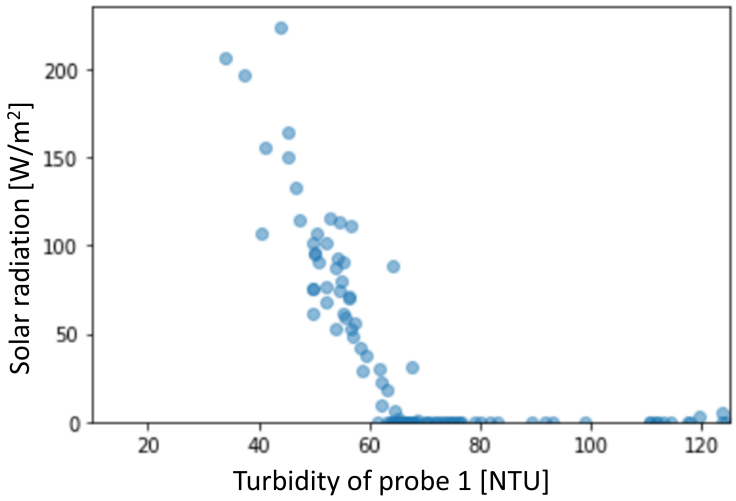

Figure A.8: The effect of solar radiation of the attenuation DF Robot probe readings.

tations in providing consistently accurate readings, especially under varying environmental influences (e.g. influence of daylight on sensor readings).

In the context of scientific data collection, the current version of these sensors requires further refinement. Despite our innovative and safer calibration approach using soy milk, variability in sensor readings and poor repeatability were notable issues. These challenges have formed the foundation of my own sensor development in Chapters 3 and 4, where I aimed to address these shortcomings.

This endeavor to enhance turbidity sensor technology underscores a broader commitment to advancing educational tools. By integrating more sophisticated yet cost-effective components and refining calibration procedures for greater accuracy, I seek to significantly improve the utility and reliability of these sensors. The evolution of this technology is pivotal in empowering student scientists, enabling them to contribute more effectively to environmental monitoring efforts, democratize water data, and deepen our collective understanding of freshwater systems. This transition from identifying the limitations of existing tools to pioneering a novel sensor design encapsulates the iterative nature of scientific inquiry and technological advancement.

Appendix B Nature Water - News & Views

Open-source self-made sensors show high potential in river research

Jessica Droujko & Peter Molnar
Institute of Environmental Engineering, ETH Zurich, Zurich, Switzerland

The adoption of open hardware technology is changing current river research monitoring practices, reducing the need for scientists to allocate large portions of their budgets to expensive instrumentation.

Rivers play a particularly important role in the hydrological cycle, which is affected by the climate crisis leading to an increase of storms, floods, landslides, droughts, and other natural disasters, especially compound events (AghaKouchak et al., 2020). Rivers transport water, nutrients and sediment from land to sea, providing numerous key ecosystem functions. At the same time, rivers are heavily impacted by human activities, with only a few free-flowing large rivers remaining (Grill et al., 2019). Agriculture accelerats sediment input and dams reduce it (Syvitski et al., 2022). Pesticides deteriorate water quality (Maggi et al., 2023), and the impacts of rivers on the global biogeochemical and carbon cycle remain poorly understood (Battin et al., 2023). In these circumstances, it is essential to improve monitoring of water and sediment flows and to explore new measurement opportunities to address emerging challenges.

One attractive opportunity is to complement existing expensive river monitoring stations with long-term data at few locations and with open access self-made sensors that are cheap and can be easily deployed at many locations with a targeted aim. This approach benefits not only scientists in river research, but it also broadly empowers citizen science and education in environmental and ecological topics (Fraisl et al., 2022). We are convinced that such locally collected data may even aid community-led adaptation to systemic climate change risks in general (Oliver et al., 2023), as these data are of immediate relevance to the communities affected by climate crisis.

Now writing in Nature Water, Theodore Langhorst and coauthors (Langhorst et al., 2023) show that obtaining suspended sediment data need not be expensive and can be done using an open-source sensor that can be ordered almost fully assembled, eliminating the complexity of building the devices.

The transfer of sediment from land to sea is crucial for several reasons. Monitoring the sediment flux, specifically the variability in suspended sediment concentrations (SSCs), allows for the understanding of human impacts on sediment production and provides insights into long-term variability due to climate change. Furthermore, turbidity, which accompanies high SSCs, is a standard water quality indicator of pollution. The current practice for continuous high-resolution SSC monitoring is through dedicated in-situ turbidity sensors. However, their high cost inhibits widespread use and limits our understanding of fluvial

geomorphic processes of sediment production and transport.

Langhorst et al. (2023) developed an open-source sensor called the OpenOBS, which is capable of measuring temperature, pressure, and turbidity. It is designed to enable easy assembly by anyone. To test the sensor's capabilities and accuracy, the team conducted two field campaigns along various rivers in Alaska. To evaluate the sensor's ease if assembly, a group of middle school students to build and deploy their own sensors.

For the turbidity measurements, the team utilized a reverse-biased photodiode and transimpedance amplifier, which isvery similar to the design of commercial sensors. Their sensor is built using off-the-shelf PVC tubing for the housing and a 3D printer for thesensor head., The sensor gives a linear response across a wide range of SSCs (< 5g/L). The team also designed a custom printed circuit board that can be ordered pre-assembled, thereby enhancing the accessibility and facilitating assembly of the sensor for the general public.

Langhorst et al. (2023) conducted one of the most extensive testing campaigns for an open-source turbidity sensor. They deployed 19 sensors in three different field campaigns to test the full capability of the OpenOBS. In the first campaign, 10 sensors were installed on 35km of the Sagavanirktok river in Alaska. The authors measured the change in turbidity across three months in the Summer and observed hysteresis loops that are typical in Arctic rivers.

In the second campaign, the authors deployed the sensors in a more "high risk" environment. They equipped three of their sensors with Iridium satellite modules in order to send data remotely and installed these sensors in October 2022 on the Tanana river in Alaska. Typically, scientists hesitate to install expensive sensors in remote areas where they cannot easily visit and service them. Similarly, they are reluctant to install these sensors in locations prone to large flood and debris flow events, heavy sedimentation, or ice, even though such events could provide interesting and valuable data. The authorswere able to measure turbidity until late Fall and observed a sediment wave with their sensors. Afterwards, the sensors froze in place on the river and in the data transmission was halted until May. This campaign perfectly exemplifies the kind of risks scientists can take to obtain interesting measurements once they are not concerned about losing a $5000 piece of equipment.

The last campaign had an educational flavor, and involved 39 middle-school students from Fairbanks and Nenana, Alaska. Together with Langhorst, the students built 16 sensors and deployed six sensors in the Tanana river for one month. Not only were the students able to build these sensors, but they also developed hypotheses about where they thought sediment would be highest along the river and they decided themselves where to install the sensors. This campaign demonstrates how open-hardware makes data collection accessible to a broad range of stakeholders, beyond well-funded universities. Furthermore, it shows how river sensing can be used effectively in education about climate change and other environmental topics (Figure B.1).

The distributed and long-term sensing deployments by Langhorst et al. (2023) demonstrate the practical applications of the OpenOBS sensor. Open-hardware sensors, like the OpenOBS, are capable of delivering long-term and high-quality data under extreme conditions and in remote regions such as the Arctic Sagavanirktok and Tanana rivers. Unlike commercial sensors, the OpenOBS sensor exhibits high accessibility - it can be assembled by middle-school students. The success of the OpenOBS highlights the importance of

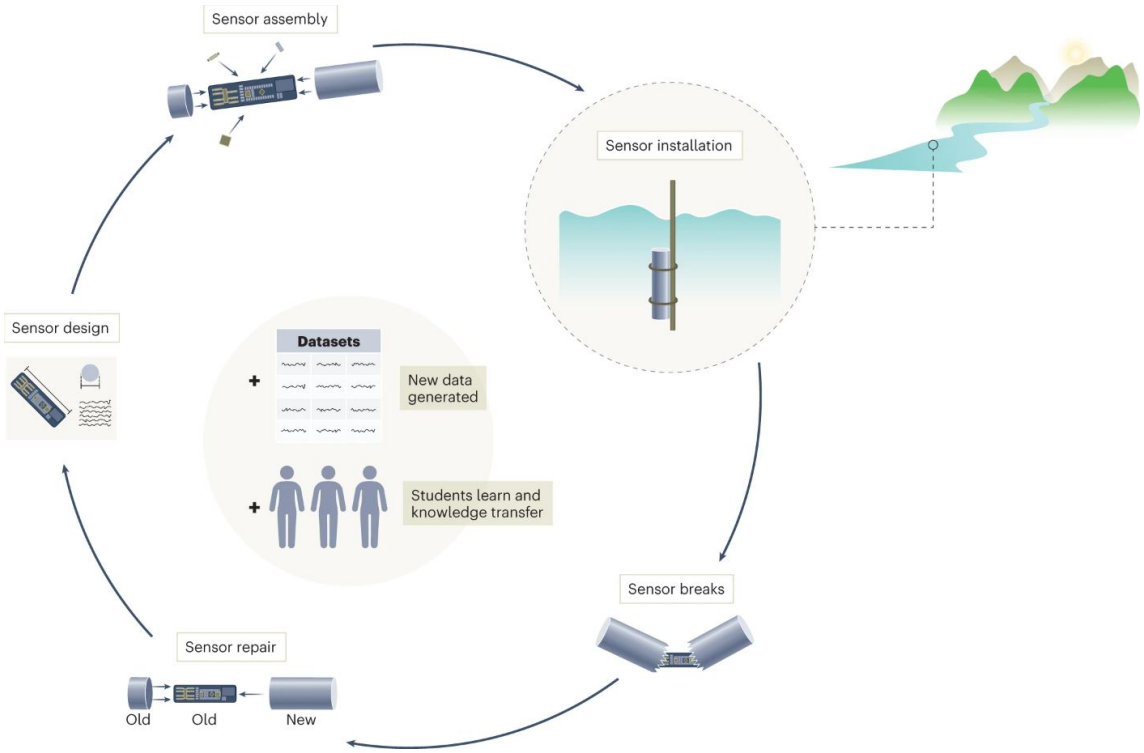

Figure B.1: A sensor is designed, assembled and then deployed along a river. If the sensor is open hardware, then it can be repaired once broken. When the sensor is used by scientists in the field and later repaired (when needed), this information can be used to inform the next generation of designs. The next generation of designs can be made by the same researcher, another researcher in the same group, or another group. Some by-products of this open-hardware cycle are knowledge exchange and creation of new data.

sharing data and sensor designs within the open-hardware community. The contributions of the previous iteration of the OpenOBS (Eidam et al., 2022) and the iterations by other authors (Matos et al., 2019; Trevathan et al., 2020; Kelley et al., 2014) have been crucial to the success of this project. Without these collaborative efforts the OpenOBS would not have achieved its current level of success.

A barrier that slows down the propagation of open-hardware technology is its acceptance in a (measurement) field where long-standing sensor companies have already staked their claim. One way for the authors to overcome this challenge would be to conduct a mixing tank experiment (Droujko and Molnar, 2022) under laboratory conditions, directly comparing their OpenOBS sensor to commercially accepted alternatives.

Appendix C Supplementary Material to Chapter 2

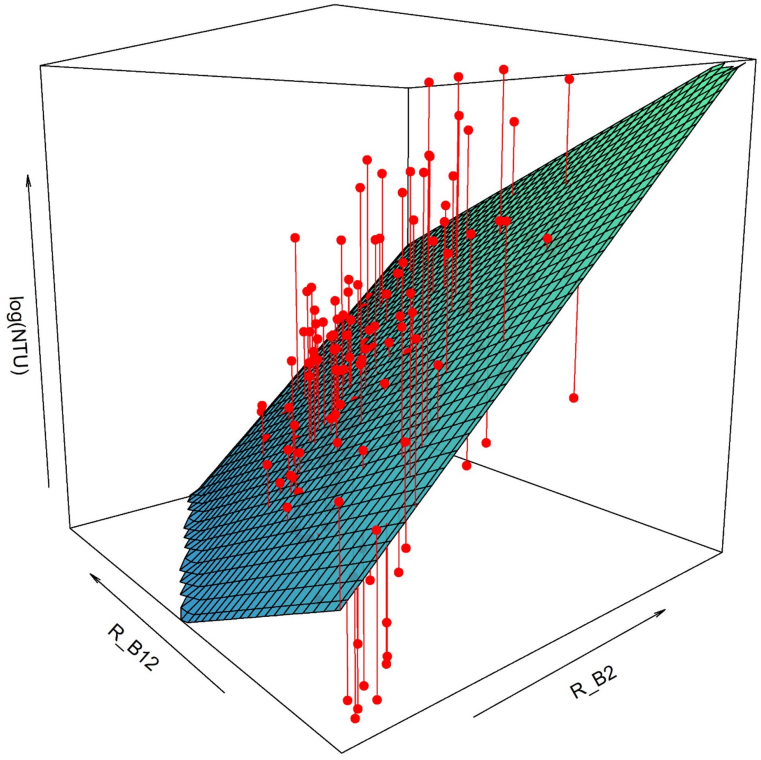

Figure C.1: 3D regression plot of log(Turbidity) vs. reflectance bands for equation (1)

ROI (station number, name)	R_R1 (coastal aerosol)	R_R2 (Blue)	R_R3 (Green)	R_R4 (Red)	R_R5 (Vegetation red edge)	R_R6 (Vegetation red edge)	R_R7 (Vegetation red edge)	R_R8 (NIR)	R_R8A (Vegetation red edge)	R_R11 (SWIR)	R_R12 (SWIR)
5, Pocem	0.83	0.82	0.82	0.8	0.78	0.69	0.69	0.66	0.62	-0.14	-0.19
24, Dragot	0.05	0.27	0.23	0.3	0.22	0.04	0.01	-0.03	-0.11	-0.38	-0.37
31, Lower Aoos	0.51	0.53	0.49	0.54	0.5	0.41	0.39	0.4	0.37	0.06	-0.01
43, Konitsa	0.28	0.45	0.46	0.49	0.43	0.33	0.32	0.32	0.27	0.21	0.21
All	0.33	0.48	0.46	0.45	0.37	0.20	0.18	0.18	0.11	-0.07	-0.09

Table C.1: Correlation values between log(Turbidity) and the different bands of Sentinel-2 for the four stations (ROIs) and for all of the data points together. The correlation values in orange are those that are > 0.4.

Appendix D Supplementary Material to Chapter 3

Supplementary Methods - First Prototype

A first prototype of the sensor was created. The sensor's head, which houses the LED and detectors, was 3D printed and its drawing is shown in Figure D.1 RIGHT. Black filament was chosen to prevent internal reflections within the sensor head. The 3D printed sensor head was attached to a grey PVC tube (Fig. D.1 LEFT) in order to minimize stray ambient light and to hold a larger sample volume of calibration liquid. Attached to the sensor head and grey PVC tube is a prototyping breadboard which held the electronic components; all three are shown in Fig. D.1. All of the CAD files can be found at this project's repository (Droujko, 2021b).

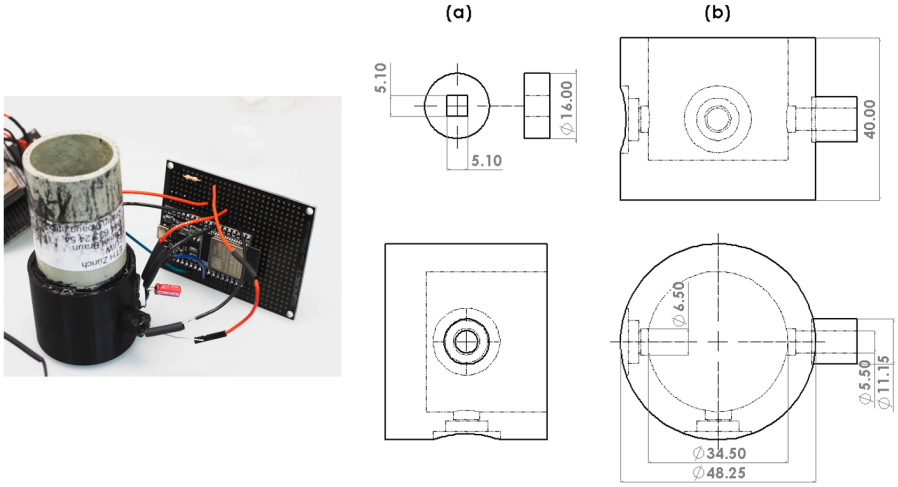

Figure D.1: LEFT: First prototype of the turbidity sensor, RIGHT: drawing of the 3D printed sensing head.

Four different versions of this turbidity sensor were created and are summarized in Table D.1. The first sensor (Sensor 1) is one with detectors at 90° and 180° and flat glass separating/protecting the LED and detectors from the liquid sample. The second sensor (Sensor 2) has detectors again at 90° and 180° but with plano-convex focusing lenses instead of flat glass. These selected focusing lenses are made of H-K1 glass with a 6mm diameter and an 8.873mm focal length. The third sensor (Sensor 3) has detectors at 90° and 135° and again plano-convex lenses. It was also built in a manner to insert/remove long-pass filters. The long-pass filters selected pass everything longer than 750nm, therefore all visible light should not be able to reach the detectors whereas the 850nm LED signal should be able to reach the detectors. Finally, the fourth sensor (Sensor 4) has detectors at 45° and 135° and the same plano-convex lenses.

In order to take a measurement with these sensors, a sample is poured into the grey PVC + 3D printed sensing head (Fig. D.1 LEFT). Since the detectors output a digital frequency, a pulse-counting program was written and uploaded onto the ESP32 to count the pulses and compute the frequency from both detectors simultaneously. This program was based off of

Table D.1: List of sensor versions.

Sensor version	Detector Orientations	Type of lens
1	90°, 180°	no lens
2	90°, 180°	lens
3	90°, 135°	lens + insertable long-pass filters
4	45°, 135°	lens

David Antliff's *frequency_count.h* library and the full code can be found on this project's repository (Droujko, 2021b). The principle behind the pulse-counting program is that it uses one timer to count the number of digital pulses while the second timer simultanuously counts the amount of time elapsed. This then gives one frequency datapoint in hertz. For all of our measurements, we consider one frequency datapoint to be an average of 10 frequency measurements (number of pulses divided by the elapsed time) taken in the span of a few miliseconds.

Formazin calibration

In order to select the version of the sensor that works best for turbidity measurements, three different experiments were run and are summarized in Table D.2. The first experiment, illustrated in Figure D.2, was to see the effect of including the focusing lens in front of the LED and detectors (using Sensors 1 & 2). The second experiment, illustrated in Figure D.3, was to determine which detector orientations relative to the LED gave the best results in the full 0-4000 NTU range (using Sensors 2, 3 & 4). Three detector orientations relative to the LED were tested: 90° and 180°, 90° and 135°, and 45° and 135°. Figure D.4 illustrates the third experiment, which was used to determine the effect of ambient light leakage and whether the long-pass filters could minimize the ambient light interference (using Sensor 3 with & without the long-pass filters).

Table D.2: List of experiments.

Experiment	Sensor name	Lens [Y/N]	Detector orientations	Filters [Y/N]	Ambient light [Y/N]
1	1	N	90°, 180°	N	N
	2	Y	90°, 180°	N	N
	2	Y	90°, 180°	N	N
2	3	Y	90°, 135°	N	N
	4	Y	45°, 135°	N	N
3	3	Y	90°, 135°	N	Y
	3	Y	90°, 135°	Y	Y

Several dilutions of Formazin, a popular calibration liquid for turbidity sensors, were created. The Formazin purchased was rated at 4000 NTU and, using deionized water, dilutions were created: 0, 2, 4, 6, 8, 10, 20, 40, 60, 80, 100, 250, 500, 800, 1000, 2000, and 4000 NTU. This standard calibration liquid was used instead of preparing test solutions using another liquid of unknown NTU and a commercial turbidity sensor to obtain the liquid's NTU value (similar to Gillett and Marchiori (2019)). This was done because often these sensors do not report an accurate value for NTU (Felix, 2017) and therefore report unreliable NTU units. Each Formazin dilution was then poured into the Sensors 1-4 in order to carry out

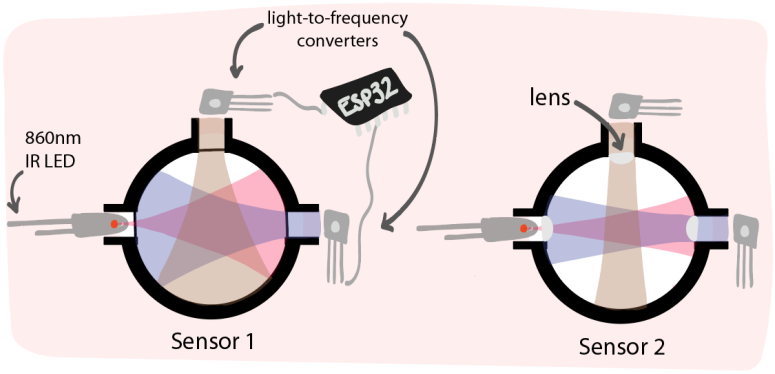

Figure D.2: Lens effect experiment. LEFT: sensor without lenses, RIGHT: sensor with lenses.

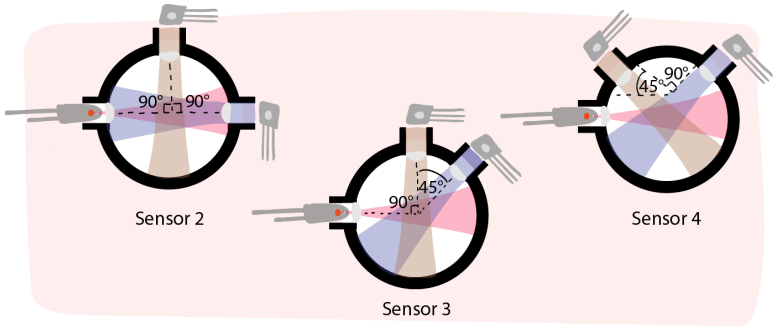

Figure D.3: Detector orientation experiment. LEFT: Sensor 2 with 90° and 180° detectors, MIDDLE: Sensor 3 with 90° and 135° detectors, RIGHT: Sensor 4 with 45° and 135° detectors.

the experiments listed in Table D.2.

To build a sensor which has high dynamic range, common error compensation (due to water, colour, and attenuation), low sensitivity to the bandwidth of the optical source, and high reliability, Postolache et al. (2007) found that a light scattering measurement using the LED and detector(s) should be immediately proceeded by a scattering measurement where the LED is turned off. Matos et al. (2020) found that the LED off-on measurement is necessary since this type of optical device is influenced by external light. With this in mind, 100 frequency data points were recorded at 1Hz for each detector, first with the IR LED off, then again with the IR LED on.

From the 100 datapoints, the mean and standard deviations were calculated for both when the LED was off and on. Then the mean values of the LED-off frequency was subtracted from the mean value of the LED-on frequency in order to create the final frequency values for each detector. This was repeated three times at each NTU dilution and for every experiment.

Effect of adding focusing lenses

Figure D.5 shows the mean and errors (+/- standard deviation) for both the 180^o and 90^o detectors for Sensor 1 (Fig. D.5a) and Sensor 2 (Fig. D.5b) for experiment 1.

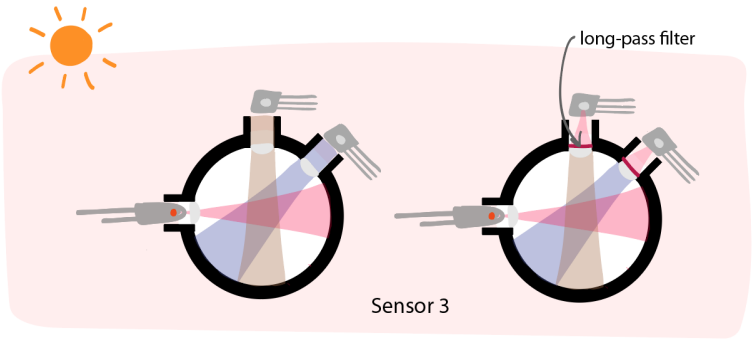

Figure D.4: Ambient light experiment. LEFT: without long-pass filters, RIGHT: with long-pass filters.

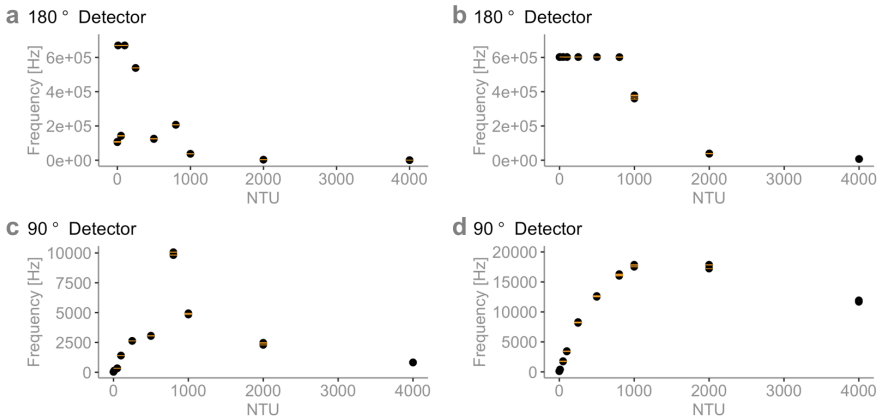

Figure D.5: Quantity of light in hertz [Hz] reaching the detector for each NTU dilution. The mean (black points) and errors (orange bars from +/- standard deviation) for both the 180^o and 90^o detectors for Sensor 1 without lenses (a and c) and Sensor 2 with lenses (b and d). The mean and error were found by subtracting the mean of when the LED was off to the mean of when the LED was on.

Figure D.5 is reporting on the amount of light (in digital frequency) reaching each detector at any given NTU dilution. Here, we would expect smooth curves (Sadar, 1998). In this figure, we see that there is no clear relationship between frequency in the 180^o and 90^o detectors and NTU when there are no lenses. When we include lenses (Fig. D.5b), both the 180^o and 90^o detectors begin to have a clear relationship with NTU (similar to the one found in Figure 11 by Sadar (1998)), however the 180^o detector is cut off at NTUs below 1000 probably because the detector has reached its saturation limit. From these results, it is reasonable to conclude that our sensors require focusing lenses.

Effect of Detector Orientation

Figure D.6 shows the mean and errors (+/- standard deviation) for Sensors 2-4 with 180^o and 90^o detectors (Sensor 2 in Fig. D.6 a and d), 135^o and 90^o detectors (Sensor 3 in Fig. D.6 b and e), and 135^o and 45^o detectors (Sensor 4 in Fig. D.6 c and f) in experiment 2.

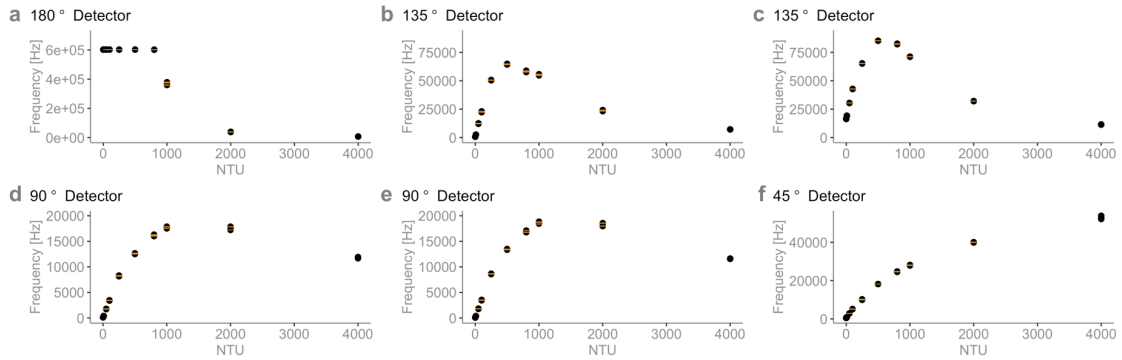

Figure D.6: Quantity of light in hertz [Hz] reaching the detector for each NTU dilution. The mean (black points) and errors (orange bars from +/- standard deviation) for Sensor 2 (a and d: 180^o and 90^o detectors), Sensor 3 (b and e: 135^o and 90^o detectors), and Sensor 4 (c and f: 135^o and 45^o detectors). The mean and error were found by subtracting the mean of when the LED was off to the mean of when the LED was on.

In this figure, we see that there is a clear relationship between the amount of light reaching the detectors (frequency in hertz) and NTU, similar to those reported by Sadar (1998). Figure D.6a again shows that the frequency is cut off below 1000 NTU. Figures D.6 b and c report different maxima from the 135^o detector, this is probably due to a difference in the sensors' construction and shows the importance of calibration when making these homemade sensors. From these results, it is reasonable to conclude that a sensor with detectors at 45^o, 90^o, and/or 135^o would be suitable for our purposes.

Model creation

Several models were created both for experiments 2 and 3. Figure D.7 shows a comparison of four different multivariable models for Sensor 3 (data taken from experiment 2). The models are of the form:

$$NTU = \alpha + (\beta_1 \times d_{90^0}) + (\beta_2 \times d_{135^o}) \tag{D.1}$$

$$NTU = \alpha + (\beta_1 \times d_{90^0}) + (\beta_2 \times d_{135^o}) + (\gamma_1 \times d^2_{90^0}) + (\gamma_2 \times d^2_{135^o}) \tag{D.2}$$

$$NTU = \alpha + (\beta_1 \times d_{90^0}) + (\beta_2 \times d_{135^o}) + (\gamma_1 \times d^2_{90^0}) + (\gamma_2 \times d^2_{135^o}) + (\delta_1 \times d^3_{90^0}) + (\delta_2 \times d^3_{135^o}) \tag{D.3}$$

$$\begin{aligned} NTU = \alpha + (\beta_1 \times d_{90^0}) + (\beta_2 \times d_{135^o}) + (\gamma_1 \times d^2_{90^0}) + (\gamma_2 \times d^2_{135^o}) + (\delta_1 \times d^3_{90^0}) + \\ (\delta_2 \times d^3_{135^o}) + (\eta_1 \times d^4_{90^0}) + (\eta_2 \times d^4_{135^o}) \end{aligned} \tag{D.4}$$

For the full range of data (Fig. D.7a) none of the given models are able to accurately predict NTU, except for the fourth order model which is able to predict down to 250 NTU. However, in Fig. D.7b, we see that it is unable to predict at NTUs lower than 250. In order to calibrate these sensors in the 0-250 NTU range, a separate model needs to be created for this range. The final calibration for this sensor would be a model in the 0-250 NTU range and a fourth order model in the 250-4000 NTU range. Due to the unnecessary complexity

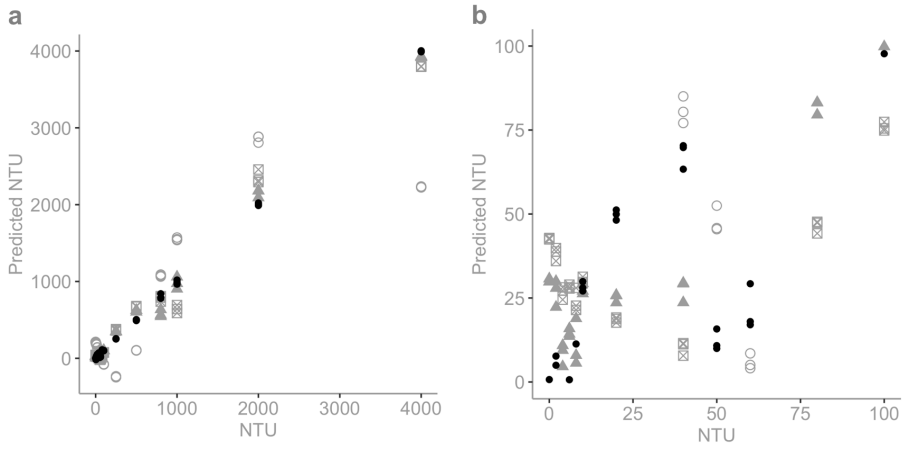

Figure D.7: Comparison of four different multivariable models for Sensor 3: a) 0 to 4000 NTU and b) 0 to 100 NTU. The four different models are on the order of n=1 (equation 1 - grey, hollow circle), n=2 (equation 2 - grey, square with cross), n=3 (equation 3 - grey, solid diamond), and n=4 (equation 4 - black, solid circle).

of the fourth order model, we decided instead to fit the data using the simplest multiple linear regression model in four different ranges (0-10 NTU, 10-100 NTU, 100-1000 NTU, 1000-4000 NTU), as this is often done by commercial turbidity sensors. The model is of the form:

$$NTU = \alpha + (\beta_1 \times d_{90^0}) + (\beta_2 \times d_{135^o}) \tag{D.5}$$

where α is the y-intercept, and β_1 and β_2 are the coefficients associated with the first detector (d_{90^0}) and second detector (d_{135^o}), respectively. The new model for Sensor 3 is shown in Fig. D.8. The same model was also applied to Sensor 4, which is also shown in Fig. D.8 with the model coefficients of both sensors in Table D.3.

Table D.3: Model Coefficients for Sensors 3 and 4.

Sensor	**Range [NTU]**	α	β_1	β_2	R^2	**p-value**
3	0-10	-2.0546316	0.0261069	0.0003605	0.9931	$<$ 2.2e-16
3	10-100	-1.4655810	0.0253945	0.0001387	0.9952	$<$ 2.2e-16
3	100-1000	32.0347677	0.0778393	-0.0090305	0.9981	$<$ 2.2e-16
3	1000-4000	6.773e+03	-2.209e-01	-2.990e-02	0.9978	4.526e-09
4	0-10	-2.222e+00	1.934e-02	-4.128e-04	0.996	$<$ 2.2e-16
4	10-100	-1.150e+01	1.943e-02	-4.556e-05	0.9914	1.453e-14
4	100-1000	49.2023705	0.0436498	-0.0039107	0.9992	$<$ 2.2e-16
4	1000-4000	-7.726e+03	2.129e-01	3.855e-02	0.9928	1.576e-07

Effect of ambient light and long-pass filter

Figure D.9 shows the mean and errors (+/- standard deviation) for Sensor 3 under ambient light conditions both without and with long-pass filters in front of the detectors, for experiment 3.

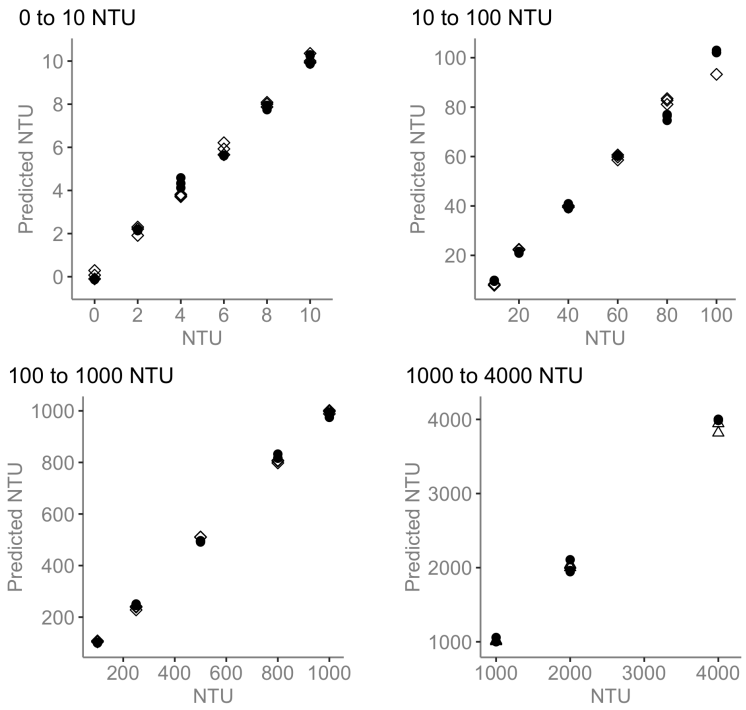

Figure D.8: Model predictions of NTU for Sensor 3 (black point) and Sensor 4 (white diamond) in four different ranges: TOP-LEFT 0-10 NTU; TOP-RIGHT 10-100 NTU; BOTTOM-LEFT 100-1000 NTU; and BOTTOM-RIGHT 1000-4000 NTU.

From this figure, we see that it is very difficult to notice an improvement in the data from the long-pass filters. Figure SD.9 shows a slight decrease in frequency when the long-pass filters are applied, as expected.

Model applied to experiment 3

When applying the same linear model from the previous subsection to the ambient data obtained in experiment 3, we obtain Fig. D.10. In this figure we present Sensor 3 exposed to ambient light with (white circles) and without (black triangle) long-pass filters in the 0-10 NTU range (since this range is the most likely to be affected by ambient light). We see that the off-on differencing measurements seem to be enough to eliminate ambient stray light. Additionally, the long-pass filters (white circles) might not have been aligned perfectly when building the sensor and so the predicted NTU is worse (less precise) than the case without filters (black diamond). From this figure and from Fig. D.9, we see no reason to opt for the long-pass filters when the off-on measurement is sufficient to eliminate stray light even in the 0-10NTU range. These lenses also add to the cost of the sensor (8 USD extra per sensor, each lens costs 4 USD).

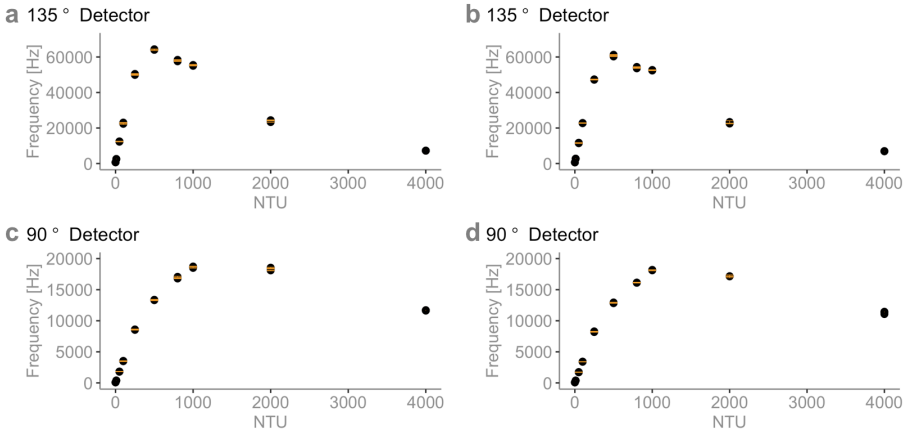

Figure D.9: Quantity of light in hertz [Hz] reaching the detector for each NTU dilution. The mean (black points) and errors (orange bars from +/- standard deviation) for Sensor 3 under ambient light without long-pass filters (a and c) and with long-pass filters (b and d). The mean and error were found by subtracting the mean of when the LED was off to the mean of when the LED was on.

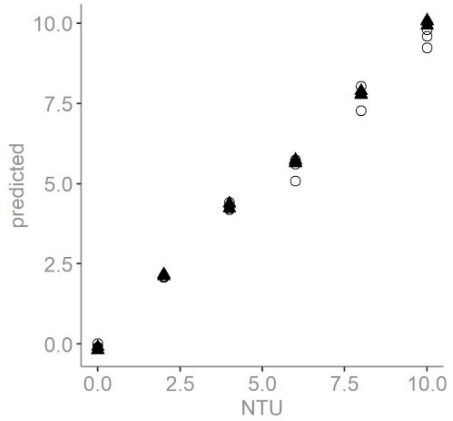

Figure D.10: Model predictions of NTU for Sensor 3 with (white circles) and without (black triangles) long-pass filters in the 0-10 NTU range.

Additional Tables and Figures

Table D.4: List of sensor versions for the second prototype.

Sensor name	**Sensor version**	**Detector Orientations**	**Method**
1	A	90°, 135°	Machined PVC
2	A	90°, 135°	Machined PVC
3	A	90°, 135°	Machined PVC
4	B	45°, 135°	Machined PVC
5	B	45°, 135°	Machined PVC
6	B	45°, 135°	Machined PVC
7	C	90°, 135°	3D printed
8	C	90°, 135°	3D printed

Table D.5: Model coefficients for sensor 6.

Sensor	**Range [NTU]**	α	β	γ	R^2	**p-value**
6	0-10	-10.62472490	0.01891566	-	0.9970	$<$ 2.2e-16
6	10-100	-12.9745875	0.0204973	-	0.9996	$<$ 2.2e-16
6	100-1000	1.039077e+2	-1.191820e-2	2.123267e-6	0.9983	$<$ 2.2e-16
6	1000-4000	4.904038e+3	-3.846541e-1	9.306911e-6	0.9995	$<$ 2.2e-16

Table D.6: The cost of one open-source sensor (second prototype).

Item	**Part number**	**Quantity**	**Cost/item [CHF]**
ESP32 Dev board	ESP32-DEVKITC-32D		8.90
DC/DC Converter	TSR 1-2450E		3.53
MicroSD module	DFR0229		4.63
P-Channel MOSFET	AOI21357	3	0.58
N-Channel MOSFET	IRLZ44NPBF	2	0.96
Slide Switch	GF-123-0054		1.11
9V Battery			1.69
9V Leads			0.45
10k resistors	CFR50J10K	7	0.062
IR LED	TSHG6200		0.93
Detectors	TSL237-S-LF-ND	2	3.14
Capacitors	C315C104M5U5TA7303	2	0.09
Prototyping board	DFRobot FIT0099		1.34
Lenses	Jingliang Optical Technology Co.	2	2.24
O rings	O-ring NBR 70 36624 82x2,5mm	2	1.88
PVC sensing head	Machined by technician		20
Total			61.37

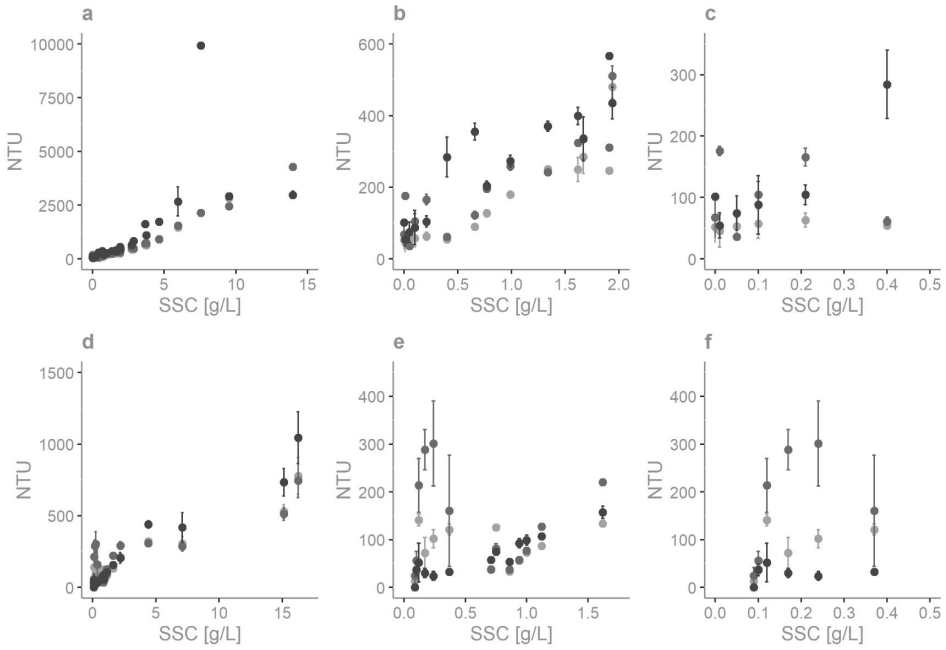

Figure D.11: **NTU vs. SSC comparison of three E&H sensors** (first CUS51D in light-grey, second CUS51D in mid-grey, CUS52D in dark grey). a) Feldspar powder in the full measurement range 0-16 g/L, b) Feldspar powder in the 0-2 g/L range, c) Feldspar powder in the 0-0.5 g/L range, d) Fieschertal sediment in the full measurement range 0-16 g/L, e) Fieschertal sediment in the 0-2 g/L range, f) Fieschertal sediment in the 0-0.5 g/L range. Error bars represent +/- one standard deviation. All of the E&H sensors are rated for 0-4000 NTU (see Methods section in Chapter 3 for more details on E&H sensors). However, on the E&H website they state that the CUS51Ds are used in applications with medium to high turbidities (Endress + Hauser, 2021a), whereas the CUS52D is used at every quality control point in drinking water production (from inlet to outlet), down to the lowest turbidities (Endress + Hauser, 2021b). We would like to investigate how these sensors report NTU at various sediment concentrations and if we could use commercial sensors to build a distributed turbidity sensor network. Panel a) shows that the two CUS51Ds report similar NTU readings in feldspar sediment at higher SSCs, meaning that these two sensors give "reproducible" results. Therefore, at higher concentrations (in feldspar) these two sensors can be placed in a catchment and their turbidities compared. However, at SSCs below 2 g/L (panels b and c) both CUS51D sensors are not able to provide reproducible or sensible results, since (no clear relationship between NTU and SSC), perhaps since these sensors are meant for high turbidities. Observing the CUS52D sensor (dark grey) in panel a), we find that the NTUs are higher relative to the two CUS51Ds between 3-6 g/L, abruptly peak at 7.5 g/L and read 10,000 NTU (possibly an error or bubbles present), and after 7.5 g/L the readings plateau at 3000 NTU. Since the CUS52D is meant for drinking water applications, possibly it is unable to take measurements above 7.5 g/L. However, this sensor is also not able to give sensible results below 2 g/L (panels b and c), although this is stated by E&H. Overall, the measurements from the CUS51Ds and CUS52D are non-comparable, since readings differ highly at SSCs above ∼2 g/L and no clear relationship between NTU and SSC can be observed below ∼2 g/L for both sensors. Comparing these results to the Fieschertal sediment results in panels d-f, we see again that the CUS51Ds are able to report reproducible results for the full range of data except below 2 g/L, where no meaningful relationship between NTU and SSC can be observed. Additionally, all three sensors inexplicably plateau between 5-15 g/L (possibly due to bubbles). In panels d-e, we find that the CUS52D (dark grey) reports better results between 1-5 g/L (NTU follows some trend with SSC), which is expected. However, this sensor reports unusable results below 0.25 g/L. In both cases, for feldspar and Fieschertal sediments, the CUS51Ds' results cannot be compared to the CUS52D's results, even if both sensors are from the same manufacturer and have been calibrated from 0-4000 NTU. Therefore, the NTU values reported by these sensors should not be compared but analyzed individually. None of the sensors are able to give sensible results for the entire 0-16 g/L range. It should be noted that the sensors were borrowed from scientists who use them in the field, so recalibration could lead to better results.

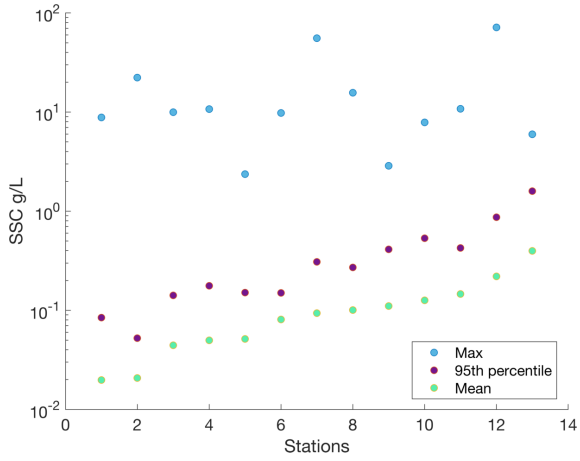

Figure D.12: **Observed SSCs in Switzerland.** The mean, 95% percentile, and maximum observed SSC in g/L at 13 stations of the Federal Office for the Environment (BAFU) network where automatic measurements are taking place. We consider these the typical Alpine river SSCs. There is an average 3,400 measurements at each station (twice weekly roughly). The mean across the 13 stations is 0.11 g/L. And the mean of 11 rivers, excluding the two rivers with the lowest mean SSC, is 0.129 g/L. The measurement that is exceeded on average 5% of the time is about 0.4 g/L. All of the maximum events fall below 23 g/L except for two events (at 55.6 g/L and 71.4 g/L).

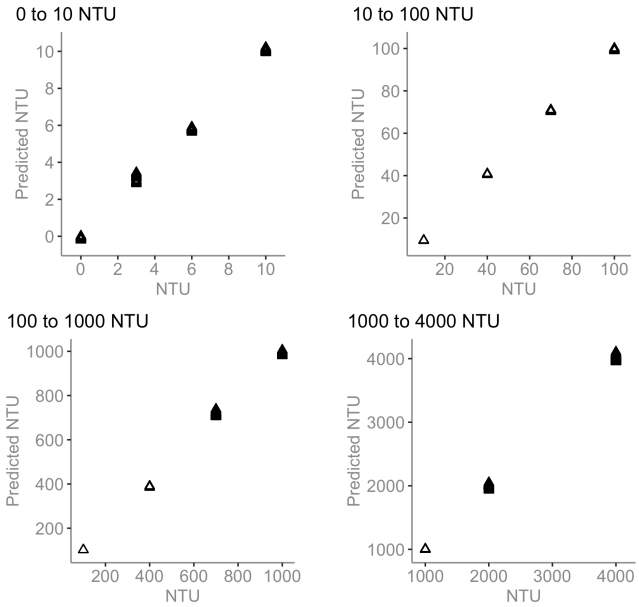

Figure D.13: Model predictions of NTU for Sensor 6 in four different ranges: TOP-LEFT 0-10 NTU; TOP-RIGHT 10-100 NTU; BOTTOM-LEFT 100-1000 NTU; and BOTTOM-RIGHT 1000-4000 NTU.

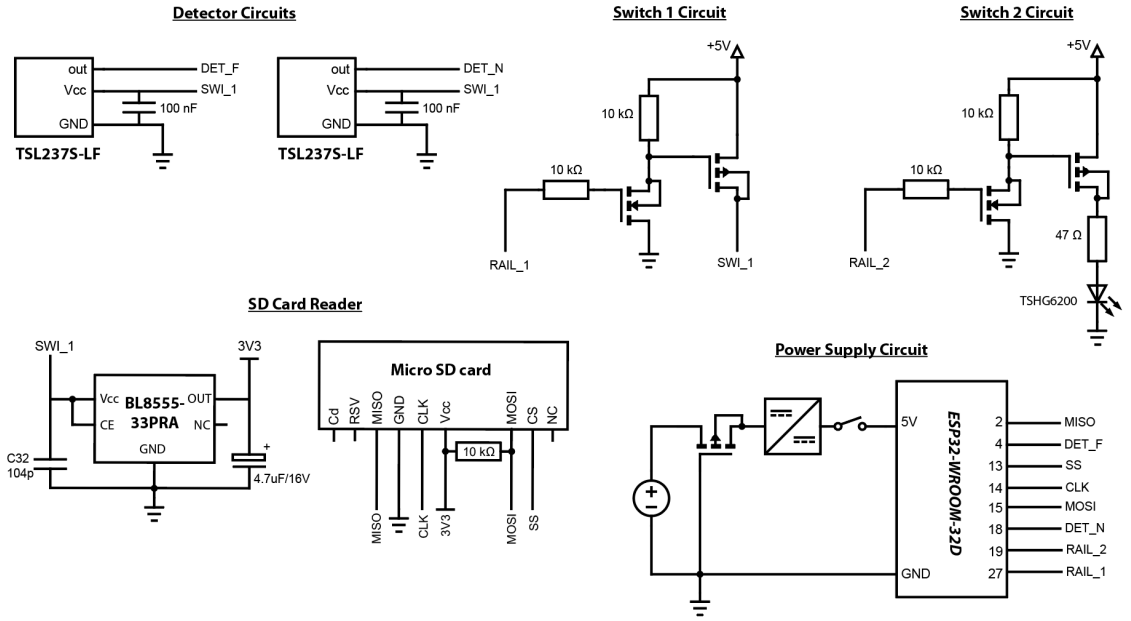

Figure D.14: **Electronic schematic of second prototype.** The sensor has five sub-circuits. A 9V battery is connected to the Power Supply Circuit, which supplies power to the entire system. The P-channel MOSFET here is used to prevent any damage to the ESP32 microchip in case the battery is accidentally connected backwards. The DC-DC converter is used to step down the battery voltage from 9V to the ESP32-WROOM-32D input voltage of 5V and a slide switch is installed between this converter and the 5V line to turn the sensor on and off. Both switch circuits are controlled from pins on the ESP32-WROOM-32D module by setting the pins from high (3.3V) to low (0V). Both circuits have an N- and P-channel MOSFET combination which are used to supply or cut the current flowing from +5V. Switch 1 Circuit is used to turn off and on all of the electronic components (detectors, SD card reader) between readings to save power. By setting pin 27 on the ESP32-WROOM-32D to high and low in the code for Switch 1 Circuit, current would either flow from 5V to SWI_1 (high) or no current would flow (low). When current flows, everything connected to SWI_1 is supplied with power. The same principle is used for Switch 2 Circuit; when pin 19 on the ESP32-WROOM-32D is set to high, current flows from +5V to ground and supplies power to the TSHG6200 LED. When pin 19 is low, the LED is off. The ESP is programmed to take a measurement every minute and between readings it will enter deep sleep. When the ESP is taking a measurement, it will set pin 27 to high and supply power to the SD Card Reader and the Detector Circuits. At the same time, it will take a frequency reading first with pin 19 set to low (LED off) and then again with pin 19 set to high (LED on), for the off-on differencing measurement. Once the differencing measurement is finished, the ESP will turn pin 27 low which should cut all power to the detectors and the SD card reader, then the ESP will enter deep-sleep (ESP-IDF Programming Guide, 2021) until it is time to take another measurement.

Supplementary Discussion - Problems with calibrating NTU with Formazin

A sensor that is simply meant to provide a clarity estimate can undergo a calibration to NTU with formazin. This is the traditional calibration of a turbidity sensor and our open-sourced sensors can also be used and calibrated in this way. However, within this unit of measure is hidden many complex processes, such as particle size, configuration, refractive index, organic matter and other floating debris, algae, air bubbles and water discoloration (wavelength absorption), which all determine the spatial distribution of the scattered light intensity around a particle (Dabney et al., 2006; Sadar, 1998). These processes cannot be deciphered from an NTU unit, especially when comparing units using sensors made by different manufacturers or by the same manufacturer but different sensor models. Kitchener et al. (2017) has shown that NTU is not a physically valid unit of turbidity (and suggests to record data in the SI unit of radiated intensity [mW/sr] (Kitchener et al., 2019)) since it is based on the mass-concentrations of arbitrary polymer suspensions (e.g. Formazin), and not on the intrinsic optical properties of the particles in suspension. This is also what we see in Fig.4.5 (Chapter 3). If the purpose of the sensor would be to determine what elements cause the water's clarity to change, then it might be better to calibrate one of our sensors directly to SSC and additionally equip it with other detectors to determine, for example, the presence of organic matter. This is what Matos et al. (2019) achieved when they equipped a 90^o light scatter detector with a UV transmitter and receiver.

Another issue noted by Felix et al. (2015) is that during a flood event, commercial NTU-calibrated turbidimeters yielded up to 80% lower SSCs than those from Laser in-situ Scattering and Transmissiometry (LISST) and bottle samples when coarser particles were present. They mainly attribute this to the temporal variation in PSD; as coarser particles produce less attenuation and scattering at a given SSC (as we see with Fieschertal sediment in Fig.5 b and d (main manuscript)). For this reason, they recommend more advanced optical techniques for SSC such as LISST or Coriolis Flow- and Density Meter (CFDM) which were found to be less biased by temporary PSD variations than SSCs obtained by turbidimeters. However, these devices are generally unsuitable for field applications and raise the measurement costs to US$ 15 000 (Felix et al., 2016) - 25 000 (Rai and Kumar, 2015) (for a CFDM) and between US$ 35 000 and 100 000 (for LISST (Rai and Kumar, 2015)).

In their experiments, Felix et al. (2018) used a turbidimeter that was calibrated up to 4000NTU and they found that their NTU-SSC calibration was only valid for particles up to $d_{50} = 17\mu m$ (the variation in PSD isn't an issue when the particles present are relatively fine (Felix et al., 2016), which is the case during the majority of the time at the HPP Fieschertal storage tunnel). They found that the coarsest particles were transported according to a hysteresis pattern, affecting the NTU-SSC calibration when particles were coarser than $d_{50} = 17\mu m$, and they saw no clear correlation between SSC and d_{50}. However, they did find that the slope of their NTU-SSC calibration curve (eqn. 6 (Felix et al., 2018)) decreases with coarser particles (as seen in our Fig.4.2 in the main manuscript). Nezu and Nakagawa (2017) and Parsons et al. (2015) found that SSC and PSD, for coarser particles such as sand, vary on the short term even in steady-state flow conditions due to the random nature of turbulence and coherent flow structures.

Therefore, PSD will affect our turbidity measurements since it is not measured by our sensors and so our sensors cannot overcome its influence. Perhaps by recognizing this issue

and directly calibrating Hz-SSC, we can obtain a regression fit (Hz-SSC) which spans the entire particle size range; more accurately representing the "true" SSC and overcoming the limitation imposed by the manufacturer's standard Hz-NTU calibration. Additionally, by obtaining multiple samples during various flood events when larger particles are transported, we may improve the Hz-SSC relation since random errors due to temporal fluctuations in PSD are reduced by measuring at a suitably high frequency and time-averaging (Felix et al., 2018). It would then be worth investigating whether our site-specific Hz-SSC calibration model can consistently capture SSC as both LISST and CFDM (Felix et al., 2016).

Appendix E Qualitative Assessment of Sediment Source Identification in a Glacierized Catchment

E.1 Introduction

Glaciers are dynamic entities that profoundly influence our landscapes and undergo cycles of accumulation and ablation, shedding water and sediments into river systems. This process, while natural, has become increasingly significant in the context of climate change, especially since glaciers are expected to retreat significantly in the coming decades (Zemp et al., 2006; Radić and Hock, 2014). This phenomenon not only affects water availability (Farinotti et al., 2016) but also alters glacier sediment discharge (Koppes et al., 2009) and has several ecological effects such as increasing macroinvertebrate functional diversity (Brown et al., 2018) and a projected functional extinction of species where glaciers will disappear completely (Wilkes et al., 2023). An increase of sediment trap flushing frequency at water intakes due to increased glacial melt had also been observed (Gabbud et al., 2019; Bakker et al., 2019), and has shown to invert the summer-winter macroinvertebrate assemblages (Gabbud et al., 2019).

The Rhône glacier, a key source of fine sediment feeding into the Rhône River within the Swiss Alps, has been observed to have increased sediment discharge in conjunction with increased runoff (similar to fluvial systems) and glacier retreat (Costa et al., 2018b). Here, the variability in sediment export depends on much more than sediment transport capacity; sediment is made available for transport through a variety of hydrological conditions (Lane et al., 2017). Runoff in heavily glacierized streams basically come from three sources as summarized in Figure E.1: (a) emptying bed and bank storages in the catchment in the winter when there is little snow and ice melt, this leads to the lowest annual flows (Floriancic et al., 2022), and low background suspended sediment input; (b) snow and ice melt in the early spring, when moulins and subglacial channels start to develop, accessing subglacial sediment stores (Delaney et al., 2018b), these processes switch to ice melt dominating in late spring and summer (ablation season) when the snow cover is gone, this is the period of highest continuous sediment flux; and (c) rainfall on the ice surface and the non-ice covered catchment surfaces, here hillslope erosion can produce a lot of fine sediment input into the stream, but intermittently.

This connectivity between glaciers and river networks, and the quantification of sediment fractions contributed by different forcings, remains poorly understood. This is due to the fact that glacier river monitoring is extremely difficult because the streams are constantly shifting and changing; there are no proper banks to install sensors on and for a large part of the year the ground is covered by snow.

In this work, I aim to harness our innovative, low-cost technology created in Chapters 3 and 4 to focus on the temporal variability of sediment input into rivers, driven by the three runoff processes above, to address this knowledge gap. The Rhône glacier presents a unique opportunity to study these exports and sources (climatic forcings) of fine sediment and to deploy our sensors in a challenging and remote location. This study not only contributes to

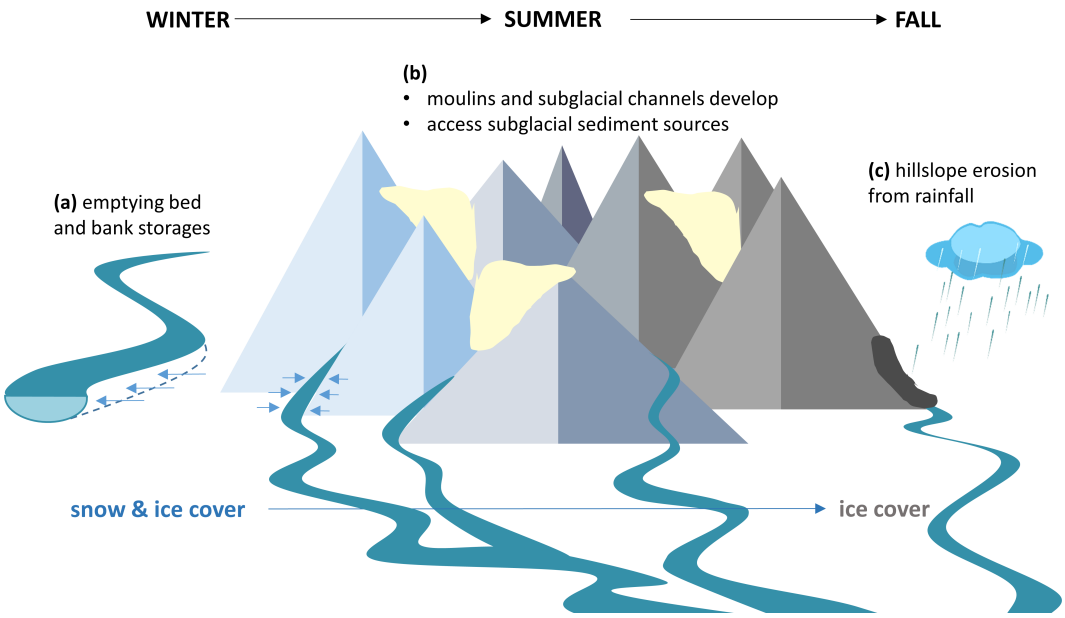

Figure E.1: Runoff in heavily glacierized streams comes from three processes: (a) emptying bed and bank storages in the catchment in the winter (little snow and ice melt); (b) snow and ice melt in the early spring, when moulins and subglacial channels start to develop, accessing subglacial sediment stores, these processes switch to ice melt dominating in late spring and summer (ablation season); and (c) rainfall on ice and non-ice covered catchment surfaces.

our grasp of glacial-riverine connectivity but also demonstrates how such approaches can enhance our ability to monitor hard-to-reach, yet critically important, processes. In doing so, I aim to answer the pressing questions surrounding the contributions of sediment sources to river sediment loads, and how these are modulated by both hydroclimatic forces and the seasonal regime. Since I have only obtained one ablation season record, the sediment sources cannot be partitioned statistically, but I provide a first look at the possible cause-and-effect relation for future investigations.

E.2 Methods

E.2.1 Rhône Glacier Study Site Description

The Rhône glacier, with an area of 17 km^2 and a length of 9 km, is one of the largest glaciers in the Swiss Alps and forms the source of the Rhône river (Goehring et al., 2011). It is found in the easternmost part of the Canton of Valais (Figure E.2), Switzerland. At the end of the glacier, there is a proglacial lake, from which the Rhône River flows and it travels 164.27 km before entering Lake Geneva near Porte-du-Scex.

On 25.03.2023, we installed our open-source sensor 2.27 km downstream of the Rhône proglacial lake, close to the town of Gletsch. The sensor we used was an improvement on the Ötz-T from Chapter 4 and is shown in Figure E.3a. This new version, called the "GlacierGuard," has a bigger battery and one custom PCB (instead of a custom PCB stacked on top of the Arduino MRK WAN). It was installed along the banks of the river and measured the water turbidity, pressure, and temperature for the entire ablation season at a

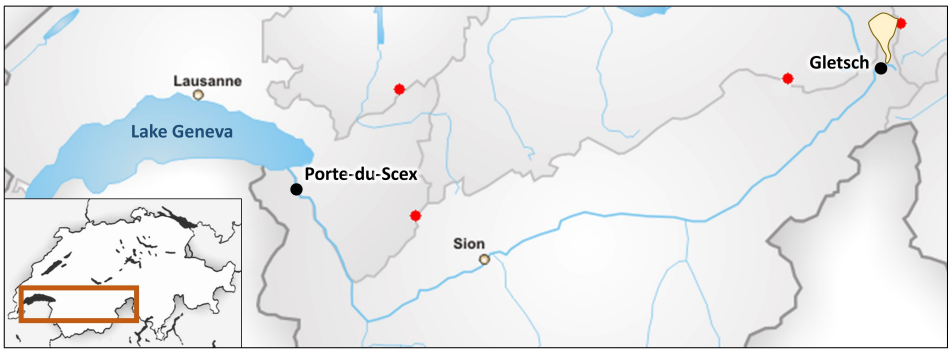

Figure E.2: The Rhône river starting from the mouth of the glacier near Gletsch (black dot) and flowing towards Porte-du-Scex (black dot) and Lake Geneva. Our sensor was installed downstream of the glacier, 2.27 km upstream of Gletsch. The BAFU stations are at Gletsch and at Porte-du-Scex.

sampling resolution of one measurement per hour. The sensor was removed on 29.09.2023. To complement this data, we also have turbidity data (measurements every 5 minutes) and suspended sediment sampling data (twice weekly) at the Porte-du-Scex measurement station run by the Swiss Federal Office for the Environment (BAFU). We have this data for the same measurement period as our GlacierGuard sensor.

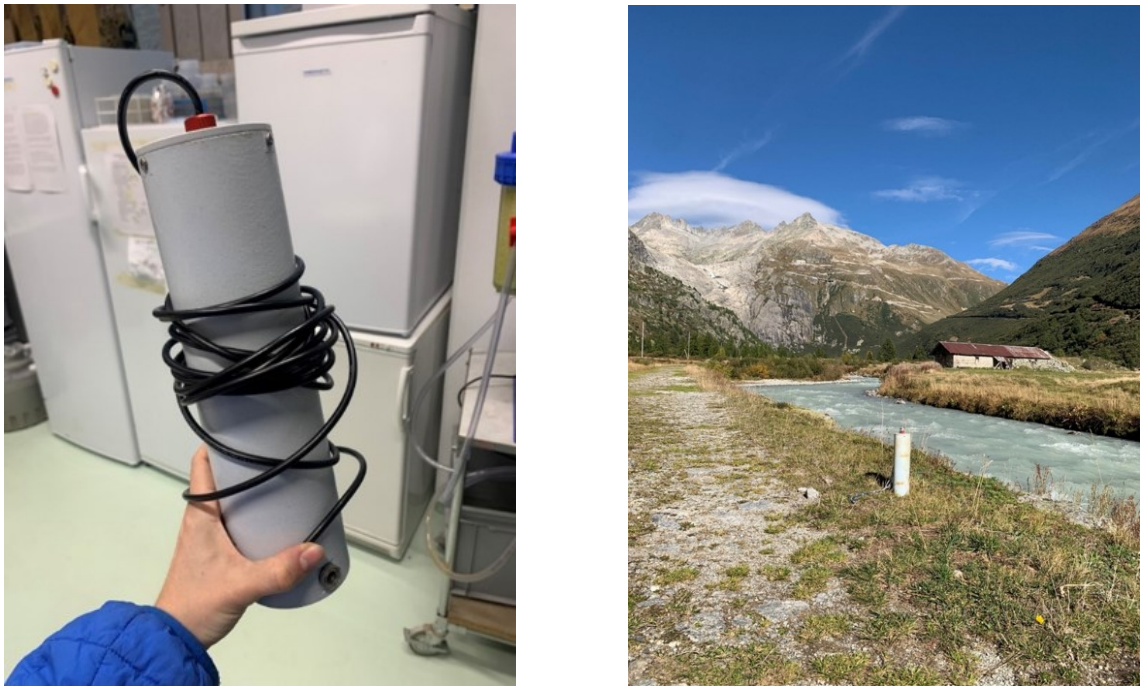

Figure E.3: LEFT - the GlacierGuard sensor before deployment. RIGHT - the GlacierGuard next to the Rhône River once it was retrieved in the Fall.

E.2.2 Integrating Meteorological and Hydrological Data

We obtained the daily total precipitation [mm] and the mean air temperature [^oC] from the nearby Grimsel Hospiz Meteoswiss weather station. The discharge data was taken from the Gletsch gauging station and the turbidity [BSTU] was taken from the Porte-du-Scex

station, both run by BAFU. The Normalized Difference Snow Index (NDSI) was taken from Copernicus and is a combination of bands 2, 3, 4, and 11 from Sentinel-2, computed over the glacier area for the period from 25.03.2023 to 29.09.2023.

E.3 Results

Figure E.4 shows the data collected over the ablation season. We find that the turbidity measured at Gletsch is stable across the entire measurement period until late August, where a clear spike ($\sim$ 450 NTU) coincides with a rainfall event. The mean air temperature (Fig. E.4 - second panel) increases steadily throughout the Spring until July, and this increase is also reflected by the increase in discharge, which is indicative of snow and ice melt driven runoff (Fig. E.4 - second panel). The turbidity at Porte-du-Scex also observes several spikes throughout the measurement period, including a large spike around late August at $\sim$ 3000 BSTU. The NDSI over the glacier area (Fig. E.4 - bottom panel) also shows a steady decrease throughout the Spring until July.

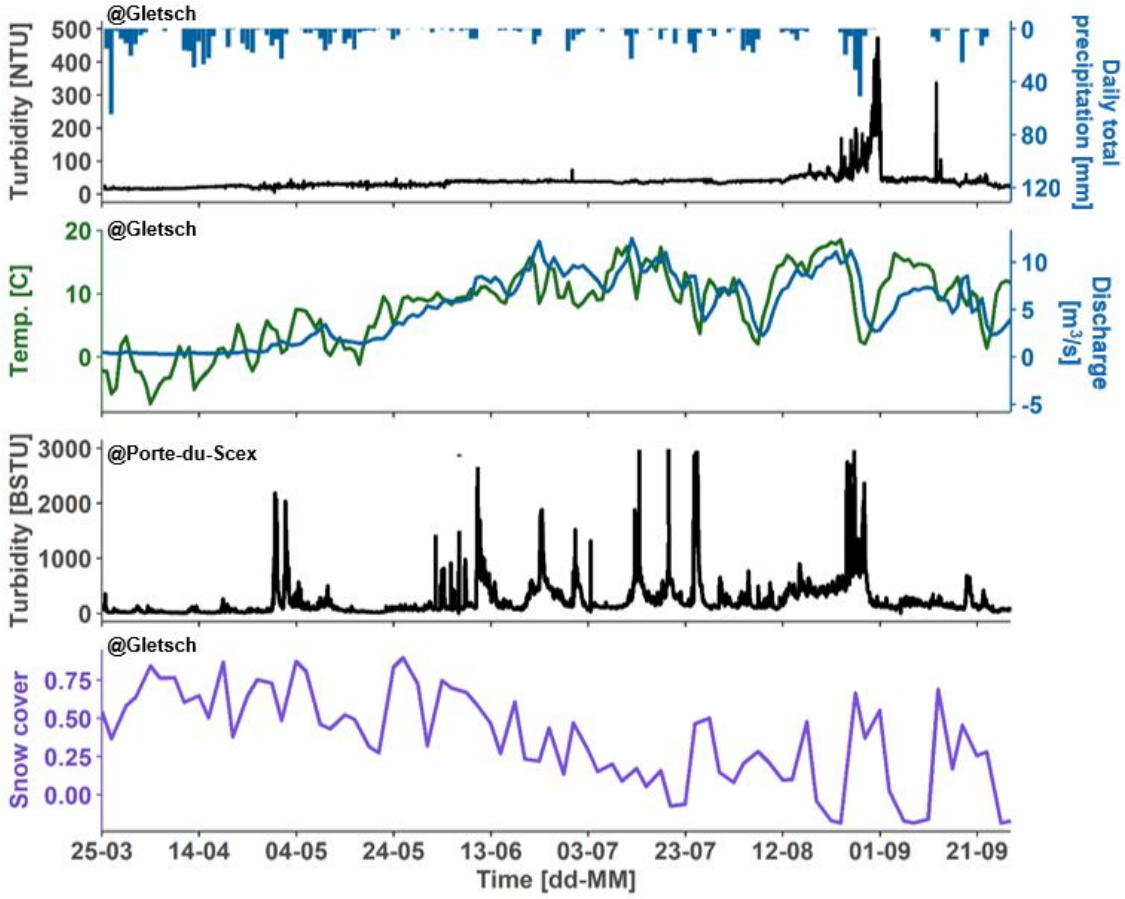

Figure E.4: Rhône ablation season data from 23.03.2023 to 29.09.2023. The top panel shows the turbidity data [NTU] measured by the sensor near Gletsch (black) and the daily total precipitation [mm] from the nearby Grimsel Hospiz meteorological station (blue). The second panel shows the daily mean air temperature [^oC] from the nearby Grimsel Hospiz meteorological station (green) and the discharge data measured at Gletsch by BAFU. The third panel shows the turbidity [BSTU] measured by BAFU at Porte-du-Scex. The bottom panel shows the NDSI over the Rhône glacier derived from satellite images of the glacier.

E.4 Discussion

E.4.1 Interpreting Turbidity Variations

The turbidity signal from Gletsch is shown on a log plot in Figure E.5. The ablation season can be clearly distinguished as the turbidity increases from $\sim$ 15 NTU in March to $\sim$ 40 NTU in early June and stays around 40 NTU until late September. The ablation season is also represented by the glacier NDSI (Fig. E.4 - bottom panel), which also observes a steady decline, and the corresponding increase in air temperature and river discharge (Fig. E.4 - second panel). In this period, the dominant sediment sources go from the emptying of the bed and bank storages in the catchment (Floriancic et al., 2022) to the delivery of sediment via melt accessing subglacial sediment stores (from source (a) to (b) in Fig. E.1).

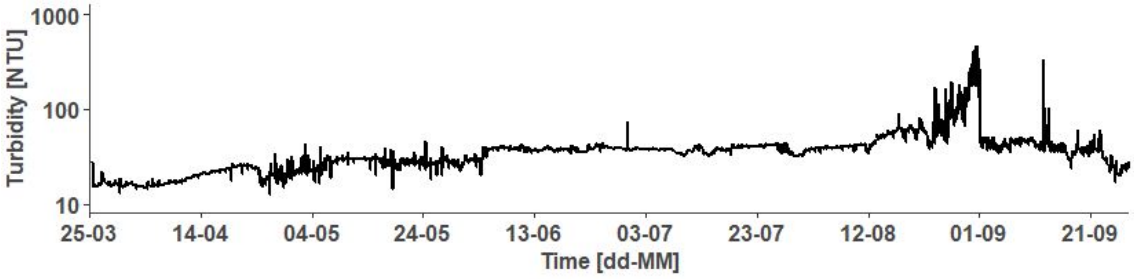

Figure E.5: Turbidity signal as measured by our sensor installed in the Rhône near Gletsch.

E.4.2 Qualitatively Interpreting Sediment Sources Along the Rhône River

The late-August turbidity peak ($\sim$450 NTU in Fig. E.4 - top panel) is further investigated in Figure E.6. First, it is clear that the decrease in mean daily air temperature (Fig. E.6 - third panel, green line) causes a delayed decrease in river discharge. This also reflects that the discharge at Gletsch is mostly driven by glacial dynamics, modulated by the storage and release of water from the small natural proglacial lake at the terminus of the glacier. The precipitation event on August 28th (Fig. E.6 - top panel, blue bars) did not cause an increase in river discharge because it fell as snow onto the glacier. This is also reflected by the increase in NDSI on August 28th (Fig. E.6 - bottom panel). The small peaks in turbidity at Porte-du-Scex (Fig. E.6 - second panel) in this period could be caused by rainfall-activated hillslope erosion at lower elevations in the non-glacierized part of the catchment (sediment source (c) in Fig. E.1) as shown by the mean basin precipitation.

Most interesting in the dataset is the gradual long increase in turbidity on 29 August in the river (Fig. E.6 - top panel), when precipitation has ceased and discharge is constant. The increase in discharge would normally lead to an increase in fine sediments in the river. This could be due to the fine sediments that have settled along the riverbed being suspended with the increase in discharge and shear stress. An increase in fine sediments could also point to an activation of sediment pockets within the subglacial channel network, which is normally seen with a large precipitation event and subsequent increase in discharge (Delaney et al., 2018b). However, as we do not have an increase in discharge, the spike in turbidity on August 29th is caused by another factor.

I hypothesize for the following two causes of the turbidity peak on August 29th. The first (1) possibility is that the SSC of the proglacial lake increased before subsequently spilling

into the river and creating the spike. The lake then acts as a sort of "buffer" by delaying the turbidity signal from when the subglacial channels input fine sediment into the lake to when that same signal is measured downstream by our sensor at Gletsch. The second (2) possibility is that this peak is caused by snowmelt as the temperature increases, bringing hillslope sediment into the glacial stream with a very low increase in discharge (sediment source (c) in Fig. E.1).

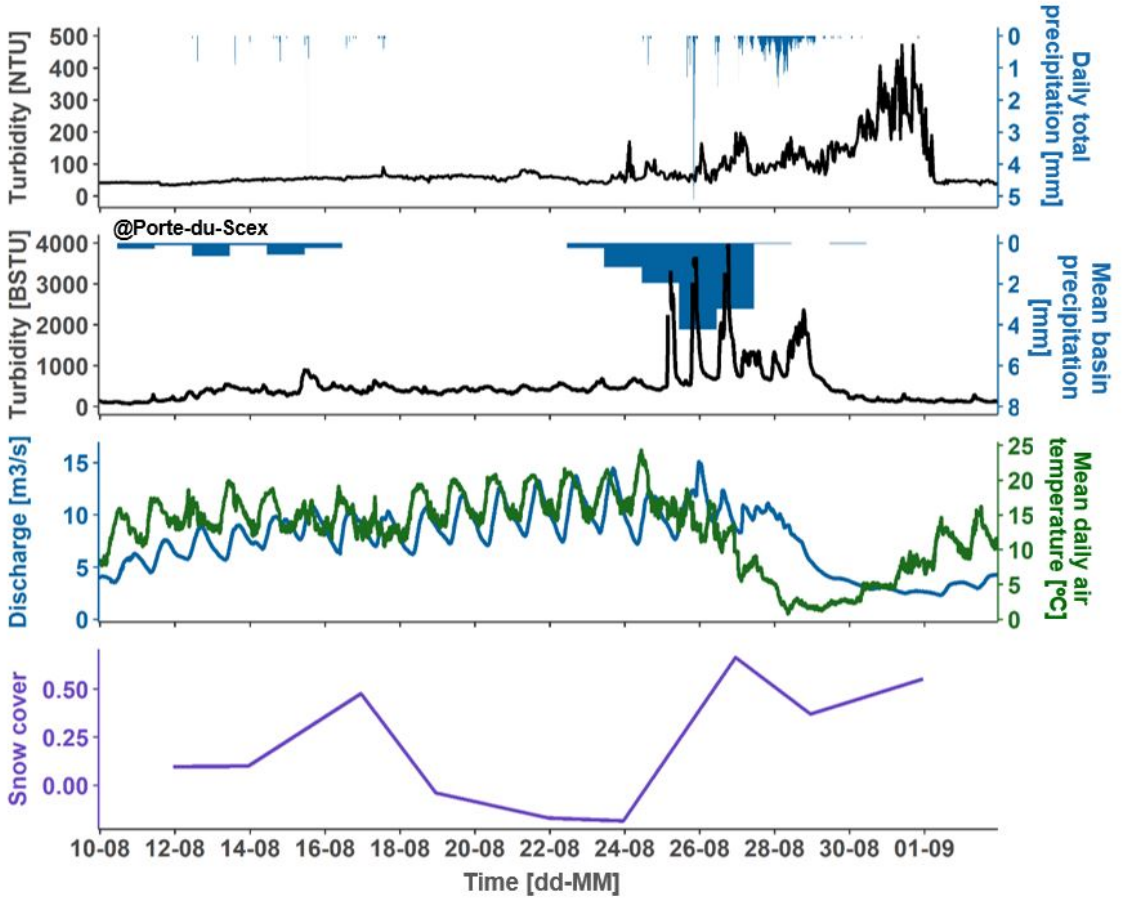

Figure E.6: Rhône data from 10.08.2023 to 03.09.2023. The top panel shows the turbidity data [NTU] measured by the sensor near Gletsch (black) and the daily total precipitation [mm] from the nearby Grimsel Hospiz meteorological station (blue). The second panel shows the turbidity [BSTU] measured by BAFU at Porte-du-Scex and the mean basin precipitation [mm]. The third panel shows the daily mean air temperature [^oC] from the nearby Grimsel Hospiz meteorological station (green) and the discharge data measured at Gletsch by the Swiss Federal Office for the Environment. The bottom panel shows the NDSI over the Rhône glacier derived from aerial images of the glacier.

It is additionally interesting to see that the high influx of fine sediments seen at Gletsch are not later seen downstream at Porte-du-Scex (Fig. E.6 - second panel). This is most likely because the total sediment yield (mass) produced by the Rhône glacier in this period is too small to have an impact on SSCs at the outlet of the catchment 164 km downstream. The previous three peaks of turbidity at Porte-du-Scex (Fig. E.6 - second panel) were not coming from the Rhône catchment, but from other sources within the lower part of the catchment, as from the 24th of August on, and especially on the 25, 26 and 27 August, there was substantial precipitation with basin averages up to 4 mm/day.

E.5 Conclusion

This work was an exploratory study into the effects of runoff processes on river turbidity in a glacierized catchment, employing a novel approach with a low-cost sensor to monitor these dynamics at the Rhône Glacier. This investigation shows the complex interactions between glacial melt processes and river sediment loads, particularly under the lens of temporal variability and hydroclimatic influences.

Through the deployment of a sensor from March to October 2023, we observed the clear onset of the ablation period, capturing a detailed turbidity profile. The late-August turbidity spike, observed without a corresponding increase in discharge, suggests alternative mechanisms at play, possibly involving the transient storage and release of sediments from the proglacial lake or from snowmelt without large increases in discharge. This event underscores the intricate balance of processes governing sediment mobilization in glacial environments. Furthermore, the absence of similar sediment spikes downstream at Porte-du-Scex points me to believe that the amount of sediments stemming from Gletsch are too small to be seen.

In this study, we have shown that measuring high-resolution turbidity in a glacier stream for half a year is possible with our current open-source, low-cost sensor. From our qualitative analysis, cause-and-effect relations could be elaborated when supplemented with information on climate (precipitation, temperature, snowcover). Finally, we have found confusing effects related to things like the state of sediment storages, subglacial channel development, and where exactly it rains. Therefore, long-term records are needed to conduct a proper statistical or a mechanistic hydrology-sediment modeling of these cause-and-effect relations.

My study has opened a dialogue on the temporal variability of sediment inputs from glacial sources, emphasizing the need for further research to unravel the nuanced relationships between glacier melt and sediment transport. Looking ahead, the use of low-cost sensors in remote and challenging environments like the Rhône glacier presents a promising avenue for advancing our knowledge of glacially influenced river systems. Future studies should aim to expand the sensor network by integrating additional sensors along the river's path to capture the full spectrum of sediment dynamics.

Appendix F Other Contributions to Science

During my employment at the Chair of Hydrology and Water Resources Management, I made several condtributions to science, which would not be considered traditional "academic contributions." These contributions are:

- Organized 2 bioblitzes: one on the Holderbach creek in the Hönggerwald to also bring awareness to the Waldlabor, and one along the Limmat river
  - A bioblitz is a communal citizen-science effort to record a wide variety of species at a specific location within a certain timeframe, usually by taking images of different species with mobile cameras and recording the images in an app. Bioblitzes are a way to connect people to their environments, zooming in to details they normally pass by and at the same time generating useful data for science and conservation.
  - The Home River Bioblitz focuses on the biodiversity in and around rivers, which are at the heart of all ecosystems. The event connects the stories of the people that protect, restore and celebrate these valuable places.
  - I presented a poster about the Home River Bioblitz a the 2021 EGU General Assembly (Droujko et al., 2021).
- Organized 5 Students for Rivers Camps bringing ∼180 students from around the world (including the EU, Mexico, the USA, the UK, Chile, and Canada) together to celebrate and learn about free-flowing rivers
  - The River Collective (RC) is a network of students, researchers, artists, and activists that all have one thing in common: a love of rivers. Healthy and free-flowing rivers play an essential role in preserving biodiversity and sustaining healthy living environments, especially in times of a rapidly changing climate. To promote healthy rivers, we aim to establish a strong collaboration between the world of science and local river conservation. The RC establishes these connections through our various events.
  - One of these events is the Students for Rivers Camp (SRC): A week-long program of workshops, lectures, and practical fieldwork training that engages students (bachelor's, master's, PhD) in the protection of free-flowing and thriving rivers and coastal ecosystems. We do this by combining science, art, and community empowerment for an interdisciplinary and intercultural education.
  - The SRC is usually based along the banks of a river. The following locations are where we held SRCs:
    - Soca River, Slovania (2019)
    - Lim River, Montenegro & online (2020)
    - Valbona River, Albania (2021)
    - Ötztal Ache, Austria (2022)
    - River Dart, UK (2023)
- Brought Master's student, Srividya, to fieldwork in Albania. The basis of her thesis was to further refine our satellite imagery processing methodology. I took her on her first camping experience and introduced her to the Vjosa river.

- I wrote 7 blog posts about the open-source turbidity project, which can be found at rivertechlabs.org
- I made 4 Github repositories for the open-source sensor and its derivatives in the last 4 years (github.com/rivertechlabs)

Bibliography

Copernicus DEM global and european digital elevation model. https://doi.org/10.5270/ESA-c5d3d65. Accessed: 2019-05-01.

Takaaki Abe, Shigeru Mizugaki, Toshihito Toyabe, Masahiro Maruyama, Yasuhiro Murakami, and Takashi Ishiya. High range turbidity monitoring in the mu and saru river basins: All-year monitoring of hydrology and suspended sediment transport in 2010. *International Journal of Erosion Control Engineering*, 5(1):70–79, 2012.

Robin Abell, Michele L Thieme, Carmen Revenga, Mark Bryer, Maurice Kottelat, Nina Bogutskaya, Brian Coad, Nick Mandrak, Salvador Contreras Balderas, William Bussing, et al. Freshwater ecoregions of the world: a new map of biogeographic units for freshwater biodiversity conservation. *BioScience*, 58(5):403–414, 2008.

Alessandro Acquavita, Federico Floreani, and Stefano Covelli. Occurrence and speciation of arsenic and mercury in alluvial and coastal sediments. *Current Opinion in Environmental Science & Health*, 22:100272, 2021.

Amir AghaKouchak, Felicia Chiang, Laurie S Huning, Charlotte A Love, Iman Mallakpour, Omid Mazdiyasni, Hamed Moftakhari, Simon Michael Papalexiou, Elisa Ragno, and Mojtaba Sadegh. Climate extremes and compound hazards in a warming world. *Annual Review of Earth and Planetary Sciences*, 48:519–548, 2020.

Rui Aleixo, Massimo Guerrero, Michael Nones, and Nils Ruther. Applying adcps for long-term monitoring of ssc in rivers. *Water Resources Research*, 56(1):e2019WR026087, 2020.

Roman Alther and Florian Altermatt. Fluvial network topology shapes communities of native and non-native amphipods. *Ecosphere*, 9(2):e02102, 2018.

Arduino. Arduino mkr wan 1310. https://store.arduino.cc/products/arduino-mkr-wan-1310, a. Accessed: 2022-10-06.

Arduino. Arduino ide. https://www.arduino.cc/en/software, b. Accessed: 2022-08-25.

Kevin R Arrigo, Gert van Dijken, and Sudeshna Pabi. Impact of a shrinking arctic ice cover on marine primary production. *Geophysical Research Letters*, 35(19), 2008.

Ángela H Arthington, Robert J Naiman, Michael E Mcclain, and Christer Nilsson. Preserving the biodiversity and ecological services of rivers: new challenges and research opportunities. *Freshwater biology*, 55(1):1–16, 2010.

N Bachiller-Jareno, MG Hutchins, MJ Bowes, MB Charlton, and HG Orr. A novel application of remote sensing for modelling impacts of tree shading on water quality. *Journal of Environmental Management*, 230:33–42, 2019.

BAFU. BAFU monitoring networks for sediment transport in bodies of water, 2024. URL https://www.bafu.admin.ch/bafu/en/home/topics/water/state/water--monitoring-networks/monitoring-networks-for-sediment-transport-in-bodies-of-water.html.

David B Baker, D Ellen Ewing, Laura T Johnson, Jack W Kramer, Barbara J Merryfield, Remegio B Confesor Jr, R Peter Richards, and Aaron A Roerdink. Lagrangian analysis of the transport and processing of agricultural runoff in the lower maumee river and maumee bay. *J Great Lakes Res*, 40(3):479–495, 2014.

ET Baker, DA Tennant, RA Feely, GT Lebon, and SL Walker. Field and laboratory studies on the effect of particle size and composition on optical backscattering measurements in hydrothermal plumes. *Deep Sea Research Part I: Oceanographic Research Papers*, 48 (2):593–604, 2001.

Maarten Bakker, Anna Costa, Tiago A Silva, Laura Stutenbecker, Stéphanie Girardclos, J-L Loizeau, Peter Molnar, Fritz Schlunegger, and Stuart N Lane. Combined flow abstraction and climate change impacts on an aggrading alpine river. *Water Resources Research*, 54(1):223–242, 2018.

Maarten Bakker, Gilles Antoniazza, Eliott Odermatt, and Stuart N Lane. Morphological response of an alpine braided reach to sediment-laden flow events. *Journal of Geophysical Research: Earth Surface*, 124(5):1310–1328, 2019.

Tom J Battin, Ronny Lauerwald, Emily S Bernhardt, Enrico Bertuzzo, Lluís Gómez Gener, Robert O Hall Jr, Erin R Hotchkiss, Taylor Maavara, Tamlin M Pavelsky, Lishan Ran, et al. River ecosystem metabolism and carbon biogeochemistry in a changing world. *Nature*, 613(7944):449–459, 2023.

Giulia Battista. *Numerical modelling of suspended sediment transport in pre-alpine river basins*. PhD thesis, ETH Zurich, 2021.

Giulia Battista, Peter Molnar, and Paolo Burlando. Modelling impacts of spatially variable erosion drivers on suspended sediment dynamics. *Earth Surface Dynamics*, 8(3):619–635, 2020a.

Giulia Battista, Peter Molnar, and Paolo Burlando. Modelling impacts of spatially variable erosion drivers on suspended sediment dynamics. *Earth Surface Dynamics*, 8(3):619–635, 2020b.

Giulia Battista, Fritz Schlunegger, Paolo Burlando, and Peter Molnar. Modelling localized sources of sediment in mountain catchments for provenance studies. *Earth surface processes and landforms*, 45(14):3475–3487, 2020c.

Giulia Battista, Fritz Schlunegger, Paolo Burlando, and Peter Molnar. Sediment supply effects in hydrology-sediment modeling of an alpine basin. *Water resources research*, 58 (7):e2020WR029408, 2022.

Barbara Belletti, Carlos Garcia de Leaniz, Joshua Jones, Simone Bizzi, Luca Börger, Gilles Segura, Andrea Castelletti, Wouter Van de Bund, Kim Aarestrup, James Barry, et al. More than one million barriers fragment europe's rivers. *Nature*, 588(7838):436–441, 2020.

G.L. Bennett, P. Molnar, B.W. McArdell, F. Schlunegger, and P. Burlando. Patterns and controls of sediment production, transfer and yield in the illgraben. *Geomorphology*, 188:68 – 82, 2013. ISSN 0169-555X. doi: https://doi.org/10.1016/j.geomorph.2012.11.029. URL `http://www.sciencedirect.com/science/article/pii/S0169555X12005508`. Sediment sources, source-to-sink fluxes and sedimentary budgets.

GL Bennett, Peter Molnar, BW McArdell, and Paulo Burlando. A probabilistic sediment cascade model of sediment transfer in the illgraben. *Water Resources Research*, 50(2): 1225–1244, 2014.

CY Bernard, HH Dürr, C Heinze, J Segschneider, and E Maier-Reimer. Contribution of riverine nutrients to the silicon biogeochemistry of the global ocean–a model study. *Biogeosciences*, 8(3):551–564, 2011.

Nariane Bernardo, Fernanda Watanabe, Thanan Rodrigues, and Enner Alcântara. Atmospheric correction issues for retrieving total suspended matter concentrations in inland waters using oli/landsat-8 image. *Adv Space Res*, 59(9):2335–2348, 2017.

Walter Berry, Norman Rubinstein, Brian Melzian, and Brian Hill. The biological effects of suspended and bedded sediment (sabs) in aquatic systems: a review. *United States Environmental Protection Agency, Duluth*, 32(1):54–55, 2003.

Achim A Beylich, John C Dixon, and Zbigniew Zwoliński. *Source-to-sink fluxes in undisturbed cold environments*. Cambridge University Press, 2016.

Jyotirmoy Bhardwaj, Karunesh K Gupta, and Rajiv Gupta. A review of emerging trends on water quality measurement sensors. In *2015 International Conference on Technologies for Sustainable Development (ICTSD)*, pages 1–6. IEEE, 2015.

Gary S Bilotta, Niall G Burnside, Liz Cheek, Michael J Dunbar, Magdalena K Grove, C Harrison, Christopher Joyce, C Peacock, and John Davy-Bowker. Developing environment-specific water quality guidelines for suspended particulate matter. *Water Research*, 46(7):2324–2332, 2012.

Pasquale Borrelli, David A Robinson, Larissa R Fleischer, Emanuele Lugato, Cristiano Ballabio, Christine Alewell, Katrin Meusburger, Sirio Modugno, Brigitta Schütt, Vito Ferro, et al. An assessment of the global impact of 21st century land use change on soil erosion. *Nature Communications*, 8(1):1–13, 2017.

Pasquale Borrelli, David A Robinson, Panos Panagos, Emanuele Lugato, Jae E Yang, Christine Alewell, David Wuepper, Luca Montanarella, and Cristiano Ballabio. Land use and climate change impacts on global soil erosion by water (2015-2070). *Proceedings of the National Academy of Sciences*, 117(36):21994–22001, 2020.

Andrew J Boulton, Stuart Findlay, Pierre Marmonier, Emily H Stanley, and H Maurice Valett. The functional significance of the hyporheic zone in streams and rivers. *Annual review of Ecology and systematics*, 29(1):59–81, 1998.

Christopher J Brown, Stacy D Jupiter, Simon Albert, Carissa J Klein, Sangeeta Mangubhai, Joseph M Maina, Peter Mumby, Jon Olley, Ben Stewart-Koster, Vivitskaia Tulloch, et al. Tracing the influence of land-use change on water quality and coral reefs using a bayesian model. *Sci Rep-Uk*, 7(1):1–10, 2017.

Lee E Brown, Kieran Khamis, Martin Wilkes, Phillip Blaen, John E Brittain, Jonathan L Carrivick, Sarah Fell, Nikolai Friberg, Leopold Füreder, Gisli M Gislason, et al. Functional diversity and community assembly of river invertebrates show globally consistent responses to decreasing glacier cover. *Nature Ecology & Evolution*, 2(2):325–333, 2018.

Cristina Buendia, Chris N Gibbins, Damia Vericat, Ramon J Batalla, and Alex Douglas. Detecting the structural and functional impacts of fine sediment on stream invertebrates. *Ecological indicators*, 25:184–196, 2013.

Bundesministerium für Landwirtschaft, Regionen und Tourismus. Hydrographisches jahrbuch, 2021.

HE Burgers, Aafke M Schipper, and A Jan Hendriks. Size relationships of water discharge in rivers: scaling of discharge with catchment area, main-stem length and precipitation. *Hydrol Process*, 28(23):5769–5775, 2014.

Jim A Cambray, Jackie M King, and Charel Bruwer. Spawning behaviour and early development of the clanwilliam yellowfish (barbus capensis; cyprinidae), linked to experimental dam releases in the olifants river, south africa. *Regulated Rivers: Research & Management: An International Journal Devoted to River Research and Management*, 13(6):579–602, 1997.

Franck Cattanéo, Jean Guillard, Seydina Diouf, Jane O'Rourke, and David Grimardias. Mitigation of ecological impacts on fish of large reservoir sediment management through controlled flushing–the case of the verbois dam (rhône river, switzerland). *Science of the Total Environment*, 756:144053, 2021.

Yiheng Chen and Dawei Han. Water quality monitoring in smart city: A pilot project. *Automation in Construction*, 89:307–316, 2018.

P Ciavola. Relation between river dynamics and coastal changes in albania: an assessment integrating satellite imagery with historical data. *Int J Remote Sens*, 20(3):561–584, 1999.

Sagy Cohen, Jaia Syvitski, Thomas Ashley, Roderick Lammers, Balazs Fekete, and Hong-Yi Li. Spatial trends and drivers of bedload and suspended sediment fluxes in global rivers. *Water Resour Res*, 58(6):e2021WR031583, 2022.

AL Collins, PS Naden, DA Sear, JI Jones, Ian DL Foster, and KJHP Morrow. Sediment targets for informing river catchment management: international experience and prospects. *Hydrological Processes*, 25(13):2112–2129, 2011.

Gabriele Consoli, Rudolf M Haller, Michael Doering, Saman Hashemi, and Christopher T Robinson. Tributary effects on the ecological responses of a regulated river to experimental floods. *Journal of Environmental Management*, 303:114122, 2022.

Gabriele Consoli, Andre R Siebers, Andreas Bruder, and Christopher T Robinson. Long-term reconstruction of energy fluxes in an alpine river: Effects of flow regulation and restoration. *River Research and Applications*, 39(9):1783–1794, 2023.

Alysha I Coppola, Daniel B Wiedemeier, Valier Galy, Negar Haghipour, Ulrich M Hanke, Gabriela S Nascimento, Muhammed Usman, Thomas M Blattmann, Moritz Reisser, Chantal V Freymond, et al. Global-scale evidence for the refractory nature of riverine black carbon. *Nature Geoscience*, 11(8):584–588, 2018.

Anna Costa, Daniela Anghileri, and Peter Molnar. Hydroclimatic control on suspended sediment dynamics of a regulated alpine catchment: a conceptual approach. *Hydrology and Earth System Sciences*, 22(6):3421–3434, 2018a.

Anna Costa, Peter Molnar, Laura Stutenbecker, Maarten Bakker, Tiago A Silva, Fritz Schlunegger, Stuart N Lane, Jean-Luc Loizeau, and Stéphanie Girardclos. Temperature signal in suspended sediment export from an alpine catchment. *Hydrology and Earth System Sciences*, 22(1):509–528, 2018b.

Leticia Cotrim da Cunha, Erik T Buitenhuis, Corinne Le Quéré, Xavier Giraud, and Wolfgang Ludwig. Potential impact of changes in river nutrient supply on global ocean biogeochemistry. *Global Biogeochem Cy*, 21(4), 2007.

Jacob A Covault, William H Craddock, Brian W Romans, Andrea Fildani, and Mayur Gosai. Spatial and temporal variations in landscape evolution: Historic and longer-term sediment flux through global catchments. *The Journal of Geology*, 121(1), 2013.

Giuseppe Crosa, Elena Castelli, Gaetano Gentili, and Paolo Espa. Effects of suspended sediments from reservoir flushing on fish and macroinvertebrates in an alpine stream. *Aquatic Sciences*, 72:85–95, 2010.

SM Dabney, MA Locke, and RW Steinriede. Turbidity sensors track sediment concentrations in runoff from agricultural fields. In *Proceedings of the Eighth Federal Interagency Sedimentation Conference (8thFISC), Reno, NV, USA*, 2006.

Ian Delaney, Andreas Bauder, Matthias Huss, and Yvo Weidmann. Proglacial erosion rates and processes in a glacierized catchment in the swiss alps. *Earth Surface Processes and Landforms*, 43(4):765–778, 2018a.

Ian Delaney, Andreas Bauder, Mauro A Werder, and Daniel Farinotti. Regional and annual variability in subglacial sediment transport by water for two glaciers in the swiss alps. *Frontiers in Earth Science*, 6:175, 2018b.

Nicole M DeLuca, Benjamin F Zaitchik, and Frank C Curriero. Can multispectral information improve remotely sensed estimates of total suspended solids? a statistical study in chesapeake bay. *Remote Sensing*, 10(9):1393, 2018.

Stephane Descloux, Thibault Datry, and Pierre Marmonier. Benthic and hyporheic invertebrate assemblages along a gradient of increasing streambed colmation by fine sediment. *Aquat Sci*, 75(4):493–507, 2013.

DFRobot. DF Robot gravity: Analog turbidity sensor for arduino, 2024. URL `https://www.dfrobot.com/product-1394.html`.

John Downing. Twenty-five years with obs sensors: The good, the bad, and the ugly. *Continental Shelf Research*, 26(17-18):2299–2318, 2006.

David Doxaran, J-M Froidefond, and P Castaing. A reflectance band ratio used to estimate suspended matter concentrations in sediment-dominated coastal waters. *Int J Remote Sens*, 23(23):5079–5085, 2002.

Jessica Droujko. River tech labs: Blog posts with sensor building instructions. `https://rivertechlabs.org/`, 2021a. [Online; accessed 9-May-2022].

Jessica Droujko. Supporting make files for "open-source, low-cost, in-situ turbidity sensor for river network monitoring" (v1.0.0). Dec 2021b. doi: 10.5281/zenodo.5789211.

Jessica Droujko and Peter Molnar. Open-source, low-cost, in-situ turbidity sensor for river network monitoring. *Scientific Reports*, 12(1):10341, 2022.

Jessica Droujko and Peter Molnar. Open-source self-made sensors show high potential in river research. *Nature Water*, 1(9):758–759, 2023.

Jessica Droujko, Carlos Velazco-Macías, David Faro, Jens Benöhr, Vera Knook, and Kara Lena Virik. The home river bioblitz: A world-wide collaboration between citizens to show the importance of free-flowing rivers. In *EGU General Assembly Conference Abstracts*, pages EGU21–9790, 2021.

Jessica Droujko, Felix Kunz Jr, and Peter Molnar. Ötz-t: 3d-printed open-source turbidity sensor with arduino shield for suspended sediment monitoring. *HardwareX*, 13:e00395, 2023a.

Jessica Droujko, Srividya Hariharan Sudha, Gabriel Singer, and Peter Molnar. Sediment source and sink identification using sentinel-2 and a small network of turbidimeters on the vjosa river. *Earth Surface Dynamics*, 11(5):881–897, 2023b.

David Dudgeon. The ecology of tropical asian rivers and streams in relation to biodiversity conservation. *Annual review of Ecology and Systematics*, 31(1):239–263, 2000.

Eawag: Swiss Federal Institute Of Aquatic Science And Technology and Federal Office For The Environment (FOEN). Naduf - national long-term surveillance of swiss rivers (2021-1), 2021. URL `https://opendata.eawag.ch/dataset/naduf-national-long-term-surveillance-of-swiss-rivers-2021-1`.

Emily F Eidam, Theodore Langhorst, Evan B Goldstein, and McKenzie McLean. Openobs: Open-source, low-cost optical backscatter sensors for water quality and sediment-transport research. *Limnology and Oceanography: Methods*, 20(1):46–59, 2022.

Endress + Hauser. Suspended solids sensor turbimax cus51d. `https://www.ch.endress.com/en/field-instruments-overview/liquid-analysis-product-overview/suspended-solids-turbidity-digital-sensor-cus51d`, 2021a. [Online; accessed 4-August-2021].

Endress + Hauser. Turbidity sensor turbimax cus52d. `https://www.ch.endress.com/en/field-instruments-overview/liquid-analysis-product-overview/turbidity-drinking-water-sensor-cus52d`, 2021b. [Online; accessed 4-August-2021].

ESA. Sentinel-2 user handbook. `https://sentinel.esa.int/documents/247904/685211/Sentinel-2_User_Handbook`. Accessed: 2022-10-27.

ESP-IDF Programming Guide. Sleep modes. `https://docs.espressif.com/projects/esp-idf/en/latest/esp32/api-reference/system/sleep_modes.html`, 2021. [Online; accessed 6-October-2021].

Paolo Espa, Elena Castelli, Giuseppe Crosa, and Gaetano Gentili. Environmental effects of storage preservation practices: controlled flushing of fine sediment from a small hydropower reservoir. *Environmental Management*, 52:261–276, 2013.

Paolo Espa, Ramon J Batalla, Maria Laura Brignoli, Giuseppe Crosa, Gaetano Gentili, and Silvia Quadroni. Tackling reservoir siltation by controlled sediment flushing: Impact on downstream fauna and related management issues. *PLoS One*, 14(6):e0218822, 2019.

Daniel Farinotti, Alberto Pistocchi, and Matthias Huss. From dwindling ice to headwater lakes: could dams replace glaciers in the european alps? *Environmental Research Letters*, 11(5):054022, 2016.

Alice César Fassoni-Andrade and Rodrigo Cauduro Dias de Paiva. Mapping spatial-temporal sediment dynamics of river-floodplains in the amazon. *Remote Sensing of Environment*, 221:94–107, 2019.

David Felix. Experimental investigation on suspended sediment, hydro-abrasive erosion and efficiency reductions of croated pelton turbines. *VAW-Mitteilungen*, 238, 2017.

David Felix, Ismail Albayrak, and Robert Boes. Monitoring of suspended sediment: Laboratory tests and case study in the swiss alps. *Advances in river sediment research*, pages 163–163, 2013.

David Felix, Ismail Albayrak, and Robert M Boes. Field measurements of suspended sediment using several methods. In *E-Proceedings of the 36th IAHR World Congress, 28 June-3 July, 2015, The Hague, the Netherlands*. IAHR, 2015.

David Felix, Ismail Albayrak, and Robert M Boes. Continuous measurement of suspended sediment concentration: Discussion of four techniques. *Measurement*, 89:44–47, 2016.

David Felix, Ismail Albayrak, and Robert Michael Boes. In-situ investigation on real-time suspended sediment measurement techniques: Turbidimetry, acoustic attenuation, laser diffraction (lisst) and vibrating tube densimetry. *International Journal of Sediment Research*, 33(1):3–17, 2018.

Marius G Floriancic, Daniel Spies, Ilja HJ Van Meerveld, and Peter Molnar. A multi-scale study of the dominant catchment characteristics impacting low-flow metrics. *Hydrological Processes*, 36(1):e14462, 2022.

Kyle F Flynn and Steven C Chapra. Remote sensing of submerged aquatic vegetation in a shallow non-turbid river using an unmanned aerial vehicle. *Remote Sensing*, 6(12): 12815–12836, 2014.

FOEN, Bern, Switzerland. Revitalization of running waters - strategic planning (in german). `www.bafu.admin.ch/dam/bafu/de/dokumente/wasser/uv-umwelt-vollzug/revitalisierung_fliessgewaesserstrategischeplanung.pdf`, 2012. [Accessed 2-March-2024].

Silvia Folegot, Maria Cristina Bruno, Stefano Larsen, Konstantinos Kaffas, Giuseppe R Pisaturo, Andrea Andreoli, Francesco Comiti, and Righetti Maurizio. The effects of a sediment flushing on alpine macroinvertebrate communities. *Hydrobiologia*, 848(17): 3921–3941, 2021.

Dilek Fraisl, Gerid Hager, Baptiste Bedessem, Margaret Gold, Pen-Yuan Hsing, Finn Danielsen, Colleen B Hitchcock, Joseph M Hulbert, Jaume Piera, Helen Spiers, et al. Citizen science in environmental and ecological sciences. *Nature Reviews Methods Primers*, 2(1):64, 2022.

Katharina Fricke and Björn Baschek. Temperature monitoring along the rhine river based on airborne thermal infrared remote sensing: qualitative results compared to satellite data and validation with in situ measurements. In *Remote Sensing for Agriculture, Ecosystems, and Hydrology XVI*, volume 9239, page 923909. International Society for Optics and Photonics, 2014.

Chrystelle Gabbud, Christopher T Robinson, and Stuart N Lane. Summer is in winter: Disturbance-driven shifts in macroinvertebrate communities following hydroelectric power exploitation. *Science of the Total Environment*, 650:2164–2180, 2019.

Min Gao, Junsheng Li, Shenglei Wang, Fangfang Zhang, Kai Yan, Ziyao Yin, Ya Xie, and Wei Shen. Smartphone–camera–based water reflectance measurement and typical water quality parameter inversion. *Remote Sensing*, 14(6):1371, 2022.

John R Gardner, Xiao Yang, Simon N Topp, Matthew RV Ross, Elizabeth H Altenau, and Tamlin M Pavelsky. The color of rivers. *Geophys Res Lett*, 48(1):e2020GL088946, 2021.

S Gerster and P Rey. Ökologische folgen von stauraumspülungen. schriftenreihe umwelt 219. *BUWAL, Bern, Switzerland*, 1994.

David Gillett and Alan Marchiori. A low-cost continuous turbidity monitor. *Sensors*, 19 (14):3039, 2019.

Christopher James Gippel. Potential of turbidity monitoring for measuring the transport of suspended solids in streams. *Hydrological Processes*, 9(1):83–97, 1995.

LM Goddijn and M White. Using a digital camera for water quality measurements in galway bay. *Estuarine, Coastal and Shelf Science*, 66(3-4):429–436, 2006.

Brent M Goehring, Joerg M Schaefer, Christian Schluechter, Nathaniel A Lifton, Robert C Finkel, AJ Timothy Jull, Naki Akçar, and Richard B Alley. The rhone glacier was smaller than today for most of the holocene. *Geology*, 39(7):679–682, 2011.

B Gregor. Denudation of the continents. *Nature*, 228(5268):273–275, 1970.

Günther Grill, B Lehner, Michele Thieme, B Geenen, D Tickner, F Antonelli, S Babu, Pasquale Borrelli, L Cheng, H Crochetiere, et al. Mapping the world's free-flowing rivers. *Nature*, 569(7755):215–221, 2019.

David Grimardias, Jean Guillard, and Franck Cattanéo. Drawdown flushing of a hydroelectric reservoir on the rhône river: Impacts on the fish community and implications for the sediment management. *Journal of environmental management*, 197:239–249, 2017.

Bernard Hallet, Lewis Hunter, and Jim Bogen. Rates of erosion and sediment evacuation by glaciers: A review of field data and their implications. *Global and Planetary Change*, 12(1-4):213–235, 1996.

C Hauer, H Aigner, M Fuhrmann, P Holzapfel, R Rindler, S Pessenlehner, D Pucher, K Skrame, and M Liedermann. Measuring of sediment transport and morphodynamics at the vjosa river/albania. *Report to Riverwatch*, 2019a.

C Hauer, K Skrame, and M Fuhrmann. Hydromorphologial assessment of the vjosa river at the catchment scale linking glacial history and fluvial processes. *Catena*, 207:105598, 2021.

Christoph Hauer, Patrick Leitner, Günther Unfer, Ulrich Pulg, Helmut Habersack, and Wolfram Graf. The role of sediment and sediment dynamics in the aquatic environment. In *Riverine Ecosystem Management*, pages 151–169. Springer, Cham, 2018.

Christoph Hauer, Patrick Holzapfel, Diego Tonolla, Helmut Habersack, and Guido Zolezzi. In situ measurements of fine sediment infiltration (fsi) in gravel-bed rivers with a hydropeaking flow regime. *Earth Surf Proc Land*, 44(2):433–448, 2019b.

Robert T Hensley, Matthew J Cohen, and Larry V Korhnak. Inferring nitrogen removal in large rivers from high-resolution longitudinal profiling. *Limnol Oceanogr*, 59(4):1152–1170, 2014.

Reg Herschy. The velocity-area method. *Flow measurement and instrumentation*, 4(1): 7–10, 1993.

Matthias Hinderer, Martin Kastowski, Achim Kamelger, Carlo Bartolini, and Fritz Schlunegger. River loads and modern denudation of the alps—a review. *Earth-Science Reviews*, 118:11–44, 2013.

Jacob Hirschberg, Simone Fatichi, Georgina L Bennett, Brian W McArdell, Nadav Peleg, Stuart N Lane, Fritz Schlunegger, and Peter Molnar. Climate change impacts on sediment yield and debris-flow activity in an alpine catchment. *Journal of Geophysical Research: Earth Surface*, 2020.

CP Holliday, Todd C Rasmussen, and William P Miller. Establishing the relationship between turbidity and total suspended sediment concentration. Georgia Institute of Technology, 2003.

Bangqi Hu, Houjie Wang, Zuosheng Yang, and Xiaoxia Sun. Temporal and spatial variations of sediment rating curves in the changjiang (yangtze river) basin and their implications. *Quaternary International*, 230(1-2):34–43, 2011.

Hydrographische Dienst Tirol. Hydro online. `https://wiski.tirol.gv.at/hydro/#/Wasserstand?station=201434`. Accessed: 2022-10-06.

Michele Iacobolli, Massimo Orlandi, Domenico Cimini, and Frank S Marzano. Remote sensing of coastal water-quality parameters from sentinel-2 satellite data in the tyrrhenian and adriatic seas. In *2019 PhotonIcs & Electromagnetics Research Symposium-Spring (PIERS-Spring)*, pages 2783–2788. IEEE, 2019.

David W Jensen, E Ashley Steel, Aimee H Fullerton, and George R Pess. Impact of fine sediment on egg-to-fry survival of pacific salmon: a meta-analysis of published studies. *Rev Fish Sci*, 17(3):348–359, 2009.

Lei Ji, Li Zhang, and Bruce Wylie. Analysis of dynamic thresholds for the normalized difference water index. *Photogramm Eng Rem S*, 75(11):1307–1317, 2009.

He Jiang, Yi Hu, Hui Yang, Yiwen Wang, and Shuming Ye. A highly sensitive deep-sea in-situ turbidity sensor with spectrum optimization modulation-demodulation method. *IEEE Sensors Journal*, 20(12):6441–6449, 2020.

John Iwan Jones, JF Murphy, AL Collins, DA Sear, PS Naden, and PD Armitage. The impact of fine sediment on macro-invertebrates. *River research and applications*, 28(8): 1055–1071, 2012.

Pierre Y Julien. *Erosion and sedimentation*. Cambridge university press, 2010.

Dubravko Justić, Nancy N Rabalais, R Eugene Turner, and Quay Dortch. Changes in nutrient structure of river-dominated coastal waters: stoichiometric nutrient balance and its consequences. *Estuar Coast Shelf S*, 40(3):339–356, 1995.

Essayas Kaba, William Philpot, and Tammo Steenhuis. Evaluating suitability of modis-terra images for reproducing historic sediment concentrations in water bodies: Lake tana, ethiopia. *Int J Appl Earth Obs*, 26:286–297, 2014.

Thomas R Karl, Jerry M Melillo, and Thomas C Peterson. *Global climate change impacts in the United States: a state of knowledge report from the US Global Change Research Program*. Cambridge University Press, 2009.

Christopher D Kelley, Alexander Krolick, Logan Brunner, Alison Burklund, Daniel Kahn, William P Ball, and Monroe Weber-Shirk. An affordable open-source turbidimeter. *Sensors*, 14(4):7142–7155, 2014.

Paul Kemp, David Sear, Adrian Collins, Pamela Naden, and Iwan Jones. The impacts of fine sediment on riverine fish. *Hydrol Process*, 25(11):1800–1821, 2011.

Alison Jane King, KA Ward, P O'connor, David Green, Zeb Tonkin, and John Mahoney. Adaptive management of an environmental watering event to enhance native fish spawning and recruitment. *Freshwater biology*, 55(1):17–31, 2010.

Jackie King, Jim A Cambray, and N Dean Impson. Linked effects of dam-released floods and water temperature on spawning of the clanwilliam yellowfish barbus capensis. *Hydrobiologia*, 384:245–265, 1998.

Ben GB Kitchener, John Wainwright, and Anthony J Parsons. A review of the principles of turbidity measurement. *Progress in Physical Geography*, 41(5):620–642, 2017.

Ben GB Kitchener, Simon D Dixon, Kieren O Howarth, Anthony J Parsons, John Wainwright, Mark D Bateman, James R Cooper, Graham K Hargrave, Edward J Long, and Caspar JM Hewett. A low-cost bench-top research device for turbidity measurement by radially distributed illumination intensity sensing at multiple wavelengths. *HardwareX*, 5:e00052, 2019.

Rainer Klose. Poison source in the idyll. URL: `https://www.admin.ch/gov/en/start/documentation/media-releases.msg-id-85501.html`, 10 2021.

Christopher P Konrad, Julian D Olden, David A Lytle, Theodore S Melis, John C Schmidt, Erin N Bray, Mary C Freeman, Keith B Gido, Nina P Hemphill, Mark J Kennard, et al. Large-scale flow experiments for managing river systems. *BioScience*, 61(12):948–959, 2011.

Markus Konz, Michael Chiari, Stefan Rimkus, Jens Martin Turowski, Peter Molnar, Dieter Rickenman, and Paolo Burlando. Sediment transport modelling in a distributed physically based hydrological catchment model. *Hydrology and Earth System Sciences*, 15(9):2821–2837, 2011.

Michèle Koppes, Bernard Hallet, and John Anderson. Synchronous acceleration of ice loss and glacial erosion, glaciar marinelli, chilean tierra del fuego. *Journal of Glaciology*, 55 (190):207–220, 2009.

Michele N Koppes and David R Montgomery. The relative efficacy of fluvial and glacial erosion over modern to orogenic timescales. *Nature Geoscience*, 2(9):644–647, 2009.

Tamara EC Kraus, Kurt D Carpenter, Brian A Bergamaschi, Alexander E Parker, Elizabeth B Stumpner, Bryan D Downing, Nicole M Travis, Frances P Wilkerson, Carol Kendall, and Timothy D Mussen. A river-scale lagrangian experiment examining controls on phytoplankton dynamics in the presence and absence of treated wastewater effluent high in ammonium. *Limnol and Oceanogr*, 62(3):1234–1253, 2017.

Catherine Kuhn, Aline de Matos Valerio, Nick Ward, Luke Loken, Henrique Oliveira Sawakuchi, Milton Kampel, Jeffrey Richey, Philipp Stadler, John Crawford, Rob Striegl, et al. Performance of landsat-8 and sentinel-2 surface reflectance products for river remote sensing retrievals of chlorophyll-a and turbidity. *Remote Sensing of Environment*, 224:104–118, 2019.

Theofanis P Lambrou, Christos C Anastasiou, Christos G Panayiotou, and Marios M Polycarpou. A low-cost sensor network for real-time monitoring and contamination detection in drinking water distribution systems. *IEEE Sensors Journal*, 14(8):2765–2772, 2014.

Stuart N Lane, Maarten Bakker, Chrystelle Gabbud, Natan Micheletti, and Jean-Noël Saugy. Sediment export, transient landscape response and catchment-scale connectivity following rapid climate warming and alpine glacier recession. *Geomorphology*, 277:210–227, 2017.

Theodore Langhorst, Tamlin Pavelsky, Emily Eidam, Julianne Cooper, Lillianand Davis, Katie Spellman, Sarah Clement, Christopher Arp, Allen Bondurant, Elisa Friedmann, and Colin Gleason. Increased scale and accessibility of sediment transport research in rivers through practical, open-source turbidity and depth sensors. *Nature Water*, 1(9): 760 – 768, 2023.

Thomas Leeuw and Emmanuel Boss. The hydrocolor app: Above water measurements of remote sensing reflectance and turbidity using a smartphone camera. *Sensors*, 18(1): 256, 2018.

P Leitner, W Graf, and C Hauer. Ecological assessment of high sediment loads based on macroinvertebrate communities in the bohemian massif in austria–a sensitivity analysis. *Limnologica*, 98:125941, 2023.

Dongfeng Li, Xixi Lu, Irina Overeem, Desmond E Walling, Jaia Syvitski, Albert J Kettner, Bodo Bookhagen, Yinjun Zhou, and Ting Zhang. Exceptional increases in fluvial sediment fluxes in a warmer and wetter high mountain asia. *Science*, 374(6567):599–603, 2021.

Chelsea J Little and Florian Altermatt. Species turnover and invasion of dominant freshwater invertebrates alter biodiversity–ecosystem-function relationship. *Ecological Monographs*, 88(3):461–480, 2018.

Wolfgang Ludwig, Jean-Luc Probst, and Stefan Kempe. Predicting the oceanic input of organic carbon by continental erosion. *Global Biogeochemical Cycles*, 10(1):23–41, 1996.

Federico Maggi, Fiona HM Tang, and Francesco N Tubiello. Agricultural pesticide land budget and river discharge to oceans. *Nature*, 620(7976):1013–1017, 2023.

Tim J Malthus, Renee Ohmsen, and Hendrik J van der Woerd. An evaluation of citizen science smartphone apps for inland water quality assessment. *Remote Sensing*, 12(10): 1578, 2020.

Jean-Michel Martinez, Jean-Loup Guyot, Naziano Filizola, and Francis Sondag. Increase in suspended sediment discharge of the amazon river assessed by monitoring network and satellite data. *Catena*, 79(3):257–264, 2009.

Jan Martini and Johann Waringer. Dynamic microhabitat shifts in space and time of caddisfly larvae (insecta: Trichoptera) in a first-order calcareous mountain stream. *Biologia*, 76(9):2527–2541, 2021.

Jan Martini, Franziska Walther, Tamara Schenekar, Emil Birnstiel, Remo Wüthrich, Rebecca Oester, Bernadette Schindelegger, Thea Schwingshackl, Olivia Wilfling, Florian Altermatt, et al. The last hideout: Abundance patterns of the not-quite-yet extinct mayfly prosopistoma pennigerum in the albanian vjosa river network. *Insect Conserv Diver*, 2022.

Tiago Matos, Carlos L Faria, Marcos S Martins, Renato Henriques, PA Gomes, and Luís M Goncalves. Development of a cost-effective optical sensor for continuous monitoring of turbidity and suspended particulate matter in marine environment. *Sensors*, 19(20): 4439, 2019.

Tiago Matos, CL Faria, Marcos Silva Martins, Renato Henriques, PA Gomes, and LM Goncalves. Design of a multipoint cost-effective optical instrument for continuous in-situ monitoring of turbidity and sediment. *Sensors*, 20(11):3194, 2020.

Morwenna McKenzie, Kate L Mathers, Paul J Wood, Judy England, Ian Foster, Damian Lawler, and Martin Wilkes. Potential physical effects of suspended fine sediment on lotic macroinvertebrates. *Hydrobiologia*, 847:697–711, 2020.

CJ McLaughlin, CA Smith, RW Buddemeier, JD Bartley, and BA Maxwell. Rivers, runoff, and reefs. *Global and Planetary Change*, 39(1-2):191–199, 2003.

Theodore S Melis. Effects of three high-flow experiments on the colorado river ecosystem downstream from glen canyon dam, arizona. Technical report, US Geological Survey, 2011.

MICHEL Meybeck. Origin and variable composition of present day riverborne material. *Material Fluxes on the Surface of the Earth*, pages 61–73, 1994.

Michel Meybeck. Global analysis of river systems: from earth system controls to anthropocene syndromes. *Philosophical Transactions of the Royal Society of London. Series B: Biological Sciences*, 358(1440):1935–1955, 2003.

Marcel Michael, Nicola Gaudenz, Ruedi Haller, Jachen Gaudenz, Giovanini Michelangelo, Pio Pitsch, Thomas Scheurer, Christian Schlüchter, Christopher Robinson, Peter Rey, Stefan Werner, John Hesselschwerdt, Johannes Ortlepp, and Uta Mürle. Schlussbericht umweltunfall spöl. Technical report, HYDRA AG St. Gallen, 2013.

Luke Miller. Arduino library for the ms5803_05ba pressure sensor from measurement specialties. `https://github.com/millerlp/MS5803_05`. Accessed: 2022-08-25.

John D Milliman and Katherine L Farnsworth. *River discharge to the coastal ocean: a global synthesis*. Cambridge University Press, 2013.

John D Milliman, Davide Bonaldo, and Sandro Carniel. Flux and fate of river-discharged sediments to the adriatic sea. *Advances in Oceanography and Limnology*, 7(2), 2016.

Peter Molnar, Paolo Burlando, Jörg Kirsch, and Elke Hinz. Model investigations of the effects of land-use changes and forest damage on erosion in mountainous environments. *IAHS-AISH publication*, pages 589–600, 2006.

Mark D Morehead, James P Syvitski, Eric WH Hutton, and Scott D Peckham. Modeling the temporal variability in the flux of sediment from ungauged river basins. *Global and Planetary change*, 39(1-2):95–110, 2003.

Robert A Morton. *An overview of coastal land loss: with emphasis on the Southeastern United States*. Citeseer, 2003.

Natasha K Nahirnick, Luba Reshitnyk, Marcus Campbell, Margot Hessing-Lewis, Maycira Costa, Jennifer Yakimishyn, and Lynn Lee. Mapping with confidence; delineating seagrass habitats using unoccupied aerial systems (uas). *Remote Sensing in Ecology and Conservation*, 5(2):121–135, 2019.

Martin E Nelson and Paul C Benedict. Measurement and analysis of suspended sediment loads in streams. *Transactions of the American Society of Civil Engineers*, 116(1):891–918, 1951.

Charles P Newcombe and D Donald MacDonald. Effects of suspended sediments on aquatic ecosystems. *North American journal of fisheries management*, 11(1):72–82, 1991.

Cait Newport, Oliver Padget, and Theresa Burt de Perera. High turbidity levels alter coral reef fish movement in a foraging task. *Sci Rep-Uk*, 11(1):1–10, 2021.

Iehisa Nezu and Hiroji Nakagawa. *Turbulence in open-channel flows*. Routledge, 2017.

SW Nixon, JW Ammerman, LP Atkinson, VM Berounsky, Gilles Billen, WC Boicourt, WR Boynton, TM Church, DM Ditoro, Ragnar Elmgren, et al. The fate of nitrogen and phosphorus at the land-sea margin of the north atlantic ocean. *Biogeochemistry*, 35: 141–180, 1996.

Stéfani Novoa, Marcel Wernand, and Hendrik Jan van der Woerd. Wacodi: A generic algorithm to derive the intrinsic color of natural waters from digital images. *Limnology and Oceanography: Methods*, 13(12):697–711, 2015.

Observator. Analite nep-5000-link turbidity handheld, 2024. URL `https://observator.com/products/nep-5000-link-turbidity-handheld/`.

Tom H Oliver, Prosper Bazaanah, Jeff Da Costa, Nabajyoti Deka, Andre Z Dornelles, Matthew P Greenwell, Magesh Nagarajan, Kavin Narasimhan, Emmanuel Obuobie, Marian A Osei, et al. Empowering citizen-led adaptation to systemic climate change risks. *Nature Climate Change*, pages 1–8, 2023.

Milan Onderka and Pavla Pekárová. Retrieval of suspended particulate matter concentrations in the danube river from landsat etm data. *Sci total environ*, 397(1-3):238–243, 2008.

Johannes Ortlepp and Uta Mürle. Effects of experimental flooding on brown trout (salmo trutta fario l.): The river spöl, swiss national park. *Aquatic Sciences*, 65:232–238, 2003.

I Overeem, Brian D Hudson, James PM Syvitski, Andreas B Mikkelsen, B Hasholt, MR Van Den Broeke, BPY Noël, and M Morlighem. Substantial export of suspended sediment to the global oceans from glacial erosion in greenland. *Nature Geoscience*, 10(11):859–863, 2017.

Nima Pahlevan, Sundarabalan V Balasubramanian, Sudipta Sarkar, and Bryan A Franz. Toward long-term aquatic science products from heritage landsat missions. *Remote Sens-Basel*, 10(9):1337, 2018.

Lorena Parra, Javier Rocher, Julia Escrivá, and Jaime Lloret. Design and development of low cost smart turbidity sensor for water quality monitoring in fish farms. *Aquacultural Engineering*, 81:10–18, 2018.

Anthony John Parsons, James Cooper, and John Wainwright. What is suspended sediment? *Earth Surface Processes and Landforms*, 40(10):1417–1420, 2015.

Donatella Pavanelli and Alessandro Bigi. A new indirect method to estimate suspended sediment concentration in a river monitoring programme. *Biosystems Engineering*, 92 (4):513–520, 2005.

Sebastian Pessenlehner, Marcel Liedermann, Patrick Holzapfel, Klodian Skrame, Helmut Habersack, and Christoph Hauer. Evaluation of hydropower projects in balkan rivers based on direct sediment transport measurements; challenges, limits and possible data interpretation–case study vjosa river/albania. *River Res Appl*, 2022.

Bernhard Peucker-Ehrenbrink. Land2sea database of river drainage basin sizes, annual water discharges, and suspended sediment fluxes. *Geochemistry, Geophysics, Geosystems*, 10(6), 2009.

N LeRoy Poff, J David Allan, Margaret A Palmer, David D Hart, Brian D Richter, Angela H Arthington, Kevin H Rogers, Judy L Meyer, and Jack A Stanford. River flows and water wars: emerging science for environmental decision making. *Frontiers in Ecology and the Environment*, 1(6):298–306, 2003.

Matteo Postacchini, Luca R Centurioni, Lance Braasch, Maurizio Brocchini, and Diego Vicinanza. Lagrangian observations of waves and currents from the river drifter. *IEEE J Oceanic Eng*, 41(1):94–104, 2015.

Sandra Postel, Stephen Carpenter, et al. Freshwater ecosystem services. In Gretchen Cara Daily, editor, *Nature's services: Societal dependence on natural ecosystems*, volume 195, chapter 11. Island Press, Washington, DC, 1997.

Octavian A Postolache, PMB Silva Girao, JM Dias Pereira, and Helena Maria G Ramos. Multibeam optical system and neural processing for turbidity measurement. *IEEE Sensors Journal*, 7(5):677–684, 2007.

Gaëlle Poulier, Marina Launay, Chloé Le Bescond, Fabien Thollet, Marina Coquery, and Jérôme Le Coz. Combining flux monitoring and data reconstruction to establish annual budgets of suspended particulate matter, mercury and pcb in the rhône river from lake geneva to the mediterranean sea. *Science of the Total Environment*, 658:457–473, 2019.

Shi Qiu, Zhe Zhu, and Binbin He. Fmask 4.0: Improved cloud and cloud shadow detection in landsats 4–8 and sentinel-2 imagery. *Remote Sens Environ*, 231:111205, 2019.

Valentina Radić and Regine Hock. Glaciers in the earth's hydrological cycle: assessments of glacier mass and runoff changes on global and regional scales. *Surveys in Geophysics*, 35:813–837, 2014.

Anant Kr Rai and Arun Kumar. Continuous measurement of suspended sediment concentration: Technological advancement and future outlook. *Measurement*, 76:209–227, 2015.

Jerry C Ritchie, Paul V Zimba, and James H Everitt. Remote sensing techniques to assess water quality. *Photogramm Eng Rem S*, 69(6):695–704, 2003.

rivertechlabs. rivertechlabs: babyturbidity, 2022. URL `https://github.com/rivertechlabs/babyturbidity`.

Christopher T Robinson and Urs Uehlinger. Experimental floods cause ecosystem regime shift in a regulated river. *Ecological Applications*, 18(2):511–526, 2008.

Christopher T Robinson, Urs Uehlinger, and Michael T Monaghan. Effects of a multi-year experimental flood regime on macroinvertebrates downstream of a reservoir. *Aquatic Sciences*, 65:210–222, 2003.

Christopher T Robinson, URS Uehlinger, and Michael T Monaghan. Stream ecosystem response to multiple experimental floods from a reservoir. *River Research and Applications*, 20(4):359–377, 2004.

Christopher T Robinson, Andre R Siebers, and Johannes Ortlepp. Long-term ecological responses of the river spöl to experimental floods. *Freshwater Science*, 37(3):433–447, 2018.

Christopher T Robinson, Gabriele Consoli, and Johannes Ortlepp. Importance of artificial high flows in maintaining the ecological integrity of a regulated river. *Science of The Total Environment*, 882:163569, 2023.

Javier Rocher, Mar Parra, Lorena Parra, Sandra Sendra, Jaime Lloret, and Jesús Mengual. A low-cost sensor for detecting illicit discharge in sewerage. *Journal of Sensors*, 2021: 1–16, 2021.

Javier Rocher, Abdulaziz Aldegheishem, Nabil Alrajeh, and Jaime Lloret. Develop an optical sensor to detect pollution incidents in sewerage. *IEEE Sensors Journal*, 22(24): 24449–24457, 2022.

Javier Rocher, Jose M Jimenez, Jesus Tomas, and Jaime Lloret. Low-cost turbidity sensor to determine eutrophication in water bodies. *Sensors*, 23(8):3913, 2023.

Luiz Henrique S Rotta, Deepak R Mishra, Fernanda SY Watanabe, Thanan WP Rodrigues, Enner H Alcântara, and Nilton N Imai. Analyzing the feasibility of a space-borne sensor (spot-6) to estimate the height of submerged aquatic vegetation (sav) in inland waters. *ISPRS Journal of Photogrammetry and Remote Sensing*, 144:341–356, 2018.

PS Roy, RJ Williams, AR Jones, I Yassini, PJ Gibbs, B Coates, RJ West, PR Scanes, JP Hudson, and S Nichol. Structure and function of south-east australian estuaries. *Estuarine, Coastal and Shelf Science*, 53(3):351–384, 2001.

Michael J Sadar. Turbidity science. technical information seriesbooklet no. 11. *Hach Co. Loveland CO*, 7:8, 1998.

Debi Prasad Sahoo, Bhabagrahi Sahoo, and Manoj Kumar Tiwari. Modis-landsat fusion-based single-band algorithms for tss and turbidity estimation in an urban-waste-dominated river reach. *Water Res*, page 119082, 2022.

Richard Sanders, Stephanie A Henson, Marja Koski, LDLR Christina, Stuart C Painter, Alex J Poulton, Jennifer Riley, Baris Salihoglu, Andre Visser, Andrew Yool, et al. The biological carbon pump in the north atlantic. *Progress in Oceanography*, 129:200–218, 2014.

Ueli Schälchli. The clogging of coarse gravel river beds by fine sediment. *Hydrobiologia*, 235(1):189–197, 1992.

T Scheurer and P Molinari. Experimental floods in the river spol. *Swiss National Park*, 2003.

FR Schiebe, JA Harrington Jr, and JC Ritchie. Remote sensing of suspended sediments: the lake chicot, arkansas project. *Int J Remote Sens*, 13(8):1487–1509, 1992.

Fritz Schiemer, Sajmir Beqiraj, Wolfram Graf, and Aleko Miho. *The Vjosa in Albania: a riverine ecosystem of European significance*. Acta ZooBot Austria, 2018a.

Fritz Schiemer, Anton Drescher, Christoph Hauer, and Ulrich Schwarz. The vjosa river corridor: a riverine ecosystem of european significance. *Acta ZooBot Austria*, 155(1): 1–40, 2018b.

HJ Seybold, P Molnar, HM Singer, José S Andrade Jr, Hans Jürgen Herrmann, and W Kinzelbach. Simulation of birdfoot delta formation with application to the mississippi delta. *Journal of Geophysical Research: Earth Surface*, 114(F3), 2009.

Patrick B Shafroth, Andrew C Wilcox, David A Lytle, John T Hickey, Douglas C Andersen, Vanessa B Beauchamp, Andrew Hautzinger, LAURA E McMULLEN, and Andrew Warner. Ecosystem effects of environmental flows: modelling and experimental floods in a dryland river. *Freshwater Biology*, 55(1):68–85, 2010.

Mark A Siebentritt, George G Ganf, and Keith F Walker. Effects of an enhanced flood on riparian plants of the river murray, south australia. *River Research and Applications*, 20 (7):765–774, 2004.

U Simeoni, N Pano, and P Ciavola. The coastline of albania: morphology, evolution and coastal management issues. *Bulletin-Institut Oceanographique Monaco-Numero Special-*, pages 151–168, 1997.

Softpedia.com. H2testw. `https://www.softpedia.com/get/System/System-Miscellaneous/H2testw.shtml`. Accessed: 2022-08-25.

Yves Souchon, Catherine Sabaton, Robert Deibel, Dudley Reiser, Jeffrey Kershner, Mark Gard, Christos Katopodis, Paul Leonard, N Leroy Poff, William J Miller, et al. Detecting biological responses to flow management: missed opportunities; future directions. *River Research and applications*, 24(5):506–518, 2008.

Rachel Stubbington. The hyporheic zone as an invertebrate refuge: a review of variability in space, time, taxa and behaviour. *Marine and Freshwater Research*, 63(4):293–311, 2012.

TF Sutherland, PM Lane, CL Amos, and John Downing. The calibration of optical backscatter sensors for suspended sediment of varying darkness levels. *Marine Geology*, 162(2-4):587–597, 2000.

Jaia Syvitski, Juan Restrepo Ángel, Yoshiki Saito, Irina Overeem, Charles J Vörösmarty, Houjie Wang, and Daniel Olago. Earth's sediment cycle during the anthropocene. *Nat Rev Earth Env*, 3(3):179–196, 2022.

James PM Syvitski and Albert Kettner. Sediment flux and the anthropocene. *Philosophical Transactions of the Royal Society A: Mathematical, Physical and Engineering Sciences*, 369(1938):957–975, 2011.

James PM Syvitski and John D Milliman. Geology, geography, and humans battle for dominance over the delivery of fluvial sediment to the coastal ocean. *J Geol*, 115(1): 1–19, 2007.

Jens Terhaar, Ronny Lauerwald, Pierre Regnier, Nicolas Gruber, and Laurent Bopp. Around one third of current arctic ocean primary production sustained by rivers and coastal erosion. *Nat Comm*, 12(1):1–10, 2021.

The SD Association. Sd memory card formatter. `https://www.sdcard.org/downloads/formatter/`. Accessed: 2022-08-25.

Fabien Thollet, Christophe Rousseau, Benoit Camenen, Stephane Boubkraoui, Flora Branger, François Lauters, and Julien Némery. Long term high frequency sediment observatory in an alpine catchment: The arc-isère rivers, france. *Hydrological Processes*, 35(2):e14044, 2021.

J Manuel Tierno de Figueroa, Manuel J López-Rodríguez, Stefano Fenoglio, Pedro Sánchez-Castillo, and Romolo Fochetti. Freshwater biodiversity in the rivers of the mediterranean basin. *Hydrobiologia*, 719:137–186, 2013.

Jonathan D Tonkin, Florian Altermatt, Debra S Finn, Jani Heino, Julian D Olden, Steffen U Pauls, and David A Lytle. The role of dispersal in river network metacommunities: Patterns, processes, and pathways. *Freshwater Biology*, 63(1):141–163, 2018.

Nguyen T Tran, Chris G Campbell, and Frank G Shi. Study of particle size effects on an optical fiber sensor response examined with monte carlo simulation. *Applied Optics*, 45 (29):7557–7566, 2006.

Jarrod Trevathan, Wayne Read, and Simon Schmidtke. Towards the development of an affordable and practical light attenuation turbidity sensor for remote near real-time aquatic monitoring. *Sensors*, 20(7):1993, 2020.

Jarrod Trevathan, Wayne Read, and Abdul Sattar. Implementation and calibration of an iot light attenuation turbidity sensor. *Internet of Things*, 19:100576, 2022.

Magdalena Uber, Guillaume Nord, Cédric Legout, and Luis Cea. How do modeling choices and erosion zone locations impact the representation of connectivity and the dynamics of suspended sediments in a multi-source soil erosion model? *Earth Surface Dynamics*, 9(1):123–144, 2021.

SV Ugelvig, DL Egholm, RS Anderson, and Neal R Iverson. Glacial erosion driven by variations in meltwater drainage. *Journal of Geophysical Research: Earth Surface*, 123 (11):2863–2877, 2018.

United Nations Development Programme UNDP. Hdr 2006—beyond scarcity: Power, poverty and the global water crisis. *UNDP (United Nations Development Programme)*, 2006.

Q Vanhellemont. Acolite user manual (qv - august 2, 2021). `https://github.com/acolite/acolite/releases/tag/20210802.0`. Accessed: 2022-10-27.

Quinten Vanhellemont. Adaptation of the dark spectrum fitting atmospheric correction for aquatic applications of the landsat and sentinel-2 archives. *Remote Sens Environ*, 225:175–192, 2019.

Quinten Vanhellemont and Kevin Ruddick. Advantages of high quality swir bands for ocean colour processing: Examples from landsat-8. *Remote Sens Environ*, 161:89–106, 2015.

Quinten Vanhellemont and Kevin Ruddick. Acolite for sentinel-2: Aquatic applications of msi imagery. In *Proceedings of the 2016 ESA Living Planet Symposium, Prague, Czech Republic*, pages 9–13, 2016.

Quinten Vanhellemont and Kevin Ruddick. Atmospheric correction of metre-scale optical satellite data for inland and coastal water applications. *Remote Sens Environ*, 216: 586–597, 2018.

Charles J Vörösmarty, Peter B McIntyre, Mark O Gessner, David Dudgeon, Alexander Prusevich, Pamela Green, Stanley Glidden, Stuart E Bunn, Caroline A Sullivan, C Reidy Liermann, et al. Global threats to human water security and river biodiversity. *nature*, 467(7315):555–561, 2010.

Carl Walters, Lance Gunderson, and CS Holling. Experimental policies for water management in the everglades. *Ecological applications*, 2(2):189–202, 1992.

Hanghang Wang, Jie Wang, Yuhuan Cui, and Shijiang Yan. Consistency of suspended particulate matter concentration in turbid water retrieved from sentinel-2 msi and landsat-8 oli sensors. *Sensors*, 21(5):1662, 2021.

Xuebing Wang, Difeng Wang, Fang Gong, and Xianqiang He. Remote sensing inversion of total suspended matter concentration in oujiang river based on landsat-8/oli. In *Ocean Optics and Information Technology*, volume 10850, page 108500X. International Society for Optics and Photonics, 2018a.

Ying Hsuan Wang and Hong-Gyoo Sohn. Estimation of river pollution index using landsat imagery over tamsui river, taiwan. *Ecology and Resilient Infrastructure*, 5(2):88–93, 2018.

Youchao Wang, SM Shariar Morshed Rajib, Chris Collins, and Bruce Grieve. Low-cost turbidity sensor for low-power wireless monitoring of fresh-water courses. *IEEE Sensors Journal*, 18(11):4689–4696, 2018b.

Yuxin Wang, Xianqiang He, Yan Bai, Difeng Wang, Qiankun Zhu, Fang Gong, Dingtian Yang, and Teng Li. Satellite retrieval of benthic reflectance by combining lidar and passive high-resolution imagery: Case-i water. *Remote Sensing of Environment*, 272: 112955, 2022.

Zhao-Yin Wang, Yitian Li, and Yiping He. Sediment budget of the yangtze river. *Water Resources Research*, 43(4), 2007.

Zhaocheng Wang and Enrique R Vivoni. Detecting streamflow in dryland rivers using cubesats. *Geophysical Research Letters*, 49(15):e2022GL098729, 2022.

JV Ward, Klement Tockner, and Fritz Schiemer. Biodiversity of floodplain river ecosystems: ecotones and connectivity1. *River Research and Applications*, 15(1-3):125–139, 1999.

JA Waringer. The drag coefficient of cased caddis larvae from running waters: experimental determination and ecological applications. *Freshwater Biology*, 29(3):419–427, 1993.

Johann Waringer, Simon Vitecek, Jan Martini, Carina Zittra, Ariane Vieira, and Hendrik C Kuhlmann. Case design and flow resistance in high-alpine caddisfly larvae (insecta, trichoptera). *Hydrobiologia*, 849(19):4259–4271, 2022.

PD Wass, SD Marks, JW Finch, G J [xdot] L Leeks, and JK Ingram. Monitoring and preliminary interpretation of in-river turbidity and remote sensed imagery for suspended sediment transport studies in the humber catchment. *Sci total environ*, 194:263–283, 1997.

Jianwei Wei, Zhongping Lee, Rodrigo Garcia, Laura Zoffoli, Roy A Armstrong, Zhehai Shang, Patrick Sheldon, and Robert F Chen. An assessment of landsat-8 atmospheric correction schemes and remote sensing reflectance products in coral reefs and coastal turbid waters. *Remote Sens Environ*, 215:18–32, 2018.

Gabriele Weigelhofer and Johann Waringer. Vertical distribution of benthic macroinvertebrates in riffles versus deep runs with differing contents of fine sediments (weidlingbach, austria). *International Review of Hydrobiology: A Journal Covering all Aspects of Limnology and Marine Biology*, 88(3-4):304–313, 2003.

MA Wilkes, JL Carrivick, E Castella, C Ilg, S Cauvy-Fraunié, SC Fell, L Füreder, Matthias Huss, W James, V Lencioni, et al. Glacier retreat reorganizes river habitats leaving refugia for alpine invertebrate biodiversity poorly protected. *Nature Ecology & Evolution*, pages 1–11, 2023.

Christopher N Wold and William W Hay. Estimating ancient sediment fluxes. *American Journal of Science*, 290(9):1069–1089, 1990.

DG Wren, BD Barkdoll, RA Kuhnle, and RW Derrow. Field techniques for suspended-sediment measurement. *Journal of Hydraulic Engineering*, 126(2):97–104, 2000.

World Water Assessment Programme WWAP. Water in a changing world. *The United Nations World Water Development Report 3*, 2009.

Ali P Yunus, Yoshifumi Masago, and Yasuaki Hijioka. Covid-19 and surface water quality: Improved lake water quality during the lockdown. *Sci total environ*, 731:139012, 2020.

Michael Zemp, Wilfried Haeberli, Martin Hoelzle, and Frank Paul. Alpine glaciers to disappear within decades? *Geophysical Research Letters*, 33(13), 2006.

Jürg Zobrist, Lura Sigg, and Ursula Schoenenberger. Naduf – thematische auswertung der messresultate 1974 bis 1998. Technical report, Eidgenössische Anstalt für Wasserversorgung, Abwasserreinigung und Gewässerschutz EAWAG, 2004.

Appendix G Curriculum Vitae

Education

Ph.D Environmental Engineering — *May 2024 (expected)*
ETH Zurich — Zurich, Switzerland
Supervisors: Prof. Peter Molnar and Prof. Gabriel Singer

M.Sc Mechanical Engineering — *August 2019*
ETH Zurich — Zurich, Switzerland
Specialization: Computational Fluid Dynamics and Thermoacoustic Instabilities
Masters Thesis Title: "LES Investigation of Acoustic Modes in a Sequential Burner"
Supervisor: Prof. Nicolas Noiray
Cumulative Grade Point Average: 5.43/6

B.Eng Honours Mechanical & Aeronautical Engineering — *May 2016*
McGill University — Montreal, Canada
Canadian Society of Mechanical Engineers (CSME) Gold Medal: For outstanding academic achievement
Dean's Honours List: Top 10% of graduating class
Honours Thesis Title: "Effect of Initial Temperature on the Burning Velocity of Premixed Laminar Aluminum-Air Flames"
Supervisors: Prof. Jeffrey Bergthorson & Prof. David Frost
Cumulative Grade Point Average: 3.83/4

Work Experience

Ecohydrology Department, IGB Berlin — *March - October 2019*
Research Assistant — Berlin, Germany

Combustion and Modeling group, Ansaldo Energia — *March 2018 - February 2019*
R&D Engineering Intern — Baden, Switzerland

Alternative Fuels Laboratory (AFL), McGill University — *January 2015 - May 2016*
Undergraduate Student Researcher and Lab Manager — Montreal, Canada

Pratt & Whitney Canada — *May 2014 - September 2014*
New Product Introduction (NPI) Strategic Sourcing Intern — Montreal, Canada

Publications

In Preparation
Droujko et al. Interconnected sediment dynamics in the Spöl and Inn rivers through high-resolution monitoring during environmental floods.

Earth Surface Dynamics — *September 2023*
Droujko et al. (2023). Sediment source and sink identification using Sentinel-2 and (kayak-based) lagrangian river turbidity profiles on the Vjosa River. EGUsphere, 2023, 1-24.

Nature News & Views — *September 2023*
Droujko and Molnar (2023) Open-source self-made sensors show high potential in river research. Nature News & Views.

HardwareX — *January 2023*
Droujko et al. (2023). Ötz-T: 3D-printed open-source turbidity sensor with Arduino shield for suspended sediment monitoring. HardwareX, 13, e00395.

Scientific Reports — *June 2022*
Droujko, J., and Molnar, P. (2022). Open-source, low-cost, in-situ turbidity sensor for river network monitoring. Scientific Reports, 12(1), 10341.